C3ETCV'23

Conference

Proceedings of the

1st National Conference

On Electronics, Electrical Engineering, Telecommunications, and Computer Vision
(C3ETCV' 23)

EDITORS

Khaled HARRAR

Hamza AKROUM

Mohammed AMMAR

Karim BAICHE

Abderezzak AIBECHE

Youcef TABET

Samia BELKACEM

Noureddine MESSAOUDI

Yassine MERAIHI

1st National Conference on Electronics, Electrical Engineering, Telecommunications, and Computer Vision

C3ETCV'23

Boumerdes – Algeria, Nov 06, 2023

Edition

Faculty of Technology, of the University M'Hamed Bougara of Boumerdes, Algeria

C3ETCV 2023

Editors:

Khaled HARRAR   Hamza AKROUM
Mohammed AMMAR   Karim BAICHE
Abderezzak AIBECHE   Youcef TABET
Samia BELKACEM   Noureddine MESSAOUDI
Yassine MERAIHI

Preface

Welcome to the 1ˢᵗ National Conference on Electronics, Electrical Engineering, Telecommunications, and Computer Vision (C3ETCV'23), held at the Faculty of Technology, University M'Hamed Bougara of Boumerdes, Algeria, on November 06ᵗʰ, 2023.

This conference serves as a dynamic platform for researchers, engineers, and scientists to converge and share their latest advancements and research findings in the expansive realms of Electronics, Electrical Engineering, Telecommunications, and Computer Vision. The aim is to foster a collaborative environment that stimulates the exchange of ideas and innovations, ultimately contributing to the growth and evolution of these rapidly evolving fields.

The conference encompasses three distinct tracks, each delving into specialized domains:

Track 1: Electronics and Electrical Engineering *This track encompasses a diverse range of topics, from Embedded & IoT systems to Power Electronics, providing a comprehensive exploration of contemporary challenges and breakthroughs in the field.*

Track 2: Telecommunications *With the pervasive influence of Telecommunications in our interconnected world, this track dives into Wireless Communications, Smart Grids, 5G Communication Networks, and more.*

Track 3: Computer Vision *In the era of Artificial Intelligence, Computer Vision plays a pivotal role. This track delves into Artificial Intelligence, Signal and Image Processing, Bioinformatics, and Machine Learning. The conference provides a stage for experts to showcase their work in creating intelligent systems that can perceive and interpret the visual world, with applications ranging from healthcare to multimedia.*

topics covered in this conference. The papers presented here reflect a wealth of knowledge, spanning from theoretical foundations to practical applications, and we are confident that they will inspire further exploration and innovation.

We also express our sincere appreciation to the organizing committee, reviewers, and the Faculty of Technology at the University M'Hamed Bougara of Boumerdes for their unwavering support in making this conference a reality.

Thank you for being part of C3ETCV'23.

Conference Chairs
Pr. Khaled HARRAR
Dr. Hamza AKROUM

Organizers

Honorary General Chairs

Pr. YAHI Mustapha, Rector of Univ. Boumerdes, Algeria
Pr. SAIDI Mohammed, Dean of the Faculty of Technology, Univ. Boumerdes, Algeria

Conference General Chairs

Pr. HARRAR Khaled, Univ. Boumerdes, Algeria
Dr. AKROUM Hamza, Univ. Boumerdes, Algeria

Conference General Co-Chairs

Pr. AMMAR Mohammed, Univ. Boumerdes, Algeria
Dr. AIBECHE Abderezzak, Univ. Boumerdes, Algeria
Dr. BELKACEM Samia, Univ. Boumerdes, Algeria
Dr. MESSAOUDI Noureddine, Univ. Boumerdes, Algeria
Dr. TABET Youcef, Univ. Boumerdes, Algeria

Organizing Committee Chair

Pr. MERAIHI Yassine, Univ. Boumerdes, Algeria
Dr. BAICHE Karim, Univ. Boumerdes, Algeria

Organizing Committee

Dr. AMROUCHE Dahbia, Univ. Boumerdes, Algeria
Dr. BOUSTIL Amel, Univ. Boumerdes, Algeria
Dr. DAOUI Abdelhakim, Univ. Boumerdes, Algeria
Dr. GUERBAI Yasmine, Univ. Boumerdes, Algeria
Dr. MAHDI Ismahane, Univ. Boumerdes, Algeria
Mr. HAMIDAT Ibrahim, Univ. Boumerdes, Algeria
Mr. HIOU Mohamed Yanis, Univ. Boumerdes, Algeria
Miss. IBAOUNI Faiza, Univ. Boumerdes, Algeria
Miss. MESSAOUDENE Khadidja, Univ.Boumerdes, Algeria
Miss. TIRECHE Sihem, Univ. Boumerdes, Algeria

Scientific Committee

Pr. ACHELI Dalila, Univ. Boumerdes, Algeria
Pr. AHRICHE Aimad, Univ. Boumerdes, Algeria
Pr. AMMAR Mohammed, Univ. Boumerdes, Algeria
Pr. AZRAR Arab, Univ. Boumerdes, Algeria
Pr. BENTARZI Hamid, Univ. Boumerdes, Algeria
Pr. BOUDEN Toufik, Univ. Jijel, Algeria
Pr. BOUKABOU Abdelkrim, Univ. Jijel, Algeria

Pr. BOUSHAKI Razika, Univ. Boumerdes, Algeria
Pr. CHALLAL Mouloud, Univ. Boumerdes, Algeria
Pr. DAAMOUCHE Abdelhamid, Univ. Boumerdes, Algeria
Pr. FELLAG Sid Ali, Univ. Boumerdes, Algeria
Pr. HAMADOUCHE M'Hamed, Univ. Boumerdes, Algeria
Pr. HARKAT Mohammed Faouzi, Univ. Annaba, Algeria
Pr. HARRAR Khaled, Univ. Boumerdes, Algeria
Pr. HOCINI Abdesselem, Univ. M'sila, Algeria
Pr. KESRAOUI Mohamed, Univ. Boumerdes, Algeria
Pr. KHELDOUN Aissa, Univ. Boumerdes, Algeria
Pr. KHOUAS Abdelhakim, Univ. Boumerdes, Algeria
Pr. KIDOUCHE Madjid, Univ. Boumerdes, Algeria
Pr. KOUADRI Abdelmalek, Univ. Boumerdes, Algeria
Pr. LACHOURI Abderezzak, Univ. Skikda, Algeria
Pr. MERAIHI Yassine, Univ. Boumerdes, Algeria
Pr. NADJI Bouchra, Univ. Boumerdes, Algéria
Pr. RAHMOUNE Fayçal, Univ. Boumerdes, Algeria
Pr. RECIOUI Abdelmadjid, Univ. Boumerdes, Algeria
Pr. RIAHLA Mohamed Amine, Univ. M'sila, Algeria
Dr. AIBECHE Abderezzak, Univ. Boumerdes, Algeria
Dr. AKLI Isma, CDTA, Algeria
Dr. AKROUM Hamza, Univ. Boumerdes, Algeria
Dr. AYAD Mouloud, Univ. Bouira, Algeria
Dr. BAICHE Karim, Univ. Boumerdes, Algeria
Dr. BELAIDI Hadjira, Univ. Boumerdes, Algeria
Dr. BELKACEM Samia, Univ. Boumerdes, Algeria
Dr. BENBELKACEM, CDTA, Algeria
Dr. BENLATRECHE Mohamed Salah, Univ. Mila, Algeria
Dr. BENZAOUI Amir, Univ. Skikda, Algeria
Dr. BOUDOUDA Aimad, Univ. Boumerdes, Algeria
Dr. BOURKACHE Noureddine, Univ. Tizi Ouzou, Algeria
Dr. BOUSTIL Amel, Univ. Boumerdes, Algeria
Dr. BOUZAR-BENLABIOD Lydia, ESI, Algeria
Dr. BOUZID-DAHO Abdellatif, Univ. Tizi Ouzou, Algeria
Dr. CHERRAT Nidhal, Univ. Boumerdes, Algeria
Dr. DAOUI Abdelhakim, Univ. Boumerdes, Algeria
Dr. DEKHANDJI Fatma Zohra, Univ. Boumerdes, Algeria
Dr. DOGHMANE Mohamed Zinelabidine, SONATRACH, Algeria
Dr. GUERBAI Yasmine, Univ. Boumerdes, Algeria
Dr. HENTOUT Abdelfetah, CDTA, Algeria
Dr. HOCINE Faiza, Univ. Boumerdes, Algeria
Dr. IDIR Abdelhakim, Univ. M'sila, Algeria
Dr. MAHDI Ismahane, Univ. Boumerdes, Algeria

Dr. MAHSEUR Mohammed, Univ. Alger-1, Algeria
Dr. MANSOUL Ali, CDTA Algeria
Dr. MESSAOUDI Noureddine, Univ. Boumerdes, Algeria
Dr. MOUATSI Abdelmalek, Univ. Boumerdes, Algeria
Dr. NAFA Fares, Univ. Boumerdes, Algeria
Dr. OMARI Tahar, Univ. Boumerdes, Algeria
Dr. OURARI Samia, Univ. Boumerdes, Algeria
Dr. REZZOUG Abdellah, Univ. Boumerdes, Algeria
Dr. SEDJELMACI Ibticeme, Univ. Boumerdes, Algeria
Dr. SMAANI Billel, Univ. Mila, Algeria
Dr. TABET Youcef, Univ. Boumerdes, Algeria
Dr. TIBERKAK Allal, Univ. Médéa, Algeria
Dr. TOUBAL MAAMAR Alla Eddine, Univ. Boumerdes, Algeria

Invited Speakers

Multi-agent Systems' Application

Dr. Hadjira BELAIDI
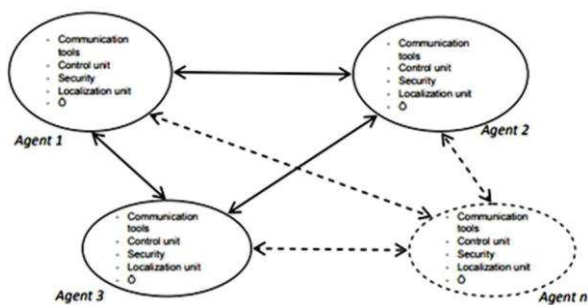Univ. Boumerdes,
Algeria

Abstract

A multi-agent system (MAS or "self-organized system") is a computerized system composed of multiple interacting intelligent agents. It can be divided to many different sub-systems as shown in Fig.1. An agent is a computer system that is embedded in a given environment and has the ability to function autonomously within that environment in order to accomplish its intended goals.

One agent can play one or more roles. All agents coordinate with subsystems. Interactions among agents can be ensured via communication network or internet. Whereas, the role of the smart agent determines the part of the system in which can receive and send the data. Therefore, all agents coordinate with each other inside the same sub-system and with the other agents out of the sub-system via the management agents.

The concept 'agent' has been integrated in a number of technologies and has been largely used in several fields; for the reason that MAS converts a centralized control system into a distributed control model at a component level

This presentation focuses on the applications of MAS in different fields in general and especially in Robotics and smart grids. Most descriptions approve that an agent is fundamentally a special software/hardware component that has some intelligence and autonomy that provides an interoperable interface to an arbitrary system and/or cooperates with some clients and other agents in pursuit of its own agenda. Hence, the communication between the agents and MAS is among the possible challenges for implementing MAS in the industry.

Biography

Hadjira BELAIDI received her Doctorate degree from the Institute of Electrical and Electronic Engineering, University M'hamed Bougara of Boumerdes in 2015. She has been an assistant professor at the Institute of Electrical and Electronic Engineering since 2014. Currently, she is the leader of the "Embedded Systems and Robotics" team in the Signals and Systems Laboratory, as well as a lecturer at the Department of Electronics at the Institute of Electrical and Electronic Engineering, University M'hamed Bougara of Boumerdes, Algeria. Her research interests include all-terrain mobile robots, environment modelling and manipulator robots, drone control, and smart-grid. She can be contacted at email: ha.belaidi@univ-boumerdes.dz.

Papers

Contents

Compact Dual-band Monopole Antenna Based On Double T Shaped Ring Patch for Sub 6 GHz 5G Applications

Fatma Zohra Hamrioui
Laboratoire des Dispositifs de Communication
et de Conversion Photovoltaïque (LDCCP)
Electronic Department
National Polytechnic School of Algiers
Algiers, Algeria
E-mail: fatma_zohra.hamrioui@g.enp.edu.dz

Rachida Touhami
Laboratoire des Dispositifs de Communication
et de Conversion Photovoltaïque (LDCCP)
Electronic Department
National Polytechnic School of Algiers
Algiers, Algeria
E-mail: rachida.touhami@g.enp.edu.dz

Mustapha C.E. Yagoub
ELEMENT Laboratory,
School of Electrical Engineering and Computer Science,
University of Ottawa
Ottawa, Canada
E-mail: myagoub@uottawa.ca

Abstract— **In this paper, a dual-band monopole antenna for sub-6GHz 5G applications is presented. Based on a double T-shaped ring patch, the proposed antenna is made up of two rings that are T-shaped, generating two separated bands: the lower at the resonant frequency of 3.55 GHz with fractional bandwidth of 38.5 % (i.e., 3.05 GHz-4.40 GHz), and the higher at the resonant frequency of 6.55 GHz with fractional bandwidth 22.17 % (i.e., 6.05 GHz-7.50 GHz). Note that the additional ring can control the second operating band without impacting the first band. This compact antenna, of size 22.5 x 23 mm^2 ($0.47\lambda_g \times 0.49\lambda_g$), exhibits a good performance in terms of impedance matching and high fractional bandwidth, providing omnidirectional pattern radiation properties over the desired operational frequency bands.**

Keywords—dual-band, T-shaped, antenna, 5G, Sub-6GHz.

I. INTRODUCTION

With the development of wireless communication technologies, the fifth generation (5G) communication technology has emerged as the leading development trend in recent years [1], mainly because of its high data rate, high speed, low latency, increased capacity, and connectivity [2]. From the allocated 5G frequency bands, the telecommunications industry places a high priority on the sub-6GHz band [3], because it meets the current data rate requirements in Gbps and wider coverage area, making it compatible with the requirement of Internet-of-things (IoT) devices that demand reliable coverage in smart applications [4]. Designing 5G systems presents new challenges and, as critical parts, the need for enhanced antennas with excellent performance such as low-profile properties, high fractional bandwidth, and ease of integration, are in high demand [1] [5] [6].

In this paper, the design of a new compact dual-band monopole antenna is presented. It starts with a single T-shaped ring patch to cover the N77 (i.e., 3.30 GHz-4.20 GHz) and N78 (i.e., 3.30 GHz-3.80 GHz) bands (called "Antenna I"). Then, a second T-shaped ring was introduced in order to create another band that covers the 6GHz 5G candidate (6.425-7.125 GHz) without interfering with the first band ("Antenna II"). With a size of 22.5 x 23 mm^2 ($0.47\lambda_g \times 0.49\lambda_g$) and a thickness of 1.62 mm, the antenna provides omnidirectional pattern radiation properties over the desired operational frequency bands.

II. DESIGN AND ANALYSIS OF THE PROPOSED ANTENNA

Fig. 1 shows the design evolution of the proposed monopole antenna while Fig. 2 shows the geometry of the proposed dual-band double T-shaped ring patch antenna along with its dimensions. This antenna is connected to 50Ω microstrip line and printed on a 1.62 mm thick FR-4 substrate with relative dielectric permittivity ε_r of 4.3 and a loss tangent (tan δ) of 0.017. The geometric dimensions are reported in table I.

To demonstrate the performance of the proposed structure, the input reflection coefficient of Antenna II is compared to Antenna I. As shown in Fig. 3, Antenna I resonates at 3.49 GHz with a minimum reflection coefficient of −24 dB and a −10 dB impedance bandwidth from 3.03 GHz to 4.52 GHz, then after introducing the second T shaped ring, Antenna II achieved dual-band operation noticing that the lower band is not affected by the additional T shaped ring. Antenna II resonates at 3.50 GHz and 6.48 GHz with good impedance matching and –10 dB fractional bandwidth of 38.5 % (3.05 GHz-4.40 GHz) and 22.17 % (6.05 GHz-7.50 GHz), respectively.
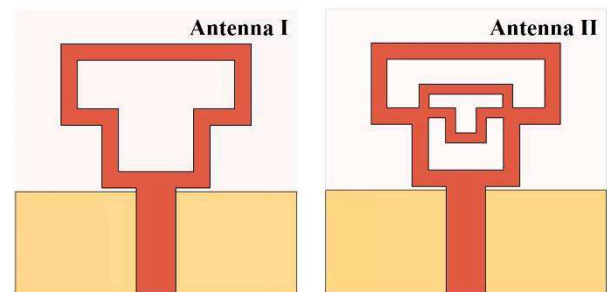
Fig. 1. The design evolution of the proposed antenna.
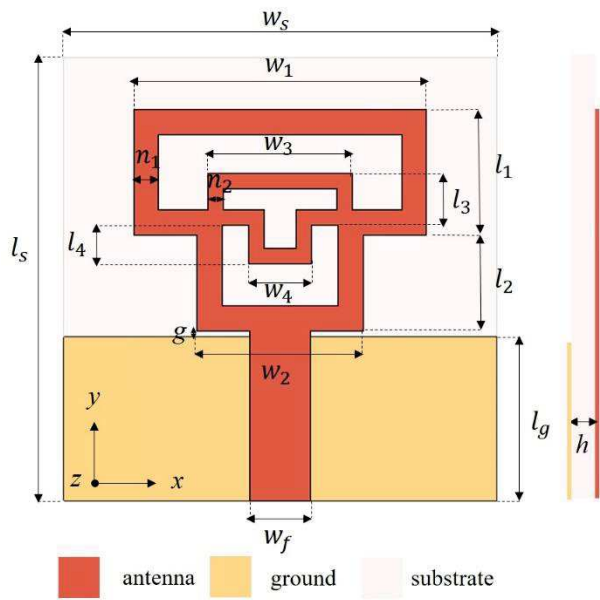
Fig. 2. Geometric structure of the proposed double T shaped patch ring monopole antenna (Antenna II)

TABLE I. DETAILED DIMENSIONS OF THE PROPOSED ANTENNA

w_s	w_1	w_2	w_3	w_4
22.5	15.2	8.6	7.5	3.25
l_s	l_1	l_2	l_3	l_4
23	6.5	5	2.7	2
w_f	l_g	g	n_1	n_2
3.17	8.5	0.3	1.3	0.8
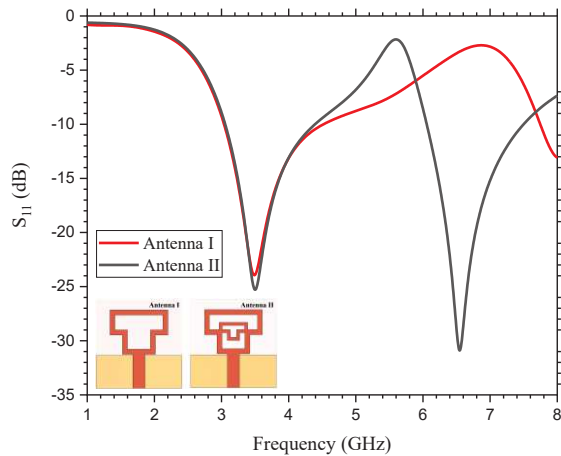
Fig. 3. Simulated input reflection coefficient of the proposed dual-band double ring T shaped monopole antenna.

Next, the effect of the strip widths n_1 and n_2 are discussed. Fig. 4-a shows the effect of increasing n_1 from 0.8 mm to 1.8 mm on the input reflection coefficient: both the lower and higher resonant frequencies are moved toward the higher frequency, while the input reflection coefficient at lower resonant

frequency is improved whereas at the higher resonant frequency is reduced. Fig. 4-b depicts the effect of increasing the parameter n_2 from 0.4 mm to 1.2 mm on the input reflection coefficient: the higher resonant frequency moves toward the higher frequency with reduced impedance matching, while the lower resonant frequency remains almost constant.
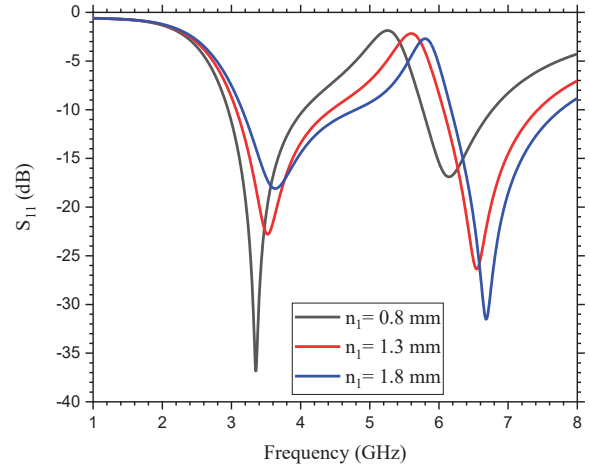
(a)
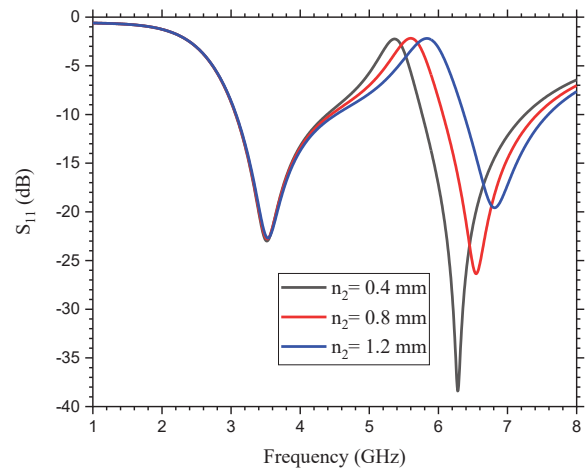
(b)

Fig. 4. Input reflection coefficient of the proposed antenna (a) n_1 is varied, (b) n_2 is varied.

To better comprehend how the antenna functions, the surface current of antenna II at 3.50 GHz and 6.45 GHz are shown in Fig. 5. Many nulls can be detected in the upper band compared to the lower band since the antenna operates at the fundamental mode at the first frequency and higher order modes at the higher frequency with the lower wavelength. Also, this figure shows the antenna parts that fix the resonant frequency. It can be seen that the current concentrates at the outer ring and is almost zero at the inner ring on the lower band, whereas at the higher band, the current concentrates on both the inner and outer rings.

Hence, the outer T shaped ring's dimensions have an impact on the two bands. But mainly control the lower band, whereas the inner T-shaped ring has only control over the higher band.

The simulated two dimensional (2D) representation of the far field radiation patterns at 3.50 GHz and 6.55 GHz in both E-plane ($\varphi = 90°$) and H-plane ($\varphi = 0°$) are shown in Fig. 6. From this figure, we can see that the antenna exhibits almost broadside omnidirectional radiation pattern at 3.50 GHz, with maximum realized gain of 1.62 dB_i and directivity of 3.24 dB_i. Whereas, at 6.55 GHz, the radiation pattern is nearly omnidirectional. The achieved gain at this operating frequency is around 0.63 dB_i and the directivity is of 2.39 dB_i . Note that the difference between the gain and directivity is due to the high radiation loss. The simulated 3D radiation patterns are illustrated in Fig. 7.

(a)

(a)

(b)

Fig. 6.   Simulated radiation patterns of the proposed Antenna at, (a) 3.50 GHz (b) 6.55 GHz

(b)

Fig. 5.   The current distribution of the proposed antenna at (a) 3.50 GHz, (b) 6.55 GHz.

(a)

(b)
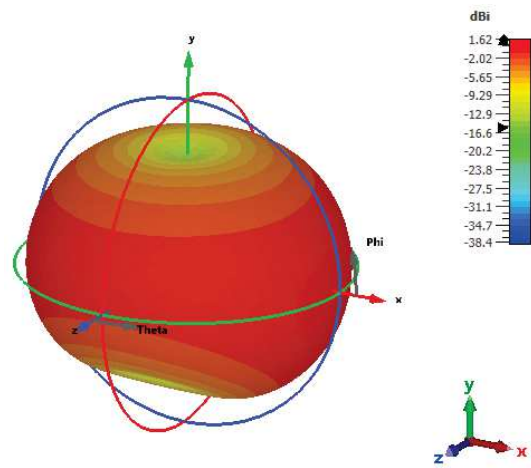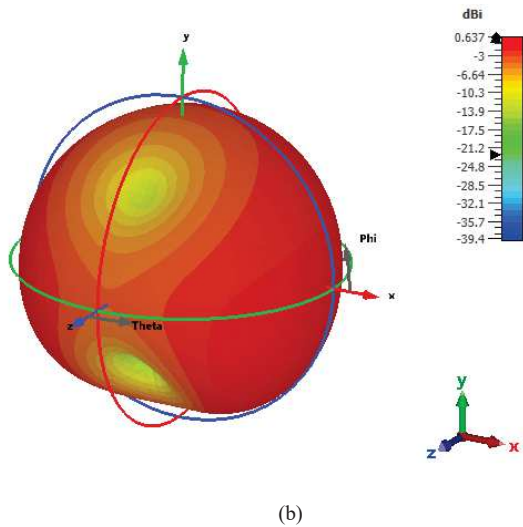
Fig. 7.   Simulated 3D radiation patterns of the proposed Antenna.
(a) Pattern at 3.50 GHz (b) pattern at 6.55 GHz.

TABLE II.   PERFORMANCE COMPARISON OF THE PROPOSED
ANTENNA WITH EXISTING WORKS (*: SIMULATED, **: MEASURED)

Works	f_r (GHz)	10 dB FBW (%)	RL (dB)	Gain (dBi)	Size (mm²)
[7] (**)	0.912	22.7	27	NM	66 x 80
	2.45	28.6	19.2	NM	($0.37\lambda g \times 0.45 \lambda g$)
[8] (**)	3.74	13.4	46	1.23	30× 30
	5.1	16.9	28	1.57	($0.68\lambda g \times 0.68\lambda g$)
[9] (**)	3.5	5.7	22	1.76	14 × 14
	5.8	6.9	32	3.32	($0.27\lambda g \times 0.27 \lambda g$)
[10] (**)	0.938	11.7	21	NM	61 × 41
	1.75	4.3	26	NM	($0.36\lambda g \times 0.24 \lambda g$)
This work (*)	3.50	38.5	25.3	1.62	22.5 x 23
	6.48	22.2	30.9	0.63	($0.47\lambda g \times 0.49\lambda g$)

f_r: Resonant Frequency, FBW: Fractional Bandwidth, RL: Return Loss And NM: Not Mentioned.

In Table II, the performance of the proposed antenna is compared to similar works, showing that the suggested antenna outperforms most of such works in terms of high fractional bandwidth. Despite the fact that [9] and [10] have a smaller footprint, their FBW does not exceed 12%. Even though the antenna described in [7] has a high FBW, its radiation pattern in the high band is not omnidirectional since the main lobes are pinched. Furthermore, the antenna in [8] exhibits an omnidirectional pattern in both bands, but its size is still much larger than that of the proposed work.

III. CONCLUSION

In this paper, a novel dual-band monopole antenna is presented. This antenna consists of double T shaped rings, interfering each other and providing dual-band response namely, 3.05 GHz-4.40 GHz and 6.05 GHz-7.50 GHz. This later can be controlled independently by the parameters of the inner T-shaped ring without influencing the lower band. The simulated results of the compact antenna (22.5×23 mm²) are promising with wide bandwid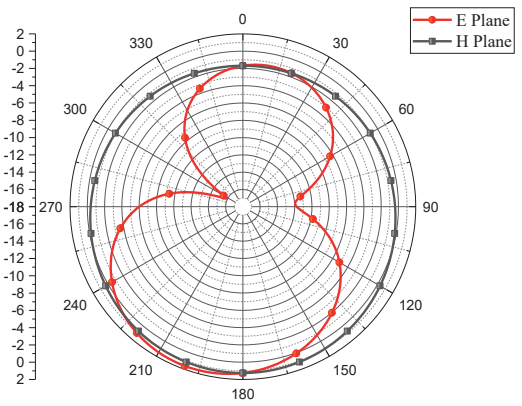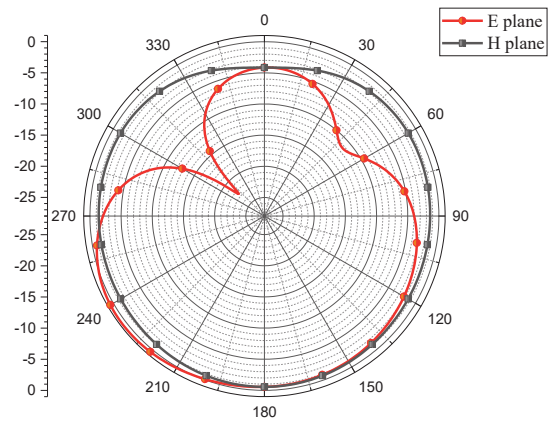th and good impedance matching. Further, its omnidirectional patterns make the proposed antenna attractive for sub-6GHz 5G applications.

REFERENCES

[1]   Y. Li, Z. Zhao, Z. Tang, and Y. Yin, "A low - profile, dual - band filtering antenna with high selectivity for 5G sub - 6 GHz applications," Microwave and Optical Technology Letters, vol. 61, no. 10, pp. 2282‑2287, Jun. 2019.

[2]   M. A. Abdelghany, M. Fathy Abo Sree, A. Desai, and A. A. Ibrahim, "Gain Improvement of a Dual-Band CPW Monopole Antenna for Sub-6 GHz 5G Applications Using AMC Structures," Electronics, vol. 11, no. 14, p. 2211, Jul. 2022.

[3]   S. Ullah, I. Ahmad, Y. Raheem, S. Ullah, T. Ahmad and U. Habib, "Hexagonal shaped CPW Feed based frequency reconfigurable antenna for WLAN and Sub-6 GHz 5G applications," International Conference on Emerging Trends in Smart Technologies, Karachi, Pakistan, 2020.

[4]   R. Krishnamoorthy, A. Desai, R. Patel, and A. Grover, "4 Element compact triple band MIMO antenna for sub-6 GHz 5G wireless applications," Wireless Networks, vol. 27, no. 6, pp. 3747–3759, Jul. 2021.

[5]   Y. Yang, R. Lu, L. Gao, and S. Gong, "4.5 GHz lithium niobate MEMS filters With 10% fractional bandwidth for 5G front-ends," Journal of microelectromechanical systems, vol. 28, no. 4, pp. 575–577, Aug. 2019.

[6]   Y. Yang, R. Lu, A. Kourani and S. Gong, "Advancing lithium niobate based thin film devices for 5G front-ends," IEEE MTT-S International Microwave Symposium, pp. 881-884, Boston, MA, USA, 2019.

[7]   M. Dehmas, A. Azrar, F. Mouhouche, K. Djafri, and M. Challal, "Compact dual band slotted triangular monopole antenna for RFID applications," Microwave and Optical Technology Letters, vol. 60, no. 2, pp. 432–436, Jan. 2018

[8]   R.S. Daniel, R. Pandeeswari, and S. Raghavan, "Dual-band monopole antenna loaded with ELC metamaterial resonator for WiMAX and WLAN applications," Applied Physics A, vol. 124, pp.570 no. 8, Jul. 2018,

[9]   Y. Mao, S. Guo, and M. Chen, "Compact dual - band monopole antenna with defected ground plane for Internet of things," IET Microwaves, Antennas & Propagation, vol. 12, no. 8, pp. 1332‑1338, Apr. 2018.

[10] K. Djafri, M. Challal, A. Azrar, M. Dehmas, R. Aksas, and F. Mouhouche, "Compact dual-band fractal hexagonal ring monopole antenna for RFID and GSM applications," Microwave and Optical Technology Letters, vol. 60, no. 11, pp. 2656–2659, Oct. 2018

Design and Analysis of Microstrip Planar inverted-F Antenna For Implantable Medical Telemetry Devices

Abdelbasset Azzouz
LESM *laboratory, dept of electronics*
university of Saida
Saida, Algeria
abdelbasset.azzouz@univ-saida.dz

Riadh Degachi
dept of electrical engineering
university of El oued
El oued, Algeria
degachi-riadh@univ-eloued.dz

Said Ghendir
dept of electrical engineering
university of El oued
El oued, Algeria
said-ghendir@univ-eloued.dz

Abstract— **Recent years have witnessed a significant increase in the use of telecommunication technologies in the medical field especially through medical telemetry. This practice, which may be conducted by implementing a medical device in the human or animal body, allows to monitor its vital signs and collect data which can be used to diagnose its health state. This work proposes the design of a narrow-band antenna operating in the MICS band (Medical Implant Communication Service) for wireless telemedicine. The proposed antenna resonates at 404.5 MHz with a reflection coefficient of -52dB and a bandwidth of 2.25MHz. Simulation showed promising results with regard to the use of gallium arsenide in the antenna substrate as well as the utility of hexagonal and circular slots in obtaining smaller resonating frequencies.**

Keywords— *Miniaturization, pifa, Implantable medical telemetry devices, Microstrip Antenna, Implantable healthcare technology*

I. INTRODUCTION

An antenna is a basic component of any electronic system that depends on free space as a propagation medium. It may be defined as an electromagnetic transducer, used to convert, in the transmitting mode, guided waves within transmission lines to radiated free-space waves, and in the receiving mode, free-space waves to guided waves [1]. There are several types of antennas such as: wire, aperture, microstrip, array, reflector, and lens antennas [2]. Among all of these types, microstrip antenna may have been the one with the most design variations in terms of feeding method, shape and architecture.

The microstrip patch antenna first came into existence around the 1970s, approximately two decades after the first microstrip antenna was proposed by Deschamps in 1953 [3]. It has a simple design which consists of a radiated patch component, a dielectric substrate and a ground plane. The radiated patch and ground plane are usually a thin layer of copper or gold which are good conductors. In recent years, microstrip patch antennas have been widely used due to their favorable characteristics. These include being lightweight, conformable, electrically thin, and cost-effective [1]. A large number of commercial needs are met by the use of microstrip and printed antennas. These include the ubiquitous Global Positioning System (GPS), Zigbee, Bluetooth, WiMAX, Wi-Fi applications, 802.11a,b,g, medical telemetry and others [4].

The mains limitations of microstrip antenna are its narrow Bandwidth, lower Gain and weak radiating pattern. Improving these limitations have been a challenging task for researchers as achieving a good design would relax system requirements and improve the overall system performance [1].

Implantable antennas are vital components in the field of biomedical technology, enabling wireless communication and telemetry monitoring. These antennas must be compact, biocompatible, and designed to function effectively in the challenging environment of the human body. Ongoing research in implantable antennas is focused on optimizing their performance, size, and safety to advance the capabilities of implantable medical devices.

This paper proposes the design of a microstrip inverted-F antenna with a very narrow band that does not interfere with other RF applications. Its bandwidth is still limited to the MICS band (Medical Implant Communication Service).

The paper is structured into several sections. The second section offers a concise overview on the design of proposed antenna. Following that, Section III presents the simulations and results of the proposed antenna and comparative study of existing relative antennas. Finally, the paper concludes with a summary of the findings.

II. ANTENNA DESIGN

Figure 1 illustrates the structure of the proposed antenna. The antenna is rectangular in shape and comprises a ground plane, a dielectric made of high permittivity gallium arsenide ($\varepsilon r=12.9$, $h=14.5$ mm), and a patch. It is comprised of three hexagonal slots and eight circular slots, each with a radius of 1.2 mm. The antenna is fed by a coaxial cable with a dielectric constant of $\varepsilon r= 2.1$.
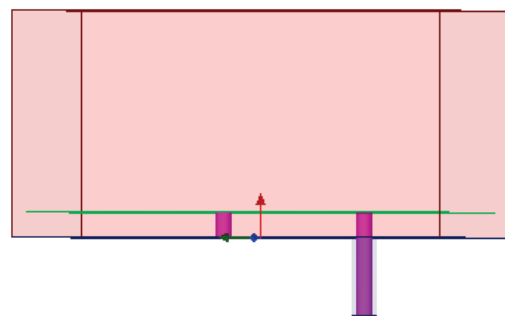
Fig. 1. The proposed antenna a) side view

The design approach is based on reducing the number of slots with different shapes on the rectangular patch, including hexagons and circles. This helped us minimize the antenna size and achieve resonance at lower frequencies, with the addition of a shorting pin. Subsequently, we selected the best-performing design. The antenna dimensions can be found in Table 1.

dielectric is used to reduce the effective wavelength and, consequently, lower the resonance frequencies.
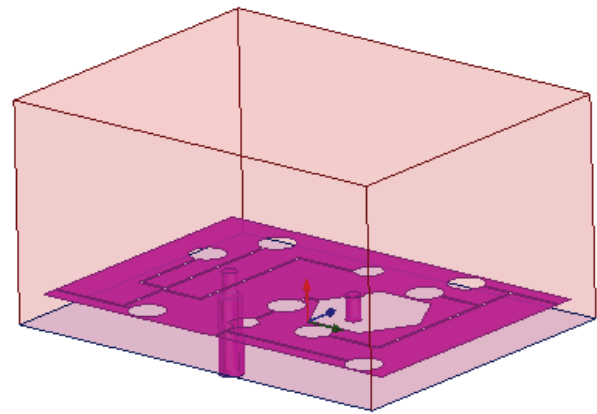
Fig. 2. 3D model of the proposed antenna

III. SIMULATION RESULTS AND DISCUSSIONS

After completing the design phase of the proposed antenna, we analysed the simulated results, including the return loss (S11 parameter), 2D radiation patterns, and 3D radiation patterns. The following waveforms illustrate the simulated results of the antenna.

A. Return Loss

Figure 3 displays the simulated return loss versus frequency plot of the proposed microstrip patch antenna obtained using HFSS software. It is evident that the designed antenna exhibits a return loss value of -52 dB at its resonant frequency of 404 MHz.

Fig. 1. The proposed antenna b) top view

TABLE I.   OPTIMIZED PARAMETERS OF THE PROPOSED ANTENNA.

Parameter	Value(mm)	Parameter	Value(mm)
L1	28.00	L19	1.00
L2	21.5	L20	9.62
L3	26.86	L21	4.12
L4	18.10	L22	9.60
L5	13.43	L23	3.00
L6	17.05	L24	12.83
L7	6.45	L25	5.97
L8	5.43	L26	3.62
L9	3.95	L27	2.00
L10	5.50	Lf	4.53
L11	9.32	Ls	2.00
L12	9.60	D1	2.4
L13	3.00	D2	1.4

The patch height is 1.6 mm. A higher-permittivity substrate is employed to maintain antenna biocompatibility and to create a separation between the metal radiator and human tissue, as illustrated in Figure 2. The high-permittivity

Fig. 3. Return loss vs Frequency

At -10 dB, the designed antenna exhibits a bandwidth of 2.25 MHz, ranging from 403.31 MHz to 405.56 MHz (BW: 0.56%), which covers the MedRadio frequency range, as illustrated in Figure 3.

B. Radiation Pattern

A radiation pattern defines the variation of the power radiated by an antenna as a function of the direction away from the antenna. Figure 4 and Figure 5 show the 2D and 3D

radiation patterns, respectively. In these figures, red corresponds to φ = 90 degrees, and blue corresponds to φ = 0 degrees
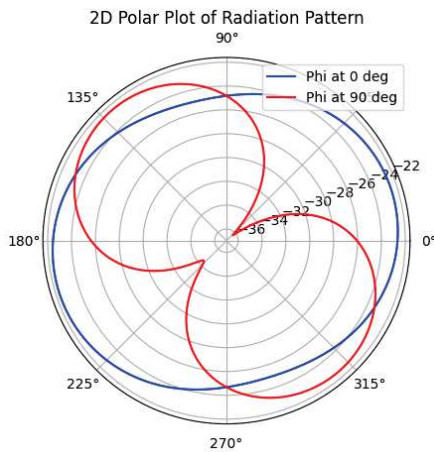
Fig. 4. 2D radiation pattern of the proposed antenna

C. Feed Point Position Performance

The impact of varying the feed positions on the performance of the designed antenna is illustrated in Figure 6. As depicted, it influences the return loss (S11) values and causes a slight shift in the resonant frequency.
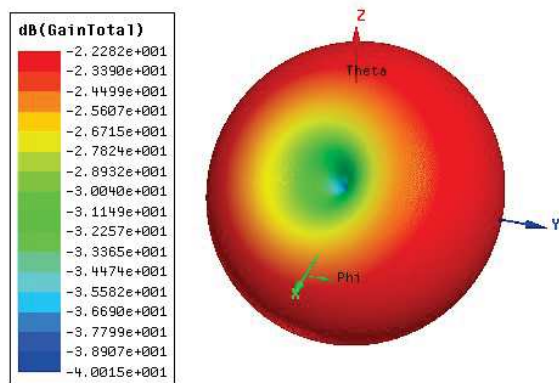
Fig. 5. 3D polar plot of the proposed antenna
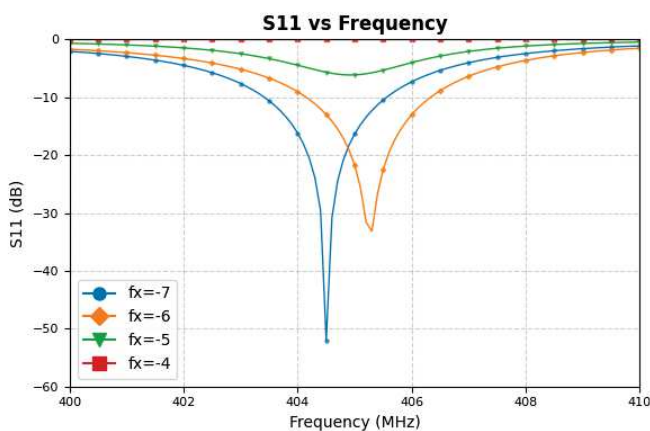
Fig. 6. Effect of feed position variations on return loss

D. Effect of Shorting Pin Placement Variations

Figure 7 clearly demonstrates that the shorting pin's position plays a crucial role, impacting both the return loss values and the resonance frequency shift.
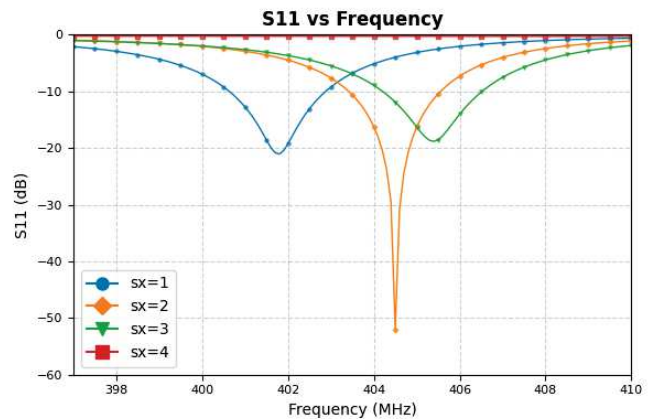
Fig. 7. Effect of shorting pin position variations on return loss

E. Effect of Substrate Thickness

Figure 8 reveals that varying substrate thicknesses have a significant impact on the bandwidth results and lead to slight changes in the resonant frequency. In the proposed antenna, the selected substrate thickness yields the highest performance compared to all other thickness values.
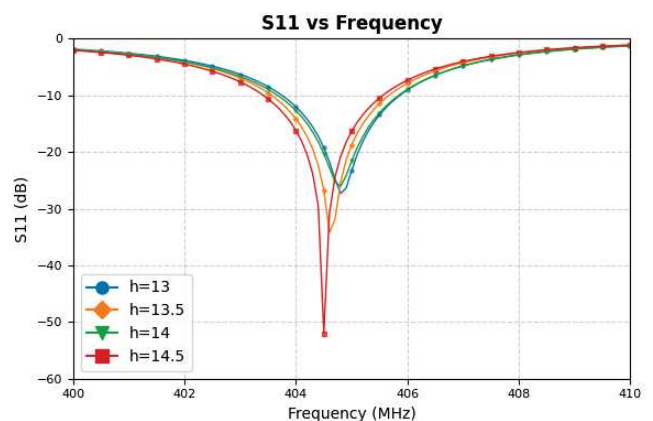
Fig. 8. Effect of substrate thickness variations

The concentrated electric field distribution, as depicted in Figure 9 at 404 MHz, offers valuable insights into the intricate nature of our antenna's performance. This concentrated field emphasizes the essential role played by the specific geometric shapes of hexagons and circles in our antenna design, particularly in achieving optimal performance within the Medical Implant Communication Service (MICS) band. The focused energy around these slots signifies their significance in shaping the antenna's radiation characteristics, underscoring the importance of these design elements for successful wireless communication in the context of implantable medical devices.
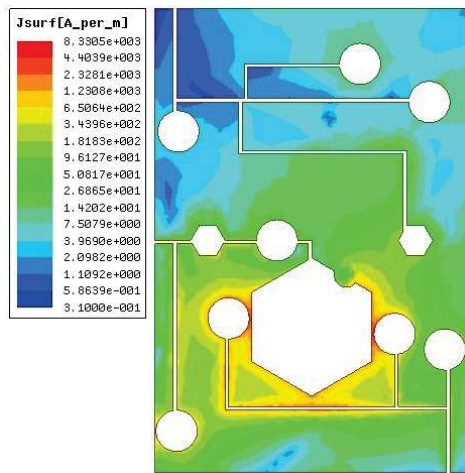
Fig. 9. The electric field distribution at 4045. MHz with logarithmic scale

TABLE II. COMPARISON OF THE PROPOSED ANTENNA WITH RELEVANT EXISTING ANTENNAS.

Ref	Resonant Frequency (MHz)	Return Loss(dB)	Gain(dB)
[5]	405	-33.16	-41.03
[6]	404	-12.01	-45.04
[7]	403	-21.77	------
This work	404.5	-52	-22.28

IV. CONCLUSION

This research contributes to the design of a novel Microstrip Planar Inverted-F Antenna intended for use in Implantable Medical Telemetry Devices. Simulation was conducted using HFSS software. The primary objective of this study was to design a narrow-band antenna operating within the MICS band (Medical Implant Communication Service) at the 404.5 MHz frequency, catering to medical applications. A comprehensive parametric study was performed to assess its performance, including substrate thickness, dielectric material, feed position, and shorting pin placement, all analysed with HFSS software.

The proposed antenna exhibits a notable return loss of -52 dB and a narrow bandwidth of 2.25 MHz, aligning precisely with the MICS frequency band. Furthermore, the utilization of gallium arsenide as the dielectric material in the antenna design demonstrated significant improvements in antenna performance when compared to other dielectric materials. These findings highlight the potential of gallium arsenide for enhancing antenna efficiency and suitability for implantable medical telemetry applications.

REFERENCES

[1] D.-G. Fang, "Antenna theory and microstrip antennas," CRC Press, 2017.

[2] C. A. Balanis, "Antenna theory: analysis and design," John Wiley & Sons, 2016.

[3] S. S. Holland, "Miniaturization of microstrip patch antennas for GPS applications," in Masters Theses, 2008, pp. 120.

[4] R. Bancroft, "Microstrip and printed antenna design," The Institution of Engineering and Technology, 2009.

[5] N. Ferdous, N. Tabassum, R. Hoque, "Design and performance of miniaturized meandered patch antenna for implantable biomedical applications," in 2015 International Conference on Electrical Engineering and Information Communication Technology (ICEEICT), 2015.

[6] T. Hossain, R. Mahmud, H. K. Juhi, et al, "Design and performance analysis of a biomedical implantable patch antenna," in 2015 International Conference on Advances in Electrical Engineering (ICAEE), 2015.

[7] S. Salama et al, "2020 J. Phys.: Conf. Ser. 1711, 012001.".

DeepFire: Enhanced Fire Detection using VGG16 Convolutional Neural Networks

1st Yasmine GUERBAI

Department of Electrical Systems Engineering
M'hammed Bougara University, Boumerdès
Boumerdès, Algeria
y.guerbai@univ-boumerdes.dz

2nd Asma SAIBI

Department of Electrical Systems Engineering
M'hammed Bougara University, Boumerdès
Boumerdès, Algeria
saibi.asma15@gmail.com

Abstract—: This study explores the application of the VGG16 convolutional neural network for accurate fire detection, particularly in forest fire scenarios, using images and videos. The urgency of timely fire detection, given the significant threats to life and property, underscores the importance of this research. Leveraging transfer learning, VGG16 is fine-tuned with a comprehensive dataset, including forest fire data. The model demonstrates outstanding performance, with high accuracy in recognizing fire-related patterns, especially within forest landscapes. Key aspects of this research involve pre-trained weights, deep architecture, and data augmentation to enhance generalization. The proposed methodology not only provides an effective fire detection solution but also holds promise for applications in forest fire monitoring, where drones can offer critical imagery and data for improved situational awareness and response coordination.

Index Terms—: Fire Detection, Forests, VGG16, convolutional neural network,computer vision,deep learning.

I. INTRODUCTION

A. Background:

Fire, a formidable force of nature, knows no boundaries and can wreak havoc on lives and properties with astonishing speed,In Algeria, a nation known for its diverse terrain, encompassing arid deserts, lush forests, and vibrant cities, the specter of fire looms as a perpetual challenge. The ability to detect fires swiftly and effectively becomes a pivotal tool in safeguarding both the environment and human lives. From the Casbah of Algiers, a UNESCO World Heritage site [1], to the dense cedar forests of the Kabylie Mountains, the need for robust fire detection transcends geographical distinctions.

B. Motivation and Objective:

Recent research has shown that computer vision and deep-learning-based techniques have achieved great success and play a vital role in the field of fire detection. Recently, image fire detection has become a hot topic of research. The technique has many advantages such as early fire detection, high accu- racy, flexible system installation, and the capability to effectively detect fires in large spaces [2]

In the domain of vision-based fire detection, researchers have delved into the utilization of Convolutional Neural Networks (CNNs) and transformers. Their investigations have paved the way for the creation of models that are adept at recognizing and isolating distinctive features within fire images. These efforts have significantly propelled the evolution of fire detection technology. [3]–[6]

This study aims to address this critical issue by harnessing the power of deep learning, specifically the VGG16 convolutional neural network architecture. The scientific problem at the heart of this research is clear: How can we develop an accurate and efficient fire detection system, particularly in scenarios like forest fires

The relevance of this research lies in its potential to save lives and mitigate property damage. Moreover, the utilization of VGG16, known for its prowess in image analysis, offers a robust foundation for our methodology. This article will delve into the methods, experiments, and results that contribute to a comprehensive solution for fire detection, with a special emphasis on forest fire scenarios.

II. LITERATURE REVIEW:

A. Introduction to CNN for Fire Detection:

This chapter lays the groundwork for understanding the fundamental principles of Convolutional Neural Networks (CNN) and their application in fire detection.

Convolutional Neural Networks (CNNs) operate on the principles of neural networks and are designed to extract meaningful features from data, particularly well-suited for tasks like fire detection. CNNs are composed of layers of interconnected neurons. These layers include the input layer, which receives the raw data, and hidden layers [7] that progressively learn hierarchical representations of the input data. These hidden layers transform the feature space in a way that aligns with the desired output, making CNNs powerful tools for complex pattern recognition tasks.

This brief explanation provides an overview of CNN architecture is explain in fig(1) [8]

1) VGG16 Architecture: VGG16 is the most commonly used version of CNN. It has a total of 16 layers with 13 convolutional and 3 fully connected layers [8] [10]VGG16 has introduced the deeper way of designing the CNN. It uses
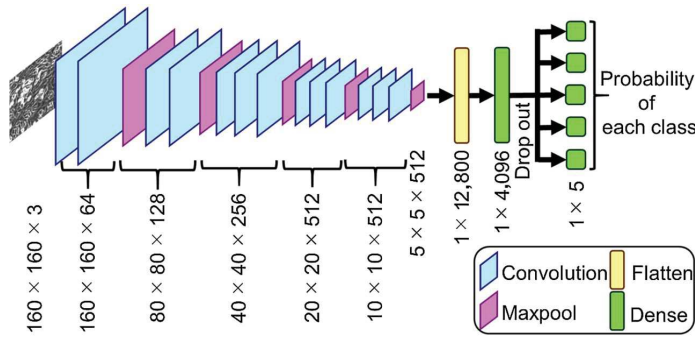
Fig. 1. Simple CNN architecture

ReLU as an activation function to improve the nonlinearity in the model, whereas the softmax function is used at the final layers for classification [5]. The basic architecture of VGG16 is presented in Fig.2
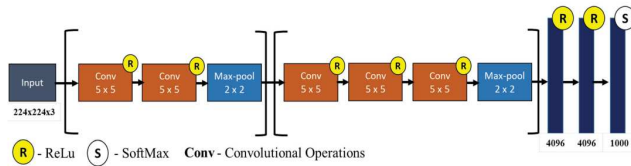
Fig. 2. Basic VGG16 architecture

III. RELATED WORK

Yang, Li, and Zhang (2021) explored fire detection in satellite remote sensing images, a critical application for timely identification of fire spots. Their method, based on Landsat-8 images, incorporated a two-step process involving threshold judgment and model-based detection. The integration of VGG networks, transfer learning, and weighted voting resulted in improved accuracy and robustness. Notably, their approach achieved an 83% correct detection rate with a low missing rate of 5%, indicating substantial progress over traditional methods. [9]

Dua et al. (2020) presented an enhanced approach to fire detection through deep learning models. Their study addressed the challenges of fire detection. When compared with other methods (Table III), their approach demonstrated a remarkable reduction in missed detection rates and false alarm rates. The use of CNN models, including AlexNet and GoogleNet, yielded superior accuracy. [11]

IV. METHODOLOGY

A. Dataset Description

Our dataset was crafted during the NASA Space Apps Challenge in 2018, with the primary aim of training a model for image recognition, specifically to identify images depicting fire. This dataset is valuable for those involved in fire detection and image classification tasks. [12]

The dataset is a binary classification challenge, consisting of "fire images" and "non-fire images." "Fire images" include 755 outdoor fire images, some with heavy smoke. "Non-fire images" comprise 244 nature scenes like forests, trees, rivers, and more, This dataset, developed during a NASA challenge, holds great potential for advancing fire detection technology and image classification, offering opportunities for innovation in safety and environmental monitoring applications.

B. Architectural Blueprint: Crafting a Robust Fire Detection Model with VGG16

model architecture plays a pivotal role. The design and configuration of the model significantly influence its capability to identify fire occurrences accurately. In this context, we delve into the architectural blueprint of a fire detection model, meticulously constructed on the foundation of the VGG16 network.

1) The Core Components:
- Base Model Selection: The journey begins with the selection of a pre-trained model. In this case, the VGG16 architecture is chosen. VGG16 is celebrated for its excellence in image classification tasks, having been pre-trained on the vast ImageNet database. It brings a wealth of knowledge about image features to the fire detection model.
- Fine-Tuning Control: To adapt the VGG16 model to the specific nuances of fire detection, a critical decision is made. The layers of the VGG16 model are set to be non-trainable. This choice ensures that the foundational features learned during ImageNet pre-training remain intact, and the model focuses on learning the nuances of fire and non-fire images.

2) Model Composition: The fire detection model takes shape through the sequential assembly of key components:
- Base Model Integration: The VGG16 architecture serves as the core of the model. It processes input images with dimensions of 224x224 pixels and 3 color channels. The 'include-top' parameter is set to 'False,' indicating that the final classification layers of VGG16 are not included. This allows for custom classification layers to be added for fire detection.
- Flattening Layer: Following the VGG16 backbone, a flattening layer is introduced. It transforms the multi-dimensional output of VGG16 into a one-dimensional feature vector. This transformation is essential for subsequent classification.
- Dropout for Regularization: To prevent overfitting and enhance model generalization, a dropout layer is included. It randomly deactivates a portion of neurons during training, promoting robustness.
- Classification Layer: The final layer is a dense layer with a single neuron. The activation function used is sigmoid, ideal for binary classification. This neuron's output provides the probability of an image containing fire.

3) Parametric Insights::
- Total Parameters: The model is informed by an impressive wealth of knowledge, amounting to 14,739,777

parameters. These parameters represent the weights and biases that steer the model's learning process.

- Trainable Parameters: While the model itself is pre-trained and non-trainable, it is augmented with 25,089 trainable parameters. These parameters belong to the custom layers added for fire detection.
- Non-Trainable Parameters: The bulk of the parameters, a staggering 14,714,688, remains non-trainable, representing the pre-existing knowledge encoded within VGG16.

V. EXPERIMENTAL RESULTS

A. CNN model result

we generated a code to show a graphical representation of our neural network model, including the connections between layers, shapes of tensors, layer names, and data types. This visualization can be helpful for understanding and sharing the architecture of your model.
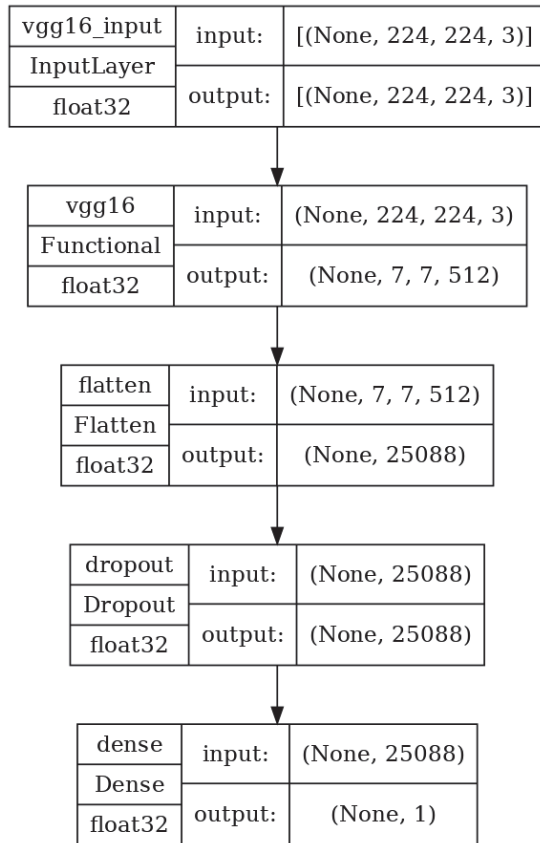
Fig. 3. neural network model

B. training results

In the model training process, a combination of optimization techniques and early stopping mechanisms was employed to achieve an accurate and efficient fire detection model. The Adam optimizer was utilized, and the binary cross-entropy loss function was chosen to evaluate the model's performance. The training was carried out over 20 epochs, during which

the model learned to distinguish fire and non-fire images with remarkable accuracy.

The results of this training were highly promising. By the end of the training process, the model exhibited a substantial improvement in accuracy. It commenced with an initial loss of 1.44 and an accuracy of 88.25% in the first epoch, and swiftly converged to achieve a final validation accuracy of 98.99%. The validation loss, a crucial metric for assessing the model's generalization, also exhibited a significant reduction, reaching a final value of 0.24. These results underscore the model's exceptional capability in accurately identifying fire images, thus demonstrating its potential as a robust tool for fire detection applications.

C. testing results

After the model was trained, a final evaluation was conducted to assess its performance on the validation dataset. The results were highly promising, with a test loss of 0.2140 and an impressive test accuracy of 98.99%. This indicates that the model is highly effective in correctly classifying fire and non-fire images. The high accuracy and low loss values provide strong evidence of the model's ability to generalize well and accurately detect fire in various image scenarios. These results reaffirm the model's potential as a robust and reliable tool for fire detection applications, demonstrating its effectiveness and efficiency in this critical domain.
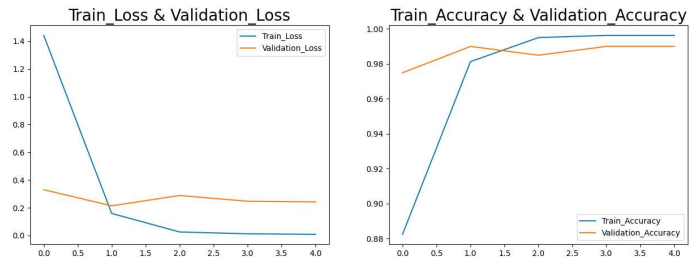
Fig. 4. curves of the training and validation loss and accuracy

D. classification reports

Class	Precision	Recall	F1-Score	Support
0 (Non-Fire)	1.00	0.99	0.99	153
1 (Fire)	0.96	1.00	0.98	46
Accuracy			0.99	199
Macro Avg	0.98	0.99	0.99	199
Weighted Avg	0.99	0.99	0.99	199

TABLE I
CLASSIFICATION REPORT FOR FIRE DETECTION MODEL

The classification report provides a detailed breakdown of the model's performance in terms of precision, recall, and F1-score for both classes (0 for non-fire and 1 for fire) based on the validation dataset.

For class 0 (non-fire images), the model achieves a precision of 1.00, indicating that when it predicts an image as non-fire, it is correct 100

For class 1 (fire images), the precision is 0.96, meaning that when the model predicts an image as fire, it is correct 96

The accuracy of the model across both classes is reported as 0.99, demonstrating its excellent overall performance. The macro average and weighted average F1-scores are both 0.99, reaffirming the model's ability to effectively classify fire and non-fire images with high accuracy and consistency. These results highlight the model's strong performance and its suitability for fire detection applications.

E. Comparative Analysis of Image Classification Models

Model Name	Topology	Epochs	Train Acc.	Validation Acc.	Test Acc.
Model 1	Basic CNN	20	98.58%	100%	99.9%
Model 2	Complex CNN	25	94.68%	N/A	98%
Our Model	VGG16	20	99.62%	98.99%	98.99%

TABLE II
COMPARATIVE ANALYSIS OF IMAGE CLASSIFICATION MODELS

In summary, Model 1 [14] appears to have very high accuracy on both the training and testing datasets, although the 100% validation accuracy suggests potential overfitting. Model 2 [15] has lower training accuracy and lacks information about validation accuracy. "Our Model" achieves high training, validation, and testing accuracies with the VGG16 architecture, indicating strong performance and good generalization to unseen data. However, it's essential to consider factors like the dataset size, class balance, and potential data preprocessing when assessing the overall quality of these models.

VI. DISCUSSION

A. Analysis of Results and Implications

The table 2 presents the performance of three image classification models. Model 1 achieves remarkably high training and testing accuracies, but a perfect validation accuracy raises concerns of overfitting. Model 2, employing a more complex CNN, shows a respectable testing accuracy, but the absence of validation data suggests a need for better generalization. In contrast, "Our Model" using the VGG16 architecture demonstrates robust performance, indicating that deeper architectures can be beneficial for image classification. Implications include the importance of model complexity, regularization techniques, and the need for larger and more diverse datasets.

B. Strengths of the Approach

The study's strength lies in its robust model selection, encompassing a simple CNN and a well-established VGG16 architecture, enabling the comparison of different complexities. "Our Model" achieves high validation and testing accuracies, affirming its effectiveness. Furthermore, the study's transparency, specifying the number of training epochs and network architectures used, enhances reproducibility.

C. Weaknesses and Limitations

However, overfitting is a concern, notably in Model 1, necessitating better regularization methods. Additionally, Model 2 could benefit from a larger dataset to improve its performance and assess its generalization.

CONCLUSION AND FUTURE WORKS

Overall, convolutional neural networks (CNNs) offer significant advantages in the forests. CNNs allow advanced analysis and processing of large amounts of data from various sources, this offering improved object recognition, real-time video analysis and intelligent decision-making systems. This translates into better traffic management, more efficient pedestrian detection, more accurate environmental monitoring and optimized resource allocation, this improving the quality of life of residents.

In conclusion, CNNs offer major advantages in large spaces like forests. Their use makes it possible to improve the quality of life and protect the Forest wealth, by contributing to the detection of fires, the preservation of species and a more efficient management of natural resources.

we are planing to do in the future a AI project o test the accuracy between machine learning and deep learning and summarizing the result in another article with all the steps needed

REFERENCES

[1] BOUKADER, Mohamed et CHENNAOUI, Youcef. The UNESCO site of the Casbah in the Master Plan of Algiers (PDAU): between heritage requirements and the need for coordination. Ge-conservación, 2022, vol. 21, no 1, p. 205-218.

[2] Muhammad, K.; Ahmad, J.; Mehmood, I.; et al. Convolutional neural networks based fire detec- tion in surveillance videos. IEEE Access 2018, 6, 18174–18183.

[3] Muhammad, K.; Ahmad, J.; Mehmood, I.; Rho, S.; Baik, S.W. Convolutional Neural Networks Based Fire Detection in Surveillance Videos. IEEE Access 2018, 6, 18174–18183. [Google Scholar] [CrossRef]

[4] Tao, C.; Zhang, J.; Wang, P. Smoke detection based on deep convolutional neural networks. In Proceedings of the 2016 International Conference on Industrial Informatics - Computing Technology, Intelligent Technology, Industrial Information Integration (ICIICII), Wuhan, China, 3–4 December 2016; pp. 150–153. [Google Scholar].

[5] Filonenko, A.; Kurnianggoro, L.; Jo, K.-H. Comparative study of modern convolutional neu- ral networks for smoke detection on image data. In Proceedings of the 2017 10th International Con- ference on Human System Interactions (HSI), Ul- san, Korea, 17–19 July 2017; pp. 64–68. [Google Scholar]

[6] Yin, Z.; Wan, B.; Yuan, F.; Xia, X.; Shi, J. A Deep Normalization and Convolutional Neural Network for Image Smoke Detection. IEEE Access 2017, 5, 18429–18438. [Google Scholar] [CrossRef]

[7] HUANG, Guang-Bin, CHEN, Yan-Qiu et BABRI, Haroon A. Classification ability of single hidden layer feedforward neural networks. IEEE transactions on neural networks, 2000, vol. 11, no 3, p. 799-801.

[8] Kim, B., Yuvaraj, N., Sri Preethaa, K. R., Arun Pandian, R. (2021). Surface crack detection using deep learning with shallow CNN architecture for enhanced computation. Neural Computing and Applications, 33(15), 9289–9305. doi:10.1007/s00521-021-05690-8

[9] DUA, Mohit, KUMAR, Mandeep, CHARAN, Gopal Singh, et al. An improved approach for fire detection using deep learning models. In : 2020 International Conference on Industry 4.0 Technology (I4Tech). IEEE, 2020. p. 171-175.

[10] Seo J, Han S, Lee S, Kim H (2015) Computer vision techniques for construction safety and health monitoring. Adv Eng Inform 29:239–251

[11] Li, P., Zhao, W. (2020). Image fire detection algorithms based on convolutional neural networks. Case Studies in Thermal Engineering, 19, 100625. doi:10.1016/j.csite.2020.100625 10.1016/j.csite.2020.100625

[12] https://www.kaggle.com/datasets/phylake1337/fire-dataset

[13] BELAID, Ouiza Nait et LOUDINI, Malik. Classification of brain tumor by combination of pre-trained vgg16 cnn. Journal of Information Technology Management, 2020, vol. 12, no 2, p. 13-25.

[14] https://www.kaggle.com/code/aesedeu/keras-cnn-fire-detection-1-00-accuracy3.-Load-Data

[15] https://www.kaggle.com/code/phchen5/firescope-cnn-and-tl-with-pytorch-98-accTesting-on-Custom-Data

Optimal coordination of directional overcurrent relays using Evaporation rate water cycle optimization algorithm

Merabet Oussama
Laboratory of Signals & Systems,Institute of Electrical and Electronic Engineering
University M'hamed Bougara boumerdes, Algeria
o.merabet@univ-boumerdes.dz

Belmadani Hamza
Faculty of Technology, Electronics Department, SET Laboratory
Blida 1 University
Blida, Algeria
belmadanihamza@etu.univ-blida.dz

Kheldoun Aissa
Laboratory of Signals & Systems,Institute of Electrical and Electronic Engineering
University M'hamed Bougara boumerdes, Algeria
aissa.kheldoun@univ-boumerdes.dz

Bouchahdane Mohamed
Laboratory of Signals & Systems,Institute of Electrical and Electronic Engineering
University M'hamed Bougara boumerdes, Algeria
m.bouchahdane@univ-boumerdes.dz

Hattabi Intissar
Faculty of Technilogy, Electronics Department, SET Laboratory
Blida 1 University
Blida, Algeria
hattabi_intissar@univ-blida.dz

Ait Mouloud Louiza
Laboratory of Signals & Systems,Institute of Electrical and Electronic Engineering
University M'hamed Bougara boumerdes, Algeria
l.aitmouloud@univ-boumerdes.dz

Abstract— **The coordination of directed overcurrent relays is a crucial part of the protective system in electrical power systems (DOCRs). The coordination between these relays must be preserved at a correct scale to decrease the total operating period of all primary-relay failure scenarios in order to reduce and finally eliminate power losses. The coordinating of DOCR is a hard and fascinating issue in nonlinear optimization. The overall working duration of all necessary relays must be kept to a minimum in order to avoid too much breakdown and interference. In order to tackle the coordination problem of the DOCR, coordination is carried out utilizing the Evaporation rate water cycle algorithm (EWCA), IEEE 3-bus, 9-bus test systems are among the test systems to which the suggested method has been implemented. The Results collected demonstrate the suggested (EWCA) efficiency in reducing the relay operation time for the DOCRs' optimum cooperation.**

Key words. : Evaporation rate water cycle algorithm (EWCA); time dial setting (TDS); plug setting (PS); DOCRs; optimal coordination.

I. INTRODUCTION

Due to the world's increasing renewable sources, fast depletion of fossil fuel sources, and rising costs, alternative energy sources are gaining popularity [1]. Hope abounds for meeting the growing electricity consumption through the utilization of renewable energy sources. Because of this, the quantity of distributed generation (DG) integration into the existing power grid is growing substantially, giving birth to the revolutionary idea of microgrids. Traditional power plants are fuelled by fossil fuels, which are non-renewable and one of the major drivers of environmental harm. Energy generated by microgrids has the potential to be clean, sustainable, and socially beneficial [2]. In rural regions that face high transmission and delivery costs, such as hilly regions, tiny islands, and other distant locales, microgrids can also be an economical way to fulfill the requirements for energy [3]. Significant protection issues are prompted by the complexity and variations in control and operation between microgrids and conventional grids. It is advised that the reader look at publications [4] and [5] that describe the protection concerns discussed by DG integration. The overcurrent relay has long been a long-time, dependable protection method employed in distribution systems (OCR). The paradigm change from traditional grids to microgrids, however, also affects how the OCR protection system is coordinated. Additionally, there are impacts on how the primary and backup protection system functions together [7]. Several scientists have created several protection measures to meet the problems brought by the running and monitoring strategy of microgrids.

As a corollary, using optimization strategies to coordinate DOCR has recently gained attention. The DOCR settings are adjusted using two design features, the Time Multiplier Settings (TMS) and the Plug Setting (PS). Deterministic techniques are unable to find the most suitable solutions because of the greater sophistication of the existing electrical networks and the associated large number of restrictions and design factors. In contrast, cos of their stochastic nature, metaheuristic algorithms have a high chance of obtaining optimal or highly optimal solutions [8]. A number of applications, like PID tuning [9], estimation of pv solar variables [10], segmentation techniques [11], tracking the maximum power point [12], etc., have recently been addressed using metaheuristic algorithms. Numerous

works used metaheuristic algorithms to resolve the DOCR problem as a result of their success: A few metaheuristic algorithms that have been used also include Enhanced Firefly Algorithm[13],Biodiversity Based Optimization[14], Harris hawk Optimization[15], Continuous Particle Swarm Optimizer[16], Hybrid Whale Optimization[17], New-rooted Tree Algorithm[18], and Modified Electro-magnetic Field Optimization Algorithm[19].

In this work, a recent population based optimizer named the Evaporation rate water cycle algorithm (EWCA) [20] is employed for the DOCR optimization problem. The proposed EWCA was tested in a 3- bus system and a 9-bus test system which have been widely considered in many works. The obtained results prove the efficiency and competitivness of the Honey badger algorithm compared to other existing techniques in the literature.

II. PROBLEM FORMULATION

The formulation of the directional overcurrent relay problem is provided as an optimization problem in the present research work. This entails reducing the total of the working times of the primary relays for various fault positions on the system under consideration. This may be stated numerically as [8]:

$$Minimize, \ T_{op} = \sum_{i=1}^{m} W \ T_{pr\,i} \tag{1}$$

T_{pri} is the operational time of relay Ri , W represents the weight corresponding to the operating time of relay Ri and as the line is considered to be short and of decent length, weight (W=1) is utilized for all relays. The above objective function is subject to the following inequality and quality constraints:

$$T_i = \frac{\alpha \times TDS_i}{\left[\left(\frac{I_{sc}}{PS_i}\right)^{\beta} - 1\right]} \tag{2}$$

Where Ti is the relay's operating time, and TDS and PS denote the time dial and plug settings, with values of 0.14 and 0.02 respectively.

The objective function expressed in equation (1) will be optimized if the following inequality conditions are met:

The first limitation is linked to the primary and backup relays meeting coordination time interval (CTI) norms. If R_{pr} and R_{bc} are the primary and backup relays for the occurrence of a failure, and T_{pr} and T_{bc} are the operating time of the primary and buckup relay respectively,   then the restriction may be expressed as follows :

$$T_{bc} - T_{pr} \geq CTI \tag{3}$$

Where CTI stands for time interval coordination between primary and buckep relays. It is set to a value of 0.2s for digital relays and 0.3s for electromechanical relays.

Moreover, the time dial setting (TDS) and plug setting(PS) limitations of relays are given as an inequality restriction as illustrated below:

$$PS_{min} \leq PS \leq PS_{max} \tag{4}$$

$$TDS_{min} \leq TDS \leq TDS_{max} \tag{5}$$

Where TDS_{min} , TDS_{max} ,PS_{min} and PS_{max} are the minimum and maximum values of the time dial settings and the plug settings of relay R_i. The values of TDS_{min} and TDS_{max} has been set as 0.025 and 1.2, respectively.

The suggested method was implemented using MATLAB R2018a running on a Windows 10, 64-bit platform with an 8 GB RAM Core i5 computer and applied to the optimal coordination issue of DOCRs in two reference systems : 3-bus and 9-bus systems to demonstrate its better performance to previous similar algorithms. The obtained results are compared with other optimization algorithms.

III. EVAPORATION RATE WATER CYCLE ALGORITHM

EWCA is a population-based metaheuristic algorithm motivated by the hydrologic cycle. Evaporated water falls back to earth and is taken into the sky as rain. Individuals (raindrops) are formed at random between the upper and lower borders. The objective function is then used to evaluate all people. The best one is chosen as the sea, while the other outstanding people are chosen as rivers. The rate of flow volume for each stream may be calculated using the following equation based on the objective function value [20].

$$Cost_i = f(R_1^i, R_2^i, R_3^i, \ldots, R_m^i) i = 1,2,3,\ldots, M_{pop} \tag{6}$$

The other individuals can be evaluated from the below equation.

$$M_{sr} = Number \ of \ Rivers + 1 \tag{7}$$

$$M_{Raindrops} = M_{pop} - M_{sr} \tag{8}$$

The following equations can be used to calculate the intensity of flow streams that directly flow to rivers or the sea.

$$MS_m = round\{|\frac{C_m}{\sum_{m=1}^{M_{sr}} C_m}| \times M_{Raindrops}\} \tag{9}$$

$$C_m = Cost_m - Cost_{M_{sr+1}} \tag{10}$$

Where M_{sr} refers to stream numbers

The location of the new streams and rivers can be given bellow.

$$R_{Stream}^{i+1} = R_{Stream}^i + rand \times K \times (R_{River}^i - R_{Stream}^i) \tag{11}$$

$$R_{Stream}^{i+1} = R_{Stream}^i + rand \times K \times (R_{Sea}^i - R_{Stream}^i) \tag{12}$$

$$R_{River}^{i+1} = R_{Stream}^i + rand \times K \times (R_{Sea}^i - R_{River}^i) \tag{13}$$

where rand is an amount ranging from 0 to 1, K is a value ranging from (1,2), and their total equals 2. If there is a gap separating the sea and the river dmax, the evaporation and rainfall phases have begun. The new flow location may be calculated using the following equation.

$$R_{Stream}^{new} = LoB + rand \times (UpB - LoB) \tag{14}$$

where UpB and LoB are the upper and lower borders, respectively. The evaporation condition is also applied to the flow of water to the sea. The new stream location may be calculated using the equation below.

$$R_{Stream}^{new} = R_{sea} + \sqrt{q} \times randn(1, M_{var}) \tag{15}$$

where q is a constant that is 0.1 and the dmax value falls based on the equation

$$d_{max}^{i+1} = d_{max}^i - \frac{d_{max}^i}{Max\_Iter} \tag{16}$$

Numerous rivers are incapable of shortening the distance to the sea. As a result, the following evaporation rate idea is added:

$$ER = \frac{Sum(MS_m)}{M_{sr} - 1} \times rand, m = 2, \ldots, M_{sr} \tag{17}$$

IV. SIMULATION AND RESULTS

A. 3-Bus test system

The IEEE 3-bus test system, as shown in Fig. 1, consists of one generator, three lines, six DOCRs, and six primary/backup relay pairs. The ideal settings for the six relays have to be found. The 12 control variables (TDS1-TDS6 and PCS1-PCS6) should be set to their optimal levels here. The upper and lower limits for TDS were 0.05 and 1.1, respectively. PS sizes range from 0.1 to 2.5. A 0.2 second CTI min was determined, as well as CT rating and fault current values for the system's primary/backup relays[24]. Table 1 contains Relay time deal parameters, plug settings, and Table 2 contains the 3-bus test system operating timings.
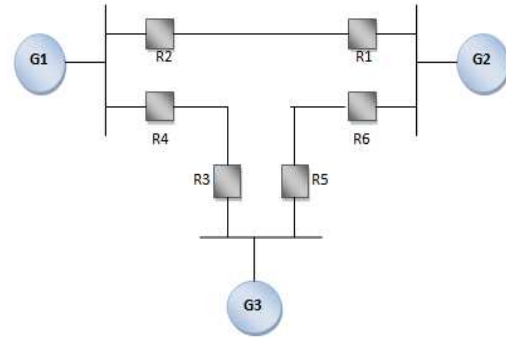
Fig. 1. 3 bus system.

TABLE I. Relay settings for the 3 bus system.

Relays	TDS	PS
1	0.1000	1.89140
2	0.1000	0.7604
3	0.1	1.5813
4	0.1616	0.4733
5	0.1000	0.9071
6	0.1000	1.3058
OF	1.39906	

TABLE II. Relay operation times for the 3 bus system.

Primary relays	Top primary	Backup relays	Top backup
1	0.2379	5	0.4378
2	0.1718	4	0.3718
3	0.2063	1	0.4063
4	0.2610	6	0.4610
5	0.3811	3	0.3811
6	0.2406	2	0.4406

(3)

B. 9-bus test system

The nine-bus test network is used in this instance to validate the suggested approach [25]. The single-line diagram for this system is shown in Figure 2. There are 24 relays (R1, R2,..., R24), 32 main and backup relay pairs, 12 lines (L1, L2,..., L12), and 24 relays in total in this system [26]. There are 48 decision variables, or TDS1 to TDS24 and Ip1 to Ip24, that need to be coordinated in order to set the 24 relays' settings. According to [25], all network buses and DOCRs are numbered in Fig. 2. TDS min and TDS max have beginning ranges of 0.025 and 1.2, and the maximum and minimum PS values are 0.05 and 2.5 respectively. Tables 3 include Relay time deal settings, plug settings and Table 4 contains the operation times of both the primary and backup relays for the 9-bus test system
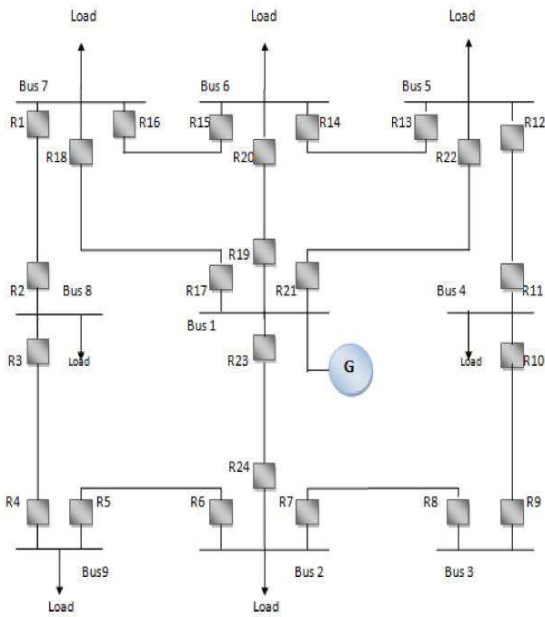
Fig. 2. 9 bus system.

TABLE III. Relay settings for the 9 bus system.

Relays	TDS	PS
1	0.0395	1.2203
2	0.0134	1.1511
3	0.0342	0.9992
4	0.0325	0.9638
5	0.0168	0.9974
6	0.0414	1.0503
7	0.0377	1.1892
8	0.0203	0.96861
9	0.0350	1.0450
10	0.0364	1.2118
11	0.0204	0.91930
12	0.0340	0.8233
13	0.0267	1.1582
14	0.0429	0.9257
15	0.0337	1.1517
16	0.0345	1.0057
17	0.0505	1.1414
18	0.0100	0.1000
19	0.0423	1.2784
20	0.01	0.5258
21	0.0394	1.2314
22	0.0100	0.5717
23	0.0393	1.1961
24	0.0100	0.7657
OF	3.3118	

TABLE IV. Relay operation times for the 9 bus system.

Primary relays	Top.pr	Backup relays	Top.bc
1	0.1306	17	0.3317
2	0.1306	4	0.4289
3	0.0894	1	0.29207
4	0.1365	6	0.34223
5	0.1324	3	0.3390
6	0.0916	8	0.2936
6	0.1338	23	0.3690
7	0.1338	5	0.3368
7	0.1298	23	0.3334
8	0.1298	10	0.3368
9	0.1081	7	0.4096
10	0.1500	12	0.3629
11	0.1635	9	0.3656
12	0.1114	14	0.3519
12	0.1217	21	0.3221
13	0.1217	11	0.3690
13	0.0991	21	0.4052
14	0.0991	16	0.3690
14	0.1338	19	0.3336
15	0.1338	13	0.4315
15	0.1169	19	0.321
16	0.1169	2	0.4315
16	0.1189	17	0.7407
18	0.0176	2	0.3407
18	0.0176	15	0.7312
20	0.0297	13	0.3334
20	0.0330	16	0.4052
22	0.1038	11	0.4052
22	0.0469	14	0.3221
24	0.1306	5	0.3334
24	0.1306	8	0.3690

C. Results and discussion

Tables 5 and 6 lists the outcomes of suggested EWCA and other algorithms. The minimal relay operation times achieved with the suggested approach were 1.3990 s, 3.3118 for 3-bus and 9-bus system respectively, based on comparison with data in the literature. It is clear from the comparative findings in Tables 5 and 6 that the suggested EWCA approach produced superior outcomes than the other algorithms described in the literature. Fig 3 display clearly the coordination times intervals between the primary and backup relays in the case of the 9 bus test system where the majority of the intervals are around 0.2s and 0.3 s.

TABLE V. Compared results for the 3 bus test system.

Method	$sum(T_{pr})$	Method	$sum(T_{pr})$
PSO[24]	1.9258	SSA[22]	4.815
SOA[25]	1.599	MRFO[22]	4.780
AFDBA[26]	2.5287	DE[26]	2.6292
BA[26]	2.7040	EWCA	1.39906

TABLE VI. Compared results for the 8 bus test system.

Method	$sum(T_{pr})$	Method	$sum(T_{pr})$
EWCA	3.3118	FFA [24]	6.340
NLP	10.87	CSA [24]	5.180
MEFO [23]	6.088	GA [24]	7.4947
BBO [23]	4.9	HAS [24]	4.9046

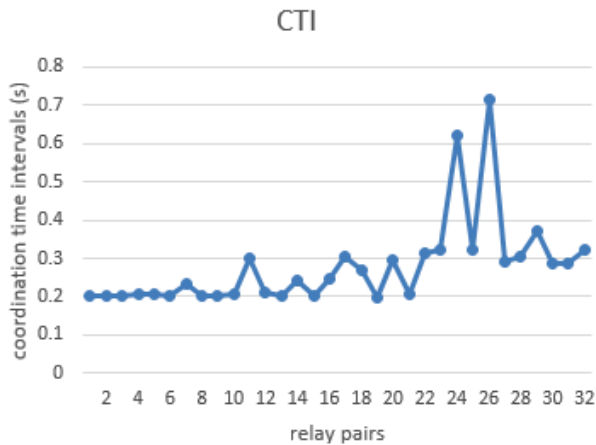Fig. 3. Coordination time intervals between primary and backup relays (9 bus test system).

V. CONCLUSION

In this study, the DOCR coordination problem is addressed utilizing the EWCA optimization approach , The goal is to reduce the total working time of all primary relays by selecting the TDS and PS decision variables. The proposed scheme can be expanded to an adaptive protection scheme using the advanced communication infrastructure, where the centralized controller first detects changes in the microgrid topology or DG penetration and then employs the best relay settings appropriate for the current system configuration. It has been found that the proposed EWCA technique performs better than other existing algorithms, Thus, it can provide a possible solution to the relay coordination problems.

REFERENCES

[1] Usama, M., Moghavvemi, M., Mokhlis, H., Mansor, N. N., Farooq, H., & Pourdaryaei, A. (2021). Optimal protection coordination scheme for radial distribution network considering ON/OFF-grid. *Ieee Access*, 9, 34921-34937.

[2] Bouzid, A., & Bouchahdane, M. (2013). coordination de systemes de protection appliquee au reseau national.

[3] Kheldoun, A., Djeriou, S., Kouadri, A., & Refoufi, L. (2015). A Simple and Accurate Maximum Power Point Tracking Algorithm for Photovoltaic Systems. *Progress in Clean Energy, Volume 2:*

Novel Systems and Applications, 721-733.

[4] Oussama, M., Mohamed, B., Hamza, B., Aissa, K., Ahmed, E., & Rafik, B. (2023, March). An optimal coordination of directional overcurrent relays using a Gorilla troops optimizer. In *2023 International Conference on Advances in Electronics, Control and Communication Systems (ICAECCS)* (pp. 1-5). IEEE.

[5] Telukunta, V., Pradhan, J., Agrawal, A., Singh, M., & Srivani, S. G. (2017). Protection challenges under bulk penetration of renewable energy resources in power systems: A review. *CSEE journal of power and energy systems*, 3(4), 365-379.

[6] Serna, J., de Jesús, J., López-Lezama, J.M. Alternative methodology to calculate the directional characteristic settings of directional overcurrent re-lays in transmission and distribution networks. Energies 2019, 12, 3779.

[7] Bakhshipour, M., Namdari, F., & Samadinasab, S. (2021). Optimal coordination of overcurrent relays with constraining communication links using DE–GA algorithm. *Electrical Engineering*, 1-15.

[8] Merabet, O., Bouchahdane, M., Belmadani, H., Kheldoun, A., & Eltom, A. (2023). Optimal coordination of directional overcurrent relays in complex networks using the Elite marine predators algorithm. *Electric Power Systems Research*, 221, 109446.

[9] Mosaad, A. M., Attia, M. A., & Abdelaziz, A. Y. (2019). Whale optimization algorithm to tune PID and PIDA controllers on AVR system. Ain Shams Engineering Journal, 10(4), 755-767.

[10] Belmadani, H., Kheldoun, A., Bradai, R., Mekhilef, S., & Siddique, M. D. (2022). A twofold hunting trip African vultures algorithm for the optimal extraction of photovoltaic generator model parameters. Energy Sources, Part A: Recovery, Utilization, and Environmental Effects, 44(3), 7001-7030.

[11] Anter, A. M., & Hassenian, A. E. (2018). Computational intelligence optimization approach based on particle swarm optimizer and neutrosophic set for abdominal CT liver tumor segmentation. Journal of Computational Science, 25, 376-387.

[12] Ishaque, K., Salam, Z., Amjad, M., & Mekhilef, S. (2012). An improved particle swarm optimization (PSO)–based MPPT for PV with reduced steady-state oscillation. IEEE transactions on Power Electronics, 27(8), 3627-3638.

[13] Khurshaid, T., Wadood, A., Farkoush, S. G., Kim, C. H., Yu, J., & Rhee, S. B. (2019). Improved firefly algorithm for the optimal coordination of directional overcurrent relays. *IEEE Access*, 7, 78503-78514.

[14] Albasri, F. A., Alroomi, A. R., & Talaq, J. H. (2015). Optimal coordination of directional overcurrent relays using biogeography-based optimization algorithms. *IEEE Transactions on Power Delivery*, 30(4), 1810-1820.

[15] Irfan, M., Wadood, A., Khurshaid, T., Khan, B. M., Kim, K. C., Oh, S. R., & Rhee, S. B. (2021). An optimized adaptive protection scheme for numerical and directional overcurrent relay coordination using Harris hawk optimization. *Energies*, 14(18), 5603.

[16] Wadood, A., Kim, C. H., Khurshiad, T., Farkoush, S. G., & Rhee, S. B. (2018). Application of a continuous particle swarm optimization (CPSO) for the optimal coordination of overcurrent relays considering a penalty method. *Energies*, 11(4), 869.

[17] Khurshaid, T., Wadood, A., Farkoush, S. G., Yu, J., Kim, C. H., & Rhee, S. B. (2019). An improved optimal solution for the directional overcurrent relays coordination using hybridized whale optimization algorithm in complex power systems. *IEEE Access*, 7, 90418-90435.

[18] Wadood, A., Khurshaid, T., Farkoush, S. G., Kim, C. H., & Rhee, S. B. (2019). A bio-inspired rooted tree algorithm for optimal coordination of overcurrent relays. In *Intelligent Technologies and Applications: First International Conference, INTAP 2018, Bahawalpur, Pakistan, October 23-25, 2018, Revised Selected Papers 1* (pp. 188-201). Springer Singapore.

[19] Bouchekara, H. R. E. H., Zellagui, M., & Abido, M. A. (2017). Optimal coordination of directional overcurrent relays using a

modified electromagnetic field optimization algorithm. *Applied Soft Computing*, *54*, 267-283.

[20] Hussien, A. G., Hashim, F. A., Qaddoura, R., Abualigah, L., & Pop, A. (2022). An enhanced evaporation rate water-cycle algorithm for global optimization. *Processes*, *10*(11), 2254.

[21] Alam, M. N., Das, B., & Pant, V. (2015). A comparative study of metaheuristic optimization approaches for directional overcurrent relays coordination. *Electric Power Systems Research*, *128*, 39-52.

[22] Hamdi Tolga Kahraman, Huseyin Bakir, Serhat Duman, Mehmet Katı, Sefa ARAS, Ugur Guvenc, Dynamic FDB selection method and its application: modeling and optimizing of directional overcurrent relays coordination, Applied Intelligence (2022) 52:4873–4908.

[23] Albasri, F. A., Alroomi, A. R., & Talaq, J. H. (2015). Optimal coordination of directional overcurrent relays using biogeography-based optimization algorithms. *IEEE Transactions on Power Delivery*, *30*(4), 1810-1820.

[24] Mansour, M. M., Mekhamer, S. F., & El-Kharbawe, N. (2007). A modified particle swarm optimizer for the coordination of directional overcurrent relays. *IEEE transactions on power delivery*, *22*(3), 1400-1410.

[25] Amraee, T. (2012). Coordination of directional overcurrent relays using seeker algorithm. *IEEE Transactions on Power Delivery*, *27*(3), 1415-1422.

[26] Sampaio, F. C., Tofoli, F. L., Melo, L. S., Barroso, G. C., Sampaio, R. F., & Leão, R. P. S. (2022). Adaptive fuzzy directional bat algorithm for the optimal coordination of protection systems based on directional overcurrent relays. *Electric Power Systems Research*, *211*, 108619.

Developing A Ultrasound-Based Smart Bracelet To Guide And Assist The Blind

Mourad KEDIM
department of biomedical engineering
Mouloud Mammeri University of
Tizi-Ouzou, Algeria
mourad.kedim@ummto.dz

Abstract—**In order to meet one of the blind's needs, we thought of designing a smart bracelet that would allow this category of people to navigate their way through the obstacles of the everyday environment, so we used an ultrasound sensor, a vibrator, an acoustic indicator device (buzzer), an Arduino Nano board, and connection cables. The electrical assembly has been performed in parallel with the development of an operating algorithm, the programming of which was implemented in the Arduino environment. Functional verification of this smart bracelet prototype has been conducted under stringent and complex conditions to ensure trial reliability and provide an objective evaluation. The system gives satisfactory results with an average success rate of 76.8%, taking into account the first use of this device by the tried people and the unknown path that was traversed, in addition to the phobia caused by blindfolding the eyes. We think its use will be easier for the blind.**

Keywords— smart bracelet, Arduino Nano, ultrasonic sensor, Bazzer, vibrator, operating algorithm, blind.

I. INTRODUCTION

Sensory receptors allow organisms to know and interpret various environmental information (acoustics, visuals, flavor, touch, smell, etc.). When they occur, they pick them up and transmit them to the brain to process, analyze, and identify changes in the world around them.

Unfortunately, these senses can be damaged by accidents, illness or birth defects, creating a barrier for the affected person. Visual blindness is one of the most common stresses encountered in our society.

The World Health Organization announced that there were 36 million people with visual blindness in the world in 2015, and 173,000 people in Algeria in 2013. Over the years, this number has grown increasingly and represent a significant group in society [1].

Visual impairment and blindness pose a problem with daily mobility in different environments; this does not always meet patients' needs. Blind people regularly encounter obstacles and architectural barriers that threaten their safety and independence, forcing them to orient themselves and sometimes find their destinations in complex and dangerous places.

Even today, despite all the advances in obstacle detection and 3D mapping, blind people often rely on a white cane [2] or guide dog to help them navigate [3]. There are also modern technologies that use several technologies and sensors (laser, ultrasound, global positioning system, infrared (IR), camera, etc.) in order to provide blind people with the information necessary to locate things.

In this paper, we focus our contribution on the design and implementation of an ultrasound-based smart bracelet, allowing blind people to enjoy life to the fullest, carry out their daily activities and not feel inferior and marginalized.

II. METHOD AND MATERIALS

Helping the blind was the main motivation for us to inspire the idea of this project, which depends mainly on the simple tools used and the algorithms developed in this regard, so that the blind can wear and use this device smoothly in daily life to avoid obstacles and maintain personal safety.

For this, we used an ultrasonic sensor, which detects and measures the distance between it and stable or moving objects, in order to trigger an audible and vibratory alarm of intensity linked to the distance detected in an interval of 80 cm. This system helps the blind to protect themselves and guide them according to the block diagram described in the following (fig. 1):
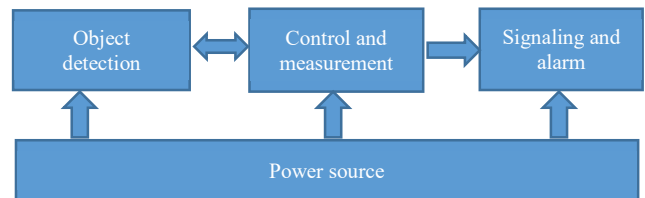
Figure. 1. Functional diagram of smart bracelet system

The ultrasonic sensor emits mechanical waves [5], at frequencies higher than audible frequency [6], for sensing objects with mechanical wave's echoes principle through which they bounce. According an algorithm, the Arduino NANO board microcontroller regulates the measurement of the distance of objects and adjusts the alertness auditory degree and sensory alarm signals to warn the blind person.

A. Object detection

Based on frequency, sound waves are divided into four groups: infrasound, audible sounds (AS), ultrasound (US), and hyper-sounds (HS). These groups are shown in the following table [5–6]:

TABLE 1. CLASSIFICATION OF ACOUSTIC WAVES.

Type	Frequency
infrasound	Frequency less than 20 HZ
audible sounds	Frequency between 20 HZ and 20 KHz
ultrasound	Frequency between 20 KHZ and 500 MHz
hyper-sounds	Frequency greater than 500MHz

The process of determining an object's distance that might limit a blind person's movement begins by applying the following relationship to the speed of the ultrasound wave's return [6].

$$D = \frac{c*\Delta t}{2} \qquad (1)$$

The ultrasound travels through the air at a speed of 340 m/s when traveling round-trip between the ultrasonic sensor and the obstruction that is duration Δt of twice the desired distance.

With molecules vibrating in the direction of energy propagation, sound waves are longitudinal pressure waves. Zones of compression and relaxation are created when the wave moves through. Subsequently, the ultrasound will experience several changes based on the characteristics of the material and its propagation environment, which includes the following.

- Celerity « c » [5] : The celerity of an ultrasonic wave is the speed of propagation of this wave in the medium expressed in m / s: it depends only on the medium, it is described by the following equation

$$c = \sqrt{\frac{E}{P}} \qquad (2)$$

With E and P are respectively the elasticity and the density of the studied tissue.

- Acoustic impedance « Z »[5] : During propagation, the ultrasonic wave is subjected to more or less stress considerable, depending on the medium traversed (water, fat, muscle, bone, etc.) because each medium exhibits a characteristic resistance to propagation called the acoustic impedance Z. It is defined as follows

$$Z = \rho c = (\rho C)^{1/2} \qquad (3)$$

With ρ the density and $c = (C/\rho)^{1/2}$ the speed of the acoustic wave, C, is the elasticity constant appropriate to the type of wave.

- Wave length « λ » [5]: The wavelength, which indicates the resolving power and measures the spatial extent of a cycle of variation, is the distance traveled by the ultrasonic pressure wave during a given amount of time. The resolutions in ultrasonography are millimeter-scale. Described by the relation

$$\lambda = \frac{c}{f} \qquad (4)$$

With, c, the celerity and f the frequency.

- Pressure « P » and intensity « I »[6]: At each point, the acoustic pressure P varies according to the frequency ultrasound wave. The energy delivered to the tissue depends on these pressure variations, which subject the particles of the medium to vibratory

movements. ultrasonic energy which crosses the unit area perpendicularly during the unit time, It is related to the sound pressure by the formula:

$$I = \frac{P^2}{2\rho c} \qquad (5)$$

With, ρ the density, c the celerity.

- Elasticity « E »[6]: The elasticity depends mainly on temperature and pressure.

B. Control and measurement

The core of this system is the microcontroller of the Arduino Nano board, which allows us to manage and control the functions of the system.

In our system, we used the HC-SR04 ultrasonic sensor (Fig. 2) to measure the distance of an object's presence from the sensor (or the blind person wearing this bracelet). The detection range is 2 cm to 4 m, with an accuracy of 3 mm and a detection angle of approximately 30 ° [7].

Sunlight and dark materials, like clothing, have no effect on this sensor, though they can be challenging to detect. [8]
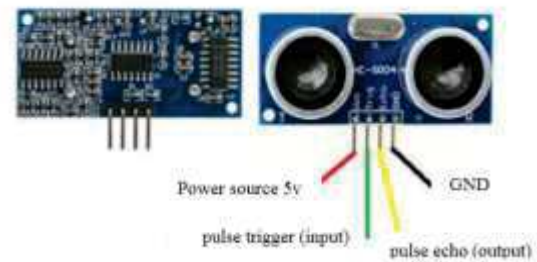
Figure. 2. Ultrasonic Sensor HC-SR04 [7]

The operating principle consists of presenting a high-level digital pulse on the Trig input of the sensor for 10 μs, this sends a series of 8 ultrasonic pulses, of 40 kHz to the sensor transmitter, and prepares the receiver to detect the echo signal [9].

The receiver translates this signal to a high-level signal on the Echo sensor output (fig. 3), its duration corresponds to the time between the ultrasound emission and reception [10], which allows us to calculate the distance between the sensor and the object [11]:

$$D = S.t \qquad (6)$$

Where « t » is the high signal duration received state, S sound speed in air: 340 m / s.

We have:

- S= 340 m/s = 34 000cm/1000 000 μs.

- The signal goes back and forth, so the distance is worth half.

So the relation becomes:

$$D(cm) = \frac{0,034.t}{2} = 0,017.t \approx t/58 \qquad (7)$$
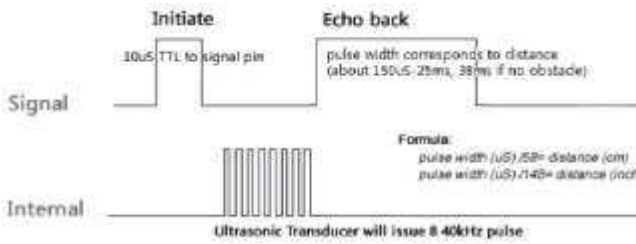
Figure. 3. The temporal diagram [7].

The following table 2 lists the specific features of the Ultrasonic Sensor HC-SR04 [12–13]:

TABLE 2. SPECIFICATIONS OF ULTRASONIC SENSORS HC-SR04.

Nature	Characteristics
Capture distance	2cm a 4m
Resolution (precision)	3mm
Operating voltage (input voltage)	5V
Current (input amperage)	15mA
Frequency of operation	40Hz
Measuring angle	30degrees
Effective angle	15 degrees
Trigger input signal	10µs. TTL impulsion
Dimension L x W x H	45mm x 20mm x 1mm
Weight	8.5g

C. Signaling and alarm

To alert the blind individual, we used a vibrator motor and an audio alarm (buzzer) whose vibration and sound frequencies and intensities matched the distance of the obstacles. We outline the implementation of electronic signaling and alarm circuits in this section.

a) Arduino buzzer connection:

Positive and negative pins from the buzzer component are connected to pins A1 on the Arduino and (-) on the battery, respectively (fig. 4).

- The positive (+) of the buzzer ➞ pin A1 of the arduino.
- The negative (-) of the buzzer ➞ pin (-) of the battery.
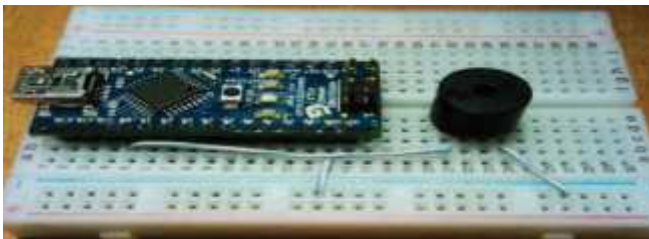
Figure. 4. Electric circuit of the buzzer.

b) The Arduino vibrator connection

Positive and negative pins from the vibrator component are connected to digital pins 3 on the Arduino and (-) on the battery, respectively (Fig. 5).

- The positive (+) of the vibrator ➞ pin 3 the arduino digital.
- The negative (-) of the vibrator ➞ the pin (-) of the battery.
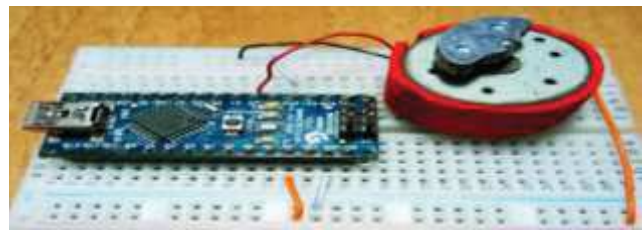
Figure. 5. Electric circuit of the vibrator.

c) The overall electrical circuit

The entire electrical circuit of the hardware component of our research, which was performed on a test plate and simulated using the ISIS Proteus environment, is shown in Figs. 6 and 7, respectively.
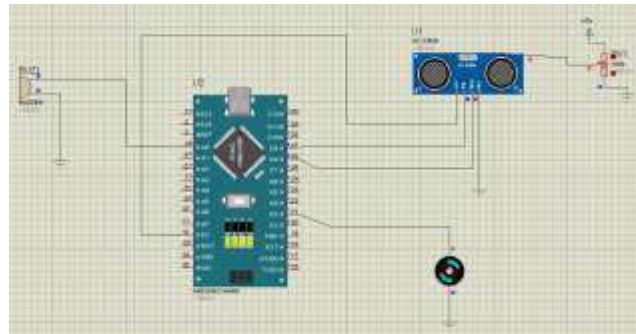
Figure. 6. the global electrical circuit
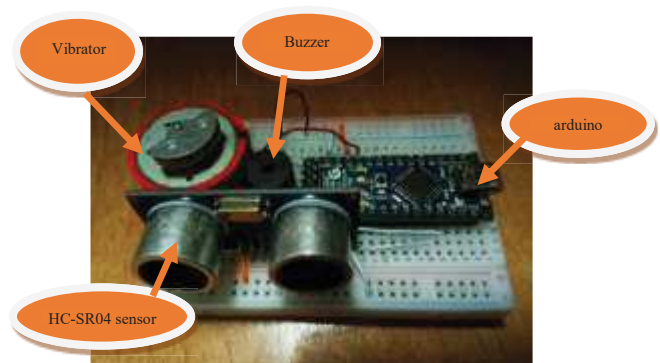
Figure. 7. Real global circuit.

D. System algorithm

The Arduino board's embedded microcontroller management program must be implemented in order for the hardware to function. The program flowchart we created in an Arduino environment is displayed in Fig. 8 and depicts the many phases of information and signaling management and control in this system.
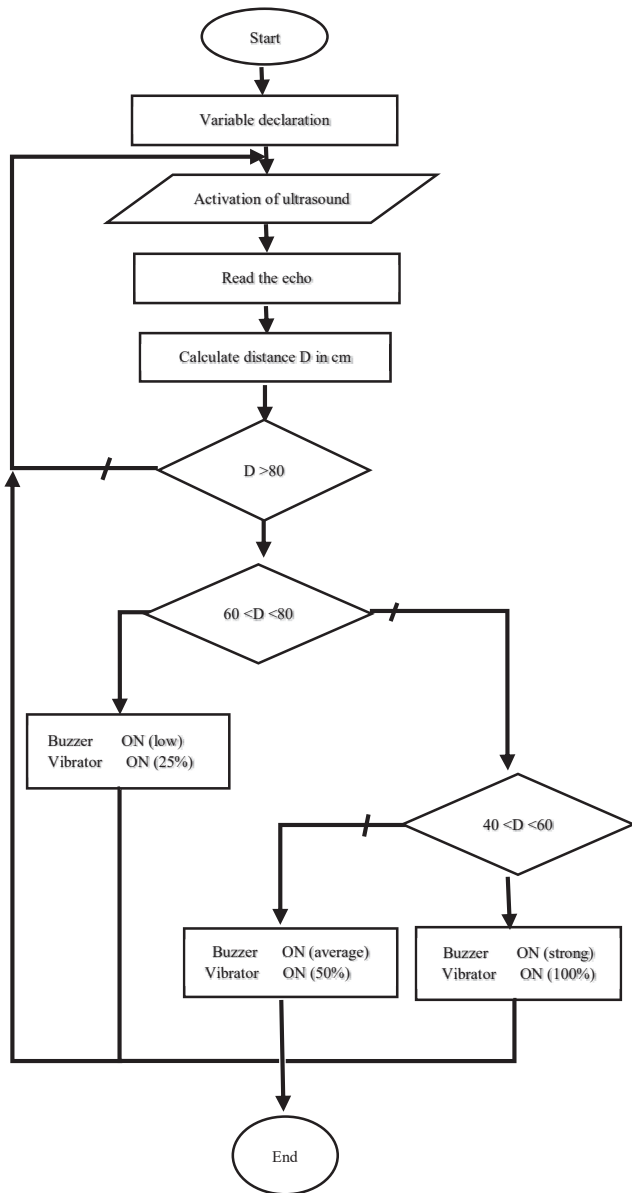
Figure. 8. The detection and measurement flowchart.

Figure. 9. Outcomes for distances greater than 80cm

Figure. 10. Results for distance range from 60 em to 80 cm
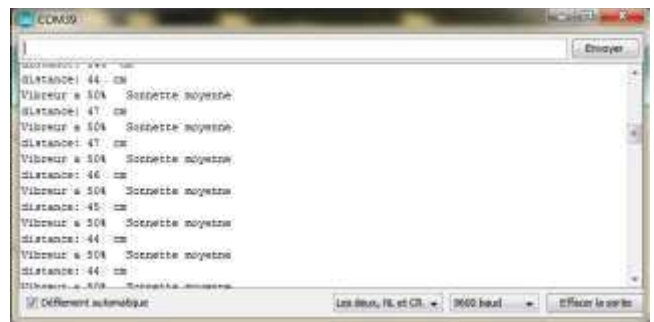
Figure. 11. Results for distance range from 40 em to 60 cm

Figure. 12. Results for distances less than 40 cm

The program is divided into three sections: the first declares the various input and output ports, the second contains instructions for loops, and the final section deals with frequency and time delay declarations (sensor, buzzer, and vibrator).

III. TESTS AND RESULTS

A. The initial test

After finishing our program, we upload it to the Arduino board using the USB cable and compile to see if there is a debug error.

The first test was run using the Arduino IDE software over the virtual COM port's serial link. The results are shown on the serial monitor following implementation in the following figures 9, 10, 11, and 12:

We observed that the system measures the distance as indicated in figure 9 after loading the program onto the Arduino board's microcontroller and receiving the results displayed above.

We thus displayed the messages at each step, changing the obstacle detection distance, as illustrated in figures 10, 11, and 12, after conducting tests to verify the proper functioning of the various steps.

B. Autonomous System Tests and Results

The ultimate smart bracelet is a battery-operated, standalone gadget worn in the hand like a watch that makes it easier for blind people to get over daily barriers and impediments. Fig. 13 and 14 display the finished prototype.

Figure. 13. the gadget's external view.
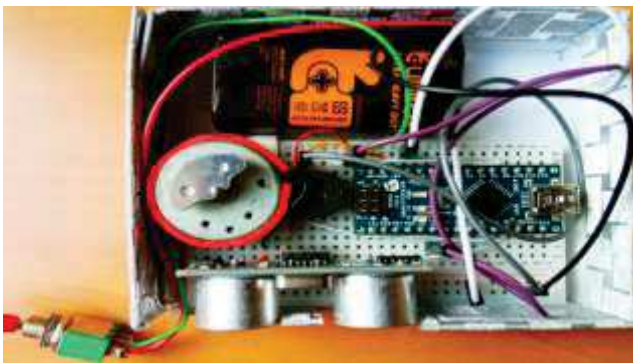
Figure. 14. internal view of the device

We carried out real experiments to make sure the device was valid for exploration and that it worked well.

For this one, we set up a path that is full of everyday objects and obstacles, as seen in fig. 15, and then we test the device on a group of individuals who are blindfolded and vary in age and gender to provide credibility to the experience and an unbiased evaluation for this gadget.

Figure. 15. The obstacle course description for the device's testing.

We have completed the pass table 3, in order to calculate the pass rate of passing through objects according to the following formula:

$$Rate = \frac{\text{Validated number of obstacles} \times 100\%}{\text{total number of barriers}} \quad (8)$$

TABLE 3. RESULTS OF EXPERIMENTAL TESTS.

Person	Obstacle							
	Chair1	Table	Chair2	Person	Armchair	Door	The passage's timing (T)	Rate (R)%
Over 50 years Women	✓	✓	×	×	✓	✓	2mn : 30 s	67%
40-50 years Women	✓	✓	✓	✓	✓	×	1mn : 05s	83%
30-40 years Man	✓	✓	✓	×	×	✓	0mn : 55s	67%
20 -30 years Women	✓	✓	✓	✓	✓	✓	0mn : 50s	100%
10-20 years Man	✓	✓	×	✓	×	✓	1mn : 17s	67%

The following formula is used to determine the average amount of time Ta needed for each test:

$$Ta = \frac{T1 + \cdots + T5}{5} = 67.4\ s$$

The following formula is used to determine the average success rate Sr:

$$Sr = \frac{R1 + \cdots + R5}{5} = 76.8\ \%$$

The table above shows the different people who have passed this validation test of our device. Observe that they are of various ages and genders, and that the 10-meter path is paved with a variety of large and small obstacles.

We found that a person in his twenties takes 50 seconds to pass through, whereas a person over fifty takes two minutes and thirty seconds.

The mean duration is 67.4 seconds. With an average success rate of 76.8%, the rate ranges from 67% for three individuals who are ten, thirty, and older to 100% for an individual who is in their twenties.

Based on the results that were obtained, which were satisfactory considering that this was people's first time using the device, the path that was taken, and the fear associated with wearing blindfolds, it is anticipated that the blind will find this device easier to use.

IV. CONCLUSION

In this paper, we centered on individuals with visual impairments and suggested a smart bracelet prototype to enable them to go about their daily lives without assistance and without risk.

We have adopted this system through less complicated and expensive means, and it consistently ensures the timely arrival of the right information by empowering the user to make an informed decision and live independently and safely.

Through our work, we were able to gain an understanding of the Arduino IDE programming environment's electronic aspects as well as the various physical mechanisms of ultrasound and intelligent control systems.

The results of the tests indicate that this prototype is effective, and we anticipate that it will be marketed and worn by the blind to give them the best and most efficient form of intelligent guidance.

This prototype has limitations even if the test results show that it is successful. We specifically point out the drawbacks of employing ultrasonic waves as they can only return to the sensor when they encounter large, high densely surfaces. The ultrasonic echo is directed by slanted surfaces to locations far from the sensor, where the sensor is unable to detect the echo. When it comes to thin and sharp things, the echo signal is completely lost. Low-density surfaces allow ultrasonic waves to travel through them, and in all of these situations, a potential hazard that may cause injury to a blind person is undetectable.

We can include certain lately used technology, such GPS, laser sensors, digital cameras, artificial intelligence, and other recently used technologies, as a forward-looking view of such devices and to prevent such flaws in our first model. But it's important to consider the device's size and usability for blind individuals since these issues tend to discourage blind people from utilizing these kinds of gadgets and instead encourage them to rely on simpler items for everyday guidance.

REFERENCES

[1] Algérie presse service, https://www.aps.dz/algerie/61363-[Last visited: 02/02/2021]

[2] World Health Organization "World report on vision – WHO", 2019.

[3] Brian M. Lempriere "ultrasond and elastic waves", Elsevier Science (USA) 2002, Library of Congress Catalog Number: 2001098014 ISBN: 0-12-443345-6

[4] Pamely Zantou , Mikaël Ange Mousse, Bethel Atohoun "An intelligent based system for blind people monitoring in a smart home", 2020, HAL Id: hal-02966150

[5] Aline Darc Piculo dos Santos, Fausto Orsi Medola, Milton José Cinelli, Alejandro Rafael Garcia Ramirez, Frode Eika Sandnes "Are electronic white canes better than traditional canes? A comparative study with blind and blindfolded participants", 2020, Springer, Universal Access in the Information Society (2021) 20:93–103

[6] Sankari Subbiah; S Ramya; G Parvathy Krishna; Senthil Nayagam " Smart Cane For Visually Impaired Based On IOT" 2019, IEEE, 3rd International Conference on Computing and Communications Technologies (ICCCT)

[7] R.N. Thurston, Allan D. Pierce and Emmanuel P. Papadakis "Ultrasonic Instruments and Devices IReference for Modem Instrumentation, Techniques, and Technology" Elsevier, Academic Press1999, 1-482 [495]

[8] K. Takeuchi, "The Palm Sonar", Available from: "http://www.palmsonar.com/", 2010.

[9] Hussain, M. A., Ullah, M. G., Fareed, A., & Sohail, B. (2016). The Smartcane for Blind People An Electronically Smart Stick to Aid Mobility. International Journal of Computer Science and Information Security, 14(4), 276.

[10] Cytron technologies, Product User's Manual – HCSR04 Ultrasonic Sensor, V1.0 May

[11] Motta, G., Ma, T., Liu, K., Pissaloux, E., Yusro, M., Ramli, K., ... & Shi, H. (2018). Overview of Smart White Canes: Connected Smart Cane from Front End to Back End. In Mobility of Visually Impaired People (pp. 469-535). Springer, Cham.

[12] 2013Chanana, P., Paul, R., Balakrishnan, M., & Rao, P. V. M. (2017). Assistive technology solutions for aiding travel of pedestrians with visual impairment. Journal of Rehabilitation and Assistive Technologies Engineering, 4, 2055668317725993.

[13] Rohit Sheth, Surabhi Rajandekar, Shalaka Laddha, Rahul Chaudhari "Smart White Cane –An Elegant and Economic Walking Aid" American Journal of Engineering Research (AJER), Vol03, Issue-10, 2014 pp-84-89

A Numerical Approach For Solving Optimal Control Problem Governed By 1D-Heat Equation With Two-Point Boundary Conditions, In The Presence Of A Scale-Invariant Parameter*

*Note: Sub-titles are not captured in Xplore and should not be used

1st Karim Benalia
Faculty of hydrocarbons and Chemistry
University of Boumerdes
Boumerdes 35000, Algeria
k.benalia@univ-boumerdes.dz

Abstract—**In this paper, we present a computational approach based on the finite difference approximation and the Variational Iteration Method (VIM) for solving optimal control problem governed by 1D-Heat equation with two-point Boundary conditions, in the presence of a Scale-Invariant parameter. We first construct the scale-invariant solutions for the one dimensional, linear heat equation, and we prove the Dirichlet Boundary controllability of 1D-Heat equation, and then we present our general problem formulation. Next, we solve the problem by applying Minimum Principe of Pontryagin, which leads to the necessary conditions of optimality. To achieve the solution of the necessary conditions optimality with a scale-invariant parameter using the Variational Iteration Method (VIM), an approach is proposed. Finally we illustrate our approach with numerical example.**

Index Terms—**Boundary optimal control, 1D-Heat equation, Scale-invariant solutions, Minimum principle of Pontryagin**

I. Introduction

Optimal control problem governed by partial differential equations (PDES), particularly for heat equation have broad applications in almost every area of modern science and engineering, such as control of selective laser melting (SLM), control of thermoelastic plate, and reaction diffusion optimisation, etc...(see for instance [1], [2]). For optimal control problem with boundary conditions on their importance, we refer the reader to [3], [4].

The optimal control problem consists of finding a control variable that minimizes a cost functional subject to a PDE. For systems described by PDES obtaining the solution, either numerically or analytically is a difficult task due to the complexity of the calculations to handle.

Recently, various methods have been applied to solve optimal control problem of systems governed by PDES (see for example [5]–[7]). These methods are still not applied for heat equation, in the presence of scale-invariant parameter, which motivates this work. We have already worked on the time

optimal control problem in the presence of a scale-invariant parameter, using a direct type method with total discretization for the one-dimensional, linear heat equation (see [8]).

In this paper, we propose a numerical approach based on the finite difference approximation and the Variational Iteration Method (VIM) [7], [9] for solving optimal control problem governed by 1D-Heat equation with two-point boundary conditions, in the presence of scale-invariant parameter. This method is applied to achieve optimality conditions of the Hamilton-Pontryagin equations, which constitute the necessary optimality conditions derived using the Minimum Principe of Pontryagin [10].

The rest of the paper is organized as follows. In section II we construct the scale-invariant solutions for the one-dimensional heat equation and we prove the Dirichlet Boundary controllability of 1D-Heat equation, then we present our general problem formulation. In section **??** we present our numerical approach for solving our optimal control problem, in the presence of a scale-invariant parameter. A numerical example is illustrated in section IV. Section V consists of a conclusion.

II. Scale-Invariant Solutions and Problem Statement

A. Construction of a scale-Invariant Solutions for the 1D-Heat Equation

It is well-known that the one dimensional, linear heat equation has a natural scaling invariance (see [11]). Let us denote by $y(t,x)$ a analytical solution, for any $(x,t) \in \mathbb{R} \times [0,t]$. Then, for any strictly positive real number Λ, the mapping:

$$(t,x) \mapsto y(t,x,\Lambda) = \Lambda y(\Lambda^2 t, \Lambda x)$$

is also a solution.
The exact analytical solution $\hat{y}$, which depends on the space variable x, the time variable t, and the scaling parameter Λ,

is given by (see see the article of K. Benalia, C.l. David and B. Oukacha [8]):

$$y(x, t, \Lambda) = y(x, t) + \varepsilon \sum_{j=1}^{N_0} \frac{1}{\Lambda} \, y \left(\frac{x}{\Lambda^j}, \frac{t}{\Lambda^{2j}} \right),$$

with $\varepsilon \in \{-1, +1\}$, $N_0 \in \mathbb{N}^\star$ Hence, we have:

$$\frac{\partial y}{\partial t}(x, t, \Lambda) = \frac{\partial y}{\partial t}(x, t) + \frac{\varepsilon}{\Lambda} \sum_{j=1}^{N_0} \frac{\partial}{\partial t} \left[y \left(\frac{x}{\Lambda^j}, \frac{t}{\Lambda^{2j}} \right) \right].$$

One builds thus an exact solution of the one-dimensional heat equation. The dependence of this solution towards the scaling parameter Λ, naturally leads to control problem governed by 1D-Heat equation with Dirichlet boundary condition, in the presence of a scale parameter.

Let $\Omega = (0, l)$ be the segment of the real axis. For a time $T > 0$, and for a scale-invariant parameter $\Lambda > 0$, we set $Q = \Omega \times (0, T) \times \mathbb{R}_+^\star$, and $K = (0, T) \times \mathbb{R}_+^\star$. We consider the following Dirichlet boundary control problem

$$\frac{\partial y}{\partial t}(x, t, \Lambda) = \frac{\partial^2 y}{\partial x^2}(x, t, \Lambda) \qquad \text{in Q,} \qquad (1)$$

$$y(x, 0, \Lambda) = y_0(x, \Lambda) \qquad \text{in } \Omega \times \mathbb{R}_+^\star, \qquad (2)$$

$$y(0, t, \Lambda) = 0 \qquad \text{on } K, \qquad (3)$$

$$y(l, t, \Lambda) = u(t, \Lambda) \qquad \text{on } K, \qquad (4)$$

where $y_0(x, \Lambda)$ is the initial temperature at the time $t = 0$, $u(t, \Lambda)$ is the control variable on the the boundary condition, in the presence of a scale-invariant parameter.

B. Controllability of (1)-(4)

The one dimensional controllability of (1)-(4) we deal with reads as follows : Let $y_T(x, .)$ be a given function that represents a desired state we hope to reach at a time T. The objective of (1)-(4) is to find a Dirichlet control u enforced at $x = l$ satisfying :

$$y(x, T, \Lambda) = y_T, \text{ in } \Omega \times \mathbb{R}_+^\star \qquad (5)$$

Let then f be arbitrarily given in $L^2(Q)$. Consider φ as the solution of the backward heat equation

$$\begin{cases} -\dot{\varphi} - \Delta \varphi = f & \text{in } Q, \\ \varphi(0, t, \Lambda) = 0 & \text{on } K, \\ \varphi(l, t, \Lambda) = 0 & \text{on } K, \\ \varphi(x, T, \Lambda) = 0 & \text{in } \Omega \times \mathbb{R}_+^\star \end{cases} \qquad (6)$$

As recalled in [12], It is well known that, for every $f \in L^2(Q)$, there exists a unique solution φ to (6), with

$$\varphi \in L^2 \left(0, T; H_0^1(\Omega \times \mathbb{R}_+^\star) \right) \cap C \left(0, T; L^2(\Omega \times \mathbb{R}_+^\star) \right).$$

Provided that the boundary is regular enough which is assumed from now on, the normal derivative $\frac{\partial \varphi}{\partial x}(l, .)$ belongs to $L^2(K)$ and is subjected to the stability

$$\|\frac{\partial \varphi}{\partial x}(l, .)\|_{L^2(K)} \leq C_0 \|f\|_{L^2(Q)} \qquad (7)$$

where C_0 denotes a positive constant.

Applying the transposition method [13] to problem (1)-(4), we come up with the following variational equation:

$$\int_Q y(x, t, \Lambda) f \, dx \, dt = - \int_K u \frac{\partial \varphi}{\partial x}(l, .) \, dt. \qquad (8)$$

The equivalence between (8) and problem (1)-(4) has been checked for instance in [14].

The existence and uniqueness for , $y \in L^2(Q)$ are direct consequences of (7) and Riesz' Theorem (see [15]).

As a consequence, we have: For any strictly positive real time T, for any scale invariant parameter $\Lambda > 0$, and for any continuous function u of $L^2(K)$, the system (1)-(4) has a unique solution $y \in L^2(Q)$ which belongs to $C \left(0, T; H^{-1}(\Omega \times \mathbb{R}_+^\star) \right)$.

As indicated and discussed in [14] for the optimal control problem, the point is to consider a subspace of admissible Dirichlet controls that brings facilities in the computations. That should be a subspace of $L^2(K)$ that allows to define the final observation $y(T) \in L^2 \left(\Omega \times \mathbb{R}_+^\star \right)$.

Making use of a Green formula (see [14]), we have this other result :

For each $y_0 \in L^2 \left(\Omega \times \mathbb{R}_+^\star \right)$, and for any scale invariant parameter $\Lambda > 0$, there exists a control u, belonging to $L^2(K)$, such that the corresponding solution of (1)-(4) satisfies (5).

C. Problem Statement

The optimal control problem governed by (1)-(4) consists of finding a control variable optimal that minimize a cost functional $J(u)$.

In the following, we focus on optimal control problem governed by 1D-Heat equation with two-point boundary conditions, in the presence of a scale-invariant parameter, which can be formulated as follows

$$\min_{u_0, u_l} J = \int_0^{\Lambda^2 T} \int_0^{\Lambda l} y^2(x, t, \Lambda) \, dx \, dt \\ + \int_0^{\Lambda^2 T} \left[q_0 \, u_0^2(t, \Lambda) + q_l \, u_l^2(t, \Lambda) \right] dt, \qquad (9)$$

subject to the 1D-heat equation with two-points boundary conditions u_0 and u_l:

$$\frac{\partial y}{\partial t}(x, t, \Lambda) = \frac{\partial^2 y}{\partial x^2}(x, t, \Lambda) \qquad \text{in Q,} \qquad (10)$$

$$y(x, 0, \Lambda) = y_0 \qquad \text{in } \Omega \times \mathbb{R}_+^\star, \qquad (11)$$

$$y(x, T, \Lambda) = y_T \qquad \text{in } \Omega \times \mathbb{R}_+^\star, \qquad (12)$$

$$y(0, t, \Lambda) = u_0 \qquad \text{on } K, \qquad (13)$$

$$y(l, t, \Lambda) = u_l \qquad \text{on } K, \qquad (14)$$

where y_0 and y_T are the initial and final temperature at the time $t = 0$ and $t = T$, respectively with a scale parameter. The function u_0 and u_l are the control variables on the two-point boundary conditions. The objective is to determine the optimal value of control u_0 and u_l used at the boundaries to

reach the final temperature y_T, while minimizing the square of temperature over the rod, in the presence of a scaling parameter.

In this paper, To solve the optimal control problem (9)-(14), first we transform the problem into a control problem governed by ordinary differential equations (ODES) [16], [17], using the finite difference approximation to discretize the PDE (10) in space direction x to obtain a set of ordinary differential equations, and we employ the trapezoidal rule for the objective function (9) to obtain a weighting quadratic objective function constituted by state and control variables with a scaling parameter Λ. Second, to obtain the solution of the resulting control problem, we utilize the minimum principle of Pontryagin [10] to deduce the necessary conditions of optimality which can be solved easily by the Variational Iteration Method [7], [9] to get the optimal control law u_0 and u_l.

III. ALGORITHM FOR THE PROPOSED APPROACH (9)-(14)

The proposed algorithm for solving problem (9)-(14) can be summarized as followings:

Step (1): Transform the 1D-heat equation with a scale-invariant parameter (10) into a ordinary differential equation by using the finite difference approximation.

Step (2): Transform the double integral (9) into a one integral, by introducing the trapezoil approximation.

Step (3): Determine the necessary optimality conditions for the an approximation of $J(u_0(\tau), u_l(\tau))$, by using the minimum principe of pontryagin [10].

Step (4): Solve the Hamilton-Pontryagin equations, by using the variational iteration method to determine the successive approximations :

$$y_k^{n+1}(\tau), p_k^{n+1}(\tau), \quad k = 1, ..., N-1$$

Step (5): set $n = 0$, $y^0(\tau) = 0$, $p^\tau = A$ is a vector which can be determined by using the boundary conditions.

Step (6): Determine the optimal control law $u_0^{n+1}(\tau)$ and u_l^{n+1}.

Step (7): Determine the value of $J(u_0^{n+1}(\tau), u_l^{n+1}(\tau))$, if $|J(u_0^{n+1}(\tau), u_l^{n+1}(\tau)) - J(u_0^n(\tau), u_l^n(\tau))| \leq \epsilon$, where ϵ is the desired threshold, Stop, if not, set n=n+1 and goto step (4).

To given a clear overview of the analysis introduced above, an illustrative numerical example of optimal control problem have been treated and to show the efficiency of the presented approach, a comparison of the obtained result is made with the shooting method.

IV. NUMERICAL EXAMPLE

We take $l = \pi$, $T = \frac{3}{2}$, $q_0 = q_l = 1$, $y_0 = 0$ and $y_T = \frac{3}{2}$. Then the optimal control problem (9)-(14), can be written as:

$$\min_{u_0, u_l} J = \int_0^{\frac{3}{2}\Lambda^2} \int_0^{\Lambda\pi} y^2(x, t, \Lambda)\, dx\, dt$$
$$+ \int_0^{\frac{3}{2}\Lambda^2} \left[u_0^2(t, \Lambda) + u_l^2(t, \Lambda) \right] dt, \quad (15)$$

subject to the 1D-Heat with scale-invariant and with two-points boundary conditions u_0 and u_l:

$$\frac{\partial y}{\partial t}(x, t, \Lambda) = \frac{\partial^2 y}{\partial x^2}(x, t, \Lambda) \qquad \text{in } Q, \quad (16)$$

$$y(x, 0, \Lambda) = y_0(x, \Lambda) = 0 \qquad \text{in } \Omega \times \mathbb{R}_+^\star, \quad (17)$$

$$y(x, \tfrac{3}{2}, \Lambda) = y_{T=\frac{3}{2}}(x, \Lambda) = \frac{3}{2} \quad \text{in } \Omega \times \mathbb{R}_+^\star, \quad (18)$$

$$y(0, t, \Lambda) = u_0 \qquad \text{on } K, \quad (19)$$

$$y(\pi, t, \Lambda) = u_{l=\pi} \qquad \text{on } K. \quad (20)$$

In practice, we choose the number of discretizations (N =5 for instance). Then we obtain the following optimal control governed by ordinary differential equations :

$$\min_{u_0, u_l} J(u_0, u_l) = \left(\frac{\Lambda\pi}{10} + 1 \right) \int_0^{\frac{3}{2}\Lambda^2} u_0^2(\tau)\, d\tau$$
$$+ \frac{\Lambda\pi}{5} \sum_{k=1}^{N-1} \int_0^{\frac{3}{2}\Lambda^2} y_k^2(\tau)\, d\tau \quad (21)$$
$$+ \left(\frac{\Lambda\pi}{10} + 1 \right) \int_0^{\frac{3}{2}\Lambda^2} u_l^2(\tau)\, d\tau,$$

subject to

$$\begin{cases} \dot{y}_1(\tau) = (\frac{5}{\Lambda\pi})^2 \left(y_2(\tau) - 2y_1(\tau) + y_0(\tau) \right), \\[2mm] \dot{y}_k(\tau) = (\frac{5}{\Lambda\pi})^2 \left(y_{k+1}(\tau) - 2y_k(\tau) + y_{k-1}(\tau) \right), k = 2..., N-2, \\[2mm] \dot{y}_{N-1}(\tau) = (\frac{5}{\Lambda\pi})^2 \left(y_N(\tau) - 2y_{N-1}(\tau) + y_{N-2}(\tau) \right), \end{cases}$$
(22)

with boundary conditions

$$y_k(0) = 0, \quad y_k(\tfrac{3\Lambda^2}{2}) = \frac{3}{2}, \quad k = 1, ..., N-1. \quad (23)$$

Using the proposed algorithm, the obtained results can be summarized as followings The optimal control is determined

TABLE I
DIFFERENCE BETWEEN TWO SUCCESSIVE ITERATIONS FOR DIFFERENT VALUES OF Λ.

n	$(J^n - J^{n-1})$ for $\Lambda = 1$	$(J^n - J^{n-1})$ for $\Lambda = 2$	$(J^n - J^{n-1})$ for $\Lambda = 10$
0	—	—	—
1	0.549981301	0.89289566	1,67698260
2	0.530959761	0.52335187	1,04756755
3	0.095084831	0.08661081	0,10156208
4	0.092011429	0.09145199	0,10723897
5	0.070163399	0.06856165	0,08039717
6	0.061676275	0.02453983	0,02877604
7	0.011121091	0.01062745	0,01246203
8	0.001455037	0.00342660	0,00409854
9	0.000277207	0.00014821	0,00083735
10	0.000019630	0.00009170	0,00009973
11	0.000001361	0.00000877	0,00000952
12	0.000000107	0.00000053	0,00000073

by assuming a threshold $\epsilon = 10^{-6}$. The obtained results show that the VIM method converges after 12 iterations. The

following figures show the evolution optimal control law and optimal trajectories with a different values of scale parameter Λ, and a comparison with the shooting method is done, show that the obtained results are very close to each other.
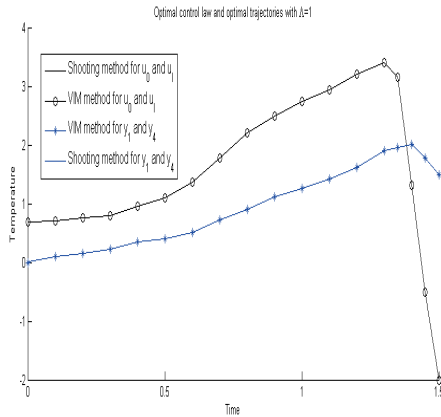

Fig. 1. Optimal control law and optimal trajectories with $\Lambda = 1$
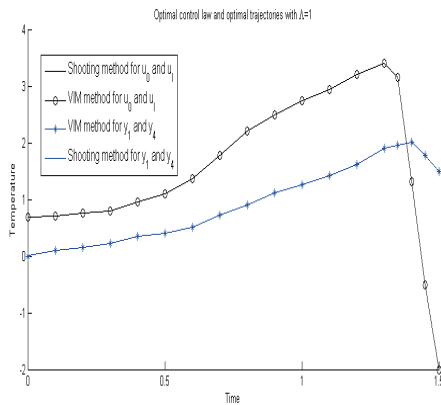

Fig. 2. Optimal control law and optimal trajectories with $\Lambda = 2$

V. CONCLUSION

In the present work we developed an efficient and accurate method for solving optimal control problem governed by 1D-Heat equation with two-points boundary conditions, in the presence of a scale-invariant parameter. By utilizing the finite difference approximation we reduced the original problem to a control problem governed by ordinary differential equation with a scale-invariant parameter (ODES). To obtain an approximate analytical solution for the resulting problem, the Variational Iteration Method (VIM) is adapted to solve the necessary optimality conditions derived by applying the minimum principe of Pontryagin. Illustrative example presented to demonstrate the validity and applicability for our approach.

REFERENCES

[1] T. M. ALAM, S. NICAISE, L. PAQUET, *An Optimal Control Problem Governed by the Heat Equation with Nonconvex Constraints Applied to the Selective Laser Melting Process*, Minimax Theory and its Applications, **06**(2021), 191–204

[2] W. F. RAMIREZ, *Process control and Identification*, Academic Press, Boston, 1994.

[3] V. BARBU, N. H. PAVEL, *Optimal control problems with two-point boundary conditions*, J Optim Theory Appl., **77**(10)(1993), 51–78.

[4] E. I. MOISEEV, A. A. KHOLOMEEVA, *An optimal boundary control problem with a dynamic boundary condition*, Diff Equat., **49**(2013), 640–644.

[5] A. FAKHARIAN, M. T. H. BEHESHTIA, *Solving linear and nonlinear optimal control problem using modified Adomian decomposition method*, J. Comput. Robot., **1**(1)(2008), 1–8.

[6] T. GEVECI, *On the approximation of the solution of an optimal control problem governed by an elliptic Equation*, RAIRO Anal. Numer., **1**(1979), 313–328.

[7] I. KUCUK, *Active optimal control of the KdV equation using the variational iteration method*, Math. Probl. Eng., **2010**(3)(2010), 1155-1156.

[8] K. BENALIA, CL. DAVID, B. OUKACHA, *An optimal time control problem for the one-dimensional, linear heat equation, in the presence of a scaling parameter*, RAIRO-Operations Research, **51**(4)(2017), 1289–1299.

[9] B. KAFASH, A. DELAVARKHALAFI, S. M. KARBASSI, *Application of variational iteration method for Hamilton–Jacobi–Bellman equations*, Appl. Math. Model., **37**(6)(2013), 3917–3928.

[10] L. S. PONTRYAGIN, V. G. BOLTYANSKII, R. V. GAMKRELIDZE, E. F. MISHCHENKO, *The Mathematical Theory of Optimal Processes*, Pergamon Press, New York, 1964.

[11] N.H. IBRAGIMOV, *Handbook of Lie Groupe Analysis of Differential Equations*, CRC Press, Boka Raton, 1996.

[12] J. L. LIONS, E. MAGENES, *Problèmes aux limites non homogènes et applications, Vol. II*, Dunod, 1968.

[13] J. L. LIONS, *Controlabilite exacte, perturbations et stabilisation des systemes distribues*. Masson, Collection RMA, Paris, 1988.

[14] F. BEN BELGACEM, C. BERNARDI, H. EL FEKIH, *Dirichlet boundary control for a parabolic equation with a final observation I: A space-time mixed formulation and penalization*, Asymptotic Analysis, **71**71 (2011), 101–121

[15] A. LOPEZ, E. ZUAZUA, *Uniform null controllability for the one dimensional heat equation with rapidly oscillating periodic density*, Annales IHP. Analyse non lineaire, **19**(2002), 543-580.

[16] * J. T. BETTS, S. L. CAMPBELL, *Discreteze then optimize, in Mathematics for Industry: Challenges and frontiers*, Philadelphia, eds SIAM, 2005.

[17] D. E. KIRK, *OptimalControl Theory. An Introduction, New Jersey*, Englewood Cliffs, Prentics-Hall, 1970.

[18] M. INOKUTI, H. SEKINE, T. MURA, *General use of the lagrange multiplier in nonlinear mathematical physics, in: S.Namat-Nasser, Variational Method in the in the Mechanics of solids*, Pergamon Press, Oxford, 1978.

An Accurate Fault Detection System for Wireless Body Area Networks

1st Mohamed Bahache
Computer science department
University of M'sila
M'sila, Algeria
medbahache@gmail.com

Abstract—**Remote health care has become a necessity and an urgent need, because it ensures the patient's control in a remote manner, especially concerning elderly peoples who usually suffer from chronic diseases such as diabetes, CVDs, and Parkinson's, so it has an increasing interest either by industrial companies or academia research, this remote health can be achieved by implanting few internet of medical things or also body sensors on, in or around the patient's body this is what is called WBANs(Wireless Body Area Networks), these body sensors characterized by their tiny sizes and limited resources (communication, processing or energy), faults is a challenge that must be handled when using or deploying this kind of networks, in this paper we have proposed an approach uses machine learning and exploits the correlation between the vital signs to detect faults in WBANs, the experiment results show that this technique deal better than several other techniques in this literature.**

Index Terms—**WBAN, fault, Machine learning, classification**

I. Introduction

Elderly peoples are in increasing around the world and this aged population is usually suffering from chronic diseases such as diabetes, Parkinson and CVDs, this last caused 18 millions deaths in 2019 according to [1], representing 32% of the global deaths and 85% among these 18 millions caused by either heart attack or stroke.

This is why remote health has become an urgent need, because it allows us to shift from classical or co-existent heath to remote health or, e-health, through the fusion between two technologies, wireless communication and sensing, this fusion of technologies yields two kinds of sensing, contactless sensing, and wearable sensing, in contactless sensing the patient does not need to wear any sensor device, where the sensing system just sends a radio frequency wave and then analyzes its reflection, to extract useful information using certain techniques, in the wearable sensing or WBANS (Wireless Body Area Networks), which is a set of body sensors implanted in, on, or around the human body to supervise its vital signs, such as T°, HR, PULSE, SpO2, the sensed data sent to PDA(Personal Device Assistant), then to an access point to reach the remote health caregiver through public network see figure(1). many of platforms have been launched such as CodeBlue [2] monitors HR, ECG and SpO2, Lifeguard [3] monitors ECG, breath, beat oximeter, and BP.

Several challenges face WBANs, among them the faults issue,in other words our system must be able to differentiate between the faulty measurement and the health state degradation of the patient, in the case of the abnormal sensed data.

Al though WBAN is a subset of the WSN which is uses the comparison as criteria to detect faults, by putting redundant sensor nodes, unfortunately we cannot put redundant body nodes, because a few body sensors should be deployed on the human body.

Thus, and to address the fault detection issue in WBANs, our approach benefits from the correlation that exists between the vital signs for decision this correlation is gathered with a decision tree, which is a machine learning tool, used for classification, where our aim is to establish an accurate fault detection mechanism.

The rest of the paper is organized as follow: In section II we present a related works concerning the fault detection in WBANs, both machine learning and statistics Section III describes briefly the decision tree classifier, our proposed approach presented in section IV, In section V, we present our experimentation . Finally, we conclude the paper in section VI.
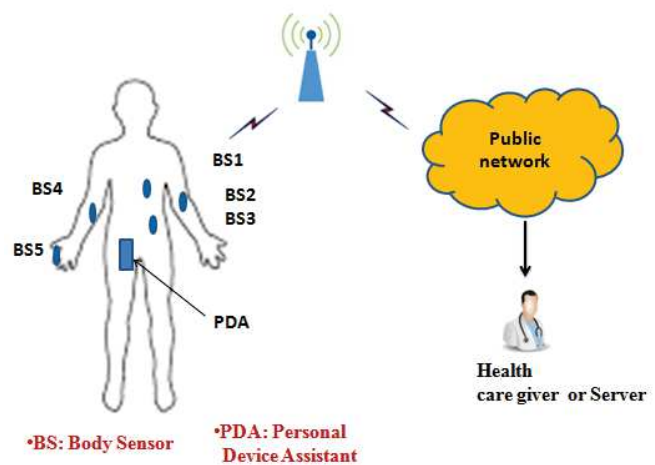

Fig. 1. Wireless Body Area Network.

II. RELATED WORKS

Both statistics and machine techniques are used for the fault detection in WBANs. In [4] The authors gathered between two techniques to detect faults in WBANs, first they used medium distance to determine the abnormal values and after that they used the majority voting algorithm to point the faulty values. A Markov chain model is proposed in [5] to detect faults in WBANs where a confusion matrix is used where the row represent the actual values and the column represent the predicted value. The machine learning techniques are also used in this scope. In [6] the authors have used the decision tree tool to classify the sensed value concerning the physiological parameters as normal or abnormal, after that and in the case of the abnormal values they used the linear regression.

In [7] the authors used the support vector machine (SVM), which is a supervised machine learning method used to classify the data that may be either normal or abnormal , then and in the case of the abnormal data the linear regression is used for prediction .

The relay technique is used in [8] where authors combined between the network coding to control links and when the link is not available, then the communication switches to the hierarchical modulation, in such scheme the channel is not completely deteriorated.

Authors in [9] have considered a multiple WBANs, and for detecting faults they used the Naive Bayesian Network for the classification .

Here it should be noted that both methods have limits and drawbacks, the statistical techniques base only on approximate calculus such as, average, standard deviation, probability estimation, medium distance, to make decision, also need homogeneous and uniform data. The learning process needs useful data (data acquisition), also needs time and space to store data this makes it expensive.

III. PRELIMINARIES

A. Decision Tree

A decision tree is a non-parametric supervised learning algorithm, which is utilized for both classification and regression tasks. It has a hierarchical, tree structure, which consists of a root node, branches, decision nodes and leaf nodes which represents the classes. As shown by the figure (2). In our case the nodes represent the vital signs.
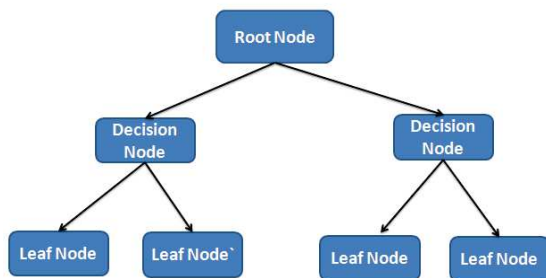

Fig. 2. Decision Tree.

in Our approach we have used C4.5 [10] which is a decision tree algorithm, where at each node chooses the best attribute for splitting or making a decision, using the entropy equation(1) and the information gain equation(2).

$$Entropy\left(X\right) = -\sum_{i=1}^{c} \beta_i \log_2 \beta_i \qquad (1)$$

where X is a matrix contains the vital signs measurements,c is the number of classes, and β_i is the probability of each class.

$$G\left(X, P_k\right) = E\left(X\right) - \sum \frac{|P_{ki}|}{|X|} E\left(P_{ki}\right) \qquad (2)$$

where $E\left(X\right)$ is the entropy, and P_{ki} is the value of the parameter P_k at the time i

IV. OUR FAULT DETECTION SYSTEM

In real world of medicine it exists a correlation between the human body's vital signs. Our system exploits this existing correlation as a criteria de decide if the received abnormal is really abnormal and in this case the patient is entering in the urgent state, and the intervention of the healthcare giver is needed. Or the received abnormal value is faulty; our fault detection technique operation consists of two steps see figure(3):
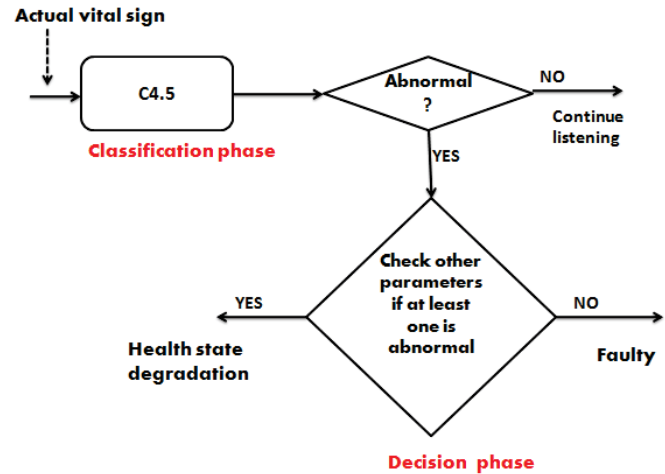
Fig. 3. Our Fault Detection System.

A. Classification Phase

When the PDA receives the sensed value concerning the actual vital sign, Injects it in the classification model (decision tree), in our case we have use C4.5 decision tree classifier to classify the actual data.

B. Decision Phase

When the received data concerning the actual physiological parameter is classified as an abnormal, then here we exploit the existing correlation between the vital signs , in other words check the other data concerning the other vital signs , if at least

one vital sign is abnormal then the patient is in the urgent case (health caregiver intervention is needed), otherwise the abnormal value of the actual vital sign is faulty.

Algorithm 1: Our fault detection algorithm

---

1 $current.value, predicted.value : real$;
2 $curent.class : ('normal', 'abnormal')$;
3 $PDA.state : ('listening', 'receiving')$;
4 $PDA.state \leftarrow' listening'$;
5 **while** ($PDA.state$ = 'receiving') **do**
6 | C4.5($current.value$);

7 | **if** $current.class =' abnormal'$ **then**
8 | | check other parameters;
            if at least one is abnormal **then**
9 | | | Trigger alarm to healthcare giver;
10 | | **else**
11 | | | The current value is faulty;
12 | | **end**
13 | **end**
14 **end**

---

the above algorithm describes the theory operating of our fault detection system see algorithm(1)

V. EXPERIMENTAL EVALUATION

To evaluate the performance of our mechanism to detect fault in WBANs, we have used the physionet bank data set [11] , which is a real clinic database, we have used the record number 221n that contains 7 vital signs and 3516 instances, ABPmean, ABPdias,ABPsys,HR,PULSE,RESP,SpO2, and we have used WEKA tool, we have used J48 decision tree which is a java implementation of C4.5 in WEKA.to compare our approach with KNN, and the majority voting.The table(I); summarizes the parameters of the experimentation.

TABLE I
EXPERIMENT PARAMETERS

Parameter	Value
Clinic BANK	PhysioBank ATM
DATA BASE	MIMIC
Record	221n
Signal1	ABPmean
Signal2	ABPsys
Signal3	ABPdias
Signal4	HR
Signal5	PULSE
Signal6	RESP
Signal7	SpO2
Topology	Star

for this comparison we have used the accuracy that computes the true classified classes , and the kappa statistics that allows us to compare the classification with the standard classifier, and the mean absolute error that computes the difference between the actual and the predicted values.

The figure(4) shows the accuracy criteria of the three approaches, we observe that our approach is more accurate where it achieve 99.6018%, followed by the KNN classifier

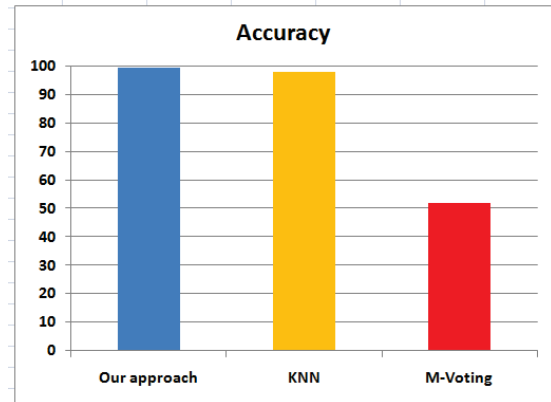with the rate of 97.9807%, and finally the majority voting that achieves 51.8203%

Fig. 4. The accuracy of the three approaches.

The figure(5) represents the mean absolute error where our approach has the smallest error which represents 0.6%, and the KNN with 1.92% then majority voting by 49.93%.
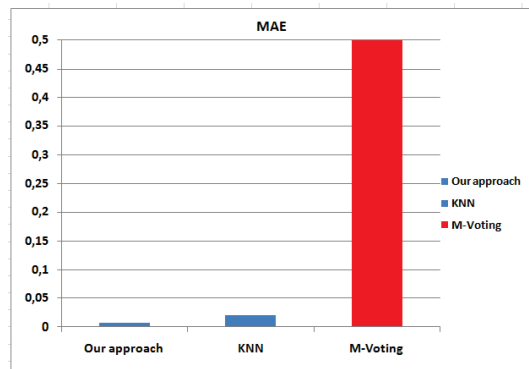

Fig. 5. The mean absolute error of the three approaches.

Concern the kappa coefficient, the figure(6) shows that our approach has the biggest rate 99.2%, followed by the KNN classifier by 95.96%.
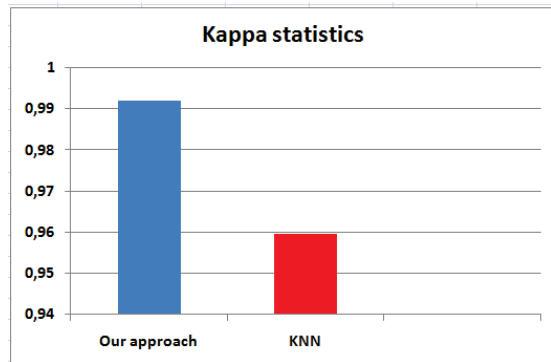

Fig. 6. The kappa coefficient of the three approaches.

VI. CONCLUSION

Remote health has become a necessity, because it ensures the control of the patient wirelessly, through implanting body sensors on the body of the patient, then the sensed data is sent to a personal device assistant, then to an access point to reach the healthcare giver through a public network, here a challenge appears and must be treated is the fault issue, means in the case of abnormal data our system should be able to distinguish between the patient health state degradation and the faulty value, in this paper we have proposed a mechanism to detect a fault, by using the decision tree classifier which is a machine learning tool, and we exploit the correlation that exists between the vital signs. In the our coming works, we intend to use block chain to address the fault detection issue in WBANs

REFERENCES

[1] World Health Organization . Available online: https://who.int/data (accessed on 17 Sept 2023)

[2] Shnayder, Victor, et al. "CodeBlue: An Architecture for Medical Sensor Networks." *Harv. Electr. Eng. Comput. Sci* (2005).

[3] Montgomery, K., et al. "Lifeguard-a personal physiological monitor for extreme environments." *The 26th Annual International Conference of the IEEE Engineering in Medicine and Biology Society*. Vol. 1. IEEE, 2004.

[4] Aderibigbe, Temilola, and Hongmei Chi. "A quick outlier detection in wireless body area networks." *Proceedings of the Practice and Experience in Advanced Research Computing 2017 on Sustainability, Success and Impact*. 2017. 1-3.

[5] Salem, Osman, et al. "Markov models for anomaly detection in wireless body area networks for secure health monitoring." *IEEE Journal on Selected Areas in Communications* 39.2 (2020): 526-540.

[6] Nezhad, Mozhgan Mohammadi, and Mohammad Eshghi. "Sensor single and multiple anomaly detection in wireless sensor networks for healthcare." *2019 27th Iranian Conference on Electrical Engineering (ICEE)*. IEEE, 2019.

[7] Salem, Osman, et al. "Anomaly detection in medical wireless sensor networks using SVM and linear regression models." *International Journal of E-Health and Medical Communications (IJEHMC)* 5.1 (2014): 20-45.

[8] Waheed, Maham, et al. "Network Coding and Hierarchical Modulation for Energy Efficient Cooperative WBAN." *International Journal of Distributed Systems and Technologies (IJDST)* 10.3 (2019): 90-111.

[9] Jin, Zilong, et al. "A prediction algorithm for coexistence problem in multiple-WBAN environment." *International Journal of Distributed Sensor Networks* 11.3 (2015): 386842.

[10] Amin, Rafik Khairul, and Yuliant Sibaroni. "Implementation of decision tree using C4. 5 algorithm in decision making of loan application by debtor (Case study: Bank pasar of Yogyakarta Special Region)." *2015 3rd International Conference on Information and Communication Technology (ICoICT)*. IEEE, 2015.

[11] PhysioNet. PhysioBank ATM. Available online: https://archive.physionet.org/cgi-bin/atm/ATM (accessed on 17 Sept 2023).

Application of Soft Computing for Optimal Control of AC/DC Interconnected Multi-Microgrid Coordinated with Fuel Cell Storage System

Nour ELYakine KOUBA

Faculty of Electrical Engineering, University of Sciences and Technology Houari Boumediene, Algiers, Algeria

E-mail: koubanour@gmail.com

Slimane SADOUDI

Faculty of Electrical Engineering, University of Sciences and Technology Houari Boumediene, Algiers, Algeria

E-mail: Sadoudi.slimane.sadoudi@gmail.com

Abstract— **This paper deals with an application of new soft computing based nature inspired metaheuristic algorithm to design an optimal frequency control scheme of interconnected AC/DC multi-area microgrid including Diesel Generator (DG, wind and solar photovoltaic power (PV) generation units coordinated with Fuel Cell (FC) storage system. The interconnection between the microgrid areas was established through a High Voltage Alternating Current (HVAC) and High Voltage Direct Current (HVDC) Transmission Links. The FC storage system was used to enhance microgrid frequency performances and avoid load shedding during disturbances. A recently artificial intelligence method inspired by the shallow water wave theory, named Water Wave Optimization (WWO) was employed to design a new optimal PID controller for interconnected multi- microgrid load frequency control system (LFC). The optimal LFC loop based WWO was applied to control both of Diesel Generator and Fuel Cell storage system. A comparative study has been performed to show the robustness of the proposed WWO method compared to other optimization algorithms available in the literature such Genetic Algorithm (GA) and Particle Swarm Optimization (PSO). The simulation results reveal the capability and robustness of the proposed strategy as an effective optimization tool for solving frequency regulation issue achieve system frequency stability in presence of renewable energies.**

Keywords—Renewable Energy, Multi-Microgrid, Wind Farm, Photovoltaic Generator (PV), Fuel Cell (FC), Frequency Control, HVAC/HVDC, PID Controller, Water Wave Optimization (WWO).

I. INTRODUCTION

During many years , different control systems have been proposed and applied to minimize the impact of load variation and green power integration such wind and solar power, which can cause destructive and permanent damage to the structures. Presently, isolated power systems such microgrid seek to integrate high levels of renewable energy, and they face new control and management challenges. The control and management of energy in such small area presents a scope of high importance. Indeed, renewable energy sources (RESs) are used to supply power to remote areas. However, randomness is the main disadvantage in these resources [1-4].

The traditional mathematical methods are sufficient to overcome some engineering issues. However, the classical approaches can cause both a loss of time and an increase in the error rate when it comes to solving some complex issues. Among the new algorithms used as artificial intelligence (AI) solution are nature inspired and metaheuristic optimization algorithms. The inspiration of those algorithms is based on the instinctive behaviors which exist in nature [5-7]. During many years, a lot of nature inspired meta-heuristic strategies have been proposed to solve different problems. Most of these methods were inspired from the analysis behavior of many nature and creatures phenomena's. All of these strategies were created based on the lifestyle and hunting behaviors of insects and animals in nature [8].

In the aim to design an intelligent microgrid control scheme a lot of meta-heuristic algorithms have been employed. In reference [9] authors have presented an application of coordinated optimal LFC controller with battery storage system using artificial intelligence tools. In reference [10] authors have proposed an intelligent control of battery energy storage for microgrid energy management using ANN method. Moreover, a lot of research works have been published on the topic of controlling a multiple microgrids as listed in reference [11], where the authors have presented a review of architectures and operation and control strategies. Additionally, some research works have addressed the use of hybrid energy storage system (HESS) to support frequency regulation in case of renewable energy integration [12-14].

The main contribution in this paper was to analyze the AC/DC interconnected multi-microgrid frequency behavior n presence of hybrid DG/wind/PV/FC power system. An application of new artificial intelligence (AI) based nature-inspired algorithm for microgrid optimization including HVAC and HVDC transmission links was also presented. The rest of the paper is organized as follows. Section 2 presents the interconnected multi-microgrid dynamic model. Section 3 was devoted to presents the suggested load frequency control loop and the Water Wave Optimization (WWO). The obtained simulation results are presented in Section 4. Finally, Section 5 concludes the paper.

II. ISLANDED MICROGRID MODEL

The configuration of the investigated AC/DC multi-area interconnected microgrid based on hybrid DG/wind/PV/FC is shown in Fig.1. The FC storage system was connected to support microgrid frequency power supply and frequency control during load changes. To show the potential of the proposed approach, the optimal LFC control strategy has been tested firstly with the two equal areas interconnected microgrid during load disturbances as shown in Fig.2, and then the proposed approach was extended to a three-area AC/DC multi-microgrid system connected via an HVAC tie-line as well as HVDC link, as shown in Fig.3.
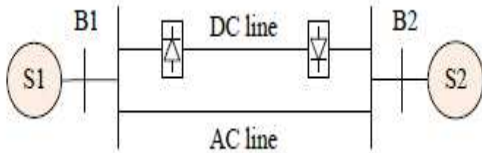

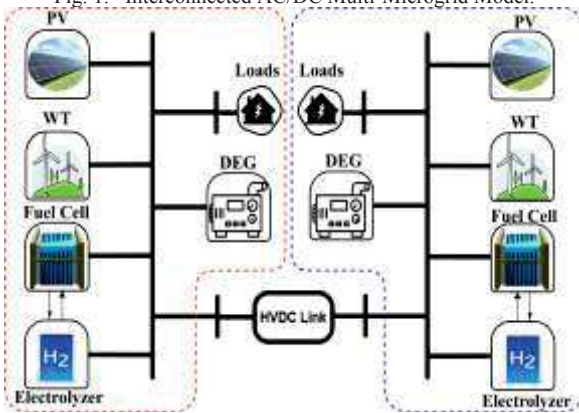Fig. 1.   Interconnected AC/DC Multi-Microgrid Model.

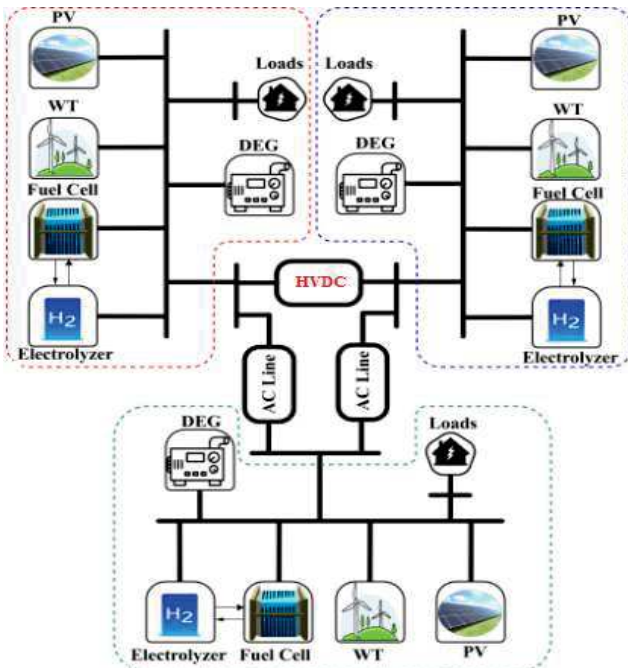Fig. 2.   Two-area Interconnected Multi-Microgrid Model.

Fig. 3.   Three-area Interconnected AC/DC Multi-Microgrid Model.

III. OPTIMAL AC/DC MULTI-MICROGRID CONTROL

A.   Application of Soft Coputing for Frequency Control

Over the last decades, Artificial Intelligence (AI) has been a very important scope in almost engineering fields, which leads to create a variety of smart and robust control actions that have shown great promise in a large number of applications esspecialy in power system operation and control. In the last few years, many frequency control strategies have been published in the literature to enhance dynamic frequency stability and control. In this section, an optimal load frequency control scheme based PID controller is presented. The PID controller parameters are tuned using the new optimization tool named Water Wave Optimization (WWO). The LFC loop was applied to control both of Diesel Generator (DG) and Fuel Cell (FC) system in each area as presented in Fig.4. The system equations of the LFC loop is presented by Eq.1-Eq.4.
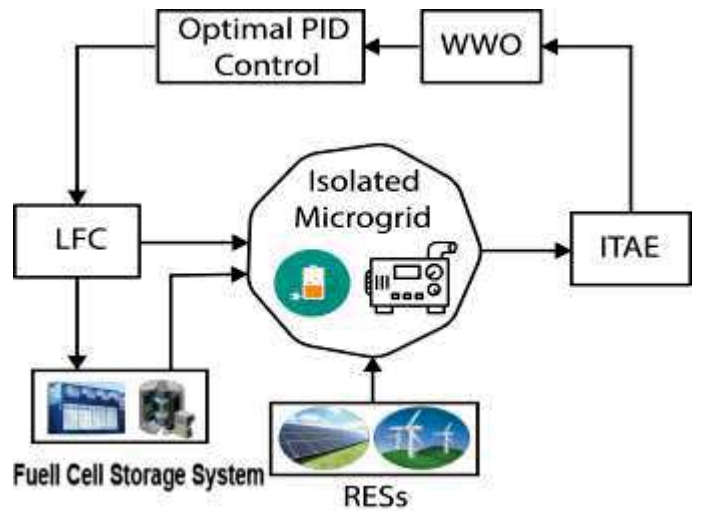

Fig. 4.   Proposed Frequency Control Strategy.

$$TF_{PID} = Kp + K_i \frac{1}{s} + K_d s \qquad (1)$$

$$ACE = \beta_f . \Delta f_{MG} + \alpha.(\Delta P_{tieHVDC} + \Delta P_{tieHVAC}) \qquad (2)$$

$$uf = \sum_{i=1}^{i=n} ACE_i \qquad (3)$$

$$U = (Kp.uf) + (Ki\int_0^t uf(t)dt) + (\frac{duf(t)}{dt}) \qquad (4)$$

B.   Water Wave Optimization (WWO)

Nature-inspired, Bio-inspired and metaheuristics optimization algorithms are a set of approaches that are illumed by the behavior of natural situations. Those approaches have been inspired by animal and insects behaviors, biology, chemical reactions, etc. Metaheuristics a algorithms are widely used to solve many optimization problems. They are often used when the problem is too complex for classical methods, or when the traditional methods are too slow [12-16].

In this section, a recently optimization algorithm named Water Wave Optimization (WWO) was introduced to be used in the AC/DC interconnected multi-microgrid frequency control. WWO algorithm was proposed by Yu-Jun Zheng in 2015 to solve optimization problems [15-17]. The WWO is a new optimization algorithm which was inspired fro the shallow water wave theory as presented in Fig.5. In general, the algorithmic framework of WWO is simple, and easy to implement to solve optimization issues with a small-size population and only a few control parameters. The pseudo code of WWO algorithm is shown in Fig.6 [17]. More detailed descriptions of all WWO algorithm steps are available in [17].
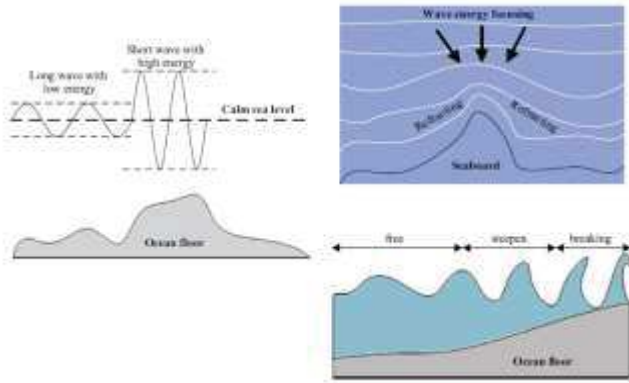

Fig. 5. Water Wave Optimization Algorithm (WWO) [15-17].

```
1   Randomly initialize a population P of n waves (solutions);
2   while stop criterion is not satisfied do
3       for each x ∈ P do
4           Propagate x to a new x′
5           if f(x′) > f(x) then
6               if f(x′) > f(x*) then
7                   Break x′
8                   Update x* with x′;
9               Replace x with x′;
10          else
11              Decrease x.h by one;
12              if x.h = 0 then
13                  Refract x to a new x′
14      Update the wavelengths
15  return x*.
```

Fig. 6. Psodocode of WWO Algorithm [15-17].

C. Objective Function

In the aim to handle with microgrid regulation problem in presence of hybrid renewable energy sources, the Integral Time multiply Absolute Error (ITAE) given in Eq. 5 was used as objective function.

$$ObjFun = \int_{0}^{tsim} t.\left(\left|\Delta f\right|+\left|\Delta P_{tie}\right|\right).dt \qquad (5)$$

IV. SIMULATION RESULTS

In this part, the simulation results of the investigated AC/DC interconnected multi-area microgrid are presented. The tie-line power flow quantities shown in the plots are in per-unit value. To analyze the dynamic behavior of the multi-microgrid, two scenarios have been simulated and discussed. In the first scenario, a two-area interconnected microgrid was simulated. In the second scenario, the simulation was extended to a three-area AC/DC interconnected microgrid. A comparative study between Genetic algorithm (GA), particle swarm optimization (PSO) and the employed optimal PID controller based WWO was performed.

A. Scenario 1:Two-Area Interconnected Microgrid

Fig.7 and Fig.8 presents the system frequency fluctuations caused by the installed wind farm and PV generator in each area of the interconnected microgrid shown in Fig.2. The tie-line power flow fluctuations is presented in Fig.9.
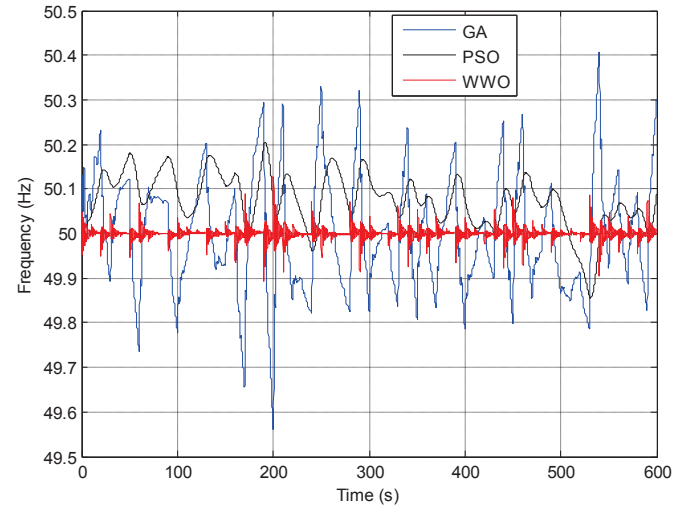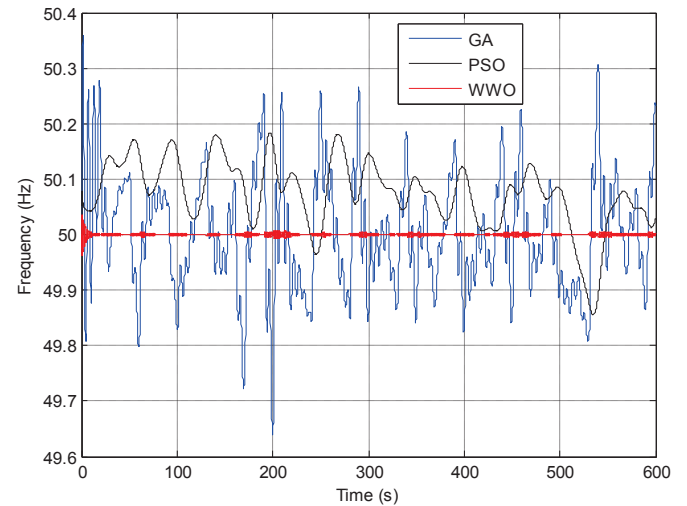

Fig. 7. Frequency Fluctuations in Area-1.

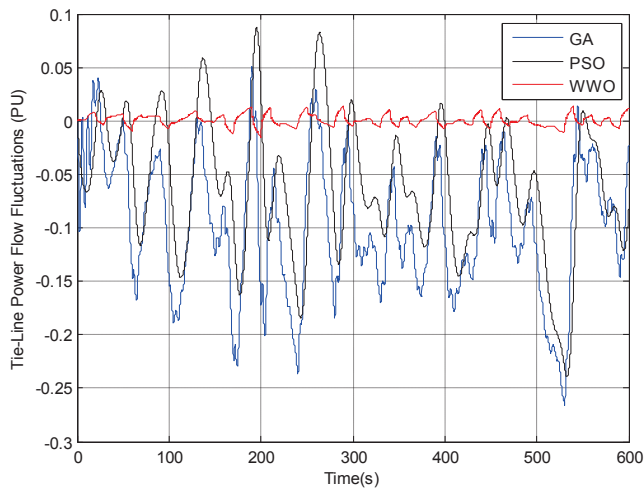Fig. 8. Frequency Fluctuations in Area-2.

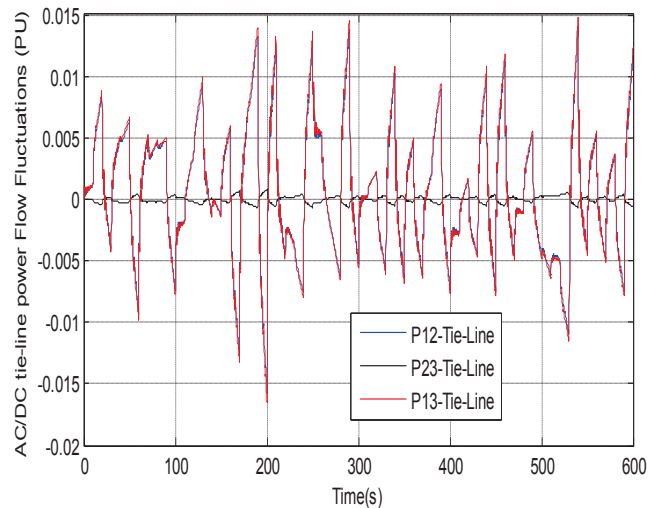Fig. 9.   HVDC Tie-line Power Flow Fluctuations.

Fig. 11. AC/DC Tie-lines Power Flow Fluctuations.

B. Scenario 2: Extension to Tree-Area AC/DC Microgrid

To demonstrate the ability of the proposed optimal LFC controller based WWO to face with frequency fluctuation and tie-line oscillations due to load changes in multi-microgrid system, the simulation was extended to a three-area AC/DC interconnected microgrid connected via an AC tie-line as well as HVDC transmission link as shown in Fig.3. The system was simulated with different optimal PID controllers for each controlled area. A comparative study between optimal PID controllers based GA,PSO and WWO were presented in Figs.10 and 11, each figures presents a comparative study between the frequency of each microgrid area and between each HVAC/HVDC tie-line. The employed WWO algorithm gives an optimal solution in view of frequency peak under/overshoot and settling time.
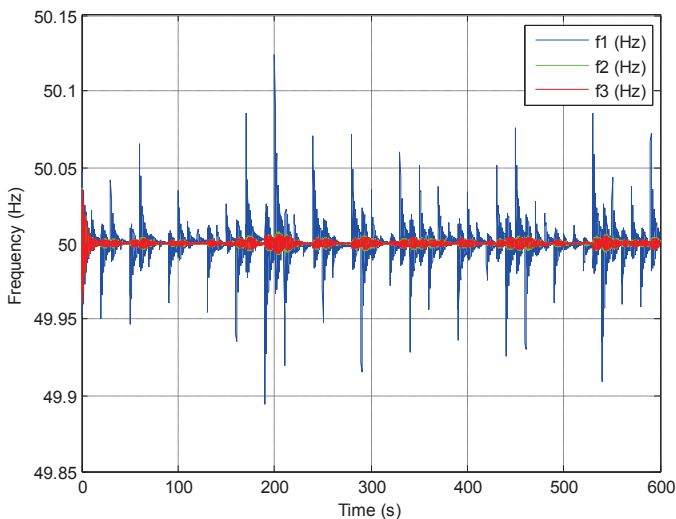
The Interconnected AC/DC multi-microgrid was analyzed in presence of hybrid renewable energy power generation units involving wind farm and PV solar generator. An optimal load frequency control loop was designed in coordination with Fuel Cell storage system to enhance frequency stability. It can be observed from the presented results that the optimal PID controller and the FC storage system can help the LFC loop to minimize frequency fluctuations the most effectively.

V. CONCLUSION

This paper has presented an application of nature-inspired optimization algorithm to solve frequency control issue in multi-microgrid including hybrid RESs coordinated with Fuel Cell storage system. The interconnected microgrid was analyzed in presence of HVAC and HVDC transmission links. A new optimal soft computing algorithm named Water Wave Optimization (WWO) was proposed to design an optimal PID controller to coup with system frequency fluctuations and enhance dynamic microgrid performances. several case studies have been presented to demonstrate the superiority of the applied strategy compared to other existing optimization methods available in the literature. The application of AI techniques achieve significant improvement in the performance of the microgrid. In addition, the use of FC storage system supporte the LFC loop and improves the microgrid stability. Finally, the investigation reveals that the coordinated performance of optimal LFC loop and FC storage system can significantly diminish system frequency deviations and quickly drive the dynamic microgrid responses to steady state under load disturbance. In the near future, this study will be extended to design an optimal power management and control tool for interconnected multi-area nanogrid and microgrid in presence of hybrid storage system and electric vehicles stations.

Fig. 10. Tree-Area Multi-Microgrid Frequency Fluctuations.

REFERENCES

[1] Nour EL Yakine KOUBA, Slimane SADOUDI,. Optimal Energy Management of Hybrid Micro-Grid Using Storage System and Fuzzy-GA Method. *Journal of Renewable Energies*, 2022, p.129-141-129–141.

[2] KOUBA, Nour EL et SADOUDI, Slimane. Using Artificial Intelligence for Microgrid Operation and Control in Presence of Sustainable Power Systems , the Second International *Conference* on Artificial Intelligence and its Applications *AIAP* 2021 held at *El-Oued* Algeria, 2021, pp.1-10.

[3] Jithin, S., and T. Rajeev. "Investigation on microgrid control and stability." *Smart Grids and Microgrids: Technology Evolution* (2022): 99-125.

[4] ZHANG, Guoqiang, KHAN, Irfan Ahmed, DARAZ, Amil, *et al.* Load Frequency Control of Marine Microgrid System Integrated with Renewable Energy Sources. *Journal of Marine Science and Engineering*, 2023, vol. 11, no 4, p. 844.

[5] TRIVEDI, Rohit et KHADEM, Shafi. Implementation of artificial intelligence techniques in microgrid control environment: Current progress and future scopes. *Energy and AI*, 2022, vol. 8, p. 100147.

[6] Nour EL Yakine KOUBA, Slimane SADOUDI, Optimal Multi-Microgrid Active Power Management and Frequency Control Coordinated With Hybrid Energy Storage System And HVDC Link, International Conference on Solar Energy and Hybrid Systems (icsehs'22), Algeria, pp.1-6.

[7] Ulusoy S, Bekdaş G, Nigdeli SM, Kim S, Geem ZW. Performance of Optimum Tuned PID Controller with Different Feedback Strategies on Active-Controlled Structures. *Applied Sciences*. 2021; 11(4):1682. https://doi.org/10.3390/app11041682

[8] SINGH, Balvender, BISHNOI, S. K., SHARMA, Mandeep, *et al.* An application of nature inspried algorithm based dual-stage frequency control strategy for multi micro-grid system. *Ain Shams Engineering Journal*, 2023, vol. 14, no 9, p. 102125.

[9] Kouba, N.EL.Y., Menaa, M., Hasni, M., Boudour, M., "Evaluation of Battery Storage System in Isolated Micro-Grid Including Intelligent Frequency Restoration Loop", *Proceedings of* the 7th International Renewable Energy Congress (IREC), Tunisia, 2016, pp: 1-6.

[10] BOUJOUDAR, Younes, AZEROUAL, Mohamed, ELMOUSSAOUI, Hassan, *et al.* Intelligent control of battery energy storage for microgrid energy management using ANN. *International Journal of Electrical & Computer Engineering (2088-8708)*, 2021, vol. 11, no 4.

[11] SAHA, Diptish, BAZMOHAMMADI, Najmeh, VASQUEZ, Juan C., *et al.* Multiple microgrids: A review of architectures and operation and control strategies. *Energies*, 2023, vol. 16, no 2, p. 600.

[12] BENLAHBIB, Boualam, BOUARROUDJ, Noureddine, MEKHILEF, Saad, *et al.* Experimental investigation of power management and control of a PV/wind/fuel cell/battery hybrid energy system microgrid. *International Journal of Hydrogen Energy*, 2020, vol. 45, no 53, p. 29110-29122.

[13] Uthpala N. Ekanayake, Uditha S. Navaratne, "A Survey on Microgrid Control Techniques in Islanded Mode", *Journal of Electrical and Computer Engineering*, vol. 2020, Article ID 6275460, 8 pages, 2020. https://doi.org/10.1155/2020/6275460

[14] LI, Sichen, CAO, Di, HU, Weihao, *et al.* Multi-Energy Management of Interconnected Multi-Microgrid System using Multi-Agent Deep Reinforcement Learning. *Journal of Modern Power Systems and Clean Energy*, 2023.

[15] ZHENG, Yu-Jun, LU, Xue-Qin, DU, Yi-Chen, *et al.* Water wave optimization for combinatorial optimization: Design strategies and applications. *Applied Soft Computing*, 2019, vol. 83, p. 105611.

[16] ZHENG, Yu-Jun et ZHANG, Bei. A simplified water wave optimization algorithm. In : *2015 IEEE Congress on Evolutionary Computation (CEC)*. IEEE, 2015. p. 807-813.

[17] ZHENG, Yu-Jun. Water wave optimization: a new nature-inspired metaheuristic. *Computers & Operations Research*, 2015, vol. 55, p.1-11.

Captured Arabic Text Document Extraction: A Learning-Free Approach

Hassina Bouressace ⏺ID
Department of Computer Science
8 Mai 1945 - Guelma University
BP 401 Guelma 24000 Algeria
bouressace.hassina@univ-guelma.dz

Abstract— **The widespread use of text recognition has given rise to various input types, including captured images, which pose significant challenges, particularly when dealing with text. In response, we present a novel approach to enhance text segmentation for challenging cases such as captured Arabic text documents. Our method, comprising image preprocessing and text line segmentation, excels in extracting text from complex scenarios. Leveraging techniques such as Multi-Scale Retinex Enhancement, Contrast Limited Adaptive Histogram Equalization (CLAHE), Color Ratio Correction, Hough Line Transform, morphological operations, and connected component analysis, we conducted experiments on a curated dataset to evaluate its effectiveness. Results demonstrate the high efficiency of our proposed method, especially in handling poor-quality images.**

Keywords_ Arabic Document, Arabic text, Learning-Free Approach, text line segmentation

I. INTRODUCTION

The textual information and its precision play a crucial role in many fields such as text mining which is be the key inputs for the textual analysis and also for the text classification, this related to the information-gathering process, which identifies the nature and kind of the text in order to prepare the textual data to be the appropriate input for the next phase, which includes activities such as tokenization, identification, normalization, and recognition. Among these activities, we specifically focus on the segmentation step since its outcomes have a direct impact on the analysis phase. Poor segmentation leads to inadequate analysis, while good recognition enables accurate analysis. The effectiveness of the segmentation step depends on the quality of the input, which can take the form of text, audio, video, or image [1, 2]. While advancements have been made in methods for these various types, challenges persist, especially when dealing with old, damaged, or poor-quality image and audio data. In today's context, the shift towards more optical inputs has been notable, primarily driven by the widespread use of smartphones equipped with high-quality cameras. This shift has brought about changes in importance and scale, prompting the search community to focus more on media inputs rather than simple text. The increased emphasis on media as input has influenced the direction of research and development in this field. Despite significant investments and the development of various techniques, image processing remains a challenging task, particularly when dealing with images in poor condition or with complex structures. These cases continue to present unsolved challenges in the field, requiring ongoing research and advancements in image recognition and processing techniques [3]. One of the challenges in image processing is dealing with images captured in poor condition. This can occur due to various factors, such as improper camera usage, capturing images in inappropriate lighting conditions, or capturing images with movement, leading to issues like gradient, motion blur, or skew problems [4]. Additionally, capturing images from computer screens introduces further complexities, including problems like grids, skew, and lighting variations. Images captured in poor condition pose significant difficulties in accurate analysis and recognition. The presence of these issues can hinder the performance of image processing algorithms, making it challenging to extract meaningful information from such images. Addressing these challenges requires the development of specialized techniques and algorithms that can handle and mitigate the effects of poor image conditions. In this work, our contributions encompass:

- Dealing with images captured in the Arabic language.
- Addressing challenges related to grids, skew, and lighting variations resulting from digital screen lighting.
- Aiming to enhance the Arabic line segmentation process.
- Focusing on detecting and resolving issues related to effectiveness and precision.
- Utilizing images from magazines and newspapers within the PATD database.
- Handling complex scenarios without the need for machine learning, thereby saving time and energy.

The paper is structured as follows: In Section 2, we offer a concise overview of related studies. Our method is presented in detail in Section 3. We provide the dataset and discuss our results in Section 4. In the concluding Section 5, we summarize our work.

II. RELATED WORKS

In terms of document images captured by smartphones, several authors have focused on poor-quality captured images containing Arabic text. In this section, we have compiled the

most relevant recent studies that address the extraction of Arabic text from captured images.

The most relevant research in this field has been conducted by El Bahi and Zatni [5], who employed deep learning techniques to recognize Arabic text within captured document images. They applied a convolutional neural network (CNN) to achieve this goal. At the text segmentation level, they utilized morphology operations and heuristic rules to extract text areas from the document image. This process was preceded by the application of the canny algorithm [6], polar coordinates, and bilinear interpretation for skew correction, along with a projection histogram for noise removal [7]. Another study closely related to our research was conducted by Lui et al. [8]. They segmented camera-captured images into lines by employing an erosion technique for noise removal, followed by the use of connected components with respect to top-down, bottom-up, and hybrid approaches, as described in [9]. Kim et al. [10] detected text blocks and lines using a discrete representation method, identifying and correcting existing distortions by employing a geometric distortions model. Another study [11] utilized a transformation matrix for skew detection and correction while addressing text blocks in the document image. Yet another study [12] combined two approaches for document analysis, where they employed adaptive mathematical morphology for text segmentation. However, it's worth noting that despite their results, none of these studies covered images captured directly from computers. This type of capture can introduce new distortions that do not typically occur when images are captured in real-world settings. This observation has inspired us to develop a new approach capable of handling these unique distortions.

III. PROPOSED APPROACH

In this section, we will introduce our proposed approach for extracting Arabic text lines from the captured-image document.
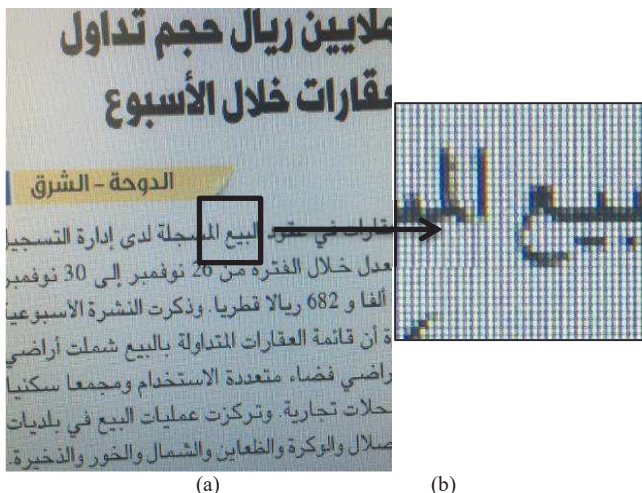

Fig.1. Effects of screen light on the capturing process. (a) The generated image with various distortions. (b) A zoomed-in section of the captured image.

This approach begins with distortion correction, addressing issues such as unstable lighting conditions, and noise removal, which includes the removal of grids and small points. The subsequent phase encompasses text detection and extraction. Fig. 1 illustrates an example of the effects of screen light on the capturing process, resulting in various distortions that we aim to address in the next steps.

A. Distortion correction

Due to the poor quality of the selected images, significant effort was devoted to eliminating distortions and enhancing image quality for text segmentation. Our initial focus was on correcting uneven lighting present in the images.

Fig. 2. Enhancement Stages for an Uneven, Poor-Quality Document Image: (a) Original Image, (b) Enhanced Image after Improving Even Lighting, (c) Enhanced Image after Further Enhancing Uneven Lighting, (d) Enhanced Image after Gridline Removal.

To address this, we employed a combination of techniques, including Multi-Scale Retinex Enhancement and Contrast Limited Adaptive Histogram Equalization (CLAHE) [13], as described below.

For the input image $I(x, y)$, the Multi-Scale Retinex Enhancement involves the following steps:

To emphasize intensity differences.

$$log_{image(x,y)} = log(1 + I(x,y)) \qquad (1)$$

For each scale s, we apply Gaussian blur to log_image and calculate the difference, then combine differences using weights for all scales i.

$$diff_{s(x,y)} = log\_image(x,y) - blur\_s(x,y). \qquad (2)$$
$$enhanced_{i(x,y)} = sum(weight\_i * diff\_i(x,y)) \qquad (3)$$

After Multi-Scale Retinex Enhancement, we apply CLAHE to the enhanced image. CLAHE can be represented by the cumulative distribution function (CDF) [14] as follows:

$$CDF(i) = sum(hist(j) for j = 0 to i) \qquad (4)$$

Where:

- *CDF(i)* is the cumulative distribution function.
- *hist(j)* is the image histogram.

Subsequently, we employ the Color Ratio Correction method, which is preceded by Gaussian blur to further mitigate the effects of uneven illumination:

$$C(x,y) = I(x,y) / B(x,y) * scale\_factor \qquad (5)$$

Where:

- *I(x, y)* is the input image
- *B(x, y)* is the blurred version of I

As shown in Figures 2(b) and 2(c), the uneven illumination was mitigated but not completely eliminated, primarily due to the presence of gridlines, which posed challenges for the illumination equalization process. To tackle this issue, we utilized two morphological operations: both opening and closing operations. These morphological operations were implemented to eliminate the smaller grid lines and restore the letters to their original appearance. As shown in Figure 2(d), the removal of extraneous black pixels, including the gridlines, has significantly improved the visibility of the Arabic words, making them easier to detect. While the initial distortions were effectively removed, the resulting image still exhibits an imbalance in text writing, with some text appearing very light while others are too strong.

(a)　　　　　　　　(b)

Fig. 3. Binarized document image: (a) Original image, (b) Binarized image using Sauvola thresholding.

To address this issue, we employed the renowned binarization technique known as Sauvola thresholding. This binarization method calculates local thresholds within a window surrounding each pixel, providing adaptability to the image content. As illustrated in Figure 3(b), the binarization process successfully enhanced the image quality.

The presence of skew also affects the segmentation of lines, especially when the lines are not perfectly vertical. In such cases, a vertical projection may yield incorrect results. As shown in Figure 4(a), the figure exhibits an incorrect perspective view slanted by a certain angle. To address this issue, we employed the renowned Hough Line Transform to detect and correct the skew. This transformation identifies lines that represent the text's baseline, allowing us to rectify the perspective, as illustrated below:

$$H = x * cos(T) + y * sin(T) \qquad (6)$$

Where:

- H: represents the distance from the origin (0,0) to the line.
- (x, y): are the coordinates of a point on the line.
- T: is the angle between the x-axis and the line, measured in radians.

(a)　　　　　　　　(b)

Fig. 4. Skew Correction Sample: (a) Original Image, (b) Corrected Image.

As shown in Figure 4(b), the skew has been corrected, and the lines are perfectly aligned with their original axis.

B. Text Detection

After the preprocessing phase, which enhances the quality of the Arabic document image, the next step is to extract the document lines. To achieve this, we employed several approaches. First, we performed a series of morphological operations to further refine the image.

The morphological operations, including opening and closing operations, are combined to ensure noise removal and to

connect closely located regions with each other. This merging process can be observed in Figure 5(b), where each line has been merged into a single, distinct line. This process greatly assists us in extracting individual lines accurately. The subsequent step involves transforming each merged black region into a connected component (CC), where each CC is characterized by its width, height, and density. We utilized these features, utilizing bounding boxes, to extract both the simple lines and the title, as depicted in Figures 5(c) and 5(d). In these figures, each line is successfully detected.
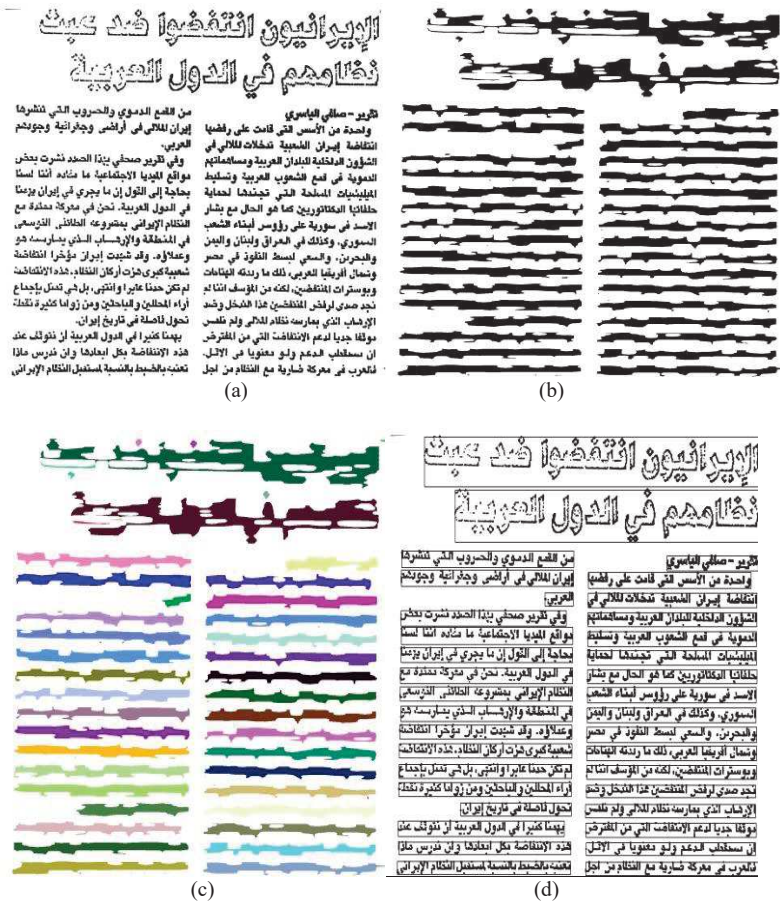

Fig. 5. Line Detection Sample: (a) Original Image, (b) Resultant Image with Merged Regions, (c) Connected Component Extraction, (d) Line Extraction.

By utilizing bounding box features, such as size and density, we can filter out irrelevant points (character points) and assign them to their respective lines (words and their associated points). Figures 6(a) and 6(b) highlight the significance of bounding box filtering, illustrating that this step is crucial for accurately detecting individual line words along with their corresponding points.

Figure 6(c) demonstrates an example of a critical case with two closely spaced lines that are effectively separated. This illustrates that our approach can successfully segment Arabic text lines even in cases where there is no typical spacing between the lines.
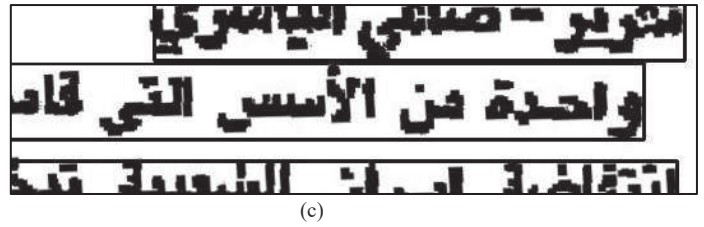

Fig. 6. Line Segmentation Sample: (a) The generated bounding box before filtering, (b) The generated bounding box after filtering, (c) A critical case of two very close lines.

IV. EVALUATION AND RESULTS

In this section, we present the comprehensive results that encompass different case rates. We begin by providing an overview of the dataset used for the evaluation, followed by a description of the evaluation method used for our results. We also compare our obtained results with the most relevant works in the field. It's worth noting that our code was implemented using Java, running on an Intel i7-8550U CPU @ 1.80GHz processor with 8.00 GB of RAM.

A. Evaluation dataset

In evaluating the performance of our study, we selected 82 computer-captured images from the PATD database (printed Arabic text database) [15] for testing. It's important to emphasize that the PATD database comprises hundreds of Arabic document images captured under various lighting conditions using three different smartphones. These images may exhibit skew, focus, and uneven light distortions. These images include magazines and newspapers, some of which contain single articles while others contain more than five articles. For this evaluation, we specifically selected document pages containing a single article, complete with a title, subtitle, author, and article content (paragraph), which may be presented in one to three columns.

B. Evaluation measures

For our evaluation, we manually created ground truth bounding boxes for each segmented line in the images using the PATD database, which contains the same samples used for automatic text line segmentation. The evaluation involves comparing the detected line bounding boxes with the manually created ground truth bounding boxes for each tested image. We use the Intersection over Union (IoU) metric to

assess the spatial overlap between manually created bounding boxes (MB) and automatically generated bounding boxes (AB) for each line defined by the coordinates (x1, y1, x2, y2) as follows:

$$Overlap_{Width} = min(x2, x2_{auto}) - max(x1, x1_{auto}) \quad (7)$$
$$Overlap_{Height} = min(y2, y2_{auto}) - max(y1, y1_{auto}) \quad (8)$$
$$Intersection\ area = Overlap_{Width} * Overlap_{Height} \quad (9)$$
$$MB = (x2 - x1) * (y2 - y1) \quad (10)$$
$$AB = (x2_{auto} - x1_{auto}) * (y2_{auto} - y1_{auto}) \quad (11)$$
$$Union\ area = MB + AB - I \quad (12)$$
$$IoU = Intersection\ Area\ /\ Union\ Area \quad (13)$$

A successful match is determined by an IoU value: If IoU > 0.95, it indicates correct segmentation.

We then calculate the following metrics:

$$Precision = TP\ /\ (TP + FP) \quad (14)$$
$$Recall = TP\ /\ (TP + FN) \quad (15)$$
$$F = 2 * (Recall * precision)/ (Recall + precision) \quad (16)$$

Where:

- TP (True Positives) is the number of correctly detected lines.
- FP (False Positives) is the number of lines that were incorrectly detected.
- FN (False Negatives) is the number of lines that were not detected but should have been.

C. Results and analysis

Table 1 showcases the line segmentation results of the proposed approach based on F measure.

TABLE I. PROPOSED APPROACH EVALUATION RESULTS USING COMPARISON MEASURE.

Sample type	Precision (%)	Recall (%)	F measure (%)
Heavily distorted	92.15	90.83	91.49
Slightly distorted	96.56	95.95	96.25
Total	94.35	93.39	93.74

The table clearly demonstrates that the proposed approach has yielded encouraging results in terms of recall, precision, and F-measure, achieving 91.49% even for heavily distorted document pages with poor quality. We were able to extract lines efficiently without employing deep learning technology, thus saving processing time, where these tasks can be successfully accomplished using a free learning approach. To ensure a realistic comparison, we evaluated our method against the closest work [16], which focus on printed line

segmentation (see tables 2). Since there are no other novel works that address line segmentation for captured-image version, we selected this study, which focuses on extracting lines from newspapers, as it is relevant to our research.

TABLE II. A TECHNIQUE COMPARISON OF RESEARCH STUDIES USING DIFFERENT APPROACHES

Authors	Precision (%)	Recall (%)	F measure (%)
Our approach	96.56	95.95	96.25
Saud et al[16]	99.18	98.38	98.74

However, a major distinction lies in the fact that they do not consider captured image versions with grids. While their results appear promising for line segmentation in newspapers and book pages, it cannot be guaranteed that their approach will yield equally effective results in our case. Our results are very encouraging, especially considering the challenges posed by critical factors such as uneven lighting, skew, and gridlines. In another work by Din et al. [17], an accuracy of 92.49% was achieved using 30 printed Urdu documents for text line segmentation in image versions. It is evident that our approach has yielded superior results compared to this work, utilizing a larger and more diverse dataset. Although we could not make a direct comparison with a work under the same circumstances and dataset, our results are highly promising when compared to similar works in our domain.

V. CONCLUSIONS AND FUTURE WORK

In this paper, we present a novel approach for extracting Arabic text from captured images, addressing challenges such as grid distortions, skew, and lighting issues. Our approach has yielded successful results. Notably, many recent works have overlooked grid distortions, which are considered a particularly challenging task to correct accurately in documents. Our system initiates with preprocessing phases that include light and skew correction, along with morphology operations and connected components for text extraction. The experiments demonstrate that our approach effectively handles grid distortions along with other cases. In future work, we plan to expand our scope to encompass various document types, including graphical element extraction in addition to textual content. We also aim to further improve the correction rate for Arabic text in smartphone-captured images.

REFERENCES

[1] M. Lukasik, B. Dadachev, G. Simoes, and K. Papineni, "Text segmentation by cross segment attention," in arXiv preprint arXiv:2004.14535, 2020.

[2] Y. S. Chernyshova, A. V. Sheshkus, and V. V. Arlazarov, "Two-step CNN framework for text line recognition in camera-captured images," in IEEE Access, vol. 8, pp. 32587-32600, 2020.

[3] P. Singh and D. V. Sharma, "Pre-Processing of Mobile Camera Captured Images for OCR," in International Journal of Intelligent Systems and Applications in Engineering, vol. 11, no. 2s, pp. 147-155, 2023.

[4] R. Hu et al., "Toward a no-reference quality metric for camera-captured images," in IEEE Transactions on Cybernetics, 2021.

[5] H. El Bahi and A. Zatni, "Text recognition in document images obtained by a smartphone based on deep convolutional and recurrent neural network," Multimedia Tools and Applications, vol. 78, 2019. doi: 10.1007/s11042-019-07855-z.

[6] J. Canny, "A computational approach to edge detection," in Readings in Computer Vision, Elsevier, pp. 184–203,1987.

[7] H. El Bahi and A. Zatni, "Pre-processing of document images obtained with a smartphone," International Review on Computers and Software, vol. 11, no. 12, pp. 1187–1198, 2016.

[8] C. Liu, Z. Yu, B. Wang, and X. Ding, "Restoring camera-captured distorted document images," Int J Doc Anal Recognit (IJDAR), vol. 18, no. 2, pp. 111–124, 2014.

[9] S. Eskenazi, P. Gomez-Kramer, and J.-M. Ogier, "A comprehensive survey of mostly textual document segmentation algorithms since 2008," Pattern Recogn, vol. 64, pp. 1–14, 2017.

[10] B. S. Kim, H. I. Koo, and N. I. Cho, "Document dewarping via text-line based optimization," Pattern Recogn, vol. 48, no. 11, pp. 3600–3614, 2015.

[11] D. M. R. Castro, A. Revel, and M. Menard, "Document image analysis by a mobile robot for autonomous indoor navigation," in 2015 13th International Conference on Document Analysis and Recognition (ICDAR), IEEE, pp. 156–160, 2015.

[12] T. A. Tran, I. S. Na, and S. H. Kim, "Page segmentation using minimum homogeneity algorithm and adaptive mathematical morphology," Int J Doc Anal Recognit (IJDAR), vol. 19, no. 3, pp. 191–209, 2016.

[13] A. M. Reza, "Realization of the contrast limited adaptive histogram equalization (CLAHE) for real-time image enhancement," in Journal of VLSI Signal Processing Systems for Signal, Image and Video Technology, vol. 38, pp. 35-44, 2004.

[14] M.-H. Chun, S.-J. Han, and N.-I. Tak, "An uncertainty importance measure using a distance metric for the change in a cumulative distribution function," in Reliability Engineering & System Safety, vol. 70, no. 3, pp. 313-321, 2000.

[15] H. Bouressace and J. Csirik, "Printed Arabic Text Database for Automatic Recognition Systems," in 5th International Conference on Computer and Technology Applications, pp. 107–111, 2019.

[16] M. Saud, S. Ahthasham, A. Arshad, A. Almogren, H. Bashir, A. Muhammad, and K. H. Kim, "An Efficient Skewed Line Segmentation Technique for Cursive Script OCR," Scientific Programming, 2020. doi: 10.1155/2020/8866041.

[17] Din IU, Malik Z, Siddiqi I, Khalid S. "Line and ligature segmentation in printed Urdu document images." J. Appl. Environ. Biol. Sci. 2016, Mar;6(3):114-120.

Modeling and Control of Wheeled Mobile Manipulator

Samah Riache
Applied Automation Laboratory,
Faculty of Hydrocarbons and
Chemestry,
M'Hamed Bougara University,
Boumerdes, Algeria
samahriache@univ-boumerdes.dz

Madjid Kidouche
Applied Automation Laboratory,
Faculty of Hydrocarbons and
Chemestry;
M'Hamed Bougara University,
Boumerdes, Algeria
mkidouche@univ-boumerdes.dz

Issam, Younes Hamadache
Department of Electrical Systems
Engineering, Faculty of Technology
M'Hamed Bougara University,
Boumerdes, Algeria.
youneshamadache513@gmail.com

Abstract— **This paper presents modeling and control for a wheeled robot equipped with a two-degree-of-freedom robotic manipulator using Sliding Mode Control (SMC). The dynamic model was developed by considering the mobile manipulator as a coupled system. In this SMC scheme, the saturation function is used to replace the discontinuous sign function in order to reduce chattering effects and to retain the robustness of the SMC. Simulation results were carried out in trajectory tracking mode and conducted to confirm the effectiveness of the proposed controller.**

Keywords—Wheeled mobile Manipulator (WMM), non-holonomic, Sliding Mode Control, Chattering,

I. INTRODUCTION

Mobile manipulation combines two fundamental robotic skills: mobility in the environment and manipulation of objects. Recently, it has gained particular importance in diverse applications such as agriculture, industry, construction, and so on [1-3]. It has been proposed with various locomotion systems including wheeled systems, legged systems, underwater robots, and aerial robots.

A wheeled mobile manipulator (WMM) consists of a wheeled mobile base with a manipulator mounted on it. This robot is known to be a non-holonomic uncertain system, which makes its modeling and control very challenging. Many studies have been conducted to solve the aforementioned problems, including nonlinear feedback control [4], input-output decoupling control [5], task space-null space decoupling control [6], and computed torque control [7]. However, these control schemes depend on the knowledge of the complex dynamics of the system and ignore external disturbances.

An adaptive robust output-feedback force/motion control strategy was presented in [8], under non-holonomic constraints in the presence of uncertainties and disturbances. An adaptive Neural Network (NN)-based control for the arm and the base was proposed in [9], for joint-space position control of a mobile manipulator. In [10], an adaptive model predictive control (AMPC) was implemented for a two-wheeled mobile robot. In [11], an optimized differential evolution algorithm based on kinematic limitations and structural complexity constraints was proposed to solve the trajectory tracking problem for a mobile manipulator robot. Adaptive control strategies were presented in [12], for a WMM operating in task space under external torques and disturbances.

Sliding Mode Control (SMC) is a robust control scheme mainly used for controlling systems in the presence of model uncertainties and external disturbances , and it can be applied to various robotic systems [13-15]. In [16], finite time SMC method was applied to WMM under uncertain tire/road structure TRs. A comparative study between conventional and dual closed loop finite time SMC was conducted in [17]. Later, in [18], the authors proposed an adaptive trajectory tracking control of the manipulator based on extreme learning machine and sliding mode control ELM-SMC.

The main drawback of SMC is the chattering effect, for which various solutions have been proposed, such as modification of the discontinuous control part, adaptive controllers, and so on. In this paper, we propose a dynamic modeling and design of a SMC scheme for trajectory tracking of a WMM, using saturation function in discountinious control part to eliminate chattering.

The remainder of this paper is organized as follows: Section II derives the dynamic model of the system, while Section III details the proposed controller design based on SMC. Section IV presents simulation results, and finally Section V concludes this work.

II. MODELING

The considered system consists of a two-link manipulator mounted on 3 degrees of freedom wheeled omnidirectional robot, and located at its gravity center, as shown in Fig1.
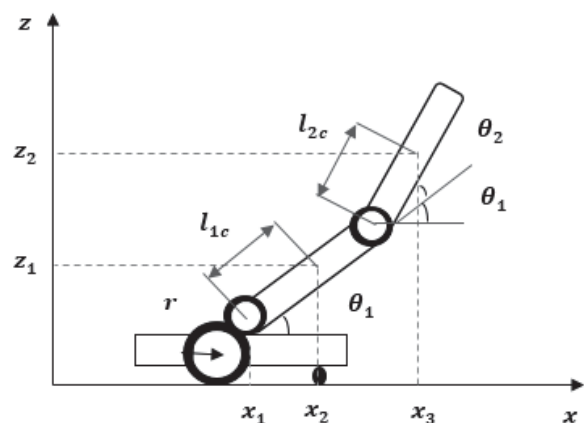

Figure 1. Wheeled mobile manipulator presented in x-z plane

The vector of generalized coordinate variables for the system is given by

$$q = \begin{bmatrix} q_m{}^T & q_p{}^T \end{bmatrix}, \tag{1}$$

where $q_m{}^T$, $q_p{}^T$ present the generalized coordinate variables for the wheeled robot and the manipulator respectively $q_m = \begin{bmatrix} \theta_1 & \theta_2 \end{bmatrix}$, with θ_1 and θ_2 represent the joint angles of the 2-DOF manipulator.

$q_p = \begin{bmatrix} x_p & y_p & \theta \end{bmatrix}$, with x_p, y_p, θ are the Cartesian coordinates of the mobile platform.

In most research on dynamic models of omnidirectional mobile manipulators, the redundant actuation of the platform is often overlooked. Additionally, the integrated dynamic model of the omnidirectional mobile manipulator, derived from the driving wheels, is not explicitly addressed [19]. Using Lagrange's theory, the dynamic model of the combined system with external disturbances can be given as follows:

$$M(q)\ddot{q} \rule{2cm}{0.4pt} + \tau_d = J^T(q)\lambda + D(q)\tau \tag{2}$$

Where

- $M(q)$ is the inertia matrix;
- $C(q,\dot{q})$ represents the vector of centripetal and Coriolis torques;
- $G(q)$ is the gravitational torque vector;
- τ is the vector of generalized input torques;
- τ_d denotes the external disturbances;
- $D(q)$ is a full rank input transformation matrix and is assumed to be known because it is the function of fixed geometry of the system;
- $J^T(q)$ is the kinematic constraints matrix;
- λ is a constraint force vector.

The non-holonomic constraints are considered independent of time and can be expressed as [19]:

$$J(q)\dot{q} = 0 \tag{3}$$

By using the following equation:

$$S(q)J(q) = S^T(q)J^T(q) = 0 \tag{4}$$

with

$$S(q) = \begin{bmatrix} \frac{r}{2}\cos\theta & \frac{r}{2}\cos\theta & 0 & 0 \\ \frac{r}{2}\sin\theta & \frac{r}{2}\sin\theta & 0 & 0 \\ \frac{r}{2} & -\frac{r}{2} & 0 & 0 \\ 0 & 0 & 1 & 0 \\ 0 & 0 & 0 & 1 \end{bmatrix}$$

r is the radius of the wheel.

The dynamic model becomes:

$$\bar{M}(q)\ddot{q} \rule{1.5cm}{0.4pt} \dot{q} + \bar{G}(q) = \bar{D}(q)\tau \tag{5}$$

with:

- $\bar{M}(q) = S(q)^T M(q) S(q)$
- $\bar{C}(q,\dot{q}) = S(q)^T (C(q,\dot{q})S(q) + M(q)\dot{S}(q))$
- $\bar{G}(q) = S(q)^T G(q)$
- $\bar{D}(q) = S(q)^T D(q)$
- $q_a = \begin{bmatrix} \theta_r & \theta_l & \theta_1 & \theta_2 \end{bmatrix}^T \quad \dot{q}_a = \begin{bmatrix} \rule{1.5cm}{0.4pt} \end{bmatrix}^T$

The changement from generalized coordinates $\begin{bmatrix} \dot{x}_p & \dot{y}_p & ,\dot{\theta} \end{bmatrix}^T$ to $\begin{bmatrix} \dot{\theta}_r & \dot{\theta}_l \end{bmatrix}^T$ is given by the following matrix:

$$\begin{bmatrix} \dot{x}_p \\ \dot{y}_p \\ \dot{\theta} \end{bmatrix} = \begin{bmatrix} \frac{r}{2}\cos\theta & \frac{r}{2}\cos\theta \\ \frac{r}{2}\sin\theta & \frac{r}{2}\sin\theta \\ \frac{r}{2} & -\frac{r}{2} \end{bmatrix} \begin{bmatrix} \dot{\theta}_r \\ \dot{\theta}_l \end{bmatrix}$$

III. CONTROL DESIGN

The proposed control scheme is based on Sliding Mode Control and the sliding variable is defined as:

$$S = \dot{e} + We \tag{6}$$

With:

$$S = \begin{bmatrix} s_1, \ldots, s_4 \end{bmatrix}^T , \quad W = diag(w_i), w_i > 0 \text{ for } (i = 1 \text{ to } 4)$$

The tracking error is given by $e = q_a - q_d$ and its derivative is $\dot{e} = \dot{q}_a - \dot{q}_d$, where the vectors q_d and $\dot{q}_d$ represents the desired trajectory and its time derivative respectively.

By assuming that $\dot{S} = 0$, we get the equivalent control as:

$$U_{eq} = \bar{C}\dot{q}_a + \bar{G} - \bar{M}\left(\rule{1cm}{0.4pt} - \ddot{q}_d \right) \tag{7}$$

The global control law is:

$$U = U_{eq} + U_{dis} = \bar{C}\dot{q}_a + \bar{G} - \bar{M}\left(\rule{1cm}{0.4pt} - \ddot{q}_d \right) - KSign(S) \tag{8}$$

In order to attenuate the chattering effects, we use in the discontinuous part the following saturation function [20]:

$$sat(s) = \begin{cases} \dfrac{s}{\varepsilon} & if \left| \dfrac{s}{\varepsilon} \right| \leq 1 \\ sign(s) & if \left| \dfrac{s}{\varepsilon} \right| > 1 \end{cases} \tag{9}$$

With:
ε length of threshold saturation function
The control law (8) becomes:

$$U = U_{eq} + U_{dis} = \bar{C}\dot{q}_a + \bar{G} - \bar{M}\left(\lambda\dot{e} - \ddot{q}_d \right) + sat(S) \tag{10}$$

IV. SIMULATION RESULTS

Simulation of the proposed controller has been carried out using an omnidirectional-wheeled robot with a 2-DOF robotic manipulator. Simulations have been performed in trajectory tracking mode using the MATLAB environment.

The initial values of all the system's generalized joints are $[\theta_r \ \theta_l \ \theta_1 \ \theta_2] = [0 \ 0 \ 0.1 \ 1]$. The desired trajectory consists of a displacement from 0 to 2m along the x-axis without any change in y and θ. Hence, to make the WMM reach the position $(x, y) = (1, 0)$, the 1st joint of the robotic arm θ_1 should track the path given by: $\theta_{1d} = t$. When θ_1 reaches 1rad, the 2nd joint θ_2 should change its angular position from 0 to 1rad through the path $\theta_{2d} = t$.

The parameters of the sliding mode controller for all joints are:

$w = diag(15, 15, 10, 10)$

$K = (15, \ 15, \ 40, \ 30) \quad \varepsilon = (0.5, \ 0.5, \ 0.5, \ \mathbf{0.5})$
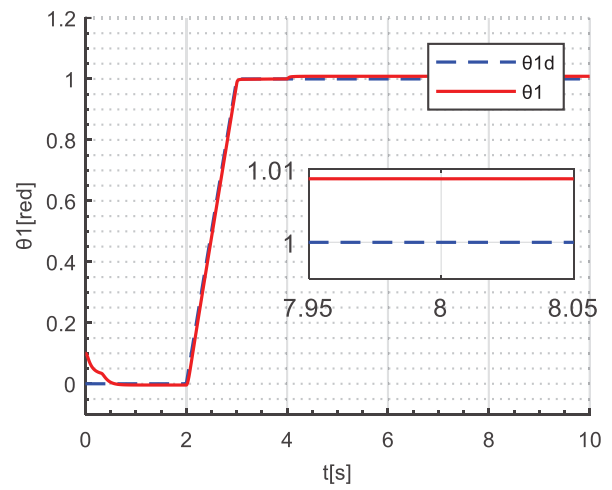
Implementing the proposed control laws SMC (equation 10), with the desired trajectory, the chosen parameters, and gains as described previously leads to the results presented in figures 2-4, which illustrate the linear and angular positions, and control signals for all controllers.
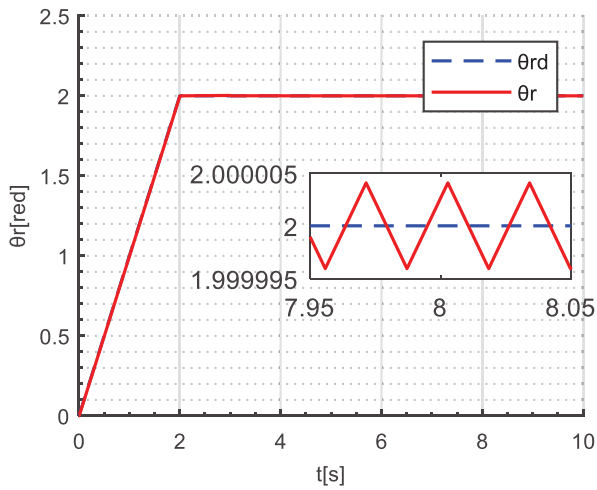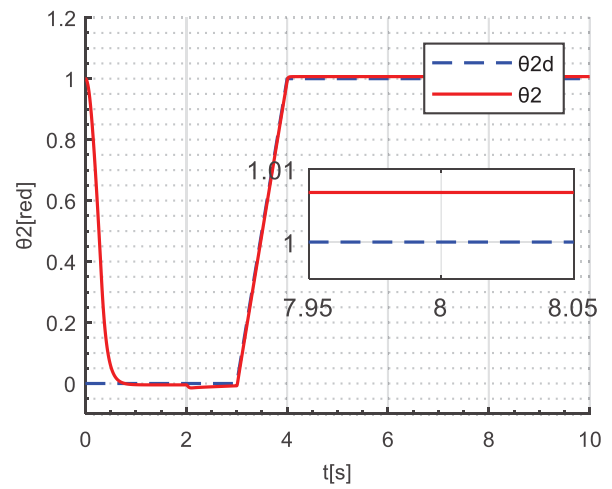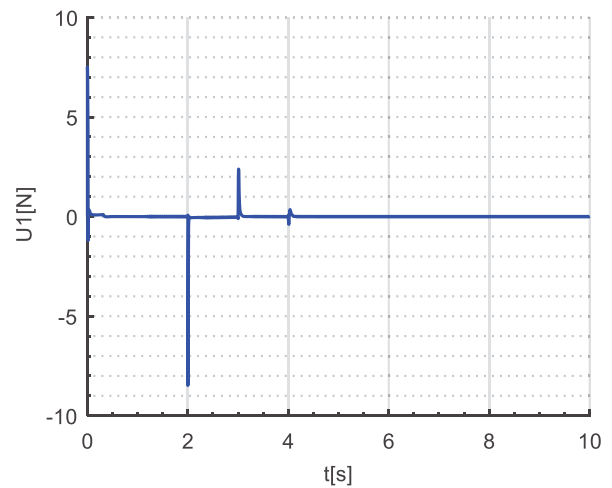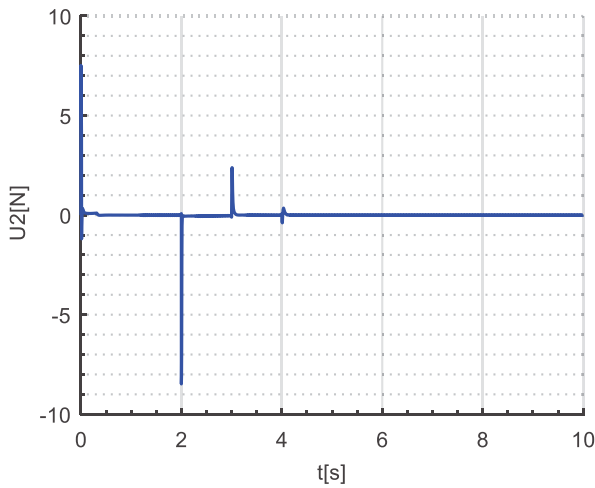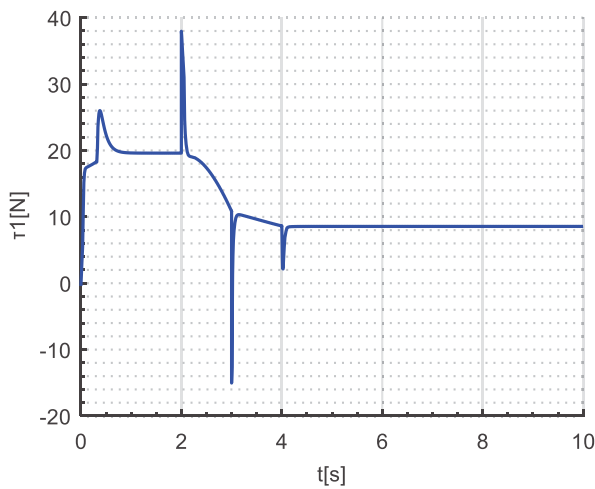

(a)
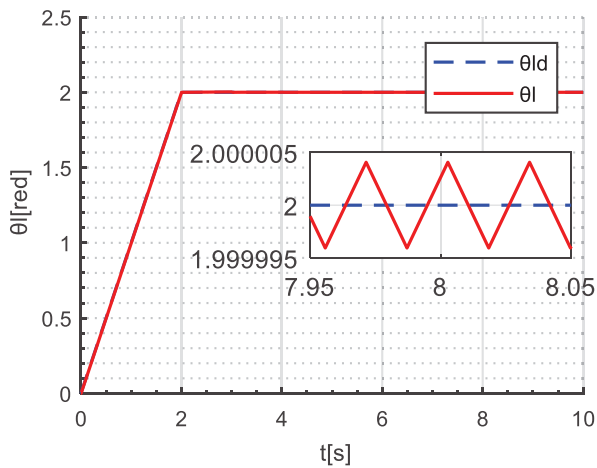
(b)

(c)

(d)

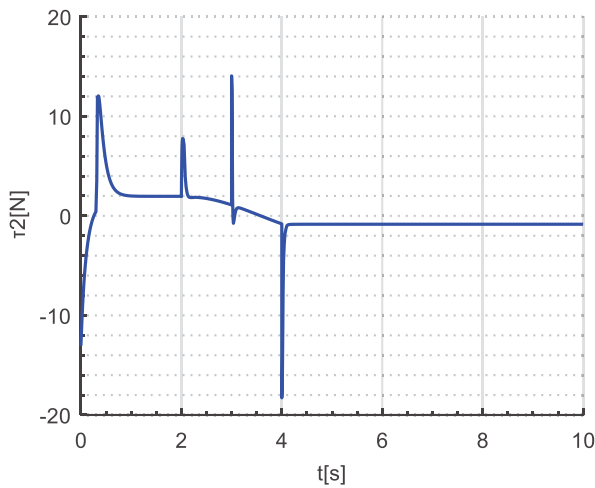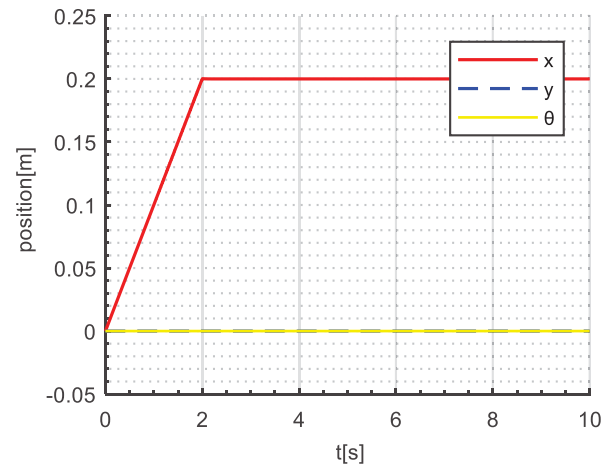Fig 2. Application of SMC in tracking trajectory mode.

(a)

(b)

Fig. 4. Platform tracking trajectory

Figure 2 shows that the WMM is able to successfully track the desired path with good precision using SMC with saturation function, particularly at the moment corresponding to the mobile base deflection at t=2s (as shown in Figure 2 (a,b)). Additionally, the saturation function applied in control law (10) allows to eliminate the chattering effects in control, as shown in Figure 3, the pics appeared in control signals are due to trajectories deflection.

V. CONCLUSION

In this paper, the Sliding Mode Control (SMC) has been applied to a wheeled robot equipped with a manipulator for trajectory tracking. The proposed control strategy has shown good performance and successfully attenuated chattering effects using saturation function. As future work, it is suggested to test these controllers under disturbances in complex trajectory tracking in order to further improve their performance and robustness.

(c)

(d)

Fig. 3. Control signals

VI. REFERENCES

[1] Y. Liu and G. Liu, ''Interaction analysis and online tip-over avoidance for a reconfigurable tracked mobile modular manipulator negotiating slopes,'' IEEE/ASME Trans. Mechatronics, vol. 15, no. 4, pp. 623–635, Aug. 2010.

[2] J. Mattila, J. Koivumaki, D. G. Caldwell, and C. Semini, ''A survey on control of hydraulic robotic manipulators with projection to future trends,'' IEEE/ASME Trans. Mechatronics, vol. 22, no. 2, pp. 669–680, Apr. 2017,

[3] S. Aguilera-Marinovic, M. Torres-Torriti, and F. Auat-Cheein, ''General dynamic model for skid-steer mobile manipulators with wheel–ground interactions,'' IEEE/ASME Trans. Mechatronics, vol. 22, no. 1, pp. 433–444, Feb. 2017,

[4] Y. Yamamoto, X. Yun, "Effect of the dynamic interaction on coordinated control of mobile manipulators", IEEE Transactions on Automatic Control 42, pp 816–824, 1996.

[5] A. Mazur, New approach to designing input–output decoupling controllers for mobile manipulators, Bulletin of the Polish Academy of Sciences, Technical Sciences 53 (1), 2005.

[6] G. White, R. Bhatt, V. Krovi, Dynamic redundancy resolution in a nonholonomic wheeled mobile manipulator, Robotica 25 (2), pp 147–156, 2007.

[7] E. Papadopoulos, J. Poulakakis, "Planning and model based control for mobile manipulators", in: Proceedings of the IEEE/RSJ International Conference on Intelligent Robots and Systems,, pp. 1810–1815., 2000.

[8] Z. Li, W. Chen, "Adaptive neural fuzzy of uncertain constrained multiple coordinated nonholonomic mobile manipulators", Engineering Applications of Artificial Intelligence vol 21 (7), pp 985–1000, 2008.

[9] Yukun Zheng, Yixiang Liu, Rui Song, Xin Ma, Yibin Li, "Adaptive neural control for mobile manipulator systems based on adaptive state observer", Neurocomputing, Vol 489, pp 504-520, 2022.

[10] M. Önkol and C. Kasnakoğlu, "Adaptive Model Predictive Control of a Two-wheeled Robot Manipulator with Varying Mass", Measurement and Control, pp 1–19, 2018.

[11] Lijun Qiao, Xiao Luo, and Qingsheng Luo, "Control of Trajectory Tracking for Mobile Manipulator Robot with Kinematic Limitations and Self-Collision Avoidance", Machines, 10, 1232, 2022.

[12] M. Boukattaya., M. Jallouli? & T.Damak, "On trajectory tracking control for non-holonomic mobile manipulators with dynamic uncertainties and external torque disturbances". Robotics and autonomous systems, vol 60(12), pp 1640-1647, 2012.

[13] S. Riache, M. Kidouche and A.Rezoug, "Adaptive robust nonsingular terminal sliding mode design controller for quadrotor aerial manipulator", Telkomnika, vol. 17(3),pp. 1501-1512, 2019.

[14] M.Z,Doghmane, M. Kidocuhe, S.Riache, and A. Aibeche, "Hybrid Adaptive Backstepping-Sliding Mode Control Design for Non-linear Under-Actuated Systems., Hatti, M., Ed.; Lecture Notes in Networks and Systems; Springer: Cham, Switzerland; Vol 361, 2022.

[15] M. Kidouche, S. Riache, A. Rezoug, "Adaptive Sliding Mode Control for Quadrotor Helicopter," International Conference on Technological Advances in Electrical Engineering Skikda, Algeria, 2016.

[16] Z. Cao, Yugang. Niu, "Finite-time sliding mode control of Markovian jump systems subject to actuator nonlinearities and its application to wheeled mobile manipulator", Journal of the Franklin Institute,Vol 355(16), pp 7865-7894, 2018.

[17] In Seok Seo, Seong Ik Han, "Dual closed-loop sliding mode control for a decoupled three-link wheeled mobile manipulator", ISA Transactions, Vol 80, pp 322-335, 2018.

[18] X. Wang, D. Wang, M. Du, K. Song, Y. Ni and Y. Li, "A Two-Layer Trajectory Tracking Control Scheme of Manipulator Based on ELM-SMC for Autonomous Robotic Vehicle," IEEE Transactions on Automation Science and Engineering, pp1-12, 2023.

[19] M. Boukattaya, M. Jallouli, T. Damak, On trajectory tracking control for nonholonomic mobile manipulators with dynamic uncertainties and external torque disturbances, Robotics and Autonomous Systems, Vol 60 (12) pp 1640-1647, 2012.

[20] V. BREGEAULT, « Quelques contributions à la théorie de la mode glissant », Phd Thesis, ECOLE CENTRALE DE NANTES, décembre 2010.

Some Applications envisaged for the new generation of communications networks 6G

1st S. Latreche
University of Abderrahmane Mira Bejaia
LGEB Laboratory
sofiane.latreche@univ-bejaia.dz

2nd H. Bellahsene
University of Abderrahmane Mira Bejaia
LGEB Laboratory
hocine.bellahsene@univ-bejaia.dz

3rd A. Taleb-Ahmed
Valenciennes University
IEMN DOAE Laboratory
abdelmalik.taleb-ahmed@uphf.fr

Abstract—Future applications such as intelligent vehicles, the Internet of Things and holographic telepresence are already highlighting the limits of existing fifth-generation (5G) mobile networks. These limitations relate to data throughput, latency, reliability, availability, processing, connection density and global coverage, whether terrestrial, submarine or space-based. To remedy this, research institutes have begun to look beyond IMT2020, and as a result, 6G should provide effective solutions to 5G's shortcomings. 6G will offer high quality of service and energy efficiency to meet the demands of future applications that are unimaginable to most people. In this article, we present the future applications and services promised by 6G.

Index Terms—5G, 6G, Application, IA, IOE

I. INTRODUCTION

The evolution of mobile networks has witnessed remarkable growth since their inception in the 1980s. Transitioning from one generation to the next occurred at an astonishing pace. Initially dedicated solely to telephony, these networks then gradually integrated Short Message Service (SMS) and Multimedia Messaging Service (MMS). Subsequently, they evolved into a more multimedia-oriented generation with 3G technology, followed by a focus on high-speed data transmission with the advent of 4G and the establishment of all-IP networks. The introduction of 5G technology further pushed the boundaries, reducing latency and providing exceptionally high-speed, high-capacity connections that rendered services and applications previously deemed impossible just two decades ago not only feasible but also seamless [1].

However, the rapid development of future applications, such as smart vehicles, the Internet of Things (IoT), and holographic telepresence, is already revealing the constraints of existing 5th generation (5G) mobile networks. These constraints encompass aspects like data transmission rates, latency, reliability, network availability, processing capabilities, connection density, and global coverage, whether on terrestrial, submarine, or space-based platforms. In response to these limitations, research institutions have begun to explore possibilities beyond the confines of the International Mobile Telecommunications-2020 (IMT-2020) framework. As a result, the emergence of 6G technology is anticipated to provide innovative solutions to address the shortcomings of 5G [2].

6G is poised to deliver a high-quality service and enhance energy efficiency, thereby meeting the evolving demands of future applications.

II. MOBILE NETWORK EVOLUTION

Mobile networks have undergone rapid and remarkable development since their inception in the 1980s. This continuous evolution has given rise to several generations of mobile telephony, with each succeeding generation being introduced approximately every decade [3]. Figure 1 provides a visual representation of the progression of mobile network evolution.

A. FIRST STEPS FROM 1G TO 3G

The inception of cellular networks dates back to the 1980s when the first generation was introduced, primarily designed for voice services and capable of data rates up to 2.4 kbps. In contrast to the analog systems of the first generation, the second generation embraced digital modulation technologies like Time Division Multiple Access (TDMA) and Code Division Multiple Access (CDMA). This technological shift brought about a significant enhancement, offering data rates of up to 64 kbps and introducing features such as short message service (SMS) [4].

The dawn of the third generation in the year 2000 marked a pivotal moment in mobile network evolution, aiming to provide high-speed data transmission. The 3G network was a game-changer, offering a minimum data transfer rate of 2 Mbps and granting users access to the vast realm of the internet. This transformation enabled an array of advanced services previously unsupported by the 1G and 2G networks, including web browsing, TV streaming, navigation maps, and video services [5].

B. 4G EVOLUTION

The advent of 4G marked a significant milestone in the evolution of mobile networks, introduced in the late 2000s. This all-IP network was designed to deliver exceptionally high-speed data rates, reaching up to 1 Gbps for downlink and 500 Mbps for uplink transmissions. Its core enhancements included improvements in spectral efficiency and a reduction in latency, making it well-suited to meet the requirements of demanding applications such as digital video broadcasting (DVB), high-definition TV content delivery, and seamless video chat experiences [6]. Notably, Long Term Evolution-Advanced (LTE-A) and Wireless Interoperability for Microwave Access (WiMax) were both recognized as 4G standards. The foundation of 4G, LTE, integrated a blend of existing and novel technologies,
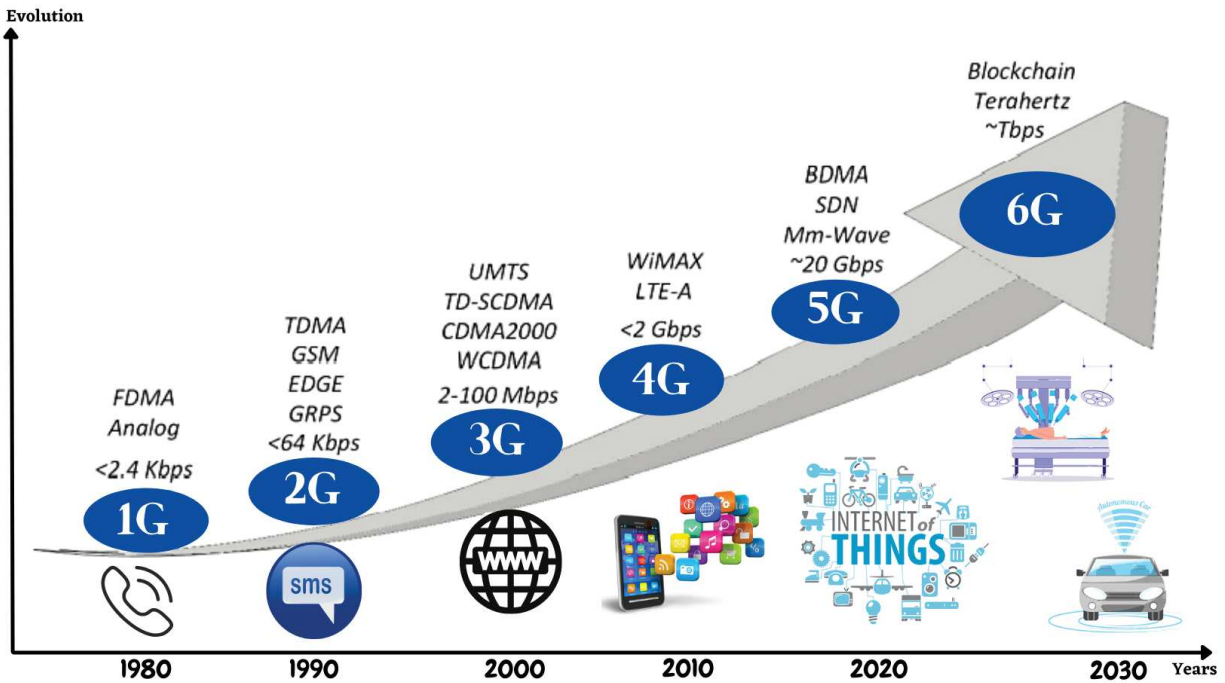
Fig. 1: Evolution of mobile wireless systems.

including coordinated multiple transmit/receive (CoMP), multiple input multiple output (MIMO), and orthogonal frequency division multiplexing (OFDM) [7].

C. 5G DYNAMICS

The primary objective of 5G technology is to achieve groundbreaking advancements in terms of throughput, latency, network reliability, and energy efficiency, all while ensuring extensive connectivity. Unlike its predecessors, 5G harnesses not only the new sub-6GHz spectrum, which includes the C-band and the broader 6GHz band but also, for the first time, delves into the millimeter-wave band, enabling significantly higher data rates, reaching up to an impressive ten Gbps. 5G relies on advanced access technologies, including beam division multiple access (BDMA), real-time division multiple access, and filter bank multiple access (FBMC) [1].

To enhance network performance, 5G incorporates a myriad of emerging technologies. These innovations encompass massive MIMO to bolster network capacity, software-defined networks (SDN) for increased network flexibility, device-to-device (D2D) communication to improve spectral efficiency, information-centric networking (ICN) to reduce network traffic, and network slicing to facilitate the swift deployment of numerous services [8].

Within the framework of IMT 2020, three primary usage scenarios have been proposed for 5G technology: enhanced mobile broadband (eMBB) to cater to high-speed data requirements, ultra-reliable low-latency communications (URLLC) for mission-critical applications, and massive Machine Type Communications (mMTC) to support the proliferation of connected devices and the Internet of Things [9].

III. FUTURE WITH THE 6G

As 5G progresses into its commercial deployment phase, research institutions worldwide are already directing their attention towards the development of 6G, which is slated for deployment around the year 2030. The anticipated capabilities of 6G are poised to usher in a new era of information transmission performance, promising peak data rates of up to one Terabit and achieving ultra-low latency in mere microseconds. A defining feature of 6G is its utilization of communication frequencies in the terahertz range, offering spatial multiplexing capabilities that could potentially provide up to 1000 times the network capacity of 5G systems [10].

One of the central objectives of 6G is the establishment of ubiquitous connectivity, and this is envisaged through the integration of satellite and undersea communication networks, thereby ensuring global coverage [1]. Three distinct categories of 6G services have been outlined to address the evolving needs of users: ubiquitous mobile ultra-broadband (uMUB), ultra-high-speed low-latency communications (uHSLLC), and ultra-high data density (uHDD) [11]. These evolving requirements will be met through the deployment of emerging technologies, including the exploitation of the THz spectrum, federated learning (FL), edge artificial intelligence (AI), compressive sensing (CS), blockchain, and more.

Table 1 serves as a performance comparison tool between 6G and 5G, highlighting the differences and advancements in various key metrics.

IV. 6G NEW SERVICES

6G services are poised to revolutionize the landscape of mobile communications, reshaping traditional concepts of

Performance	6G	5G	Effect
Rate	Peak rate: 100 Gbps-1 Tbps	Peak rate: 10 Gbps-20 Gbps	10–100 times
Latency	0.1 ms, on-time processing	1 ms	10 times
Traffic density	100- 10,000 Tbps/square meter	10 Tbps/square meter	10–100 times
Connection density	Maximum 0.1 billion connections/square meter	1 million connections/square meter	100 times
Mobility	higher than 1000 km/h	500 km/h	2 times
Spectrum efficiency	200–300 bps/Hz	100 bps/Hz	2–3 times
Positioning	Outdoor 1 meter, Indoor 10 cm	Outdoor 10 meter, Indoor around 1 meter	10 times
Spectrum support	Regular carrier bandwidth 20 Ghz	Sub 6 G Regular carrier bandwidth 100 Ghz,	50–100 times
Reliability	lower than 1/1000,000	lower than 1/100,000	10 times
Network efficiency	200 bits/J	100 bits/J	2 times

TABLE I: Performance comparison between 6G and 5G [4]

ultra-reliable low-latency communications (uRLLC), enhanced mobile broadband (eMBB), and massive Machine Type Communications (mMTC). In doing so, they will introduce a host of novel and innovative services, marking a significant departure from the existing paradigm of 5G.

A. MASSIVE URLLC

Smart factories represent one of the key applications of 5G technology, with ultra-reliable low-latency communications (uRLLC) playing a pivotal role in ensuring the reliability and minimal latency of data uplinks within these environments. However, as we look ahead to 6G, there is an anticipation of a significant evolution in the realm of uRLLC. This evolution will introduce an entirely new dimension, giving rise to a novel service known as massive uRLLC (mURLLC). This groundbreaking mURLLC service is not only expected to maintain the stringent requirements of 5G uRLLC but also to coexist seamlessly with the existing massive Machine Type Communications (mMTC) framework [12]. MuRLLC is set to take the delicate balance between reliability, latency, and scalability to unprecedented heights, marking a remarkable advancement in the capability of future communication networks [13].

B. MOBILE BROADBAND RELIABLE LOW LATENCY COMMUNICATION

The capabilities of enhanced mobile broadband (eMBB) and ultra-reliable low-latency communication (uRLLC) that were sufficient for 5G applications will no longer meet the demands of 6G applications, particularly those involving Extended Reality (XR). These cutting-edge applications necessitate exceptionally high reliability, ultra-low latency, and extremely high data rates. Consequently, a novel service known as Mobile Broadband Reliable Low Latency Communication (MBRLLC) has emerged to address these requirements within 6G networks. MBRLLC is designed to empower 6G networks with

the necessary performance attributes to navigate the intricate trade-offs between data rate, reliability, and latency, effectively accommodating the ever-evolving landscape of next-generation applications [14].

C. MULTI-PURPOSE 3CLS AND ENERGY SERVICES

The forthcoming 6G cellular networks are poised to introduce a spectrum of innovative services, primarily focusing on 3D Connectivity, Localization, and Sensing (3CLS), with the ultimate goal of enabling wireless energy transfer (WET) services for an array of smart devices [15]. Many of these 3CLS applications, encompassing both connectivity and power services (MPS), will place new demands on the 6G network infrastructure. To effectively cater to these requirements, 6G networks must exhibit robust performance attributes, including stringent criteria for latency stability, efficient energy transfer mechanisms, precise localization capabilities, and advanced data processing capabilities. These foundational elements are vital for supporting the diverse range of services and applications expected to define the 6G era [16].

D. NETWORK SLICING

Network slicing has emerged as a pivotal solution to cater to a diverse range of service requirements within the context of 6G networks. Slicing effectively generates multiple logical networks, each precisely configured to serve a specific type of service, all coexisting on a shared physical infrastructure. Notably, the ITU-R has proposed the implementation of distinct slices for each of the fundamental 5G services, namely ultra-reliable low-latency communications (uRLLC), enhanced mobile broadband (eMBB), and massive Machine Type Communications (mMTC) [17].

To further refine and distinguish the unique requirements of different industries or business areas residing within a given slice, the 3rd Generation Partnership Project (3GPP) specifications have recommended the incorporation of an

additional parameter known as a "slice differentiator" (SD). This extension, in a sense, augments the existing horizontal slicing by expanding it vertically. The rationale behind this inclusion lies in the fact that not all industries operating within a single slice can conveniently adopt the same protocol stack. In scenarios where different protocol stacks are necessary, it becomes essential to subdivide the individual slices [18].

However, an aspect that remains underaddressed in current literature is the concept of grouping services that can harmoniously share the same protocol stack within a given slice. This approach carries the potential to unveil the true capabilities of network slicing, enabling it to effectively meet the intricate and multifaceted requirements stipulated in the context of 6G networks.

V. 6G APPLICATIONS

5G-enabled applications will indeed be at the heart of 6G, even at larger scales (supporting huge, large networks such as safes cities).For 6G the following applications are described:

A. CONNECTED ROBOTICS AND AUTONOMOUS SYSTEMS (CRAS)

The deployment of new CRAS applications has been the main driver behind the 6G movement. CRAS incorporates flying vehicle delivery systems, autonomous cars, drone swarms, vehicle platoons, and autonomous robotics [19]. These applications are not another IoT uplink service, like many applications introduced in 5G. However, they require stringent latency requirements and extremely high throughput [11].

B. EXTENDED REALITY

Extended reality (XR) technologies include augmented reality (AR), mixed reality (MR), and virtual reality (VR) [17]. XR is an emerging immersive technology that merges the physical and virtual worlds [11].

Mixed reality is not about overlaying any content from the physical world like AR. However, it eliminates the distinctions between real reality and virtual reality in which computer-generated objects show something obscure in the physical environment.

AR, VR, MR, XR use different sensors to collect data regarding location, orientation and acceleration. This requires strong connectivity, extreme data rates, High resolution and extremely low latency, which should be facilitated by 6G.

C. INTERNET OF EVERYTHING (IOE)

IoE is an extended version of IoT that includes, things, data, people and processes. The main concept of IoE is to integrate various sensing devices that can be linked to "everything" to identify, monitor the status and make decisions in an intelligent way to create new insights.

IoE sensors are capable of acquiring many parameters such as speed, position, light, biological signals, pressure and temperature. These sensors are used in applications ranging from health systems, safes cities, to various industrial fields. 6G is expected to become a key component of IoE, as it requires the ability to connect N smart devices, where N is scalable and can reach billions. In addition, IoE will need high data rates to easily support N devices with low latency [20].

D. UAV BASED MOBILITY

UAVs have been widely used for defense and military attack applications, such as remotely operated aircraft, autonomous drones, and others. Over the years, the applications of UAVs have been expanded in the military and civilian fields. For example, drones have been proposed for disaster relief, agricultural plantation protection, traffic monitoring, and environmental sensing [21]. Drones are also expected to be an essential module for future wireless technologies such as 6G, which supports high-speed data transmission for communities living remotely, facing disaster situations such as earthquakes, terrorist attacks, and in the absence of typical cellular infrastructure.

The main characteristics associated with UAVs compared to fixed infrastructure are: ease of deployment, line-of-sight (LoS) connectivity [11] and most importantly, controlled mobility. The rapid development of UAV technologies will enable new areas such as automated logistics and military operations. With the emergence of 6G and IoE, researchers will explore the use of UAV-to-Everything (U2X) network that expands the paradigm of sensing applications by adjusting communication modes to their full potential.

E. HOLOGRAPHIC TELEPRESENCE

Holographic telepresence (HT) can project realistic three-dimensional (3D) images, in real time and in motion, of remote people and objects, with a high level of realism that rivals physical presence. It can be used for 3D video conferencing in motion, information dissemination etc.

The principle of HT consists of capturing sequences of people and surrounding objects, which are compressed and transmitted over a broadband network in the initial phase. Later, the transmitted information is decompressed on the receiver side and projected with laser beams into the scene to be virtualized. HT technology minimizes the costs of business travel and allows people to appear at many locations simultaneously [22]. In the case of multimedia applications and in order to engage the audience in a full immersive experience, tactile and interactive devices will be implemented using 6G with latency as low as 100 μs with a data rate of several Gbps.

F. WIRELESS BRAIN-COMPUTER INTERACTIONS (BCI)

In addition to XR applications, smart body implants and BCIs will become essential in 6G to support the healthcare revolution. Current healthcare applications are limited to controlling biometric implants (e.g., controlling prosthetic limbs or controlling functionality with brain implants). In 6G, wireless brain-computer interaction and interface with smart body implants will bring a huge change in the healthcare system. It

Fig. 2: Some Applications envisaged for 6G.

will introduce new techniques requiring 6G specifications for massive connectivity for innovative operation [23].

These applications require stringent requirements (such as high data rates, ultra-low latency and high reliability) like XR. However, BCI applications are much more sensitive than XR, and QoPE must be assured.

G. PERSONALIZED BODY AREA NETWORKS

Body Area Networks (BANs) with integrated mobile health systems (mHealth) are advancing toward personalized health monitoring and management. These personalized networks can collect health information from multiple sensors, dynamically exchange this information with the environment, and interact with networking services, including social networks [24].

Personalized BAN systems have a wide range of applications, covering both medical and non-medical domains. For example, personalized BANs can be used to avoid the need for wiring in polysomnography tests (also known as sleep disorder diagnosis). Custom BANs have also been used in non-medical applications such as emotion detection, entertainment, and secure authentication applications.

H. BLOCKCHAIN AND DISTRIBUTED LEDGER TECH-NOLOGIES (DLT)

Blockchain and DLT devices are still underdeveloped in many sectors, in addition to being immature. However, they have great potential in these next-generation distributed systems in terms of moving from centralized to distributed systems for the purpose of data validation. They require high connectivity, a synergistic mix of uRLLC and massive machine

type communications (mMTC) to maintain low latency, and reliable connectivity [25].

I. INTELLIGENT HEALTHCARE

The health sector will undergo various evolutions. These will evolve and will now be named healthcare 5.0 with the emergence of digital wellness. AI based smart healthcare will be developed based on several new methodologies including Quality of Life (QoL), Intelligent Wearable Devices (IWD) etc. With recent advances in wearable sensors and computing devices, it is possible to monitor and measure health data in real time. The sensing data collected from wearable devices can be prepared by the nearest edge node and then sent to doctors for remote diagnosis [26]. Moreover, with the realization of holographic communications, touch internet and 6G smart robots, the doctor can perform the surgery remotely. Such telesurgery would eliminate the need for on-site operations and avoid the risks caused by the spread of viruses, especially in the presence of epidemics, such as Coronavirus-19 and other communicable diseases (see fig.3).

J. INDUSTRY 5.0

Industry 5.0 refers to people working alongside robots and smart machines to add a human touch to the Industry 4.0 pillars of automation and efficiency. The drivers of the future will be based on 6G and IoE as a considerable number of objects in this type of industry will be connected via wires or wireless. The goal will provide various services through the full integration of cloud/edge computing, big data, and AI [27].
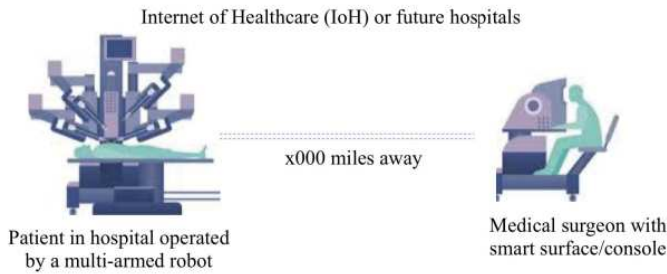
Fig. 3: Application for healthcare in 6G [11].

VI. CONCLUSION

Mobile networks have evolved very rapidly since their appearance in the 1980s. This article presents the evolution of mobile networks from the 1st generation to the 6th generation, with a focus on the defining principles of this latest generation. What sets 6G apart is its inherent capability to usher in a realm of applications and services that were once beyond the bounds of most people's imagination. This capacity becomes possible because 6G is designed to deliver exceptional quality of service and unrivaled energy efficiency, effectively meeting the diverse demands of future applications.

The 6th Generation envisages to know an unprecedented breakthrough by integrating the traditional terrestrial mobile networks with the emerging space, air and submarine networks in order to provide an access to the network at any time and in any place. What allows to have an underwater connection that will give the possibility to develop several applications, as the underwater tourism, to have direct emissions of the life of the underwater species, to have autonomous submarines and several other applications.

REFERENCES

[1] ARSHAD, Qazi Kamal Ud Din, KASHIF, Ahsan Ullah, et QUERSHI, Ijaz Mansoor. A review on the evolution of cellular technologies. In: 2019 16th International Bhurban Conference on Applied Sciences and Technology (IBCAST). IEEE, 2019. p. 989-993.J. Clerk Maxwell, A Treatise on Electricity and Magnetism, 3rd ed., vol. 2. Oxford: Clarendon, 1892, pp.68–73.

[2] A 5G Americas White Paper. State of Mobile Network Evolution. Sept 2023.

[3] TONGYI HUANG, WU YANG, JUN WU, (Member, IEEE),JIN MA,XIAOFEI ZHANG, and DAOYIN ZHANG, "A Survey on Green 6G Network: Architecture and Technologies", School of Electronic Information and Electrical Engineering, Shanghai Jiao Tong University, Shanghai 200240, China. Information Security Research Center, Harbin Engineering University, Harbin 150001, China. State Grid Electric Power Research Institute, Nanjing 211000, China. December 18, 2019.

[4] SHARMA, Pankaj. Evolution of mobile wireless communication networks-1G to 5G as well as future prospective of next generation communication network. International Journal of Computer Science and Mobile Computing, 2013, vol. 2, no 8, p. 47-53.

[5] BHANDARI, Nikhil, DEVRA, Shivinder, et SINGH, Karamdeep. Evolution of cellular network: from 1G to 5G. International journal of engineering and techniques, 2017, vol. 3, no 5, p. 98-105.

[6] KUMAR, Amit, LIU, Yunfei, SENGUPTA, Jyotsna, et al. Evolution of mobile wireless communication networks: 1G to 4G. International Journal of electronics and communication technology, 2010, vol. 1, no 1, p. 68-72.

[7] PARK, Yongsuk et PARK, Taejoon. A survey of security threats on 4G networks. In : 2007 IEEE Globecom workshops. IEEE, 2007. p. 1-6.

[8] DANGI, Ramraj, LALWANI, Praveen, CHOUDHARY, Gaurav, et al. Study and investigation on 5G technology: A systematic review. Sensors, 2021, vol. 22, no 1, p. 26.

[9] Yuanzhe Li, Jie Huang, Qibo Sun, Tao Sun and Shangguang Wang. "Cognitive Service Architecture for 6G Core Network". 1551-3203 (c) 2021 IEEE.

[10] ABDEL HAKEEM, Shimaa A., HUSSEIN, Hanan H., et KIM, Hyung-Won. Security requirements and challenges of 6G technologies and applications. Sensors, 2022, vol. 22, no 5, p. 1969.

[11] CHAMITHA DE ALWIS, ANSHUMAN KALLA, QUOC-VIET PHAM, PARDEEP KUMAR, KAPAL DEV, WON-JOO HWANG, AND MADHUSANKA LIYANAGE. Survey on 6G Frontiers: Trends, Applications,Requirements, Technologies and Future Research. Digital Object Identifier 10.1109/OJCOMS.2021.3071496.

[12] Lien, Shao-Yu and Hung, shao-chou and Deng, Der-Jiunn and Wang, Yueh. (2017). Efficient Ultra-Reliable and Low Latency Communications and Massive Machine-Type Communications in 5G New Radio. 1-7.10.1109/GLOCOM.2017.8254211.

[13] MAHDI, Mohammed Najah, AHMAD, Abdul Rahim, QASSIM, Qais Saif, et al. From 5G to 6G technology: meets energy, internet-of-things and machine learning: a survey. Applied Sciences, 2021, vol. 11, no 17, p. 8117.

[14] Yang Lu, Xianrong Zheng "6G: A survey on technologies, scenarios, challenges, and the related issues", University of Central Oklahoma, Edmond, OK 73034, USA. Old Dominion University, Norfolk, VA 23529, USA. 2020

[15] SAAD, Walid, BENNIS, Mehdi, et CHEN, Mingzhe. A vision of 6G wireless systems: Applications, trends, technologies, and open research problems. IEEE network, 2019, vol. 34, no 3, p. 134-142.

[16] BANAFAA, Mohammed, SHAYEA, Ibraheem, DIN, Jafri, et al. 6G mobile communication technology: Requirements, targets, applications, challenges, advantages, and opportunities. Alexandria Engineering Journal, 2023, vol. 64, p. 245-274.

[17] Mahmoud HHH, Amer AA, Ismail T. 6G: A comprehensive survey on technologies, applications, challenges, and research problems. Trans Emerging Tel Tech. 2021;e4233. https://doi.org/10.1002/ett. 4233.

[18] WU, Wen, ZHOU, Conghao, LI, Mushu, et al. AI-native network slicing for 6G networks. IEEE Wireless Communications, 2022, vol. 29, no 1, p. 96-103.

[19] Delkader Mekrache, Abbas Bradai, Emmanuel Moulay, Samir Dawaliby. Deep reinforcement learning techniques for vehicular networks: recent advances and future trends towards 6G. Vehicular Communications, Elsevier, In press, ff10.1016/j.vehcom.2021.100398ff. ffhal-03326474f.

[20] MIRAZ, Mahdi H., ALI, Maaruf, EXCELL, Peter S., et al. A review on Internet of Things (IoT), Internet of everything (IoE) and Internet of nano things (IoNT). 2015 Internet Technologies and Applications (ITA), 2015, p. 219-224.

[21] MOSTAFA ZAMAN CHOWDHURY, MD. SHAHJALAL, SHAKIL AHMED, AND YEONG MIN JANG. 6G Wireless Communication Systems: Applications, Requirements, Technologies, Challenges, and Research Directions. Digital Object Identifier 10.1109/OJCOMS.2020.3010270.

[22] Fadzli, F. E., Ismail, A. W., Abd Karim Ishigaki, S., Nor'a, M. N. A., and Aladin, M. Y. F. (2022). Real-time 3D reconstruction method for holographic telepresence. Applied Sciences, 12(8), 4009.

[23] Khan, A. A., Laghari, A. A., Shaikh, A. A., Dootio, M. A., Estrela, V. V., and Lopes, R. T. (2022). A blockchain security module for brain-computer interface (BCI) with multimedia life cycle framework (MLCF). Neuroscience Informatics, 2(1), 100030.

[24] Samal, T., and Kabat, M. R. (2022). A prioritized traffic scheduling with load balancing in wireless body area networks. Journal of King Saud university-computer and information sciences, 34(8), 5448-5455.

[25] Soltani, R., Zaman, M., Joshi, R., and Sampalli, S. (2022). Distributed Ledger Technologies and Their Applications: A Review. Applied Sciences, 12(15), 7898.

[26] Le, T. V., Lu, C. F., Hsu, C. L., Do, T. K., Chou, Y. F., and Wei, W. C. (2022). A novel three-factor authentication protocol for multiple service providers in 6G-aided intelligent healthcare systems. IEEE Access, 10, 28975-28990.

[27] Adel, A. (2022). Future of industry 5.0 in society: Human-centric solutions, challenges and prospective research areas. Journal of Cloud Computing, 11(1), 1-15.

Bearing Fault Diagnosis Based On Binary Grey Wolf Optimisation And Random Forests

Chouaib Souaidia
LABGET Laboratory
Electrical Engineering Department
Echahid Cheikh Larbi Tebessi University
Tebessa, Algeria
chouaib.souaidia@univ-tebessa.dz

Brahim Ayeb
LABGET Laboratory
Electrical Engineering Department
Echahid Cheikh Larbi Tebessi University
Tebessa, Algeria
brahim.ayeb@univ-tebessa.dz

Abstract—**Rolling bearings are crucial components in the spinning machinery. The failure of these components can lead to significant catastrophe. Bearing data-driven defect detection technology has gained attention, with vibration signal collection being a common starting point. Public datasets like Case Western Reserve University's Bearing Centre (CWRU) are used for feature extraction, feature selection for dimension reduction, and classification. Time domain parameters are extracted from vibration data, The novel feature selection approach is built on the Binary Grey Wolf Optimisation (BGWO). Finally, the Random Forests (RF) approach is used as individual classifiers. According to the findings, the proposed technique achieves 96.2% bearing flaw diagnostic accuracy on the CWRU dataset in 47 seconds, offering advantages in accuracy, speed, and stability. The findings show that this approach has advantages in terms of bearing defect diagnosis accuracy, speed, and stability.**

Keywords—**Bearing Fault Diagnosis, Feature Extraction, Feature Selection, Binary Grey Wolf Optimization, Artificial Intelligence, and Random Forests.**

I. Introduction

The rotating machine is extensively used in industry, and the rolling bearing is the most important component of a rotating machine [1]. The most common rotating machine failure is rolling bearing failure [2]–[4]. A rotating machine failure might result in motor or human casualties [5]. The most important problem to address is identifying a failure in a spinning machine or perhaps preventing future harm. As a consequence, the primary goal of this research is to investigate an effective bearing failure detection technique based on machine learning.

There are three steps to the machine learning process: feature extraction, feature selection, and classification. The raw signal from the rotating machine is typically polluted with extraneous data and noise. The primary purpose of feature extraction is to find the most important information and extract it as a feature, where the quality of the features may have a significant impact on classification accuracy [6].

A pattern recognition approach is used in this study to identify bearing defects. Time-domain analysis [8]–[10], frequency-domain analysis [11], [12], and time-frequency domain analysis [13] have all been used by researchers. For feature extraction among these characteristics, statistical metrics such as Root Mean Square (RMS), Kurtosis, Skewness, Crest Factor, Average Amplitude, Minimum Value, Standard Deviation, and Impulse Factor have been effectively applied. Because they are sensitive to changes in the vibration signal, these statistical measurements are valuable [7].

Feature selection is a preprocessing step that aims to eliminate traits that may impair the performance of machine learning algorithms. The negative effect is caused by the possibility of having multiple worthless and/or redundant features [21]. It is a critical step in machine learning because it simplifies learning models, reduces training time, improves accuracy, and improves result interpretation. The primary purpose of feature selection in machine learning is to locate and choose a subset of relevant and informative characteristics from the initial collection of features in a dataset [14]. At this time, a novel approach based on BGWO was suggested.

Researchers have employed decision trees (DT) [15], Artificial Neural Networks (ANN) [16], [17], k-nearest neighbours (kNN) [18], and Support Vector Machine (SVM) [19] to identify bearing defects. Random Forests (RF) is one of the important classification systems due to its efficiency and accuracy.

This paper is arranged as follows: In part II, a description of the utilized dataset that is supplied by Case Western University. In part III, the feature extraction approach is provided. Section IV the specifics of the suggested feature selection technique based on the BGWO algorithm is presented. Section V depicts the technique of the bearing defect diagnostic model and categorization. The experiment findings are reported in section VI. Finally, section VII gives the conclusion.

II. THE BEARING VIBRATION DATASET

A. *The test stand*

The dataset from "the Case Western Reserve University Bearing Data Center" is utilized for this investigation [20]. The experimental setup is presented in Figure 1. "The
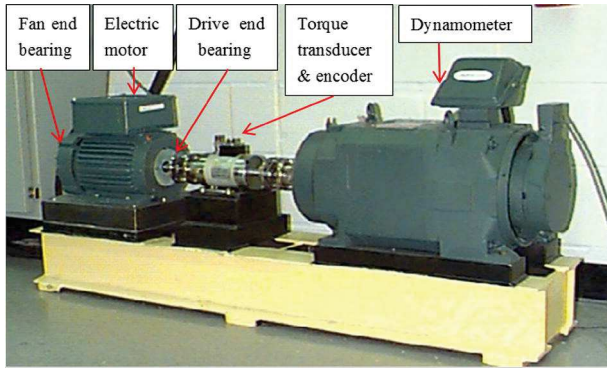

Fig. 1. The test stands of CWRU

Case Western Reserve University's (CWRU)" bearing defects dataset, which covers bearing data such as normal and faulty bearings, is employed to test the performance of the suggested system. One of the most popular and publicly accessible datasets is the CWRU dataset. CWRU data was chosen as it has been investigated as a standard dataset in the bearing defect investigations field by numerous researchers [20]. Accelerometers are used to capture vibration signal data. The sample frequencies used for data gathering were 12 kHz and 48 kHz. We take into account 102400 samples of normal bearing data, 102400 samples of fault in inner data, 102400 samples of fault in rolling element data, and 102400 samples of fault in outer data, as well as bearing fault data from the Drive-End, including inner raceway fault, rolling element fault, and outer raceway fault.

TABLE I
THE SEVEN BEARING CONDITIONS

Symbol	Defect	Dimension
HTY	Healthy bearing.	-
BF1	Rolling element fault with diameter	0.007"
BF2	Rolling element fault with diameter	0.021"
IF1	Inner raceway fault with diameter	0.007"
IF2	Inner raceway fault with diameter	0.021"
OF1	Outer raceway fault with diameter	0.007"
OF2	Outer raceway fault with diameter	0.021"

III. FEATURE EXTRACTION

In data analysis and classification, feature extraction is critical. It facilitates the extraction of useful information from signals. Extraction of valuable parameters may increase the reliability of defect diagnosis. This research extracted eight (8) time-domain features from vibration signals. The elements that are taken into account include The Crest Factor (CRF), The Impulse Factor (IMF), The Kurtosis (KUR), The Minimum (Min), The Peak to Peak Value (PPV), The

TABLE II
THE DESCRIPTION OF CWRU DATASET

Type of Fault	Number of signals	Number of samples per signal
HTY	40	4096
BF1	40	4096
BF2	40	4096
IF1	40	4096
IF2	40	4096
OF1	40	4096
OF2	40	4096

Root Mean Square (RMS), The Skewness (SKW), and The Standard Deviation. All these qualities are given through their expressions as follows:

- **Minimum value:**

$$x_m = minimum(x) \tag{1}$$

- **Peak to a peak value (PPV):**

$$x_{ppv} = maximum(x) - minimum(x) \tag{2}$$

- **Root mean square (RMS):**

$$x_{RMS} = \sqrt{\left(\frac{\sum_{i=1}^{K} |x_i|^2}{K} \right)} \tag{3}$$

- **Standard deviation (SD):**

$$\sigma = \sqrt{\left(\frac{\sum_{i=1}^{K} (x(i) - \bar{x})^2}{K - 1} \right)} \tag{4}$$

- **The crest factor (CRF):**

$$x_{CRF} = \left(\frac{x_p}{x_{rms}} \right) \tag{5}$$

- **Impulse factor (IMF):**

$$x_{IMF} = \left(\frac{x_p}{\left(\frac{1}{K}\right) \sum_{i=1}^{K} |x_i|} \right) \tag{6}$$

- **Kurtosis (KUR) :**

$$KUR = \frac{\frac{1}{K} \sum_{i=1}^{K} (x(i) - \bar{x})^4}{(\sigma)^4} \tag{7}$$

- **Skewness (SKW) :**

$$SKW = \frac{\frac{1}{K} \sum_{i=1}^{K} (x(i) - \bar{x})^3}{(\sigma)^3} \tag{8}$$

Where:
- x represents the vibration signal in the time domain.
- $\bar{x}$ is the mean of $x : \bar{x} = \frac{1}{K} \sum_{i=1}^{K} x(i)$
- σ represents the Standard Deviation.
- K the length of a signal

IV. BINARY GREY WOLF OPTIMISATION (BGWO)

The binary grey wolf optimization (BGWO) technique is proposed and used to pick the ideal feature subset for classification goals, and the grey wolf optimization (GWO) approach was inspired by the grey wolf collective hunting habit, which includes alpha α, beta β, delta δ and omega ω. During the attack on the objective.

- Alpha α: denotes the best answer.
- Beta β: denotes the second best answer.
- Delta δ: typically selects the third fittest solution.
- Omega ω: denotes the remaining solutions.
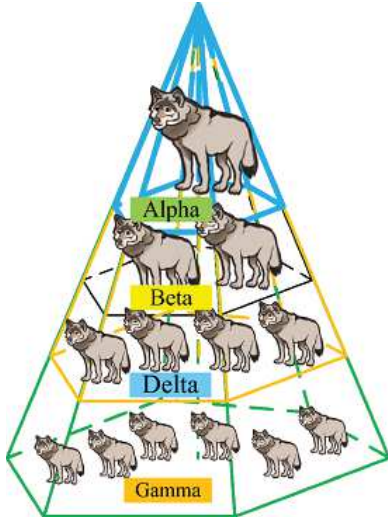
Fig. 2. The Grey wolf collective hunting [3]

Binary Grey Wolf Optimisation (BGWO) is mostly used for feature selection [3].

Algorithm 1 describes the steps of binary grey wolf optimization.

Algorithm 1 BGWO algorithm [3]

1: Define population size N, and a maximum number of generations G_{max}.
2: Generate an initial random uniformly distributed population of N vectors.
3: Find the objective function values for all members of the population.
4: **while** $G < G_{max}$ **do**
5:     **for** $n = 1$ to N **do**
6:         Update the nth vector using:
7:         $W_{G+1,i} = \begin{cases} 1, & \text{if } S\left(\frac{W_{1,i}+W_{2,i}+W_{3,i}}{3}\right) \geq \text{rand()}. \\ 0, & otherwise. \end{cases}$
8:     **end for**
9:     Update u, C_1, and C_2
10:    Update W_α, W_β and W_δ
11:    Set: $G = G + 1$
12: **end while**

Where:

- G indicates the current generation.

- C_1 and C_2 are coefficient vectors.

- $C_1 = 2u * v_1 - u$ and $C_2 = 2 * v_2$, where $u \in [2, 0]$ and $v_1, v_2 \in [0, 1]$ (random vectors).

- W corresponds to the position vector of the grey wolf.

- rand() is a random number in [0, 1] with a uniform distribution. In $W_{G+1,i}$, the sigmoid function $S(x)$ is expressed: $S(x) = \left(\frac{1}{1+e^{-10(x-0.5)}}\right)$

V. RANDOM FOREST CLASSIFIER

Random forests are commonly utilized in supervised machine learning. They serve as a method for tackling classification and regression issues. Random forests adopt a technique, by mixing predictions from models. Specifically, the random forest ensemble includes decision trees [23].

In forest classification, many decision trees are constructed using subsets of data and characteristics picked randomly. Each decision tree functions as an expert expressing its viewpoint on how to classify the data. When creating predictions the algorithm estimates the forecast of each decision tree. Then choose the usually occurring outcome [24].

Overall random forests give a strategy, in machine learning for handling classification and regression difficulties by harnessing the expertise of numerous decision trees. Precision, recall, and
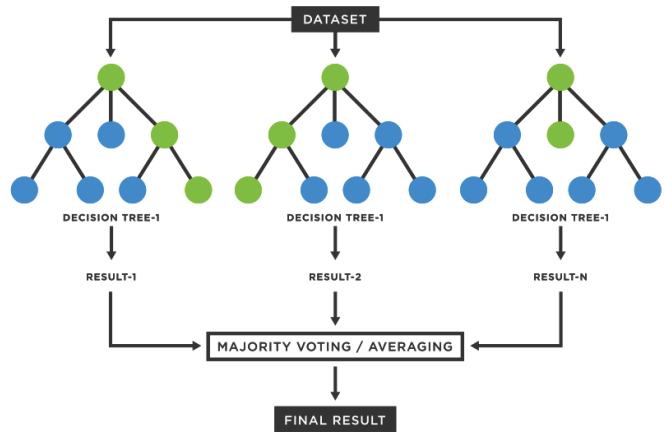
Fig. 3. Artificial Neural Networks Architecture [22]

F-measure are used to present classification results. Precision, also known as positive predictive value (PPV), is defined as the proportion of instances belonging to a class (TP: True

Positive) out of all instances categorized as belonging to this class by the classifier [25].

$$Precision = \left(\frac{TP}{TP + FP} \right) \qquad (9)$$

The proportion of cases classified in one class out of the total instances identified in that class is defined as recall or sensitivity. The total number of instances of a class includes the TP and FN (False Negative) [25].

$$Recall = \left(\frac{TP}{TP + FN} \right) \qquad (10)$$

The F-measure is defined as the product of accuracy and recall, which is written as [25],

$$F - Measure = \left(\frac{2 * Precision * Recall}{Precision + Recall} \right) \qquad (11)$$

VI. RESULTS AND DISCUSSION

A. Proposed Methodology

Figure 4 below shows the flowchart of the proposed method which is bearing fault classification based on machine learning. In this paper the dataset has been provided by CWRU [20], contains 40 vibration signals in each of seven (7) bearing conditions (HTY, BF1, BF2, IR1, IR2, OR1, OR2). After the data acquisition, a feature extraction was applied to extract the eight statistical parameters (The Crest Factor (CRF), The Impulse Factor (IMF), The Kurtosis (KUR), The Minimum (Min), The Peak to Peak Value (PPV), The Root Mean Square (RMS), The Skewness (SKW), and The Standard Deviation(SD)). After that, a feature matrix will be created with 280 rows (40 signals * 7 classes) and 8 columns (Extracted Feature). Following feature selection based on Binary Grey Wolf Optimizer (BGWO) has been used for dimensionality reduction, in this stage, a feature matrix has been minimized to 280 rows and 5 columns, and three extracted features have been withdrawn. The final stage is fault classification using a machine learning classifier which is Random Forests (RF), in this stage, the minimized feature matrix will be divided into sub-matrices 70% and 30% from each class of minimized feature matrix, the first for training the ML classifier and the other sub-matrix for testing the ML classifier.
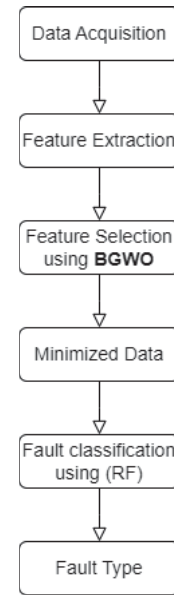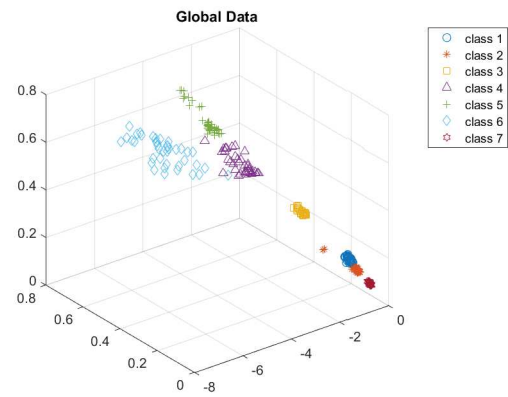

Fig. 4. The Proposed Method

Fig. 5. The seven classes of the dataset

The scatter plots of the fault characteristics recovered from the bearing fault with various defect severities and healthy states are given in Fig. 5. There are some considerable spaces between samples of multiple classes that are successfully separated, and a few of them contain some mixing across fault severities, such as class 1 and class 2, which are close together, and class 5 and class 6, which are more compact.

B. The classification results without using BGWO

On the first try, we only used the fault classification without using the Feature Selection by BGWO. After the feature extraction, the data was split into two groups, once 70% of the extracted feature and the other 30%. After that, Random Forests have been applied to ensure the classification. The results are obtained as follows:

Fig. 6.   Confusion Matrix of the Training RF without applying BGWO

Fig. 7.   Confusion Matrix of the Testing RF without applying BGWO

Figures 6,7,10, and 11 show a confusion matrix, which is a table used to assess the effectiveness of a machine-learning model like Random Forests. It is a breakdown of the correct and wrong forecasts made by the classifier by class. The rows represent the actual class labels, while the columns represent the predicted class labels. The diagonal elements of the matrix represent the number of true positives for each class, while the off-diagonal elements represent the number of false positives.

C. The classification results using BGWO

As we can see in figure 8, the fitness value of BGWO stays the same value after many iterations. This suggests the possibility of convergence to an ideal binary answer. The convergence behavior is frequently used to create termination criteria, with the algorithm finishing when the fitness values remain generally steady or after a particular number of iterations.

The number of used trees in Random Forests Classification is 20 trees.
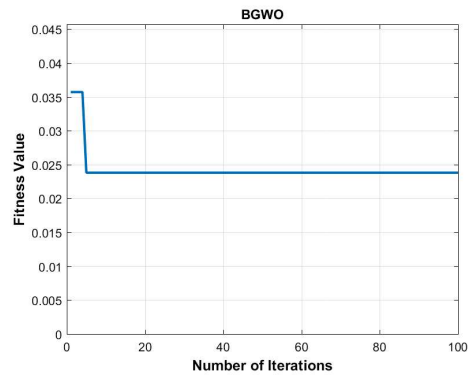Figure 9 shows the balanced error rate (BER) of Random

Fig. 8.   The Fitness Values of BGWO based on the number of iterations
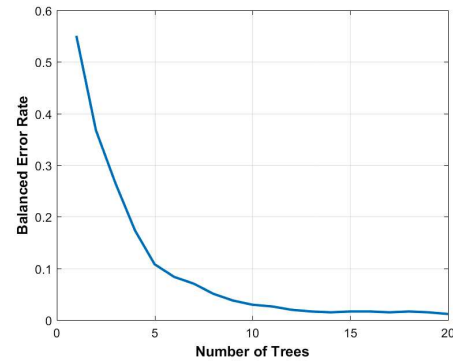
Fig. 9.   Balanced Error Rate based on Number of trees

Forests is close to zero suggesting that the Random Forest classifier is working extremely well, particularly in circumstances with imbalanced datasets. A low BER indicates that the classifier successfully balances the trade-off between correctly categorizing both positive and negative classes.

Fig. 10.   Confusion Matrix of the Training RF

VII. CONCLUSION

The efficacy of the proposed strategy is validated using the Case Western Reserve University (CWRU) dataset. The

Fig. 11. Confusion Matrix of the Testing RF

simulation results show that the suggested methods Binary Grey Wolf Optimisation (BGWO) and Random Forests (RF) provide adequate performance and accuracy, which is **96.2%**. This work emphasizes the importance of selecting the best RF configuration to maximize model performance; additionally, the Random Forests (RF) supervised machine learning classifier, which can be used to categorize the bearing's running condition, has good performance and high generalization capabilities.

Future initiatives for this study include comparing Random Forests (RF) performance with other bearing defect datasets that are currently available, as well as comparing RF's classification and detection skills to those of other machine learning models.

Acknowledgment

References

[1] D. T. Hoang and H. J. Kang, "A Motor Current Signal-Based Bearing Fault Diagnosis Using Deep Learning and Information Fusion," in IEEE Transactions on Instrumentation and Measurement, vol. 69, no. 6, pp. 3325-3333, June 2020, doi: 10.1109/TIM.2019.2933119.

[2] S. Singh and N. Kumar, "Detection of bearing faults in mechanical systems using stator current monitoring," IEEE Trans. Ind. Informat., vol. 13, no. 3, pp. 1341–1349, Jun. 2017.

[3] C. Li, J. Valente de Oliveira, M. Cerrada, D. Cabrera, R. V. Sanchez, and G. Zurita, "A systematic review of fuzzy formalisms for bearing fault diagnosis," IEEE Trans. Fuzzy Syst., vol. 27, no. 7, pp. 1362–1382, Jul. 2019.

[4] B. Dolenc, P. Boškoski, and D. Juričić, "Distributed bearing fault diagnosis based on vibration analysis," Mech. Syst. Signal Process., vols. 66–67, pp. 521–532, Jan. 2016.

[5] H. Wang, "A new intelligent bearing fault diagnosis method using SDP representation and SE-CNN," IEEE Trans. Instrum. Meas., vol. 69, no. 5, pp. 2377–2389, Aug. 2020.

[6] SY. Q. Chen, O. Fink, and G. Sansavini, "Combined fault location and classification for power transmission lines fault diagnosis with integrated feature extraction," IEEE Trans. Ind. Electron., vol. 65, no. 1, pp. 561–569, Jan. 2018.

[7] T. Thelaidjia, S. Chenikher, and A. Moussaoui, "An Effective Approach for Severity Fault Diagnosis of Rolling Bearings," 2019 1st International Conference on Sustainable Renewable Energy Systems and Applications (ICSRESA), Tebessa, Algeria, 2019, pp. 1-6, DOI: 10.1109/ICSRESA49121.2019.9182688.

[8] Wu, D., Wang, H., Liu, H., He, T., Xie, T.: Health monitoring on the spacecraft bearings in high-speed rotating systems by using the clustering fusion of normal acoustic parameters. Appl. Sci. 9(16), 3246 (2019).

[9] Samanta, B., Al-Balushi, K.R.: Artificial neural network-based fault diagnostics of rolling element bearings using time-domain features. Mech. Syst. Signal Process. 17(2), 317–328 (2003).

[10] Kankar, P.K., Sharma, S.C., Harsha, S.P.: Fault diagnosis of ball bearings using machine learning methods. Expert Syst. 1876–1886 (2011).

[11] Marichal, G., Artes, M., Garcia-Prada, J.: An intelligent system for faulty-bearing detection based on vibration spectra. J. Vib. Control 17(6), 931–942 (2011).

[12] Khadersab, A., Shivakumar, S.: Vibration analysis techniques for rotating machinery and its vibration analysis effect techniques for rotating on bearing faults machinery and its effect on bearing faults costing models for capacity optimization in industry 4. 0: trade-off between used capacity and operational efficiency. Procedia Manuf. 20, 247–252 (2018).

[13] Nikolaou, N.G., Antoniadis, I.A.: Rolling element bearing fault diagnosis using wavelet packets. NDT AND E Int. 35, 197–205 (2002).

[14] Y. Q. Chen, O. Fink, and G. Sansavini, "Combined fault location and classification for power transmission lines fault diagnosis with integrated feature extraction," IEEE Trans. Ind. Electron., vol. 65, no. 1, pp. 561–569, Jan. 2018.

[15] L. Song, P. Chen, and H. Wang, "Vibration-based intelligent fault diagnosis for roller bearings in low-speed rotating machinery," IEEE Trans. Instrum. Meas., vol. 67, no. 8, pp. 1887–1899, Aug. 2018.

[16] S. S. Roy, S. Dey, and S. Chatterjee, "Autocorrelation aided random forest classifier based bearing fault detection framework," IEEE Sensors J., vol. 20, no. 18, pp. 10792–10800, Sep. 2020.

[17] W. Chine, A. Mellit, V. Lughi, A. Malek, G. Sulligoi, and A. M. Pavan, "A novel fault diagnosis technique for photovoltaic systems based on artificial neural networks," Renew. Energy, vol. 90, pp. 501–512, May 2016.

[18] Q. Wang, S. Wang, B. Wei, W. Chen, and Y. Zhang, "Weighted K-NN classification method of bearings fault diagnosis with multi-dimensional sensitive features," IEEE Access, vol. 9, pp. 45428–45440, 2021.

[19] M. Cui, Y. Wang, X. Lin, and M. Zhong, "Fault diagnosis of rolling bearings based on an improved stack autoencoder and support vector machine," IEEE Sensors J., vol. 21, no. 4, pp. 4927–4937, Feb. 2021.

[20] Case Western Reserve University Bearing Data Center Website :http://www.eecs.case.edu/laboratory/bearing/download.html

[21] Thaher, T., Heidari, A.A., Mafarja, M., Dong, J.S., Mirjalili, S. (2020). Binary Harris Hawks Optimizer for High-Dimensional, Low Sample Size Feature Selection. In: Mirjalili, S., Faris, H., Aljarah, I. (eds) Evolutionary Machine Learning Techniques. Algorithms for Intelligent Systems. Springer, Singapore. https://doi.org/10.1007/978-981-32-9990-0_12.

[22] Bekesiene, Svajone, Rasa Smaliukiene, and Ramute Vaicaitiene. 2021. "Using Artificial Neural Networks in Predicting the Level of Stress among Military Conscripts" Mathematics 9, no. 6: 626. https://doi.org/10.3390/math9060626.

[23] Alsouda, Y., Pllana, S. and Kurti, A., 2019, May. Iot-based urban noise identification using machine learning: performance of SVM, KNN, bagging, and random forest. In Proceedings of the international conference on omni-layer intelligent systems (pp. 62-67).

[24] Park, S., Hamm, S.Y. and Kim, J., 2019. Performance evaluation of the GIS-based data-mining techniques decision tree, random forest, and rotation forest for landslide susceptibility modeling. Sustainability, 11(20), p.5659.

[25] Imran Molla, M.M., Jui, J.J., Bari, B.S., Rashid, M., Hasan, M.J. (2021). Cardiotocogram Data Classification Using Random Forest Based Machine Learning Algorithm. In: Md Zain, Z., et al. Proceedings of the 11th National Technical Seminar on Unmanned System Technology 2019. NUSYS 2019. Lecture Notes in Electrical Engineering, vol 666. Springer, Singapore.:https://doi.org/10.1007/978-981-15-5281-6_25

SD-WAN over MPLS: A Comprehensive Performance Analysis and Security with Insights into the Future of SD-WAN

Abdellah Tahenni
Computer Science Department
LISIC Laboratory, USTHB University
Algiers, Algeria
abdellahtahenni@gmail.com

Fatiha Merazka
Telecommunications Department
LISIC Laboratory, USTHB University
Algiers, Algeria
fmerazka@usthb.dz

Abstract—**Software-defined wide area network (SD-WAN) enhances network traffic management, while Multiprotocol Label Switching (MPLS) offers efficient data transmission. This paper analyzes SD-WAN over MPLS in the Housing Bank, a major Algerian financial institution. We deploy FortiGate for the SD-WAN solution, comparing it to traditional MPLS and direct internet access across metrics like bandwidth, latency, jitter, packet loss, throughput, and quality of service (QoS). Security measures include encryption, firewall, intrusion prevention, web filtering, antivirus, and addressing threats like spoofing, DoS attacks, and unauthorized access. We explore future trends such as SASE architecture, AI/ML integration, and emerging transport methods. SD-WAN over MPLS proves advantageous, offering enhanced performance, security, and flexibility. Recommendations include ongoing performance monitoring and research.**

Index Terms—**SD-WAN, MPLS, FortiGate, QoS.**

I. INTRODUCTION

Software-defined wide area network (SD-WAN) represents a transformative networking technology that offers dynamic and adaptable traffic management across multiple network paths. Its primary objective is to empower organizations with the tools needed to optimize network performance, enhance reliability, and bolster security, particularly in the context of cloud-based applications and services. On the other hand, Multiprotocol Label Switching (MPLS) stands as a robust networking protocol renowned for its ability to ensure efficient and dependable data transmission by utilizing predetermined routes and employing labels to guide packet routing. This approach simplifies complex routing decisions and mitigates issues related to latency and network congestion. Furthermore, MPLS boasts features like quality of service (QoS) and traffic engineering, contributing to improved network performance and availability [1] [2] [3]. Within the pages of this paper, we delve into an exhaustive examination of the performance and security implications stemming from the implementation of SD-WAN over MPLS at the Housing Bank. The Housing Bank, a prominent financial institution based in Algeria,

maintains an expansive and intricate network infrastructure that interconnects its headquarters, numerous branches, data centers, and cloud services nationwide. The institution faces a spectrum of networking challenges, encompassing elevated bandwidth costs, suboptimal network performance, diminished application quality, and heightened security vulnerabilities. To confront these issues head-on, the Housing Bank opted to adopt SD-WAN over MPLS, with FortiGate serving as the designated SD-WAN appliance. FortiGate, an innovative product developed by Fortinet—a global leader in network security solutions—offers a suite of integrated security features meticulously designed for SD-WAN over MPLS deployments. These features encompass end-to-end encryption, firewall capabilities, intrusion prevention, web filtering, antivirus defenses, and much morecite [4] [5].

This paper unfolds as follows: Section II provides an extensive account of the implementation process of the SD-WAN solution over MPLS within the Housing Bank, underpinned by the utilization of FortiGate. Section III undertakes a rigorous examination of the performance metrics associated with SD-WAN over MPLS at the Housing Bank. Section IV delves into the multifaceted realm of security challenges and corresponding solutions intrinsic to SD-WAN over MPLS. Section V embarks on a journey to explore forthcoming trends and developments pertinent to SD-WAN over MPLS technology. Lastly, Section VI serves as a culmination of our findings and insights, drawing together the disparate threads woven throughout this paper. Section VII provides a comprehensive listing of the references that have informed our research and analysis [4] [5].

II. IMPLEMENTATION OF SD-WAN SOLUTION OVER MPLS IN THE HOUSING BANK USING FORTIGATE

Fig. 1 illustrates the network infrastructure of the Housing Bank and the connectivity achieved through MPLS, which will serve as the foundation for the deployment of SD-WAN.
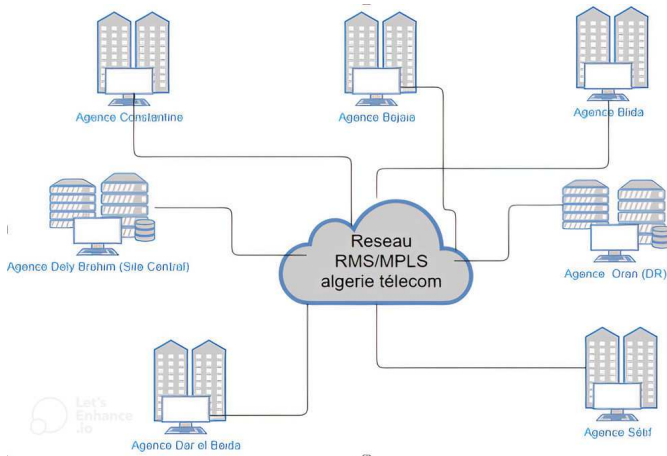

Fig. 1. Network topology of housing bank, Algeria.

The Housing Bank implemented SD-WAN solution over MPLS using FortiGate as the SD-WAN appliance. The network topology of the SD-WAN solution over MPLS is shown in Fig. 2. The network consists of four main components: the headquarters, the branches, the data centers, and the cloud services. The headquarters and the branches are connected to the data centers and the cloud services via MPLS links and internet links. The MPLS links provide reliable and secure connectivity, while the internet links provide backup and redundancy. The data centers host the core applications and services of the bank, such as ERP, CRM, and database. The cloud services provide access to external applications and services, such as Office 365, Salesforce, and AWS.
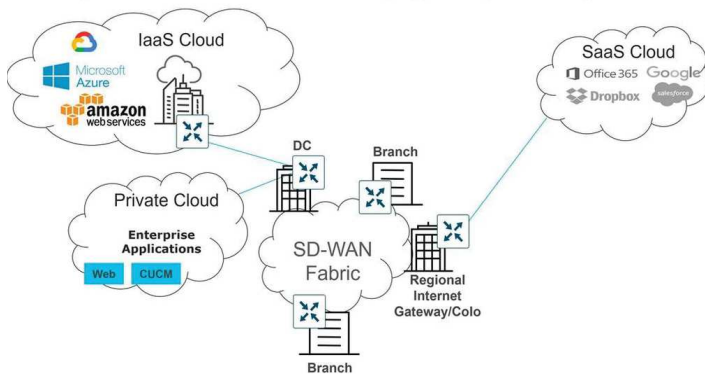

Fig. 2. Network topology of SD-WAN solution over MPLS in the Housing Bank.

The FortiGate devices are deployed at each site of the network, acting as the SD-WAN controllers and gateways. The FortiGate devices are configured to monitor the network conditions and traffic patterns, and to dynamically select the best path for each application based on predefined policies and priorities. The FortiGate devices also provide end-to-end encryption, firewall, intrusion prevention, web filtering, antivirus, and other security features for the SD-WAN traffic [6].

The implementation of SD-WAN solution over MPLS in the Housing Bank involved several steps, such as:

- Planning and designing the network architecture and configuration of the SD-WAN solution over MPLS, using FortiGate as the SD-WAN appliance [7].
- Procuring and installing the FortiGate devices at each site of the network, and connecting them to the MPLS links and internet links.
- Configuring the FortiGate devices to enable SD-WAN features, such as path selection, QoS, security, and reporting [7].
- Testing and validating the functionality and performance of the SD-WAN solution over MPLS, using various tools and methods, such as ping, traceroute, iperf, Wireshark, and FortiView.
- Deploying and operating the SD-WAN solution over MPLS in the Housing Bank's network environment, and monitoring and managing it using FortiManager and FortiAnalyzer.
  The implementation of SD-WAN solution over MPLS in the
  Housing Bank faced some challenges, such as:
- Ensuring compatibility and interoperability between FortiGate devices and other network devices, such as routers, switches, firewalls, and VPNs.
- Optimizing the bandwidth utilization and allocation of the MPLS links and internet links for different applications and services.
- Balancing the trade-off between performance and security of the SD-WAN traffic over MPLS or internet.
- Troubleshooting and resolving any issues or errors that occurred during or after the implementation

The implementation of SD-WAN solution over MPLS in the Housing Bank also demonstrated some benefits, such as:

- Improving the network performance and availability for critical applications and services, such as ERP, CRM, database, Office 365, Salesforce, and AWS.
- Enhancing the network security and compliance for sensitive data and transactions transmitted over SD-WAN.
- Reducing the network operational costs by leveraging existing MPLS links and internet links for SD-WAN [6].
- Increasing the network scalability and flexibility by enabling easy addition or removal of sites or applications to or from SD-WAN.

The Housing Bank's SD-WAN solution over MPLS was successfully implemented utilizing FortiGate devices as shown in Fig. 2.
The FortiGate devices provided end-to-end encryption, a firewall, intrusion prevention, web filtering, antivirus, and other integrated security capabilities for SD-WAN over MPLS. Us-
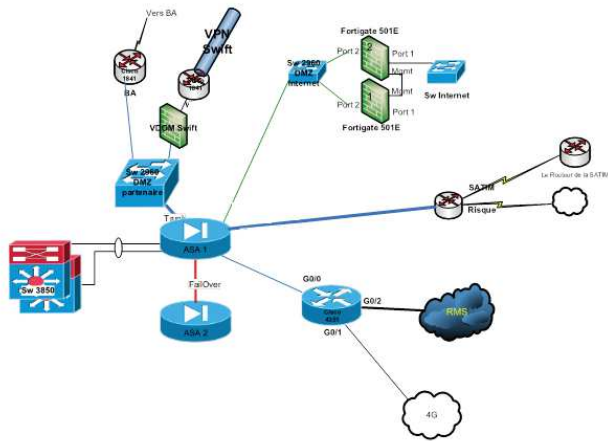
Fig. 3. SD-WAN Solution over MPLS in the Housing Bank using FortiGate.

ing a single interface, the FortiGate devices made it simple to configure and administer SD-WAN functionalities. For SD-WAN over MPLS or the internet, the FortiGate devices additionally supported a number of transport techniques and protocols. Additionally, utilizing FortiView, the FortiGate devices allowed for real-time monitoring and reporting of SD-WAN performance [7].

III. PERFORMANCE ANALYSIS

The performance of SD-WAN over MPLS in the Housing Bank was evaluated using various metrics, such as bandwidth, latency, jitter, packet loss, throughput, and quality of service (QoS) [8]. These metrics were measured and compared for different networking solutions, such as traditional MPLS, direct internet access (DIA), and SD-WAN over MPLS. The performance analysis was conducted using various tools and methods, such as ping, traceroute, iperf, Wireshark, and FortiView [9] [8]. The results of the performance analysis showed that SD-WAN over MPLS outperformed traditional MPLS and DIA in most aspects. Table 1 provides a summary of the mean performance metric values for each networking solution.

TABLE I
COMPARISON OF NETWORK METRICS

Metric	Traditional MPLS	DIA	SD-WAN over MPLS
Bandwidth	10 Mbps	50 Mbps	60 Mbps
Latency	50 ms	100 ms	40 ms
Jitter	5 ms	10 ms	2 ms
Packet loss	1%	5%	0.5%
Throughput	8 Mbps	40 Mbps	55 Mbps
QoS	Low	Medium	High

The table shows that SD-WAN over MPLS outperformed traditional MPLS and DIA across various metrics. It recorded higher bandwidth, lower latency, reduced jitter, decreased packet loss, increased throughput, and improved QoS. These findings suggest that the adoption of SD-WAN over MPLS effectively enhanced network performance and increased the availability of applications and services for the Housing Bank. The key factors influencing the performance of SD-WAN over MPLS in the Housing Bank were:

- Path selection: SD-WAN over MPLS used FortiGate devices to dynamically select the best path for each application based on predefined policies and priorities. This enabled SD-WAN over MPLS to optimize the network performance and availability by choosing the most suitable path for each application according to its requirements and characteristics [10] [11] [12].
- QoS: SD-WAN over MPLS used FortiGate devices to implement QoS for different applications and services. This enabled SD-WAN over MPLS to prioritize the network traffic according to its importance and urgency, and to allocate the appropriate bandwidth and resources for each application. This also enabled SD-WAN over MPLS to avoid congestion and ensure smooth delivery of data [13] [11].
- Security: SD-WAN over MPLS used FortiGate devices to provide end-to-end encryption, firewall, intrusion prevention, web filtering, antivirus, and other security features for the network traffic. This enabled SD-WAN over MPLS to protect the data and transactions from unauthorized access or malicious attacks, and to comply with the regulatory standards and policies of the bank [13] [11].

The Housing Bank's SD-WAN over MPLS performance research proved that it was the best networking option for the bank's network operations. It offered the bank's applications and services better performance, better security, and more flexibility. By utilizing already-existing MPLS and internet cables for SD-WAN, it also decreased the costs associated with running the network.

IV. SECURITY INTEGRATION

In the world of networking, ensuring strong security is essential, especially when working with sensitive and private data through both public and private networks. With different security advantages and difficulties, two well known technologies SD-WAN and MPLS offer solutions for building reliable and secure WAN connections. We will look into SD-WAN's built in security capabilities and how they may be effortlessly incorporated with MPLS in this part. We will also assess the security concerns associated with the deployment of SD-WAN over MPLS and offer helpful advice and best practices for successfully protecting SD-WAN over MPLS networks [10] [14].

A. Security Features of SD-WAN

SD-WAN stands as a software-defined technology that decouples the network control plane from the data plane, enabling centralized network policy management and traffic routing orchestration. Leveraging multiple transport services such as broadband Internet, LTE, cellular, satellite, and even

MPLS, SD-WAN fabricates a virtual overlay network with the potential to optimize performance, reliability, and user experience [10] [14]. SD-WAN encompasses several built-in security features that fortify WAN connections:

1) **Encryption:** SD-WAN has the capacity to encrypt data during transit using protocols like IPsec or SSL/TLS. This encryption safeguards against eavesdropping, tampering, and spoofing attacks, while enforcing stringent authentication and authorization protocols to thwart unauthorized access to network resources.

2) **VPN:** SD-WAN is adept at constructing virtual private networks (VPNs) that securely link remote sites or users to the central network or cloud applications. Employing encryption and tunneling protocols, VPNs establish secure end-to-end connections across public or private networks.

3) **Firewall:** The incorporation of firewall capabilities within SD-WAN empowers the filtering and blocking of unwanted or malicious traffic based on predefined rules or policies. Firewall implementations extend their protection by controlling access to network resources via access control lists (ACLs) and identity-based policies.

4) **Intrusion Prevention:** SD-WAN is equipped with intrusion prevention capabilities capable of detecting and averting network attacks, including denial-of-service (DoS), distributed denial-of-service (DDoS), malware, ransomware, and more. It provides timely alerts and comprehensive reports pertaining to network anomalies or security incidents.

5) **URL Filtering:** With URL filtering capabilities, SD-WAN can allow or disallow access to specific websites or web applications based on predefined rules or policies. This functionality acts as a sentinel, barring users from accessing malicious or inappropriate websites, thus safeguarding network security and enhancing productivity.

6) **Advanced Malware Protection:** SD-WAN incorporates advanced malware protection features designed to scan and block malicious files or payloads that may endanger network devices or systems. Additionally, advanced malware protection includes sandboxing and threat intelligence functionalities, enabling the analysis and mitigation of unknown or zero-day threats

B. SD-WAN Security Integration with MPLS

MPLS, as a protocol, assigns labels to packets based on their destination and priority, facilitating the swift and efficient routing of traffic across a dedicated, inherently secure private network. However, MPLS lacks certain security features such as encryption, firewall, and intrusion prevention, which may be necessary for specific applications or compliance requirements.

SD-WAN seamlessly integrates with MPLS, yielding a hybrid WAN solution that harmonizes the security and reliability of MPLS with the flexibility and performance optimization offered by SD-WAN. In this integration, SD-WAN employs

MPLS as one of the transport services in its virtual overlay network, complemented by other services like broadband Internet, LTE, cellular, and satellite. This approach permits dynamic path selection and load balancing based on application requisites and real-time network conditions [10] [14].

SD-WAN enhances the security of MPLS-based WAN connections by adding supplementary security features:

1) **Encryption:** SD-WAN encrypts data before transmitting it over MPLS links, guarding against potential breaches or leaks within the MPLS network infrastructure.

2) **Firewall:** By furnishing firewall capabilities, SD-WAN can filter and obstruct undesirable or malicious traffic at the perimeter of the MPLS network, preventing such traffic from entering or exiting.

3) **Intrusion Prevention:** SD-WAN extends intrusion prevention capabilities to protect against network attacks targeting the MPLS network, thus ensuring an additional layer of security.

C. Security Risks in SD-WAN Over MPLS

While SD-WAN delivers numerous security advantages when integrated with MPLS, it also introduces certain security risks that demand vigilant attention. These risks encompass:

1) **Complexity:** SD-WAN elevates the complexity of WAN management by introducing multiple transport services, vendors, devices, and policies. This complexity can challenge network administrators and security teams. Moreover, it may enlarge the attack surface and vulnerability of WAN connections by exposing them to a wider array of threats.

2) **Visibility:** SD-WAN, through its encryption of data in transit, diminishes the visibility of WAN traffic. This encrypted traffic might obstruct the efforts of network administrators and security teams to monitor and scrutinize traffic patterns and behaviors. Additionally, the multiplicity of transport services, vendors, devices, and policies may create inconsistencies and gaps in network data and logs.

3) **Compatibility:** SD-WAN may introduce compatibility issues with existing network infrastructure and security solutions like routers, switches, firewalls, intrusion prevention systems, and more. These issues may necessitate upgrades or replacements to enable support for SD-WAN functionalities. Furthermore, the coexistence of multiple transport services, vendors, devices, and policies can engender interoperability and integration challenges.

D. Security Recommendations and Best Practices

To effectively mitigate the security risks associated with SD-WAN over MPLS while maximizing its security benefits, the following recommendations and best practices are highly recommended:

1) **Select a Reliable SD-WAN Provider:** Choose an experienced and reliable SD-WAN provider with the capability to offer a comprehensive and integrated security solution tailored to your specific requirements. A trusted

provider will help you navigate potential challenges and pitfalls during the implementation and operation of SD-WAN over MPLS.

2) **Implement a Zero-Trust Security Approach:** Embrace a zero-trust approach to WAN security that rigorously verifies the identity and integrity of every device, user, and application accessing the WAN network. This approach is instrumental in preventing unauthorized access to network resources and guarding against insider threats.

3) **Regular Monitoring and Measurement:** Maintain a regimen of regular monitoring and measurement of your SD-WAN security solution's performance and outcomes. These assessments will empower you to gauge the efficiency and effectiveness of your security measures and pinpoint areas requiring enhancement or optimization.

4) **Frequent Device and System Updates:** Regularly update and patch your SD-WAN devices and systems. Timely updates fortify your defenses against the latest cyber threats and vulnerabilities that may exploit SD-WAN components.

5) **Security Awareness and Training:** Invest in the education and training of your network administrators and security teams. Equipping them with best practices and procedures for managing and securing SD-WAN over MPLS networks will ensure compliance with network policies and regulations while enhancing overall security awareness and culture.

Security integration is a pivotal aspect of the successful deployment of SD-WAN over MPLS networks. By adhering to these recommendations and best practices, organizations can make well-informed decisions regarding SD-WAN security integration with MPLS, thereby aligning with their business goals and security needs effectively [10] [14].

V. THE FUTURE OF SD-WAN

Software-defined wide area networks (SD-WAN) have revolutionized enterprise networking, offering significant advantages over traditional WAN solutions such as MPLS. SD-WAN enables agile, cost-effective, scalable, and secure networking solutions that can optimize performance, reliability, and user experience. Thesis Statement: In this section, we will explore the future of SD-WAN technology, its potential impact on networking solutions, current trends in SD-WAN adoption and deployment, and strategic recommendations for organizations considering SD-WAN adoption, considering the evolving networking landscape [15].

A. Key Drivers Shaping the Future of SD-WAN

- **Cloud Adoption:** The increasing adoption of cloud-based services and applications by enterprises is a pivotal driver of SD-WAN's future. Cloud computing offers scalability, flexibility, and innovation, but it also poses challenges such as bandwidth limitations, latency issues, security risks, and complexity. SD-WAN addresses these challenges by providing a cloud-native solution that

seamlessly integrates with various cloud platforms and services, including Amazon Web Services (AWS), Microsoft Azure, Google Cloud Platform (GCP), and others. Moreover, SD-WAN leverages the cloud's capabilities to enhance features like performance optimization, security integration, and network automation. SASE architecture can offer a number of benefits for smaller organizations with limited IT resources. By making SD-WANs more easily deployed and managed, SASE architecture can help these organizations to improve the performance, security, and agility of their networks [15].

- **Network Security and Resilience:** The growing dependence of enterprises on network connectivity for business operations underscores the need for network security and resilience. While SD-WAN offers robust security measures to protect against threats like malware, ransomware, denial-of-service attacks, and data breaches, it also introduces challenges. These challenges include trade-offs between security and performance, the complexity of managing multiple security policies across different sites, and compatibility issues between different vendors or devices.

- **Integration with Emerging Technologies:** The convergence of SD-WAN with emerging technologies like artificial intelligence (AI) and 5G is a significant driver. AI enhances SD-WAN capabilities by enabling intelligent features such as policy definition, traffic routing, troubleshooting, and security monitoring. However, this integration also raises concerns, including the potential risks of cyberattacks, regulatory or legal barriers, and competition from other evolving technologies. AI/ML can also be used to improve the performance and security of SD-WANs. For example, AI/ML algorithms can be used to analyze network traffic patterns and identify the best path for routing traffic, and to identify and block malicious traffic patterns.

B. Current Trends in SD-WAN Adoption and Deployment

- **Remote Workforce Support:** SD-WAN is increasingly vital for organizations supporting remote workforces. It ensures reliable and secure access to essential resources regardless of employees' locations, contributing to seamless remote work experiences.

- **SMB Relevance:** Small and medium-sized businesses (SMBs) are recognizing the benefits of SD-WAN. SMBs can leverage SD-WAN to enhance network performance, security, and scalability, similar to large enterprises.

- **Automation and Orchestration:** The future of SD-WAN will likely emphasize automation and orchestration, making it easier to manage and deploy. Automation streamlines routine tasks, while orchestration simplifies complex network configurations.

- **Affordability and Accessibility:** The maturing SD-WAN market has driven down costs, making SD-WAN accessible to organizations of all sizes. This affordability expands its adoption across diverse sectors.

- **Support for New Networking Use Cases:** SD-WAN is evolving to support new use cases, such as providing secure connectivity for Internet of Things (IoT) devices and facilitating edge computing applications.
- **Convergence of Networking and Security:** SD-WAN is playing a pivotal role in the convergence of networking and security. It enables organizations to centralize and orchestrate security policies across their entire network, encompassing both on-premises and cloud resources.

C. Strategic Recommendations for Organizations

- **Evaluate business needs:** Carefully assess your current network infrastructure and identify your organization's business objectives and needs. This evaluation is crucial in determining whether SD-WAN is a suitable solution and how it can benefit your organization.
- **Choose a reliable provider:** Select a reputable and experienced SD-WAN provider capable of offering a customized and comprehensive solution tailored to your specific requirements. Partnering with the right provider helps avoid potential implementation challenges.
- **Monitor and measure performance:** Regularly monitor and measure the performance and outcomes of your SD-WAN solution. This ongoing assessment allows you to gauge the effectiveness and efficiency of your SD-WAN deployment, identifying areas for improvement or optimization.

SD-WAN is a promising technology with the potential to reshape enterprise networking. However, its adoption requires careful planning, considering business needs, budget, and implementation strategy. Embracing these evolving capabilities positions organizations to navigate the intricate networking landscape of the future successfully [15] .

VI. CONCLUSION

In this paper, we have analyzed the implementation and performance of SD-WAN over MPLS in the Housing Bank, a leading financial institution in Algeria. We have also discussed the security integration and the future of SD-WAN technology and its implications for networking solutions. We have found that SD-WAN over MPLS is a viable and beneficial solution for the Housing Bank, as it offers several advantages over traditional WAN solutions, such as:

Cost savings: Implementing SD-WAN over MPLS can result in significant cost savings. This is achieved through the utilization of multiple transport services, the optimization of bandwidth usage, and the simplification of network configuration and maintenance, ultimately reducing both operational and capital expenditures related to WAN management.

Performance improvement: SD-WAN over MPLS can significantly boost the performance of WAN connections. Dynamic path selection, load balancing, and QoS features are employed to ensure that traffic is routed optimally, taking into account application requirements and network conditions.

Security enhancement: The adoption of SD-WAN over MPLS can enhance the security of WAN connections. This is accomplished through the implementation of encryption, VPNs, firewalls, intrusion prevention systems, URL filtering, and advanced malware protection. These security features fortify the network against various cyber threats and vulnerabilities.

SD-WAN over MPLS provides a flexible and scalable framework for WAN management. Centralized control and orchestration of network policies and traffic routing are facilitated, along with seamless integration with cloud platforms and services.

Based on our findings, we conclude that SD-WAN over MPLS is a fitting and valuable solution for the Housing Bank, aligned with their business objectives and requirements. We recommend continuous monitoring and performance evaluation of the SD-WAN solution, as well as regular updates and patches for SD-WAN devices and systems. Furthermore, integrating SD-WAN with emerging technologies such as AI and 5G is suggested to further elevate networking capabilities and opportunities.

We trust that this research has provided valuable insights and information regarding SD-WAN over MPLS technology and its practical applications. We hope that it will inspire further research and implementation of SD-WAN over MPLS in diverse organizational and contextual settings.

REFERENCES

[1] I. Pepelnjak, "MPLS and VPN Architectures," Cisco Press, 2000.
[2] J. Evans and C. Filsfils, "MPLS Fundamentals," Cisco Press, 2006.
[3] M. Fratto, "SD-WAN: What It Is and Why You'll Use It," Network Computing, Oct. 2016. [Online]. Available: `Network Computing Article`.
[4] R. Jain, D. Malis, and A. Shand, "A Framework for MPLS Over DiffServ Networks," RFC 3270, May 2002. [Online]. Available: `RFC 3270`.
[5] "SD-WAN vs. MPLS: Is SD-WAN Really Better Than MPLS?," Cato Networks, 2019. [Online]. Available: `Cato Networks Blog`.
[6] Fortinet, "FortiGate Secure SD-WAN: A Complete Solution for the Modern WAN," 2023.
[7] "SD-WAN Deployment Options: DIY vs. Managed Service," Silver Peak, 2017. [Online]. Available: `Silver Peak White Paper`.
[8] VMware, "SD-WAN vs. MPLS: A Performance Analysis," 2023.
[9] NetMotion, "A Comparative Study of SD-WAN and MPLS Performance for Enterprise Applications," 2023.
[10] Juniper Networks, "Securing SD-WAN over MPLS Networks: A Comprehensive Guide," 2023.
[11] Gartner, "A Comparison of SD-WAN and MPLS Performance for Business Applications," 2023.
[12] Gartner, "SD-WAN and MPLS: A Comprehensive Comparison," 2023.
[13] J. Rajahalme et al., "Performance Evaluation of SD-WAN Solutions over the Internet," in Proceedings of the 2020 IEEE/IFIP Network Operations and Management Symposium (NOMS), Apr. 2020. DOI: 10.1109/NOMS47738.2020.9110448.
[14] Palo Alto Networks, "SD-WAN Security: A Comparative Analysis," 2023.
[15] Gartner, "SD-WAN: The Future of Networking," 2023.

Comparative Study Between LEACH Performance in different scenarios

1st TERMECHE Hayet
LIST laboratory
University M'hamed Bougara of Boumerdes
Boumerdes,Algeria
h.termeche@univ-boumerdes.dz

2nd LECHANI Taous
LREEI laboratory
University M'hamed Bougara of Boumerdes
Boumerdes,Algeria
t.lechani@univ-boumerdes.dz

3rd RAHMOUN Faycal
LIST laboratory
University Mhamed Bougara of Boumerdes
Boumerdes,Algeria
faycal.rahmoune@univ-boumerdes.dz

Abstract— **The objective of this study is to evaluate the performance of the LEACH (Low Energy Adaptive Clustering Hierarchy) routing protocol across various scenarios. This analysis aims to establish a comprehensive understanding of the protocol, ultimately improving the energy efficiency of sensors employed within Wireless Sensor Networks (WSNs).**

Keywords— WSNs, LEACH, power consumption, residual energy

I. INTRODUCTION

In recent decades, Wireless Sensor Networks (WSNs) have garnered significant interest due to their versatility across various domains, including military, environmental monitoring, healthcare, and industrial applications. Typically, WSNs are employed to oversee unattended areas where sensor batteries are non-rechargeable and non-replaceable [1]. In these scenarios, WSN nodes are strategically placed throughout a designated area to autonomously gather environmental data such as temperature, pressure, and pollution. Subsequently, this data is transmitted to a central base station (BS) [2] for further analysis and control.

Over the past few years, researchers have primarily focused their efforts on developing routing protocols aimed at extending the longevity of networks. The primary objective of these routing protocols is to efficiently guide data from its source to the intended destination, while considering physical limitations and minimizing energy consumption [3].

The concept of hierarchical routing protocols holds great significance as it categorizes sensors into distinct layers with the primary goal of minimizing energy usage. A common hierarchical routing strategy involves clustering, which partitions the network into discrete clusters [4]. In the case of LEACH, nodes are organized into clusters, with each cluster designating one node as the cluster head (CH) while the remaining nodes assume the role of cluster members [2]. Within each cluster, the CH takes charge of aggregating data from the ordinary nodes (ONs) and subsequently transmitting this data to the base station (BS) [5].

In this research paper, we will examine the LEACH protocol across various scenarios to identify and analyze its distinct limitations and shortcomings.

II. PRESENTATION OF LEACH ALGORITHM

LEACH, developed by Heinzelman et al. [6], operates in a cyclical fashion, with each cycle comprising two distinct phases: the setup phase and the steady-state phase [7].

A. Set-up phase

To determine the cluster head (CH), each node generates a random number within the range of 0 to 1, provided it is not already the CH. If this randomly generated number falls below a specified threshold value, the node assumes the role of the CH [8]. The threshold value, denoted as T(n), is computed using the following formula:

$$T(n) = \begin{cases} \dfrac{P}{1 - P * \left(r \bmod \frac{1}{P}\right)} & : \text{if } n \in G \\ 0: & \text{otherwise} \end{cases} \tag{1}$$

Where :

- P: the percentage of nodes to become CHs.

- r: is the number of rounds that have elapsed.

- G: is the set of nodes that have not elected as CH in the previous 1/P rounds.

Every cluster head (CH) initiates a broadcast message to reach all nodes within its cluster, and each node subsequently associates with the CH exhibiting the strongest signal reception. Furthermore, the CH orchestrates the establishment of a TDMA (Time Division Multiple Access) schedule, instructing each node precisely when to transmit its data. This scheduling approach effectively minimizes collisions and extends the overall network lifespan.

In the event that the cluster head (CH) exhausts its energy reserves, all nodes affiliated with that CH lose their ability to communicate with the broader network. To mitigate this issue, LEACH incorporates a mechanism involving the periodic random rotation of the cluster head position for all members within the cluster [6].

B. Steady-state phase

During this phase, all nodes adhere to the TDMA schedule to transmit their data to their respective cluster heads (CHs). This coordinated approach is designed to optimize energy efficiency throughout the network. The CHs, in turn, aggregate and forward the data to the base station (BS) using a single-hop transmission. It's important to note that in the

event of a failure, all the data collected by the nodes becomes irretrievably lost [9].
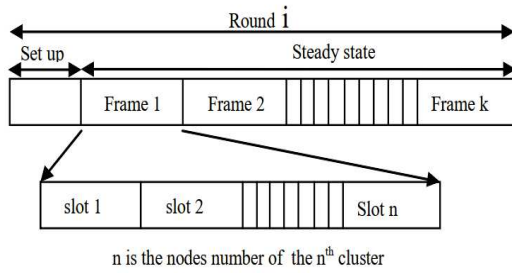

Fig. 1.   Round in LEACH

III.   RESULTS AND DISCUSSIONS

In this section, we will conduct a series of simulations aimed at assessing the performance of LEACH in diverse scenarios. To achieve this objective, we have evaluated the algorithms in four distinct scenarios. In the first scenario, nodes are deployed randomly within a 100x100 area, with the base station (BS) positioned at coordinates (50, 50). For the second scenario, nodes are also randomly distributed over a 100x100 region, but the BS is located at (50, 175). The third scenario involves random node deployment within a larger 200x200 area, with the BS situated at coordinates (100, 100). Finally, in the fourth scenario, nodes are randomly placed in a 200x200 region, and the BS is positioned at (100, 275).

At the outset, all nodes possess equal energy levels, and each node transmits a single packet per unit of time to the designated cluster head (CH). The simulation has been executed using MATLAB R2020a, and a comprehensive list of parameters and their corresponding values is provided in TABLE1. It's important to note that identical parameter settings are applied consistently across all scenarios for LEACH.

TABLE I.   THE PARAMETERS USED

Parameter	Scenario 1	Scenario 2	Scenario 2	Scenario 2
Network size	100x100 m	100x100 m	200x200 m	200x200 m
Base station location	(50,50)	(50,175)	(100,100)	(100,275)
Numberof nodes	100	100	100	100
Data packet size	5000bit	5000bit	5000bit	5000bit
Aggregation energy	5nJ	5nJ	5nJ	5nJ
Initialy energy of nodes	2J	2J	2J	2J
Percentage of CHs	5%	5%	5%	5%
Maximum number of rounds	10000	10000	10000	10000

In Fig. 2, the LEACH clustering is visually represented, with nodes belonging to the same cluster distinguished by a uniform color. It's worth noting that in LEACH, the quantity of clusters is randomly determined and often deviates significantly from the ideal value of five clusters (e.g., there

may be 8 clusters in round 1). This randomness in cluster creation contributes to the observed load imbalance within the LEACH protocol.
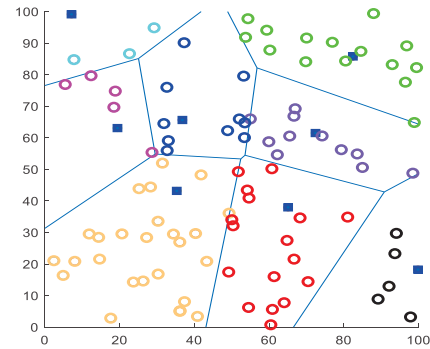

Fig. 2.   Clustering in LEACH in 100x100 area in round 1

In this research, we will evaluate the performance of LEACH by primarily focusing on two critical factors: network lifetime and residual energy.

Figures 3, 4, 5, and 6 depict the evolution of the number of active nodes per round in LEACH across different scenarios, namely scenario 1, scenario 2, scenario 3, and scenario 4, respectively. In scenario 1, the initial node depletion in LEACH occurred during round 2431, with the final node depletion taking place in round 3554. For scenario 2, the first instance of node depletion in LEACH emerged in round 48, culminating in the last node depletion in round 2316. In scenario 3, LEACH experienced its first node depletion in round 38, concluding with the final node depletion in round 3268. Finally, in scenario 4, the initial node depletion within LEACH was recorded in round 23, followed by the last node depletion occurring in round 2069.
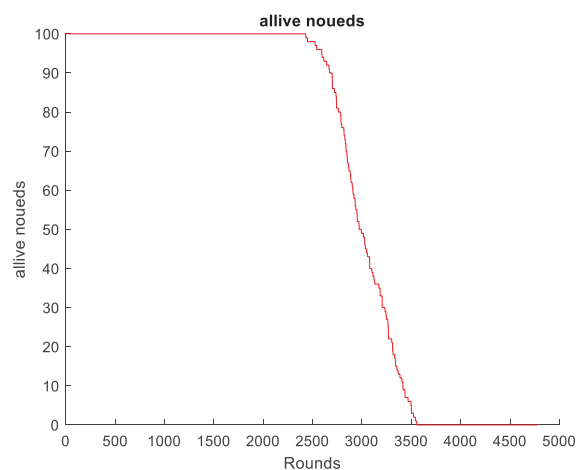

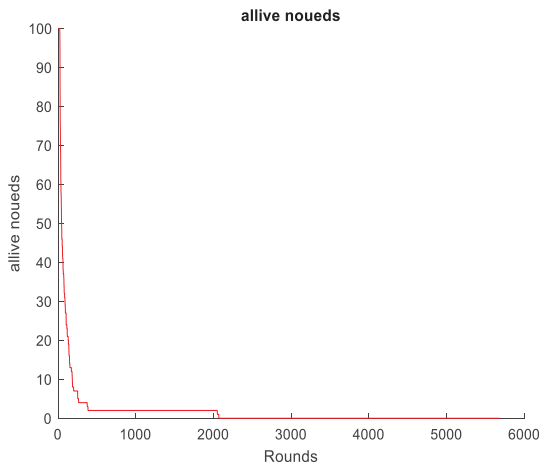Fig. 3.   Alive nodes per round in LEACH in (100x100) area and BS(50,50)

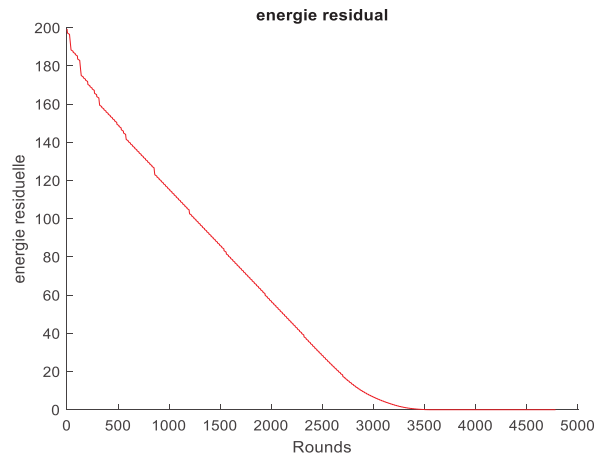Fig. 4.   Alive nodes per round in LEACH in (100x100) area and BS(50,175)

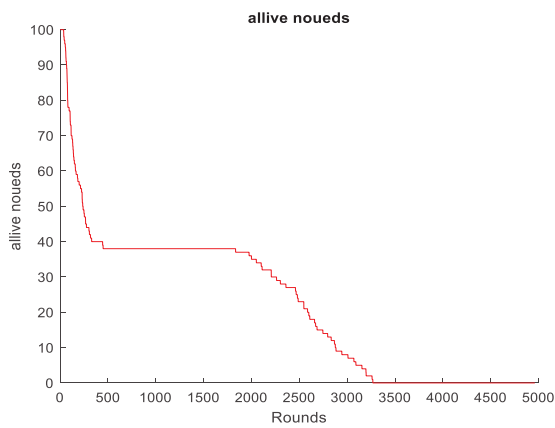Fig. 5.   Alive nodes per round in LEACH in (200 x200) area and BS(100,100)

Fig. 6.   Alive nodes per round in LEACH in (200 x 200) area and BS(100x275)

Fig. 7.   Residual energy per round in LEACH in (100 x100) area and BS(50,50)

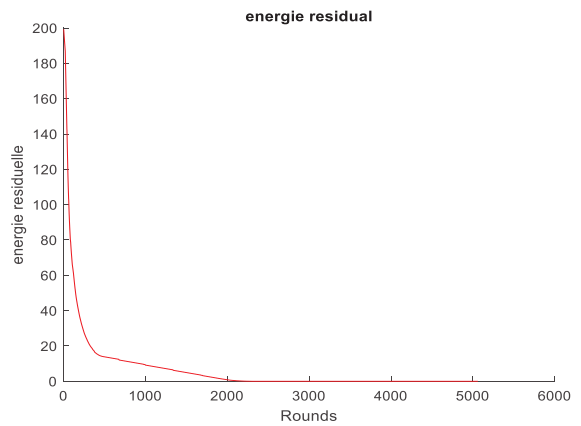Fig. 8.   Residual energy per round in LEACH in (100 x100) area and BS(50,175)

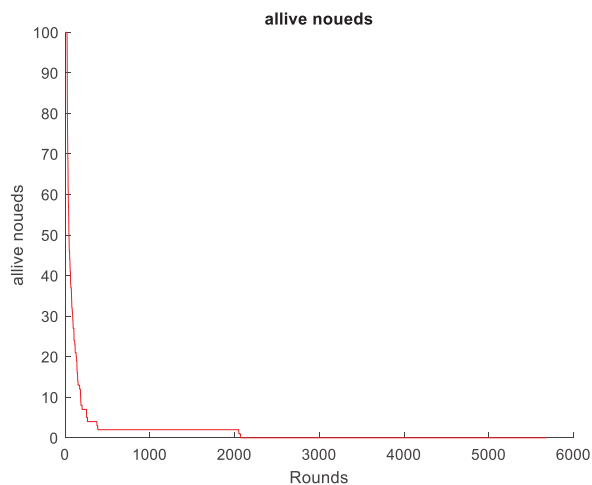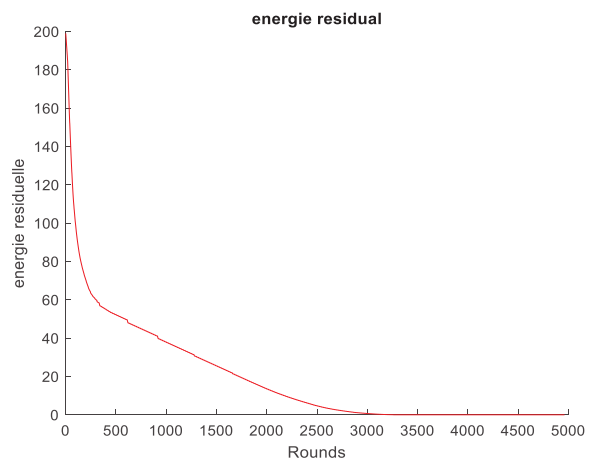Fig. 9.   Residual energy per round in LEACH in (200 x200) area and BS(100,100)

Figures 7, 8, 9, and 10 show the residual energy per round for LEACH In scenario 1, scenario 2, scenario3 and scenario4 successively.
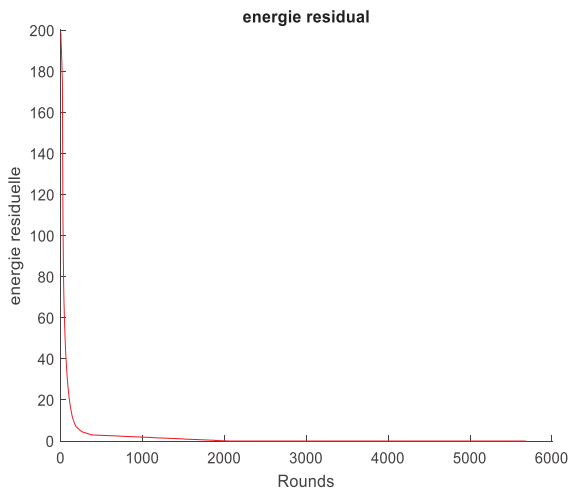
- 70 -

Fig. 10. Residual energy per round in LEACH in (200 x200) area and BS(100,275)

TABLE II.   COMPARISON OF NETWORK LIFETIME OF PROTOCOL LEACH IN DIFFERENT SCENARIOS

Scenario	% Dead node	Nbr of round
Scenario 1	1(FND)	2431
	100(LND)	3554
Scenario 2	1(FND)	48
	100(LND)	2316
Scenario 3	1(FND)	38
	100(LND)	3268
Scenario 4	1(FND)	23
	100(LND)	2069

TABLE III.   COMPARISON OF RESIDUAL ENERGY OF PROTOCOL LEACH IN DIFFERENT SCENARIOS

Scenario	% Energy consumption	Nbr of round
Scenario 1	50	1249
	100	3554
Scenario 2	50	64
	100	2316
Scenario 3	50	97
	100	3268
Scenario 4	50	29
	100	2069

IV. CONCLUSION

This paper presents a comprehensive investigation of the LEACH protocol across various scenarios, with a specific emphasis on network lifetime and residual energy as performance metrics for comparative analysis. Our findings reveal that in scenario 1, the network's lifespan surpasses that of scenario 2, scenario 3, and scenario 4. This suggests that networks deployed in smaller areas exhibit greater longevity compared to those in larger regions. Additionally, both scenario 1 and scenario 3 demonstrate an extended network lifespan in contrast to scenario 2 and scenario 4, highlighting the superior results achieved when the base station (BS) is centrally positioned.

REFERENCES

[1] Sun, Haibin, et al. "LPLL-LEACH: A study of a low-power and low-delay routing protocol based on LEACH." *Ad Hoc Networks* 140 (2023): 103064.

[2] Lechani, Taous, Victor Tourtchine, and Saïd Amari. "A new modification of LEACH for efficient energy in WSN." Indonesian Journal of Electrical Engineering and Computer Science 20.3 (2020): 1495-1506.

[3] Termeche, Hayet, Rahmoun Faycal, and Lechani Taous. "On the comparative study between LEACH and VSG-LEACH protocole. " *Proceedings of the the 1st National Workshop on Wireless Network, Cloud Computing and Cryptography (WWN3C'23)*. IEEE, 2000.

[4] Heinzelman, Wendi Rabiner, Anantha Chandrakasan, and Hari Balakrishnan. "Energy-efficient communication protocol for wireless microsensor networks." *Proceedings of the 33rd annual* Hawaii international conference on system sciences. IEEE, 2000.

[5] Wang A , Yang D , Sun D . A clustering algorithm based on energy information and cluster heads expectation for wireless sensor networks. Computers and Electrical Engineering, vol. 38,no. 3, pp.662-671, 2012.

[6] Pang Z , Zhang W, Wang S . Energy-efficient Improvements in Mod-LEACH Protocol on Optimal Cluster Heads Selection. IEEE Conference on Internet of Things,Green Computing and Communications,Cyber,Physical and Social Computing,Smart Data,Blockchain,Computer and Information Technology,Congress on Cybermatics. pp.1765-1769 ,2018

[7] Daanoune, Ikram, Baghdad Abdennaceur, and Abdelhakim Ballouk. "A comprehensive survey on LEACH-based clustering routing protocols in Wireless Sensor Networks." *Ad Hoc Networks* 114 (2021): 102409.

Design of an Automatic FPGA-based Ceramic Tiles Inspection/Classification Platform

Djihad Bouakaz
Laboratory of Signals and Systems
University M'Hamed Boughara of
Boumerdes, Algeria
djihbou@gmail.com

Ahmed Maache
Laboratory of Signals and Systems
University M'Hamed Boughara of
Boumerdes, Algeria
a.maache@univ-boumerdes.dz

Abstract— **This work describes the development of a real-time system for automatic inspection of moving ceramic tiles and detection and identification of their surface defects at high-speed using OpenCV and (Field Programmable Gate Array) FPGA/ (Hard Processor System) HPS. Based on vision techniques, the system consists of a camera and embedded Linux running on FPGA DE-10 Standard board to create an image processing hardware and software environment. It allows the visualization of the surface and by means of a data base, it will detect and proceed to the identification of the defects of surface during the production cycle. This process classifies ceramic tiles automatically and allows for making the necessary corrections in due time.**

Keywords— Ceramic tiles classification, embedded Linux, OpenCV, FPGA, Hard Processor System

I. INTRODUCTION

In ceramic tile manufacturing processes, great importance is given to the surface condition and inspection possibilities of the products during their production. The simple visual inspection is in fact unable to follow the product which is in movement even at low speed. The inspection of the surface can only be carried out as a sampling which obviously remains non-exhaustive and where error is inevitable. End-of-process inspection is not the ideal solution because it can only trace the history of the process and provide information on its trends. Consequently, defects in the final product that are not detected and corrected lead to downgrading of the products and induce additional costs.

Image processing plays a key role in finding solution to several problems in fields such as medical, industry, security, remote sensing applications and so on. But in some applications system performance presents a bottle neck. Most of image processing systems are developed based on Desktop PC which is a more generic option. Along with the development of advanced and computationally intensive image processing algorithms, computational platforms based on FPGA chip and HPS processor are also developed. This project presents an image processing system for an automatic ceramic tile classification based on an FPGA chip and HPS processor. The main contribution of this work is to gauge the performance that could be achieved using such constrained embedded platform to perform an automatic image processing task using OpenCV. The design is based on an industrial case study performed at the Algerian ceramic company SAFCER [1] to extend their classification procedure.

The rest of this paper is organized as follow: Section II explains the main procedures in the ceramic tiles' production and the existing classification methods with their advantages and disadvantages. Section III demonstrates the design and implementation of the proposed platform. Section IV presents the results and discussion of this work. Conclusions and future directions are outlined in Section V.

II. CERAMIC TILES PRODUCTION PROCESS

In the ceramic tiles production, several processes are involved starting by weighing and grinding the raw material then pressing it using specific machines in the shape of a fixed dimensions rectangle. The tile is then dried to be more solid. This is followed by the enameling and engobing step, where the two materials: enamel and engobe are added. During the printing step, a drawing will be printed on the tile prior to being cooked at high temperature. Finally, control and classification are performed at this stage to check if the product meets the minimum requirement and classify it based on its quality and dimension. Even though the company uses high technology and tries to keep the product as clean and good as possible, certain problems can occur during the production, which prevent the ceramic tiles to be as the desired ones. Therefore, a certain classification of the product has to be done in terms of dimension, quality and form.

During the cooking of the tile, a curvature (convexity or concavity) may be noticeable. Perfect tiles (flat tile) are considered Premium-choice. A tile is classified as Commercial-choice if it suffers from a little curving, without exceeding a specific range. Third-choice are none-useable tiles that can have either: a large crack on the surface of the depositing tile, a big break in the surface, a big difference in the colors, or a big printing error. These are all the classification criteria that we base on to classify a tile as a premium-choice (dimension class: A, B, C, or D), commercial-choice or a third-choice (non-usable tile) as shown in Table 1.

TABLE I.   CLASSIFICATION BASED ON DIMENSION [2]

Tile choice	Class	Length error (%)		Width error (%)		Height (mm)
		From	To	From	To	
Premium	A	-0.25	-0.125	-0.25	-0.125	10.4
Premium	B	-0.125	+0.125	-0.125	+0.125	10.4
Premium	C	+0.125	+0.375	+0.125	+0.375	10.4
Premium	D	+0.375	+0.5	+0.375	+0.5	10.4
Commer	/	<- 0.25 and > +0.5		< -0.25 and > +0.5		10.4

The existing classification method in the company is divided into two parts:

Visual classification: two employees are classifying the tiles visually. If any surface deflect is noticed, the tile is classified as commercial choice, however, if the deflect is too big, it is directly taken out of the line to be classified as a third-choice product.

Automatic classification: the company uses machines to measure the dimension of the tiles to classify them based on

the figures mentioned in Table 1, the marks made by the employee in the visual classification, and the flatness of the tile. The automatic check is based on a system that uses four Infrared sensors to measure the distance and get the dimension of the tile, and seven others to measure the percentage of the error of the flatness. This system also contains a mark reader, it reads the marks made by employees.

Generally, employees working in the visual classification method work eight hours a day. This could be a problem, because employees get tired, as time passes, and the percentage of misclassification errors increases. Therefore, they may allow some defected tiles to pass as premium choice. Also, this technique takes a lot of time to visually detect defects as the worker stops the line, and sometime has to get a supervisor's opinion about a defect. This process is clearly time consuming and for a company that produces 17,000 m2 a day, a slight delay per tile counts.

III. PROPOSED EXTENSION TO AUTOMATIC CLASSIFICATION

A. Hardware design

The proposed solution aims to extend the existing automatic classification system to make it faster and more accurate. The system is designed to inspect ceramic tiles for mechanical, glaze, and decorative defects and classify them according to their quality and size. An overall system diagram is depicted in Fig. 1. The system will be equipped with five ultrasonics sensors to measure the flatness of the tile, it will be also equipped with an IR sensor to detect when the tile is coming so the camera would take a photo and process the image. The five echo pins of the five sensors are connected to the GPIO pins of the FPGA and are declared as outputs to send the sound signal, and the five trig pins are connected to other five GPIO pins and declared as inputs to read the signal coming from the obstacle (in our case the tile). The value of read by the LDR sensor will be transmitted to the FPGA, and from this value the FPGA can control the LEDs by supplying the right voltage to the LEDs. This system replaces human inspection by identifying defects in a wide range of floor tiles at a speed of 3 seconds for each tile.
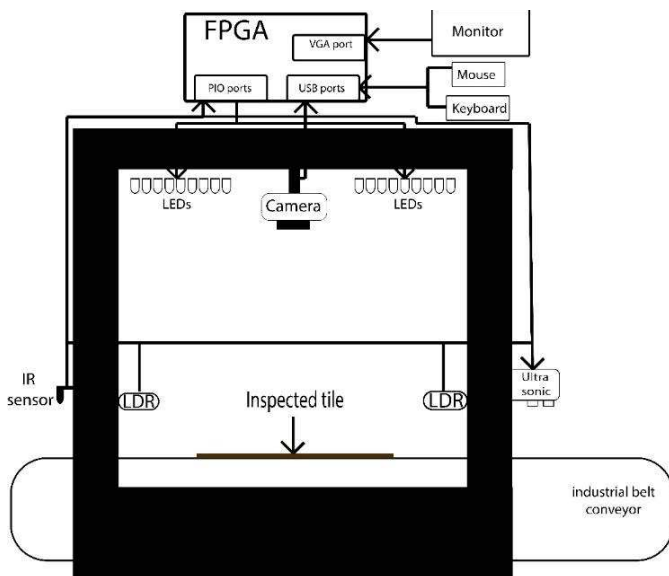

Fig. 1.   Proposed classification system

PIO ports are connected to the FPGA reconfigurable part. But, since the systems is based on HPS, so it is essential to enable the exchange of data between FPGA and HPS via the lightweight-AXI-FPGA-to-HPS-bridge as seen in Fig. 2 [3]. To control the PIO from the HPS, we first have to get the virtual memory address since the LXDE maps the actually physical address to a new virtual memory address, and to do so, embedded shell application has been used. Memory addresses of the PIOs are used as pointers to send and receive data.
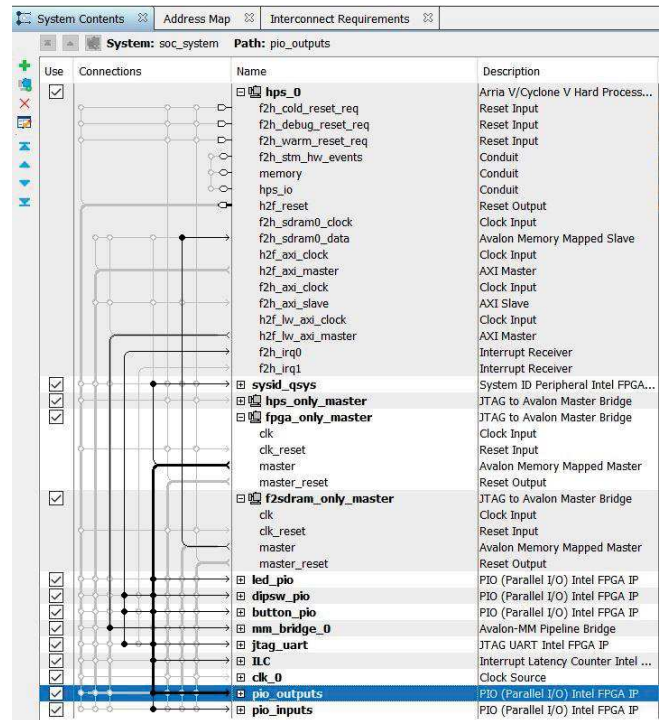

Fig. 2.   QSYS design of the on-chip system

The tiles are classified according to:

Dimension: A tile that has a deviation of 0.3% in the length of a category will not be classified as premium-choice product as described by Equation 1.

$$|X_n - X_m| < 0.3\% \text{ and } |X_n - Y_m| < 0.3\% \text{ and } |Y_n - Y_m| < 0.3\%$$
(m,n = {1,2} to represent each edge of the tile)   (1)

Flatness: The system is equipped with five ultrasonic sensors; each ultrasonic sensor takes five values (total of 25 values) the values of the flatness of 25 points that are shown in Fig. 3. Based on these values, a certain calculation will be made and it will ensure that the flatness of the tile is maintained and does not exceed a certain percentage. The overall flatness coefficient is calculated which is the average of the 25 measured values where it must be less than 3.5mm.

Health of the surface: the first-choice tile may contain some cracks, but these cracks must be less than 1cm.
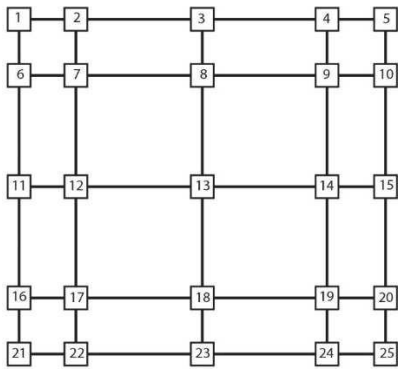
Fig. 3. Points to be measured by the ultrasonic sensors.

B. Software design

When starting the program, the human operator is requested to enter the model and the size of the tile that it is going to be classified. After entering these values, the IR sensor will check whether the tile has arrived into the system or not by measuring the distance. When a tile is detected, the camera will wait until the tile is in the center of the machine then it will take a picture of it. The image then will be processed by applying first the grayscale filter and the gaussian blur filter. This will help to apply the canny filter to detect the edges. Once the edges are detected, it will detect all the closed shapes. The system will neglect the small shapes to gain time and it will only get the shapes that has 4 corners (rectangles) and get the biggest one out of all of these shapes. This will be our tile. After detecting the tile, its image will be
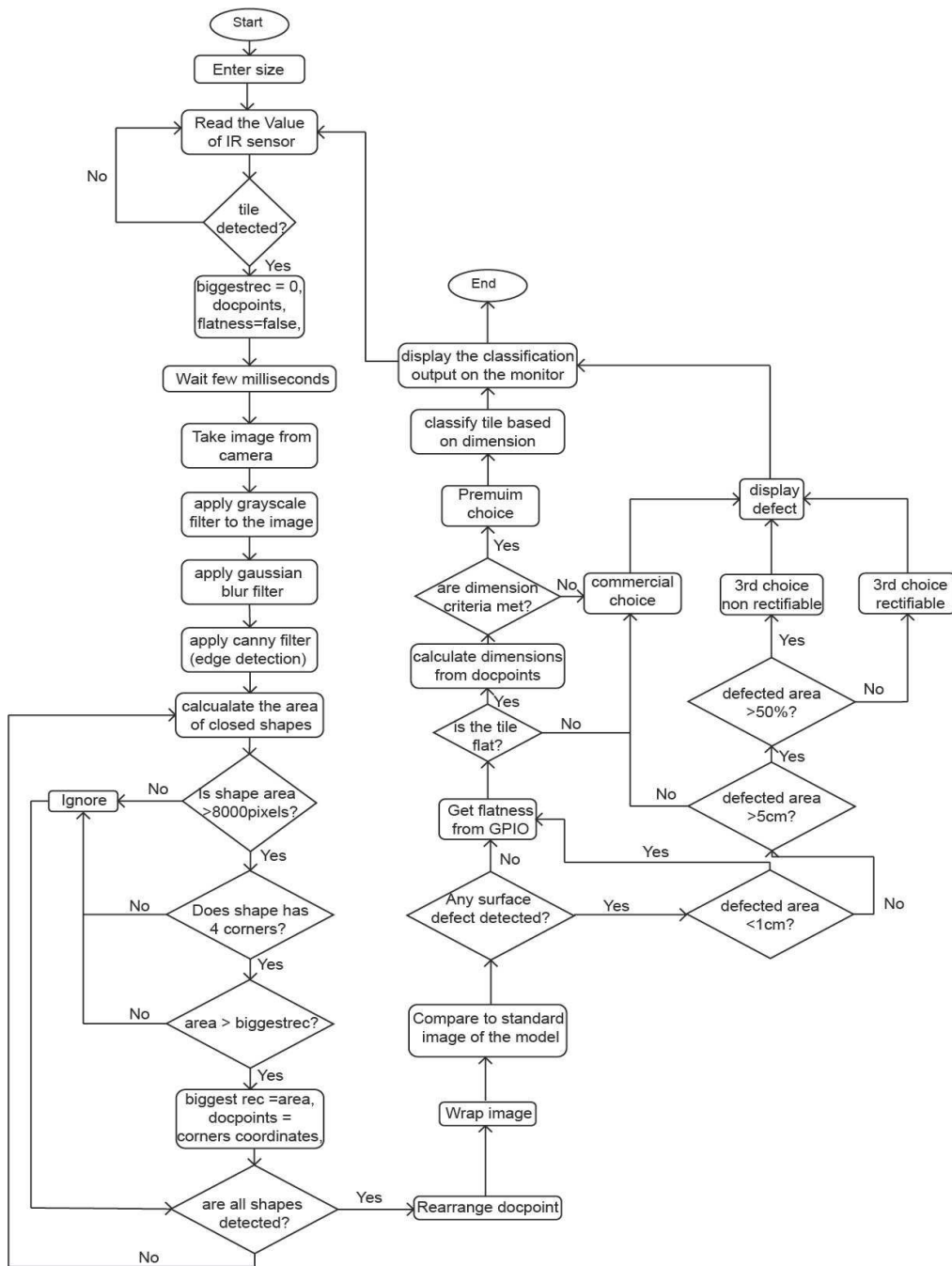

Fig. 4. Classification system flowchart

wrapped after rearranging the points (corners) to be compared to the standard image that is already saved in the system. By comparing the two images the area of the defects, the dimensions of the tile and the flatness rate will be calculated. The system will classify the tiles based on the criteria mentioned earlier and display the output with the defects detected from the tile on the monitor. The classification system flowchart is shown in Fig. 4.

C. Inspection/Classification Steps

The steps involved in inspection/classification are illustrated in Fig. 5.

(a)   (b)

(c)   (d)

(e)   (f)

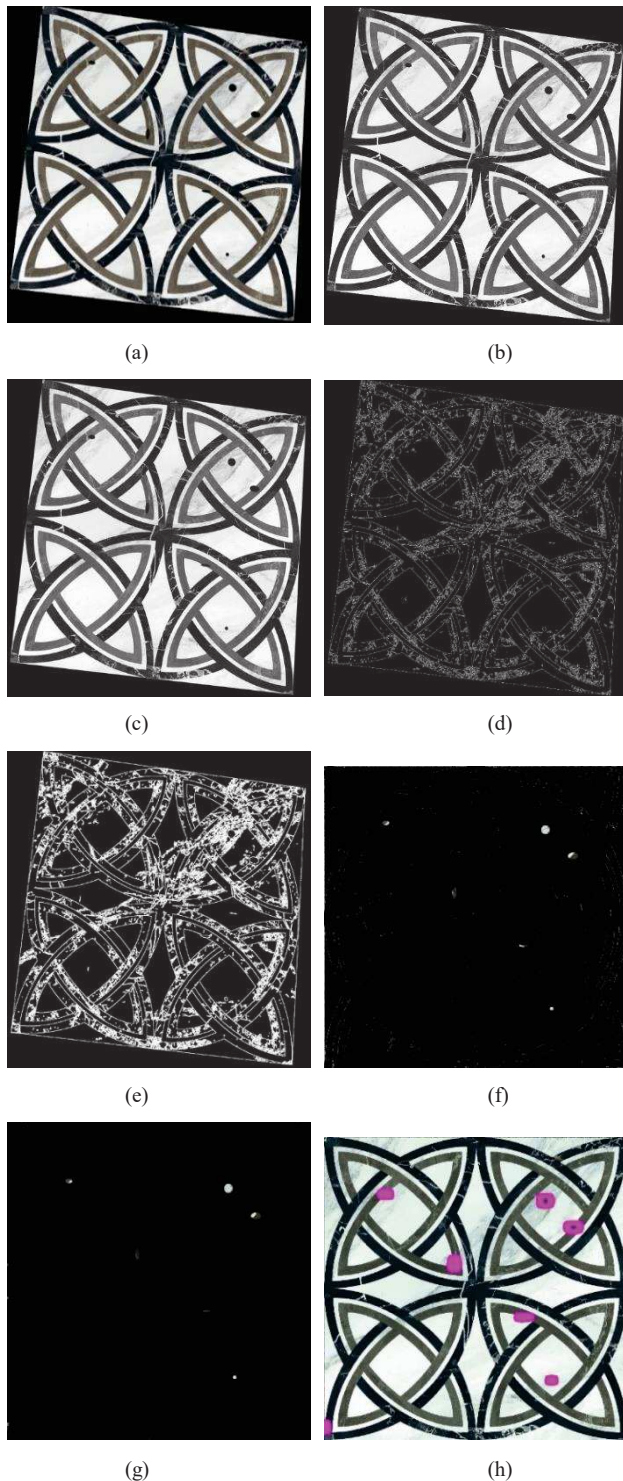(g)   (h)

Fig. 5.   Inspection/Classification steps

1. The first step will be taking the image from the camera. The image that will be entered (in the worst-case scenario) will look like the example image demonstrated in Fig. 5 (a). It will have some defect on the surface and will not have the shape of a perfect rectangle.

2. Grayscale filter is applied to the captured image to convert it to grayscale [4]. The output image should look like the image in Fig. 5 (b).

3. The blur filter is applied in the next step to reduce the noise [5] as seen in Fig. 5 (c).

4. The canny filter (edge detection operator) is applied in the next step in order to detect tiles' edges [6-8]. The result of this step is illustrated in Fig. 5(d).

5. The edges detected in the image by the previous step in are very thin. Therefore, they have to be dilated to look like the result seen in Fig. 5(e) [9].

6. Next step is to get the biggest rectangle in the image, which will obviously be the tile. The software then gets the coordinates of its corners. These corners are then rearranged (top left, then top right, bottom left, then bottom right) and the image is wrapped based on the coordinates of the new points.

7. This image is compared to the original one. The values of each pixel will be subtracted from the value of the corresponding pixel (same coordinates) in the standard image that is already saved in the system. The result of this process is depicted in Fig. 5(f). It can easily be noticed that some white lines appeared on the result. This is basically resulting from the difference in the dimensions and can be removed by applying a filter to produce the resulting image in Fig. 5(g).

8. Then the system will apply the exact same filters mentioned before; grayscale filter, Gaussian blur filter, and the canny filter to get the edges of the defects. It will get the coordinates of these defects and draw these edges with a pink color in the already wrapped image of the tile to show their places as demonstrated in Fig. 5(h).

IV. RESULTS AND DISCUSSION

The purpose of this project was to implement a comparator system that helps to automatically classify tiles with different drawings automatically. A prototype implementation was tested offline. This system is only effective when working with the geometric and unicolor drawing on the tile. It took approximately 2.5 seconds for each tile to be inspected and that is more than enough since the industrial belt conveyer passes one tile each 4 seconds in its maximum speed and when the production is in its prime. But for random drawings, the system took more than 30 minutes to compile and execute the code for a single tile. That is because of the 1GB RAM which is too low for such searches. The second problem found is the camera. It was too difficult to find a camera that is compatible with the light Linux, and that has a quite acceptable resolution and quality that helps in the inspection of the. This led to decrease the resolution to 320 x 240, where the edge detection became difficult at some point, and camera was detecting defects even that they didn't exist, and that is because of the low quality of the camera and the bad edge detection due to

the low resolution. This system would achieve better results if it uses a better CPU, more RAM and, more importantly, a high-quality camera with a higher resolution a higher frame captured per second [10, 11].

The system was also tested by reading high resolution images that were already saved in an on-board SD card. When working with images with high resolution, the system took 3.5 seconds to classify a tile. This experiment was conducted to verify that if the resources were provided the system would have worked much better and the accuracy would have been much higher.

The obtained results from our prototype are really promising and can be a proof of concept that helps extend the company's current classification system.

V. CONCLUSION

As a conclusion, this work used image processing techniques and libraries based on FPGA and HPS to perform the process of ceramic tile classification targeting an industrial environment. The proposed system delivers an appropriate result compared to the current employed system when it comes to classifying the ceramic tile. The results are promising and can be a proof of concept that helps extend the company's current classification system.

The system can be developed more and is flexible to modify to inspect tiles for other companies based on their criteria of classification. It can also be applied to products that need visual inspection on the final product.

As a future work, the system can be implemented using a better CPU, more RAM, and a better camera. Machine learning techniques can also be used to classify random model tiles.

REFERENCES

[1] SAFCER, https://www.safcergroup.com/, accessed on 03/10/2023.

[2] ISO Standard, ISO 10545-2:2010, Ceramic Tiles Determination of dimensions and surface quality, 2010.

[3] Intel, AN 796: Cyclone V and Arria V SoC Device Design Guidelines, 20 february 2017. access date: april 2021, Online: https://www.intel.com/content/www/us/en/docs/programmable/683360/18-0/guidelines-for-interconnecting-the-hps.html.

[4] Gonzalez, Rafael, Digital image processing. New York, NY, Pearson, 2018.

[5] Patrick Hébert, "Introduction to artificial vision", Master course, University of Laval, 2017.

[6] Canny, J., A Computational Approach to Edge Detection, IEEE Transactions on Pattern Analysis and Machine Intelligence, 8(6):679–698, 1986.

[7] R. Deriche, Using Canny's criteria to derive a recursively implemented optimal edge detector, Int. J. Computer Vision, Vol. 1, pp. 167–187, April 1987.

[8] Lindeberg, Tony "Edge detection and ridge detection with automatic scale selection", International Journal of Computer Vision, 30, 2, pp 117—154, 1998.

[9] Gary Bradsk and Andrian Kaehler, "Learning OpenCV", third edition, 2008

[10] Shaonan Zhang "Real Time Image Processing on FPGAs ", Master thesis, University of Liverpool 2018.

[11] Chatzigeorgiou Georgios, "Design and implementation of an autonomous SoC FPGA based UAV (QUADCOPTER) for data image and acquisition and processing", Master thesis, University of Patras, 2021.

Design of Compact F-Inverted Patch Antenna for IoT Applications

Mohamed Bedra
L.E.A, Department of Electronics
University of Batna 2
05000 Batna, Algeria.
mohamed.bedra@univ-batna2.dz

Akram Bedaif
L.E.A, Department of Electronics
University of Batna 2
05000 Batna, Algeria.
akram.bediaf@univ-batna2.dz

Sami Bedra
Department of Industrial Engineering
University of Khenchela
40004, Khenchela, Algeria
bedra_sami@univ-khenchela.dz

Djamel Benatia
L.E.A, Department of Electronics
University of Batna 2
05000 Batna, Algeria.
d.benatia@univ-batna2.dz

Djemai Arar
L.E.A, Department of Electronics
University of Batna 2
05000 Batna, Algeria.
d.arar@univ-batna2.dz

Abstract—**This research investigates the role of compact microstrip patch antennas on the Internet of Things (IoT), highlighting the importance of miniaturization and dual-frequency capabilities. It optimizes antenna configurations using HFSS modeling, beginning with a rectangular patch and progressing to E-shape and inverted F-shape configurations. The study attempts to find the best-performing design with reflection coefficients less than -10dB and fine-tune it with morphological modifications for ideal IoT performance.**

Keywords— rectangular microstrip antennas; bandwidth; Radiation pattern; dual frequency antenna; inverted F-shape; E-shape; IoT applications; reflection coefficient.

I. INTRODUCTION

Of all remarkable achievements of modern life, Internet of things (IoT) is one that has become pivotal part where it's applied on a large scale on data acquisition and wireless communications. This lot concept functions and works via sensors for conveying information and data through a wireless network configuration. Health care systems, the military, smart city, smart home and agricultural applications are all examples of applications that are based on wireless sensor networks (WSN) technologies [1]. Yet, the current applications of IoT imply antenna miniaturization and, in some cases, multiple resonant frequencies, because it's less expensive and small size so that is readily merge to IoT devices. to obtain these terms, it is highly recommended to design a microstrip patch antenna that has a low profile, while keeping in mind the preservation of all antenna traits, such as good impedance matching and omnidirectional coverage [2]. Moreover, dual frequency microstrip antennas have several advantages, including the ability to double system capacity through frequency reuse and high antenna connection performance through polarization diversity [3].

Among the many varieties of antenna currently being studied in wireless communication is the rectangular patch antenna. Which is characterized by its appreciable radiation pattern, wide bandwidth, ease of manufacture and simple structure [4-10]. This specific kind of antenna has a massive disadvantages This includes moderate radiation characteristics (Directivité,gain…) due to the narrow bandwidth issues.

In order to find the best structural parameters and shape that allow for solving the previously mentioned issues, it is necessary to use the appropriate software. In addition, the design helps to take into account the imperfection of the dielectric and conductive parameters of the materials selected, in order to be closer to the future antennas produced. Therefore, the choice of a suitable electromagnetic simulator is essential. Among the many existing simulation tools, we were able to test one, namely HFSS (High Frequency Structure Simulator) for calculating the finite element method for rectangular patch antennas with a compact shape. the HFSS software was chosen for its ideal combination of both calculation accuracy and speed of resolution.

This paper tackles the effect of various structural parameters on the Directivity of a compact dual band (2.4/5 GHz) antenna to get the best radiation and performance. At first; We designed a rectangular patch antenna with two slots then we transformed it into E-shape lastly, into an inverted F-shape looking for better results we will benchmark these structures to select the best among them. To achieve the best comparison, this work suggests inspecting the reflection coefficient, targeting a reflection amount less than or equal to -10dB. The next step after getting the most significant structure we will search the most accurate results by adjusting it morphological parameters (substrate thickness, substrate material type and ground plane length).

II. ANTENNA DESIGN

This section will be devoted to the simulation of the structures proposed in this paper, of which Figure 1 (a) has also evolved in two stages ((b) then (c)).
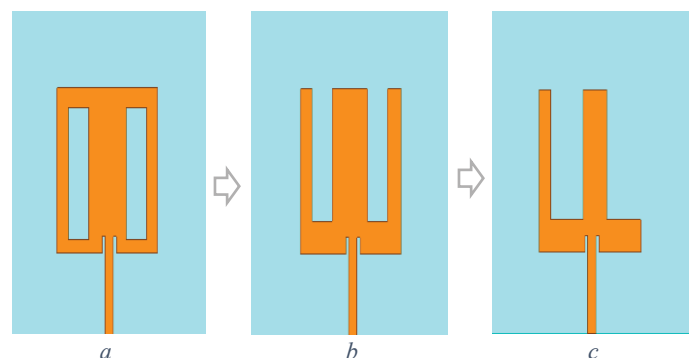

Fig. 1. Configuration and evolution of the proposed structure.

Hence that the study of important parameters that influence the antenna's performance is showcased in figure 2.

This last reveal that structure (c) has a double band with notches observed in the frequency at 2.4Ghz and ~5Ghz with S11 approximately equals to -34 dB and -19dB respectively.

In contrast, (a) and (b) illustrate an unstable pattern represented with more than three bands, most of the time resulting in a reflection coefficient greater than -10dB, except for some resonant frequencies where S11 is varying around [-20dB, -11dB]. As a result, we can distinguish that (c) inverted F-shape is the right choice because of it's stable resonant behavior dual bandwidth and relevant reflection coefficient. Now after getting the suitable choice, we can move on in our study where the final structure of the inverted F-shaped antenna is presented in fig 3.
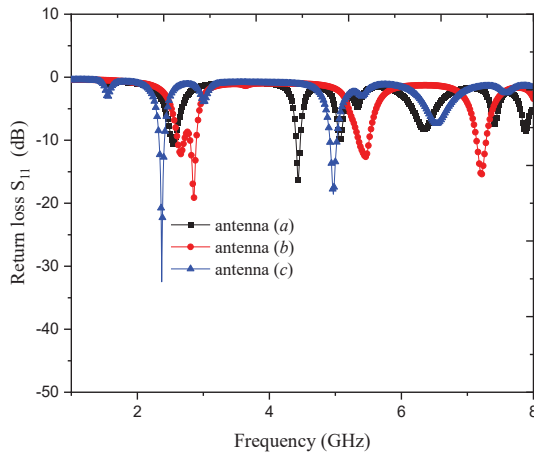

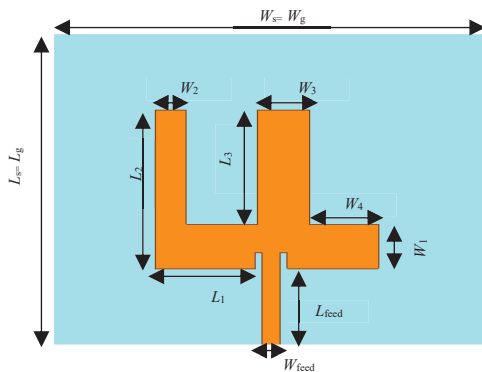Fig. 2. Reflection coefficient as a function of frequency for different proposed structures a, b and c.

Fig. 3. Final structure of the optimized antenna.

Next in the coming section parametric study for the chosen structure will be discussed.

III. DISCUSSION OF NUMERICAL RESULTS

A. Parametric study of the proposed antenna

Now, we vary the thickness of the substrate (h=0.5, 1.4, and 2 mm) and keep all other antenna parameters fixed. The results obtained for the module of the reflection coefficient (in dB) for the three substrate thicknesses are plotted in Figure 4. We note that for the different substrate thicknesses, the resonant frequency remains almost unchanged, but the level of the reflection coefficient varies insignificantly. A subroutine for optimizing the antenna structure with respect to the height of the substrate became necessary. Figure 5 represents the effect

of the ground plane length Lg on the desired features. Notice that There is a difference of the reflection coefficient (S_{11}) as a function of frequency for the three ground plane lengths (Lg= 20, 35 and 50 mm). The minimum value of reflection coefficient starts from (S_{11})= -28.5dB and it remains below -32dB for frequencies of 2.4 GHz and 5 GHz for Lg=50mm at Lg=50mm, better findings were obtained compared to others in terms of accuracy and bandwidth.
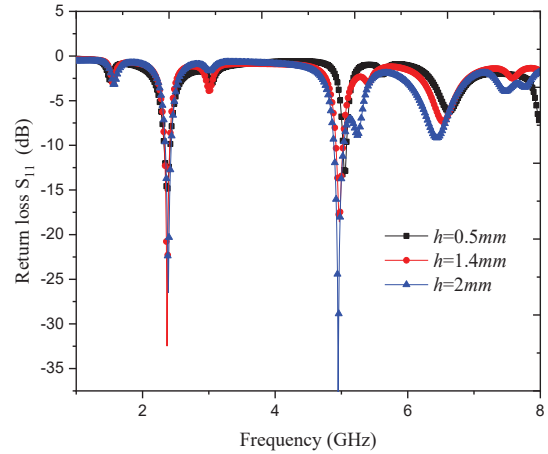

Fig. 4. flection coefficient as a function of antenna frequency for different substrate thickness values.
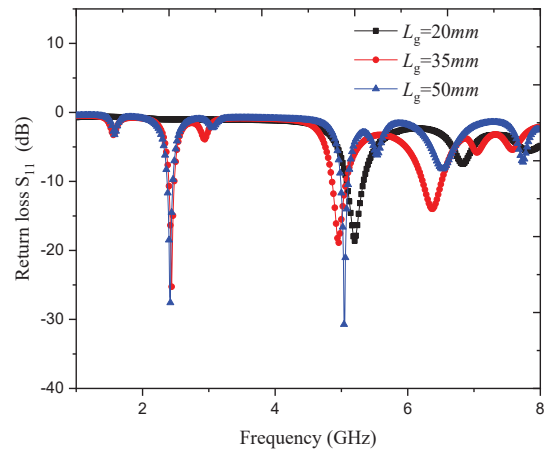

Fig. 5. Reflection coefficient as a function of antenna frequency for different sizes of ground plane Lg.

In this subsection, we are studying the impact of dielectric permittivity where substrate thickness fixed at (h=3mm) and relative permittivity set to be (ε_r=2.94, 4.4, and 5.75). We synthesize the obtained results from the reflection coefficient (S_{11}) in dB for the three dielectrics in Fig 6. We figure out that the minimum reflection coefficient is -33dB at frequency of 2.4 GHz, and -18 dB at a frequency of 5GHz. We can deduce that the resonance frequency of the antenna increases with a decrease in relative permittivity.

B. Final structure of the optimized antenna

Careful adjustment of geometric parameters were made after attempt a several numbers of experimental iterations applying the parameter sweep option in the transient solver.

Eventually, presenting in Table the perfect parameters that have been obtained for the proposed configuration (Fig.3).
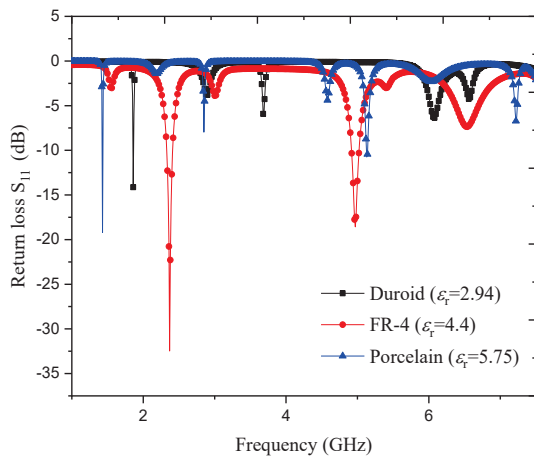

Fig. 6. Reflection coefficient as a function of antenna frequency printed on different substrates ε_r.

TABLE I. OPTIMAL PARAMETERS OF THE PROPOSED ANTENNA (*mm*).

W_s		L_s		$W1$	$L1$	$W2$	$L2$	$L3$
50		50		7	11.25	3.5	25	7
$W3$	$W4$	W_{feed}	L_{feed}	W_s				
5.75	7.75	2	15	50				

The variation in gain and radiation pattern is shown in Figure 7 (*a*) and (*b*), respectively. It can be seen from this figure that the main radiation lobes of the proposed antenna are directed almost to 0° in both planes E and H in at a frequency of 2.4 GHz. In particular, the radiation patterns are quite similar (Fig 8. (*a*)). The far-field radiation pattern results for the proposed antenna, at a specified frequency of 2.4 GHz, were simulated, as shown in Fig 8. (*b*), clarifying a polar plot of the radiation pattern in both planes: Plane E (ø = 0°), Plane H (ø = 90°).

The proposed antenna demonstrated sensitive radiation pattern characteristics with predominantly symmetrical behavior at this frequency.

The radiation patterns of the proposed three-dimensional (3D) antenna are simulated in the far field region, as shown. In Fig 8. This figure shows that the antenna radiation pattern proposed in Fig 8.a has only one main lobe while the secondary lobes are minimized. Fig 8.b shows the optimal radiation pattern of the proposed antennas, with the presence of the secondary lobes. We also note that the diagram is directional in the vertical plane H and omnidirectional in the horizontal plane E.

The performance of the proposed compact antenna is illustrated in more detail using the distributions of electric, magnetic, and surface currents simulated on the antenna structure at the resonance frequency 2.4 GHz, as shown in Fig9.

However, in fig 9, we observe that the distribution of the electric current is mainly located on the power line, and the edges of the radiant structure.
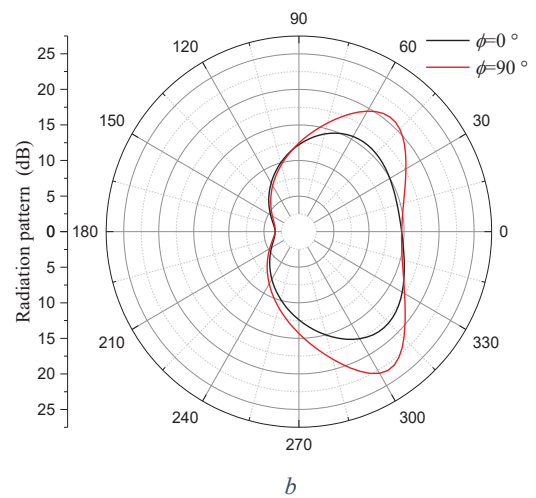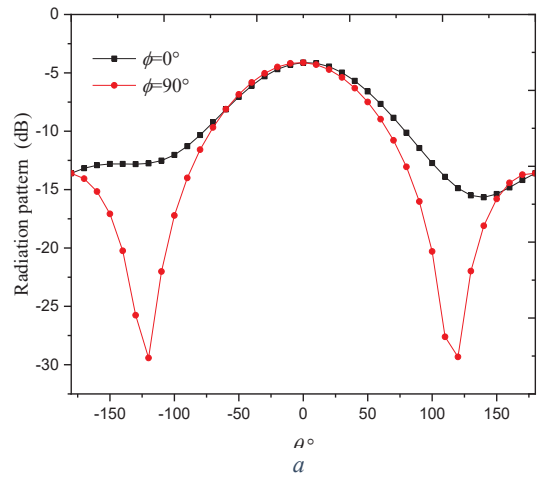

a

b

Fig. 7. Gain of the proposed antenna, (a) Gain in both E and H planes, (b) Gain radiation pattern.

IV. CONCLUSION

In this work, a miniature F-shaped microstrip antenna has been simulated and designed based on a prior study made throw a survey that includes two other shapes (rectangular antenna with two slots and E-shapes antenna) with operating frequencies for IoT applications. The survey reviled that the proposed antenna offers useful frequency, dual-band and good radiation characteristics in terms of radiation patterns. The simulated finding results acceptable gain and directivity, while the best reflection coefficient value (S_{11}) is -30 dB. These parameters are relatively good and have the potential for improvement, which promises a higher yield for wireless communications when utilizing a proposed array of antennas.

REFERENCES

[1] L. Anchidin, A. Lavric, P.-M. Mutescu, A. I. Petrariu, and V. Popa, "The Design and Development of a Microstrip Antenna for Internet of Things Applications," Sensors, vol. 23, no. 3, p. 1062, 2023.

[2] Y. Mao, S. Guo, and M. Chen, "Compact dual‐band monopole antenna with defected ground plane for Internet of things," IET Microwaves, Antennas & Propagation, vol. 12, no. 8, pp. 1332-1338, 2018.

[3] S. Katoch, H. Jotwani, S. Pani, and A. Rajawat, "A compact dual band antenna for IOT applications," in 2015 International Conference on

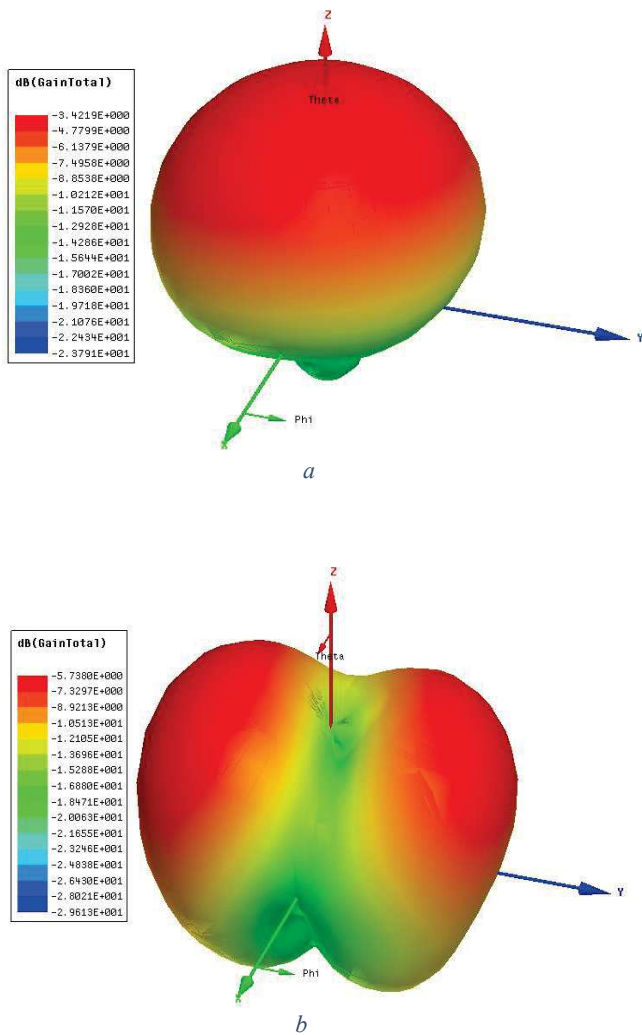Green Computing and Internet of Things (ICGCIoT), 2015: IEEE, pp. 1594-1597.

[4] Z. Zhao and T. A. Denidni, "Millimeter-wave printed-RGW hybrid coupler with symmetrical square feed," IEEE Microwave and Wireless Components Letters, vol. 30, no. 2, pp. 156-159, 2020.

[5] H. R. D. Oskouei, A. R. Dastkhosh, A. Mirtaheri, and M. Naseh, "A small cost-effective super ultra-wideband microstrip antenna with variable band-notch filtering and improved radiation pattern with 5G/IoT applications," Progress In Electromagnetics Research M, vol. 83, pp. 191-202, 2019.

[6] U. Pandey, P. Singh, R. Singh, N. P. Gupta, S. K. Arora, and E. Nizeyimana, "Miniaturized Ultrawideband Microstrip Antenna for IoT-Based Wireless Body Area Network Applications," Wireless Communications and Mobile Computing, vol. 2023, 2023.

[7] S. Bedra, R. Bedra, S. Benkouda, and T. Fortaki, "Study of an inverted rectangular patch printed on anisotropic substrates," IETE Journal of Research, vol. 68, no. 2, pp. 1056-1063, 2022.

[8] S. Rana, J. Verma, and A. K. Gautam, "Design and Analysis of Wideband Stair Step-Shaped Rectangular Ring Microstrip Antenna with DGS for IoT Applications," International Journal of Online & Biomedical Engineering, vol. 19, no. 9, 2023.

[9] D. V. Chauhan, A. Patel, A. Vala, K. Mahant, S. patel, and H. Mewada, "Microstrip Antenna for Internet of Things (IOT) Applications," Internet of Things Enabled Antennas for Biomedical Devices and Systems: Impact, Challenges and Applications, pp. 129-142, 2023.

[10] D. Tiwari, J. A. Ansari, A. K. Saroj, M. J. A.-I. J. o. E. Kumar, and Communications, "Analysis of a Miniaturized Hexagonal Sierpinski Gasket fractal microstrip antenna for modern wireless communications," vol. 123, pp. 153288, 2020.

Fig. 8. Radiation pattern of the proposed antenna: (a) 2.4GHz, (b) 5 GHz.
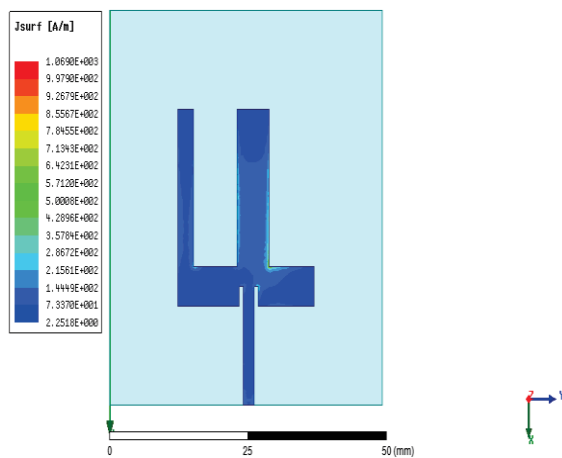
Fig. 9. Distribution of antenna current proposed.

Implementation of a low-cost LoRa-based IoT Framework

Mohammed Ibrahim Mansour Djadir
Laboratory of Signals and Systems
University M'Hamed Bougara of Boumerdes, Algeria
a.maache@univ-boumerdes.dz

Ahmed Maache
Laboratory of Signals and Systems
University M'Hamed Bougara of Boumerdes, Algeria
a.maache@univ-boumerdes.dz

Abstract—The Internet-of-Things (IoT) is one of the most growing technologies in the last few years. Various standards are currently contending to gain an edge over the competition and provide massive connectivity. Among these standards, Low-Power Wide Area Networks (LPWANs) are continuously gaining momentum, mainly due to their ability to provide long-range coverage to devices, exploiting license-free frequency bands. LoRa is emerging as one of the most promising LPWAN to establish affordable connectivity. However, how to implement a cost-effective and flexible LoRa network is still an open challenge. This work aims to design and implement a prototype for a low cost LoRa network for IoT framework including hardware and software of a LoRa end-node, single-channel LoRa gateway and a network server. A new transmission protocol between the end-node and the gateway was implemented based on the variation of the LoRa module parameter. The implementation also includes a data handling system that collects the data from the network server and save it to the cloud.

Index Terms—LoRa, Low-Power Wide Area Networks, LP-WANs, IoT, Internet-of-Things

I. INTRODUCTION

IoT is a collection of connected objects, embedding electronics, software, sensors, and wireless connectivity protocols that collect and exchange information with applications through wireless networks connected to the Internet. Nowadays IoT became a trending topic as the number of connected devices is expanding rapidly. According to estimates by the International Data Corporation, the number of IoT devices is projected to reach 41.6 billion by 2025, generating an astonishing 79.4 zettabytes of data [1]. This technology has an impact on a wide range of sectors and services, including automotive, smart buildings, smart agriculture, smart cities, industrial control, and e-health. The proliferation of connected devices presents several significant hurdles in terms of connectivity technology, which must be upgraded to accommodate and resolve the following issues:

- The high density of connected devises and achieve the best possible efficiency.
- Power consumption of the connected devices should be optimized so that these devices, which run on batteries, achieve long autonomy.
- These devices must support long-range communication.

Before a large-scale implementation, the ability of an IoT network protocol to meet these requirements must be thoroughly explored. This has heightened interest in the emerging wireless IoT connectivity family known as Low-Power Wide-Area Network (LPWAN). The latter is particularly suited to support services and use cases that require long-distance communication (hundreds of kilometres) to reach devices that must have a low power consumption budget in order to run remotely for several years on a single battery pack. The major use cases of LPWAN include Smart Cities, supply chain management with asset tracking & condition monitoring, smart grids, and smart agriculture [2].

One of the prominent LPWANs is LoRa, which is radio modulation technology invented in 2010 by the French startup Cycleo and then acquired in 2012 by Semtech (a semiconductor company). A MAC layer has been added to standardize and extend the LoRa physical communication layer onto internet networks. This MAC layer is called the LoRaWAN (LoRa for Wide Area Networks) specification. The specification is open sourced and supported by the LoRa Alliance. The LoRaWAN protocol also includes several key wireless networks feature such as E2E encryption and security, adaptive data rate optimization, quality of service, and other advanced communication applications.

The objective of this work is to implement a low-cost IoT system based on LoRa. This system will consist of a LoRa node to act as end devices, a gateway to receive data and forward it via wifi to our server.

The rest of this paper is organised as follow. Section II represents a general background about IoT technology. Section III includes the software and hardware design of the IoT node and the server-side in addition to the implementation. Results of different tests and discussion are presented in Section IV. Finally, conclusions and future work are outlined in Section V.

II. BACKGROUND

A. IoT Technology

The concept of linking things to the Internet has been intensively studied and researched during the previous two decades as a new technological breakthrough. The internet connection of embedded equipment and sensors is expected to have a significant impact on the industrial revolution, health care, and energy generation.

M2M (Machine-to-Machine) with a similar concept of connecting things has been applied in different industries since

the early 1990s [3]. However, M2M and IoT are two distinct concepts: IoT is wider and comes with many new options and touch different sectors. It also relies on new technologies in terms of connectivity, application, and storage. The main purpose of M2M is to maintain the connectivity between a specific machine and the remote host in a fixed, proprietary installation, which is generally configured to monitor and control only those specific types of machines.

Hence, M2M provides end-to-end connectivity to exchange data between machines. It oversees point-to-point systems like elevator remote controls and vending machines. The IoT notion, on the other hand, broadens the idea of M2M to create a new Internet of connected objects horizontally rather than vertically. Objects linked to the network provide data to the cloud, where humans, computer systems, and other objects receive the data, interact with each other, and integrate with other independent applications/solutions to establish horizontal connection between IoT entities. Thus, the Internet of Things aspires to build an open, scalable, standards-based, service-oriented network in which a vast number of nodes can communicate and interact with one another.

One of the primary goals of IoT is to create a horizontal, versatile, scalable, and accessible data architecture in which a large number of devices and humans communicate with one another. However, the sheer number and spread of devices on the network pose technological hurdles to the network design framework.

IoT architecture comprises a collection of physical objects, sensors, cloud services, developers, actuators, communication layers, users, business layers, and IoT protocols. Because of the wide domain of internet objects, there is no single consensus on IoT architecture, which is universally agreed. Different researchers proposed different architectures. According to most researchers' views, a conventional IoT architecture is considered as three layers [4].

LPWANs have recently been emerging as an alternative to LR-WPANs and CIoT, mainly thanks to the range limitations of LR-WPANs and to the fact that CIoT is still in a very early stage of deployment. These networks provide wireless connectivity using a star topology and long-range transmission in the unlicensed sub-GHz frequency bands [5]. The other great benefit brought by LPWANs is an increased power efficiency: many of these technologies so far have made the claim of being able to sustain a device for ten years on a couple of AA batteries.

One of the main competitors among standards for this architecture is LoRa. It is a technology that exploits a new spread spectrum design that enables a higher receiver sensitivity in order to trade data rate for coverage, decreasing the former to increase the latter. LoRa and LoRaWAN are, respectively, a proprietary modulation developed and owned by Semtech Corporation [6] and a network standard, focused on leveraging useful properties of the LoRa modulation, proposed by the LoRa Alliance [7]. The LoRa modulation allows for very good receiver sensitivities at a contained cheap cost, thus achieving long-range transmissions (up to 13 miles in a rural

environment) at the price of a reduced data rate, in the 0.3 to 50 kbps range. At the same time, the LoRaWAN standard that allows multiple LoRa devices to communicate together aims at shifting the burden of administering the network towards a central control point. This allows devices to be as simple as possible, and gives a central coordinator the power of easily tuning each device's parameters in order to accommodate new nodes in the network [8], [9].

The study in [10] compares the connectivity technologies in term of range and data rate. It demonstrated the ability of LPWAN technology to provide a very wide range compared to other technologies in addition to very low power consumption, which makes it the best connectivity solution for transmitting light-weight data for long distances.

The Messaging protocols used play a key factor when it comes to IoT domain. They can operate in both application layer and communication layer. Their main role is to facilitate the data transmission between devices; as they define how each device will be referred to and standardizing messages. Three of the dominants messaging protocols in IoT are HTTP [11], COAP [12], and MQTT [13].

III. System Design and implementation

A. System Architecture

The system is designed based on the five layer architecture discussed in [14]. The overall system architecture is demonstrated in Figure 1. At the bottom layer, we will design an IoT node that uses LoRa transceiver. The end-nodes will operate on different spreading factors to benefit from the orthogonality on this parameter. In the communication layer, a single channel LoRa gateway is used. This gateway will send an acknowledgement signal periodically. Each message is transmitted using a different spreading factor. The end-node with the corresponding factor will receive the acknowledgement signal and send the data to the gateway. With this messaging technique, up to six end-nodes can be connected to a single channel gateway. The latter will send the data via MQTT to the network server that contains an MQTT Broker and an agent that stores the data as time series and send it to the cloud.
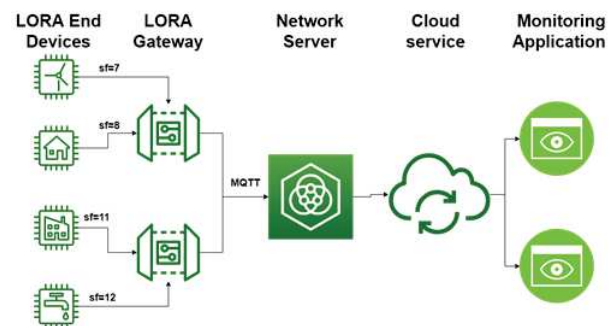

Fig. 1. Overall system architecture.

B. Hardware Design

1) LoRa end-node: The hardware design of the LoRa node consists of two main parts: the computing module that is the Microcontroller and the LoRa modem. For the best performance-to-cost ratio, the following hardware was chosen:

Microcontroller: the choice of Microcontroller is important for attaining the required results out of an embedded system and while most systems developed for IoT applications consist of Low power CPUs for longevity of the device. For this reason, the STM32L4 microcontroller was chosen due to its low power consumption [15]. The STM32L496xx devices are the ultra-low-power microcontrollers based on the high performance Arm® Cortex®-M4 32-bit RISC core operating at a frequency of up to 80 MHz. The Cortex-M4 core features a Floating point unit (FPU) single precision, which supports all Arm® single-precision data-processing instructions and data types. It also implements a full set of DSP instructions and a memory protection unit (MPU) which enhances application security. This device offer up to three 12 bit ADCs, two DAC channels low power RTC and many advanced communication interfaces such as: four I2c, three SPIs, two low power UART, two audio interfaces, two CAN, and camera interface. The variety of communication interfaces of the STM32L4 allow the user of our end-node to connect many sensor and actuators.

LoRa modem: the modem used in our node is the SEMTECH SX1278 [16]. It is a half duplex low power long range transceiver that offers bandwidth option from 7.8 kHz to 500kHz with spreading factor ranging from 6 to 12 covering only the lower UHF (Ultra High Frequency) bands (410MHz-525Mhz). All the parameter are configurable via SPI interface that gives access to configuration registers. These includes a mode auto sequencer that oversees the transition and calibration of the SX1278 between intermediate modes of operation in the fastest time possible.

After selecting the hardware, a schematic of the end-node was created as seen in Figure 2. The board contains the following:

- A USB connector dedicated for the serial communication.
- A connector for the external power source or the battery.
- A debugging connector used for debugging and programming the chip.
- Switches to select the operation mode.
- An SMA connector for the antenna.
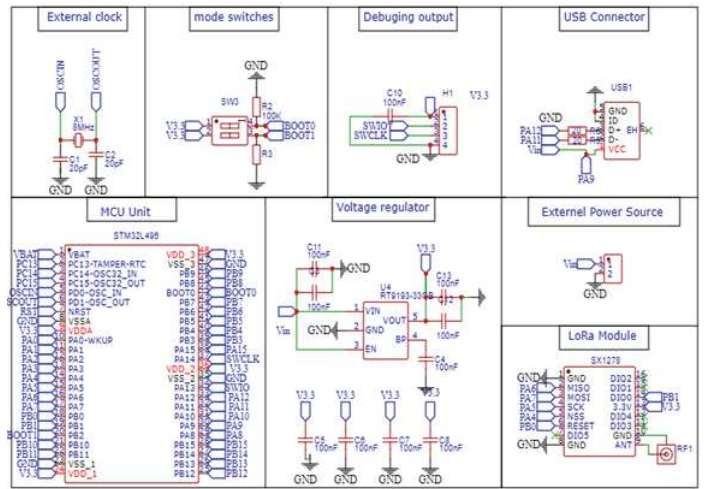- A power regulation circuit as both the microcontroller and the LoRa module operate on 3.3v.

Fig. 2. The end-node schematic.

2) LoRa Gateway: The gateway is primarily used in a stationary host location. Hence, low power is not a hard requirement, which makes the hardware choice easier. For this reason, a wifi gateway is used in our work. It consists of two parts: the SX1278 module and the ESP32 microcontroller that contains a wifi module to connect to the network server. The ESP32 will be connected to the SX1278 through SPI and the digital I/O flag is used to indicate the existence of a received message. The schematic of the gateway is shown in Figure 3.
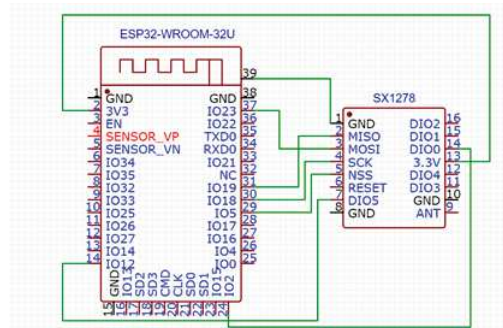

Fig. 3. The gateway schematic.

C. Software Design

First of all, a driver was developed for interfacing the SX1278 LoRa module to the STM32L4 where STmicroelectronics Cube IDE was used. The operation of developing a driver was very challenging as the LoRa module has 112 registers where 68 of them should be configured to operate in the LoRa modulation mode. The other registers are dedicated for the other modulation offered by this module. The interfacing was done via SPI. The read/write operations are done in two modes; the first is called 'one time' in which one byte is read/written to/from the FIFO register. This mode is used to access configuration registers. The second one is the 'burst mode', which is used in reading or writing the data packets. The number of bytes depends on the data received/transmitted.

All the functions implemented in the driver of the SX1278 module are listed in [16].

1) The end-node software: The software firmware of the LoRa node was developed using the driver in the previous section. The flowchart of the program is shown in Figure 4.
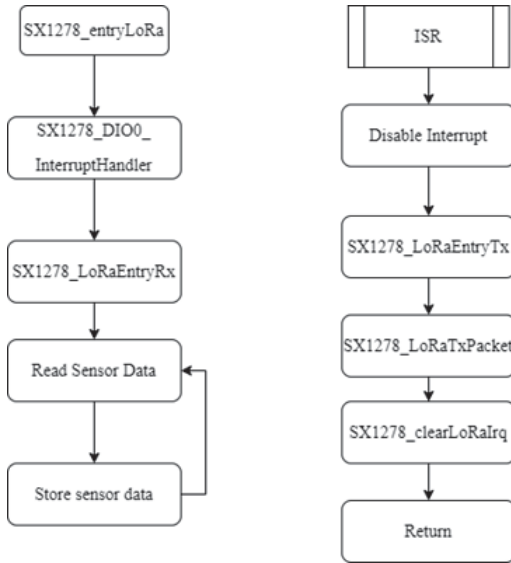
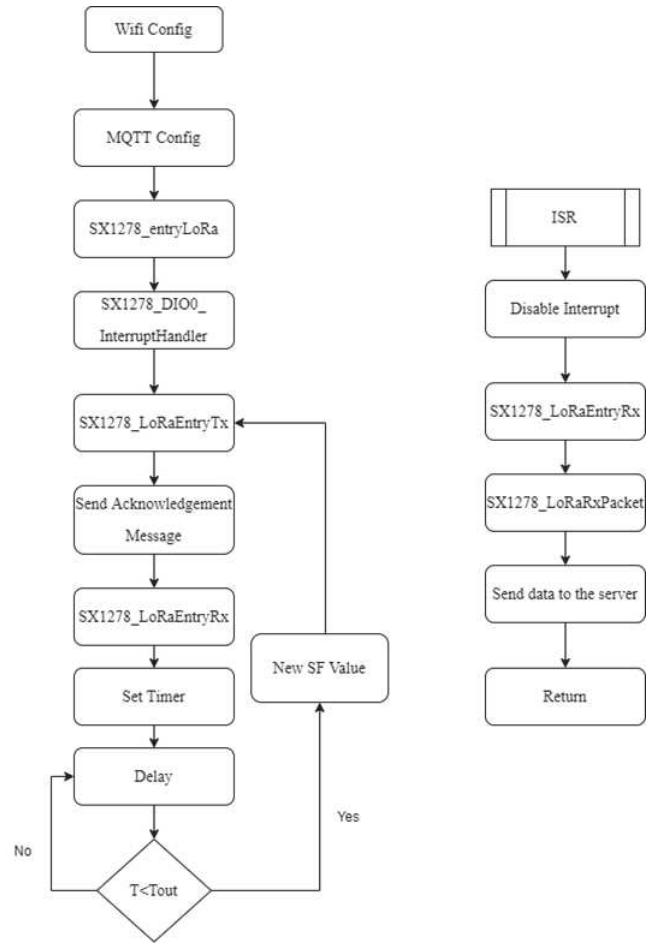

Fig. 4. The LoRa end-node software flowchart.

Fig. 5. The LoRa gateway software flowchart.

First, the software configures the LoRa module as a receiver and enables the interrupt. Then, it enters into an infinite loop reading the sensors' data, saving it into local memory, and waiting for an acknowledgement message from the gateway. When receiving the message, an interrupt is generated switching the node to transmitter mode and send the sensors' data saved to the gateway.

2) The Gateway software: A flowchart of the software controlling the gateway is illustrated in Figure 5. First, we connect to the server via wifi and configure the gateway as an MQTT publisher. Then, the gateway sends an acknowledgment message with a specific spreading factor and waits for receiving data from the end-node. If the node does not transmit the data within the timeout period, the gateway will send an acknowledgment message to another node with the next spreading factor. If the gateway receives an interrupt before timeout, it will switch to receiver mode, read the data from the LoRa modem, and send it to the MQTT server through the corresponding channel.

D. Data Collection and storage

This section covers how the server collects data from the gateway and stores it as a Time-Series Database (TSDB). An MQTT broker was used to collect the data from the gateway. Then, a server agent processes this data and saves it as a TSDB in the cloud. Figure 6 illustrates this operation.
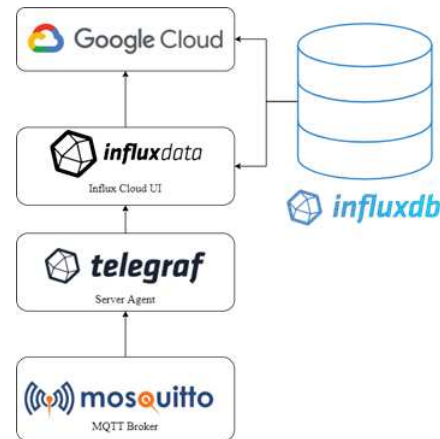

Fig. 6. Data storage system software structure.

The tools used in this system are:

- Mosquitto: is an open source message broker that implements the MQTT protocol [17].
- Influx Cloud: is a data service platform that relies on the time series data. This platform is used because it offers many services for IoT real-time data storage and monitoring [18].
- InfluxDB: is an open source time series database that is part of the influx cloud stack. It is designed to handle high write and query loads and provides an SQL-like query language called InfluxQL for interacting with data [19].
- Telegraf: is a server agent for collecting and reporting data [20]. It is the first part of the influxcloud slack that has many input plugins such as MQTT. This agent will collect data from the mosquitto broker and process this data by transforming it to influxdb line protocol by adding a time stamp and measurement name. This data will be sent to the cloud via HTTP.

IV. RESULTS AND DISCUSSION

A. Node-To-Gateway Test (close-range)

In this section, the node-to-gateway communication is tested to ensure the correct functionality of the software developed earlier. In this experiment, a node is within the gateway's range in order to test the response of the node. Figure 7 shows the hardware used in the experiment.

Fig. 7. End-node (left) to gateway (right) communication test (close-range).

The nodes were configured to operate with SF=10, both gateway and node will operate on the frequency 433Mhz. To illustrate the communication process, the gateway is connected to computer via Serial link. Figure 8 shows reading serial data from the gateway. It can be seen that the gateway gets a response only when an acknowledgement with SF=10 is sent. This is because the only node available in the range operates in that SF. This experiment confirms the proper functionality of our driver and the messaging protocol. It also confirmed the principle of avoiding interference based on the spreading factor orthogonality.

Fig. 8. Reading serial data from the gateway.

B. LoRa long-range Test

The second test was performed in a light urban area in the town of Oued Rhiou. Data were collected from three locations which are approximately 540m, 1100m and 1600m away from the gateway. The receiver was placed on the top of a building approximately 10m higher than relative ground level. A map of the three test locations and the gateway's location is shown in Figure 9. At each location, one hundred "hello" messages were transmitted. Then, the number of the received messages was recorded to obtain the Packet Error Ration (PER), whereas the receiver provided us with the Received Signal Strength Indicator (RSSI).

Fig. 9. Map of the three test locations (long-range).

Table I shows the configuration used in the test:

TABLE I
PARAMETERS USED IN THE LONG-RANGE TEST

Frequency	Power	Coding Rate (CR)	Bandwidth (BW)
433Mhz	20dBm	4/5	125Khz

The measurement results are given in Table II. RSSI values shown are average values.

The results presented confirms that our system functions correctly. It also confirms that the higher the spreading factor

TABLE II
TEST RESULTS AT LONG DISTANCES

Spreading factor (SF)	540m		1100m		1600m	
	PER%	Avg RSSI [dBm]	PER%	Avg RSSI [dBm]	PER%	Avg RSSI [dBm]
7	2%	-115.12	4%	-119,60	/	/
8	2%	-114.25	3%	-117.45	/	/
9	5%	-117.66	6%	-123.14	9%	-127.78
10	4%	-123.33	6%	-124.73	11%	-130.23
11	7%	-130.17	12%	-132.65	11%	-134.35
12	7%	-133.66	11%	-135.5	13%	-137

the larger the error. In test location 3 (1600m), the receiver lost connection with the node at spreading factor 7 and 8. The RSSI measured values are close to the values given by the manufacturer. It can be seen clearly that the PER increases when a higher spreading factor is used in addition to the slow data rate which causes several problems when dealing with sensitive and critical data.

C. Discussion

The first experiment shows the functionality of a single channel gateway. This method offers multiple node communication with a single frequency channel which make the nodes setup easier but is has some limitation in the number of nodes

The single channel (non-parallel) gateway designed in this work receives data from one node at time. Therefore, the gateway needs to send acknowledgement message periodically to different nodes. As a result, each node should wait for other nodes and can only send data every five minutes.

The low data transmission frequency allows for long intervals where the nodes will be in the receiving mode. Therefore, it saves battery and prolongs the up-time of the node. The usage of high spreading factor (10, 11, 12) offers higher range coverage. But, it has a negative effect on the performance as the packet loss rate is very high in addition to low data rate and higher power consumption.

V. CONCLUSIONS

The presented work dealt with the design and implementation of a prototype IoT system based on LoRa technology for sensor data analysis and monitoring. The goal of this system is to facilitate the use of LoRa technology as connectivity solution for IoT, develop methods to maximize the performance with low cost, and propose data storage model. Influx database was used as data storage solution. The system was tested using two experiments. The first one proved the functionality of the transmission protocol developed to avoid collusion and simplify the configuration. The obtained results were accurate. In the second test, the performance of LoRa was tested by varying different parameters mainly the distance between the node and the gateway. These results demonstrated some limitations in the case when operating in long-range.

Future improvement in the design can be made by studying the positioning of the nodes and the gateway and enhancing the transmission protocol by developing full duplex system and adding encryption to secure the data.

REFERENCES

[1] M. Shirer and C. MacGillivray. (2019) Worldwide global datasphere iot device and data forecast, 2019-2023 (idc us45066919). [Online]. Available: https://www.idc.com/getdoc.jsp?containerId=prUS45213219

[2] J. Dizdarević, F. Carpio, A. Jukan, and X. Masip-Bruin, "A survey of communication protocols for internet of things and related challenges of fog and cloud computing integration," vol. 51, no. 6, jan 2019. [Online]. Available: https://doi.org/10.1145/3292674

[3] J. Holler, V. Tsiatsis, C. Mulligan, S. Karnouskos, S. Avesand, and D. Boyle, *From machine-to-machine to the Internet of Things: introduction to a new age of Intelligence*. Elsevier Ltd, 2014.

[4] M. Jabraeil Jamali, B. Bahrami, A. Heidari, P. Allahverdizadeh, and F. Norouzi, *Towards the Internet of Things: Architectures, Security, and Applications*. Springer International Publishing, 2019.

[5] M. Centenaro, L. Vangelista, A. Zanella, and M. Zorzi, "Long-range communications in unlicensed bands: the rising stars in the iot and smart city scenarios," *IEEE Wireless Communications*, vol. 23, no. 5, pp. 60–67, 2016.

[6] Semtech corporation. [Online]. Available: http://www.semtech.com

[7] LoRa Alliance. [Online]. Available: https://www.lora-alliance.org

[8] M. A. Ertürk, M. A. Aydın, M. T. Büyükakkaşlar, and H. Evirgen, "A survey on lorawan architecture, protocol and technologies," *Future internet*, vol. 11, no. 10, p. 216, 2019.

[9] M. Knight and B. Seeber, "Decoding lora: Realizing a modern lpwan with sdr," in *Proceedings of the GNU Radio Conference*, vol. 1, no. 1, 2016.

[10] K. Mekki, E. Bajic, F. Chaxel, and F. Meyer, "A comparative study of lpwan technologies for large-scale iot deployment," *ICT Express*, vol. 5, no. 1, pp. 1–7, 2019.

[11] I. Grigorik, "Making the web faster with http 2.0," *Communications of the ACM*, vol. 56, no. 12, pp. 42–49, 2013.

[12] W. Colitti, K. Steenhaut, N. De Caro, B. Buta, and V. Dobrota, "Evaluation of constrained application protocol for wireless sensor networks," in *2011 18th IEEE Workshop on Local & Metropolitan Area Networks (LANMAN)*. IEEE, 2011, pp. 1–6.

[13] M. Rouse and P. Waher, "Mqtt (mq telemetry transport)," *IoT Agenda*, 2020.

[14] P. Sethi and S. R. Sarangi, "Internet of things: Architectures, protocols, and applications," *Journal of Electrical and Computer Engineering*, vol. 2017, no. 9324035, 2017.

[15] STMicroelectronics, *Ultra-low-power Arm Cortex-M4 32-bit MCU, STM32L496 datasheet*, 2020.

[16] SEMTECH, *SX1276/77/78/79 - 137 MHz to 1020 MHz Low Power Long Range Transceiver datasheet*, 2020.

[17] Eclipse mosquitto an open source mqtt broker. [Online]. Available: https://mosquitto.org/

[18] Influxdata. [Online]. Available: https://www.influxdata.com/

[19] S. Zhang, W. Zeng, I.-L. Yen, and F. B. Bastani, "Semantically enhanced time series databases in iot-edge-cloud infrastructure," in *2019 IEEE 19th international symposium on high assurance systems engineering (HASE)*. IEEE, 2019, pp. 25–32.

[20] Telegraf. [Online]. Available: https://www.influxdata.com/time-series-platform/telegraf/

Colorectal Polyps Segmentation with U-Net and Attention Mechanism in Colonoscopy Images

Faiza BELLA
Dep. of Computer Science
LIMOSE,University of M'hamed Bougara
Boumerdes, Algeria
f.bella@univ-boumerdes.dz

Ali BERRICHI
Dep. of Computer Science
LIMOSE,University of M'hamed Bougara
Boumerdes, Algeria
ali.berrichi@univ-boumerdes.dz

Abdelouahab MOUSSAOUI
Dep. of Computer Science
University of Ferhat Abbes Setif I
Setif, Algeria
abdelouahab.moussaoui@univ-setif.dz

Abstract—Colonoscopy stands as a highly effective diagnostic method utilized for detection of colorectal cancer. Computer-aided diagnosis techniques play a crucial role in assisting doctors, especially in identifying polyps during colonoscopies. Furthermore, medical image segmentation is indispensable in disease diagnosis, including colorectal cancer. The U-Net architecture has gained widespread adoption for image segmentation tasks. Notably, attention mechanisms have gained remarkable popularity in the field of medical image analysis, with a specific focus on segmentation. For colorectal polyps segmentation, we employed U-Net architecture in two variations, with and without an attention mechanism. These models were trained using CVC-ClinicDB dataset. The results demonstrate that the inclusion of attention mechanism successfully enhances the segmentation performance of U-Net architecture.

Index Terms—Colorectal Cancer, Polyp Segmentation, Medical Image Analysis, Attention Mechanism, Colonoscopy Images.

I. INTRODUCTION

The gastrointestinal (GI) tract is the system that includes a series of interconnected organs responsible for digestion and nutrient absorption, such as the mouth, esophagus, stomach, small intestine, and large intestine (colon). Because of its sensitivity, GI tract is more susceptible to diseases, with cancer being the most dangerous among them. Recently, there has been a rise in fatalities linked to gastrointestinal cancers, particularly colorectal cancer .

Colorectal cancer (CRC) ranks as the 3rd most common cancer worldwide [1]. In 2020, according to the World Health Organization (WHO), there were over 1.9 million newly diagnosed cases of CRC [1]. CRC exhibits similar symptoms to other GI tract organ cancers, including nausea, vomiting and abdominal pain.

Polyps are abnormal growths of tissue that can develop in different parts of the body, including the GI tract, particularly within the colon. In the early stage, they are small, fleshy growths that typically form on the inner lining of the colon or rectum. It's important to note that not all polyps

will progress to cancer. In fact, many polyps remain benign and do not develop into cancer. However, regular screening and removal of adenomatous polyps through procedures like colonoscopy can significantly reduce the risk of colorectal cancer. Early detection and treatment at the polyp or early cancer stage offer the best chance for a favorable outcome. This is why colorectal cancer screening is recommended for individuals at risk or of a certain age, as it allows for the detection and removal of polyps before they become cancerous.

A colonoscopy is a vital tool utilized in modern medicine today [2]. This technique has proven highly effective in diagnosing various colon diseases, including CRC and polyps.

In this study, we performed image segmentation of colorectal polyps using images acquired through the colonoscopy technique. We utilized a U-Net-based approach in two scenarios: the first employed the U-Net architecture alone, while the second incorporated attention mechanisms. The objective of our study is to assess the influence of attention mechanisms on improving the accuracy and performance of U-Net for segmenting colonoscopy images.

II. RELATED WORKS

This section provides an overview of relevant research related to our study, which primarily focuses on medical image segmentation using Computer-Aided Colonoscopy (CAC).

Akbari and al [10] introduced a polyp segmentation approach utilizing convolutional neural networks. the proposed method incorporates two key strategies to enhance its performance. Firstly, they employ an innovative image patch selection technique during the network's training phase. Secondly, during the testing phase, they implement effective post-processing on the probability map generated by the network. Bulut and al [9] Focused on training the U-Net model for polyp segmentation and optimizing the learning rate using the Cyclic Learning Rate policy. Yue and al [11] introduced a novel attention-guided pyramid context network (APCNet) designed for precise and resilient polyp segmentation in colonoscopy

images. Jowair and al [12] Proposed an approach based on a multi-encoder system is proposed, leveraging pre-trained CNNs to enhance feature extraction. Skip connections from these parallel encoders are concatenated and fed into the decoder, facilitating bidirectional information flow between the network's shallow and deep layers. The method's performance was evaluated through training and testing on five publicly accessible datasets. Wang and al [13] Proposed a novel encoder-decoder architecture referred to as 'Pyramid Transformer-Driven Multibranch Fusion' designed to achieve precise segmentation of various colorectal polyp types during colonoscopy.

III. U-NET ARCHITECTURE

The U-Net architecture is a convolutional neural network (CNN) architecture proposed by Olaf Ronneberger and al [3] in 2015. It was originally developed for biomedical image segmentation, particularly for for tasks including cell segmentation and medical image analysis, but has found applications in various other fields. Figure 1 illustrates the overall architecture of U-Net, which resembles the letter 'U.' This resemblance is the reason behind its name. The "Net" in "U-Net" stands for "Network."

The U-Net architecture is typically described as having two main parts:

- Encoder (Left Part): It's network used to capture the contextual information and features from input image. It situated at the architecture's top, encompasses a series of convolutional and pooling layers. These layers systematically reduce the spatial dimensions of the input image while increasing the number of feature channels. This process enables the network to extract hierarchical features from the input, facilitating the understanding of complex patterns.
- Decoder (Right Part): It's a network used for upsampling the features obtained from the encoder in order to generate a segmentation mask with the same spatial dimensions as the input image. It positioned at the architecture's bottom, is responsible for upscaling the spatial dimensions while concurrently reducing the number of feature channels. The decoder's primary function is to generate a segmentation mask or output that aligns with the original input's dimensions.

Fig. 1 illustrates the U-Net architecture's overall structure
The combination of the two previous parts, along with the skip connections, defines the U-Net architecture. These connections establish links between corresponding layers in both the encoder and decoder. This innovative approach empowers the decoder to access high-resolution feature maps from the encoder, thereby enhancing the network's ability to capture fine-grained details in the data.

The final layer of the decoder is typically composed of a convolutional layer with a sigmoid activation function. This layer generates the pixel-wise segmentation mask,
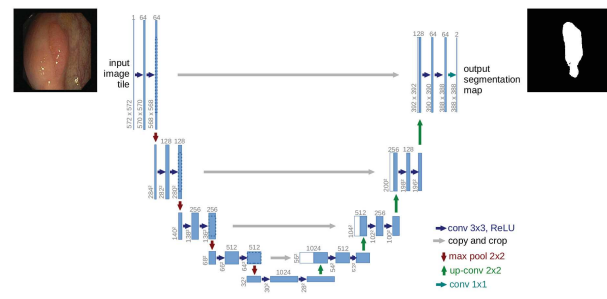

Fig. 1: U-Net architecture [3]

where each pixel in the mask signifies the likelihood of belonging to either the foreground (object) or background, making it particularly suited for tasks such as medical image segmentation.

IV. ATTENTION MECHANISM

The attention mechanism, was developed by particularly in the context of the Transformer model, was developed by Vaswani et al In 2017 [5]. Originally inspired by human visual attention, it has subsequently found applications in various domains, including computer vision. In the field of image analysis, an attention mechanism is a neural network technique that allows the model to focus on specific sections of the input image during a task.

Fig. 2 illustrates the U-Net architecture's overall structure with inclusion of an attention mechanism.

The attention gate plays a crucial role in integrating attention mechanisms into the U-Net architecture. It enables the network to focus selectively on pertinent regions within the feature maps during the segmentation process.
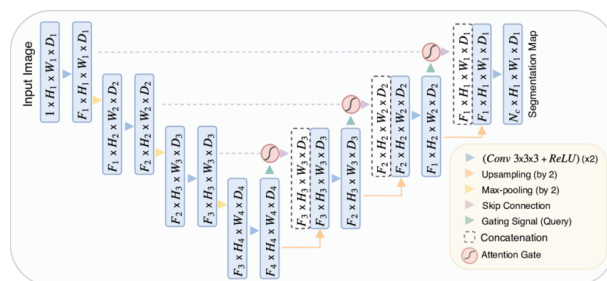

Fig. 2: U-Net architecture with attention mechanism [4]

Two types of attention:

- Hard attention: Relevant regions are emphasized through cropping, one region at a time. This approach is non-differentiable, requiring reinforcement learning. The network can either focus its attention or not, with no intermediate states. Backpropagation is not applicable in this context.
- Soft attention: Weighting various segments of the image involves assigning larger weights to relevant portions and smaller weights to less relevant ones. This weighting can be learned through backpropagation. During training,

the model adapts these weights, prioritizing attention to relevant regions.

The U-Net's skip connections merge spatial information from the down-sampling path with the up-sampling path, preserving valuable spatial details. However, this integration can also introduce suboptimal feature representation from the initial layers. To address this, soft attention is incorporated at the skip connections, effectively suppressing activations in irrelevant regions.

V. EXPERIMENTS

A. Dataset description

In order to To explore the specific impact of the attention mechanism on enhancing medical image segmentation with the U-Net architecture, we conducted a study using the CVC-ClinicDB [6]dataset from Kaggle. This dataset consists of 600 images extracted from colonoscopy videos, each paired with its corresponding segmentation mask, all at a resolution of 224x224 pixels. The dataset has a total size of 137 MB and is available in two file formats: TIFF and PNG. Throughout our experiments, we exclusively utilized the PNG format.

Fig. 3 displays sample images along with their corresponding masks from CVC-ClinicDB dataset.
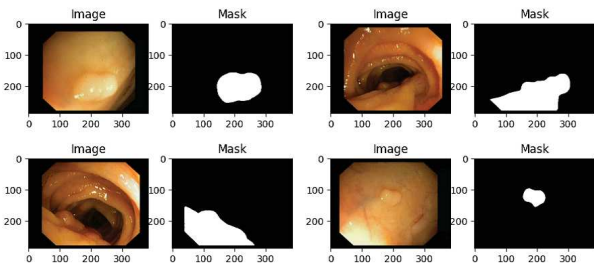

Fig. 3: Sample images along with their corresponding masks from CVC-ClinicDB dataset.

B. Proposed approach

In this study, we compared the performance of U-Net architecture in colonoscopy images with and without using Attention Mechanism. Each experiment has been trained separately on the same CVC-ClinicDB dataset , and also, the same split has been used to ensure a fair and reliable comparison. Fig 4 illustrates an overview of the proposed approach.
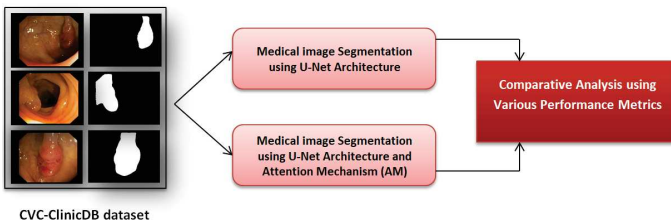

Fig. 4: Overview of the proposed approach.

C. Implementation

All experiments were conducted using Google Colab, leveraging the TensorFlow [7] and Keras frameworks [8]. We utilized the CVC-ClinicDB dataset for training our diverse segmentation models. The dataset was divided into three distinct subsets: training, testing, and validation, with proportions of 80%, 10%, and 10%, respectively. Additionally, we resized the input images to 256 pixels, resulting in tensors derived from these 3-channel RGB images. During training, we utilized the Adam optimizer for 50 epochs. We employed the binary cross-entropy loss function as our choice since we were categorizing mask pixels into two distinct classes.

1) Experiments of using U-Net without Attention Mechanism: We utilized the CVC-ClinicDB dataset for training our U-Net segmentation model. The proposed model closely resembles the architecture illustrated in Fig. 1. Following the training phase, we performed predictions on the test images. Subsequently, each input image, the corresponding real mask, and the predicted mask were juxtaposed side by side and saved in a file.

2) Experiments of using U-Net with Attention Mechanism: In the second experiment, we replicated the previous steps, this time employing the U-Net architecture with an attention mechanism. This addition allowed the model to focus on important areas in the images while reducing emphasis on less significant regions. This adjustment expedited the training phase and facilitated better learning. Nonetheless, we ensured to train the model for the same number of epochs, 50, in the second experiment. The architectural design of the proposed model, featuring an attention mechanism is depicted in Fig. 2.

VI. RESULTS

In our experiments, we have utilized evaluation metrics such as Accuracy, Recall, Precision, IoU and Dice_coef.

Before delving into various metrics formulas, let's familiarize ourselves with key terms in the context of accuracy calculation:

- True Positive (TP): The number of instances correctly predicted as positive by a model.
- True Negative (TN): The number of instances correctly predicted as negative by a model.
- False Positive (FP): The number of instances incorrectly predicted as positive by a model, also known as a Type I error.
- False Negative (FN): The number of instances incorrectly predicted as negative by a model, also known as a Type II error.

With these terms, we can express accuracy, precision, and recall in terms of TP, TN, FP, and FN:

Accuracy measures the overall correctness of predictions made by a model. The Accuracy can be computed using the following formula:

$$Accuracy = \frac{TP + TN}{TP + TN + FP + FN} \qquad (1)$$

Recall measures our model's ability to correctly identify true positives. Precision is the ratio of true positives to all positive predictions. The Recall and Precision can be computed using the following formulas:

$$Recall = \frac{TP}{TP + FN} \tag{2}$$

$$Precision = \frac{TP}{TP + FP} \tag{3}$$

IoU, short for Intersection over Union, serves as a metric utilized for gauging the degree of overlap or similarity between two sets. This metric quantifies the extent of overlap between two sets, typically predicted and ground truth bounding boxes or segmentation masks, by dividing the area of their intersection by the area of their union. It can be computed using the following formula:

$$IoU = \frac{TP}{TP + FP + FN} \tag{4}$$

The Dice coefficient, within the context of image segmentation, is formally defined as the ratio between the size of the intersection of two sets and the average size of these sets. In image segmentation tasks, a higher Dice coefficient is indicative of better segmentation accuracy. It can be computed using the following formula:

$$Dice = \frac{2 \times TP}{2 \times TP + FP + FN} \tag{5}$$

During the training of our model, we conducted two distinct experiments. The outcomes of these experiments are presented in TABLE I. and several predicted segmentation masks are displayed in Fig. 5. Upon comparing the evaluation metrics in Table I, it is evident that we achieved superior results with U-Net and attention mechanism(AM) for all the metrics considered in our study.

TABLE I: EVALUATION RESULTS

Model	Accuracy	Recall	Precision	Iou	Dice_coef
U-Net	0.9421	0.7166	0.7986	0.5127	0.5276
U-Net + AM	0.9574	0.7581	0.8812	0.5783	0.5522

On the leftmost side is the original image, in the center lies the corresponding mask, and on the rightmost side is the result generated by our model.

VII. CONCLUSION

In this research, we addressed the challenging task of detecting polyps within the gastrointestinal tract, where issues like bubbles and blood can obscure the target. Our proposed solution leverages deep learning techniques to segment polyp regions in colonoscopy images, outperforming conventional learning rate strategies. In our experimentation, we initially employed the Unet architecture alongside traditional learning rate strategies. Subsequently, we integrated an attention mechanism to enhance the Unet's performance. The experimental
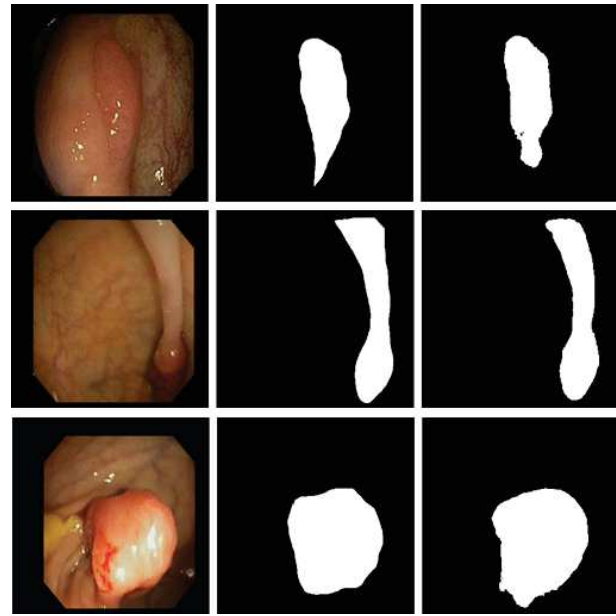

Fig. 5: Sample Result: Polyps Segmentation Utilizing U-Net Architecture and Attention Mechanism.

outcomes conclusively demonstrate that our approach consistently yields superior results across all relevant metrics when compared to using Unet alone.

In our future work, we plan to investigate additional hyperparameter optimization techniques in conjunction with the U-Net architecture. Our objective is to further enhance the accuracy and effectiveness of polyps segmentation in this crucial medical context.

REFERENCES

[1] World Health Organization - Colorectal Cancer Fact Sheet

[2] Stauffer, C. M., Pfeifer, C. (2020). Colonoscopy.

[3] Ronneberger, O., Fischer, P., Brox, T. (2015). U-net: Convolutional networks for biomedical image segmentation. In Medical Image Computing and Computer-Assisted Intervention–MICCAI 2015: 18th International Conference, Munich, Germany, October 5-9, 2015, Proceedings, Part III 18 (pp. 234-241). Springer International Publishing.

[4] Oktay, O., Schlemper, J., Folgoc, L. L., Lee, M., Heinrich, M., Misawa, K., Rueckert, D. (2018). Attention u-net: Learning where to look for the pancreas. arXiv preprint arXiv:1804.03999.

[5] Vaswani, A., Shazeer, N., Parmar, N., Uszkoreit, J., Jones, L., Gomez, A. N.,Polosukhin, I. (2017). Attention is all you need. Advances in neural information processing systems, 30.

[6] Goldbloom, A., Hamner, B., et al.: Kaggle: Your home for data science. Competition, Kaggle, Inc, https://www.kaggle.com (2019), accessed: 2019-07-12.

[7] M. Abadi et al., "TensorFlow: A system for large-scale machine learning," in Proceedings of the 12th USENIX Symposium on Operating Systems Design and Implementation, OSDI 2016, 2016, pp. 265–283, doi: 10.5555/3026877.3026899.

[8] F. Chollet, "Keras: The python deep learning library. Astrophysics Source Code Library.," Keras.Io. 2018.

[9] Bulut, B., BÜtÜn, E., Kaya, M. (2022, March). Polyp Segmentation in Colonoscopy Images using U-Net and Cyclic Learning Rate. In 2022 International Conference on Decision Aid Sciences and Applications (DASA) (pp. 1149-1152). IEEE.

[10] Akbari, M., Mohrekesh, M., Nasr-Esfahani, E., Soroushmehr, S. R., Karimi, N., Samavi, S., Najarian, K. (2018, July). Polyp segmentation in colonoscopy images using fully convolutional network. In 2018 40th

Annual International Conference of the IEEE Engineering in Medicine and Biology Society (EMBC) (pp. 69-72). IEEE.

[11] Yue, G., Li, S., Cong, R., Zhou, T., Lei, B., Wang, T. (2023). Attention-guided pyramid context network for polyp segmentation in colonoscopy images. IEEE Transactions on Instrumentation and Measurement, 72, 1-13.

[12] Al Jowair, H., Alsulaiman, M., Muhammad, G. (2023). Multi parallel U-net encoder network for effective polyp image segmentation. Image and Vision Computing, 137, 104767.

[13] Wang, A., Wu, M., Qi, H., Shi, H., Chen, J., Chen, Y., Luo, X. (2023, October). Pyramid Transformer Driven Multibranch Fusion for Polyp Segmentation in Colonoscopic Video Images. In 2023 IEEE International Conference on Image Processing (ICIP) (pp. 2350-2354). IEEE.

Application of State Feedback Control based on Quadratic Linear Regulator on Three-Tanks system DTS<<200>>

Nora Benmir
Laboratory of Applied Automation
Department of Automation
Faculty of Hydrocarbons and
Chemistry,UMBB
Boumerdes, ALGERIA
n.benmir@univ-boumerdes.dz

Hamza Akroum
Laboratory of Applied Automation
Department of Automation
Faculty of Hydrocarbons and
Chemistry,UMBB
Boumerdes, ALGERIA
akroum@yahoo.fr

Mohamed .Z.Doghman
Laboratory of Applied Automation
Department of Automation
Faculty of Hydrocarbons and
Chemistry,UMBB
Boumerdes, ALGERIA
doghmane_m@yahoo.com

Madjid Kidouche
Laboratory of Applied Automation
Department of Automation
Faculty of Hydrocarbons and
Chemistry,UMBB
Boumerdes, ALGERIA
m.kidouche@univ-boumerdes.dz

Abstract—State feedback control, a prominent modern control method, relies on the calculation of a gain matrix through pole placement or the linear quadratic regulator (LQR) approach. In this research, we delve into the application of the LQR method for state feedback regulation within the context of a three-tank hydraulic system. This laboratory-scale system is widely recognized for its utility in the analysis of multi-variable, nonlinear, and linear systems, making it an ideal tested for studying feedback control strategies. The primary objective of this study is to leverage the LQR approach to derive an optimal control law, thereby enhancing the overall performance of the three-tank hydraulic system.

Keywords—Multi-variable system, Three-Tank system, Linear quadratic regulator, state feedback, linear model, linearization, optimal control.

I. INTRODUCTION

Hydraulic systems are widely used in high-power installations due to their unique advantages over other systems. These systems provide the ability to design more efficient systems that are tailored to specific applications. Moreover, in order to store a liquid in a tank, a hydraulic system or installation is required, which must be designed based on various parameters, including the level of the liquid. [1]Level control in a tank presents a significant challenge in many industrial sites, as it affects the overall operation and performance of the system. The control of liquid level in a hydraulic system is essential to maintain the desired level and prevent overflow or underflow, which can cause damage to equipment or pose a safety hazard[2]. Thus, the design of an effective hydraulic system with reliable level control is crucial for optimizing industrial processes and ensuring safe and efficient operations. Many previous works have the same aim to modelling and control hydraulic systems such as three tanks system, In 2003[3], the author explored linearized and nonlinear decoupling methods, as well as LQ and LQR methods control on a three-tank system. In[4] 2011, Petr

Chalupa et all, initiated a project to create a precise MATLAB/Simulink model of a real-time three-tank system. By 2012[2], they developed a model for the DTS200 Three Tank System, emphasizing pump flow rate and liquid levels. In 2022[5], Jukka Kortela's study introduced a model-predictive controller (MPC) in industrial automation for the three-tank system, demonstrating its superior performance over the traditional PI controller despite nonlinearity and tank interactions. These efforts reflect a progression towards advanced control methods and accurate modeling of hydraulic systems

To solve the level control problem in tanks, various classic and advanced control methods have been developed and implemented. One of the modern control techniques is state feedback control, which is based on determining a gain matrix using either pole placement or linear quadratic regulator (LQR) approaches [6]. The pole placement method places the poles of the system in the desired locations in the complex plane to achieve the desired closed-loop behavior. On the other hand, LQR designs a feedback controller that minimizes a quadratic cost function, which incorporates the system state and input[7]. Both methods have their advantages and disadvantages, but they offer a more efficient and accurate control compared to the classic control methods. State feedback control can improve the level control in tanks and other industrial processes, leading to better performance, reduced energy consumption, and increased productivity.

In this paper, our objective is to implement state feedback control, specifically the linear quadratic regulator (LQR), to regulate the liquid level in a hydraulic system with three tanks DTS <<200>>. Due to the nonlinear nature of the system, it is necessary to linearize the model around an operating point before applying the control method. We first present the DTS <<200>> system and derive its mathematical model. Then, we explain the theoretical framework of the LQR control method and apply it to our system. Additionally, we introduce a state observer and investigate its role in our system. We estimate the state and disturbance vectors using the observer

and simulate the performance of the LQR controller on a nonlinear DTS <<200>> system. Finally, we analyze the system outputs and disturbances after the application of the LQR control method on the real nonlinear DTS <<200>> system.

This study aims to demonstrate the effectiveness of the LQR control method in regulating the liquid level in a hydraulic system with multiple tanks.

All obtained results are represented in simulations figures.

II. DTS<<200>> SYTEM MODELING

A. Description of DTS <<200>> System

The Three Tanks System is a widely recognized laboratory scale that has been extensively studied in various research fields [1]. This system is particularly useful in the analysis of linear and nonlinear systems, as well as multi-variable and feedback control systems such as Fault Detection and Isolation (FDI) and Fault-Tolerant Control (FTC) systems. The Three Tanks System is composed of three interconnected tanks with variable levels of liquid, and it serves as a great experimental platform for studying the behavior of hydraulic systems[8]. Researchers have used this system to test various control methods, including state feedback control, adaptive control, and fuzzy control, to improve its performance. With its ability to simulate real-world scenarios, the Three Tanks System has proven to be an excellent tool for researchers in the field of control systems engineering.
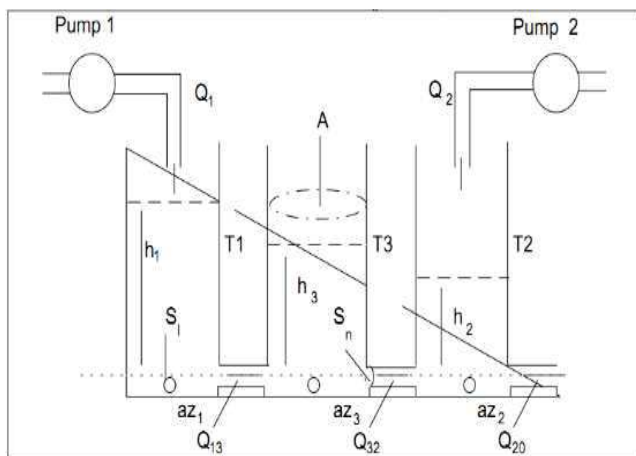

Fig 1 Diagram of three-tank system

Three-tank system under consideration in this study is the Amira DTS200 system, which is a well-known laboratory-scale system used for the analysis of linear, nonlinear, and multi-variable feedback control, as well as fault detection and isolation (FDI) and fault-tolerant control (FTC) systems [2]. The system consists of three cylindrical tanks, namely T1, T2, and T3, with a transversal constant section A, which are interconnected in series by means of cylindrical tubes with a transversal section S, as shown in Fig 1 (1). The system is designed to control the liquid level in each tank by manipulating the inflow rate of liquid into the system. This control is essential in many industrial applications to ensure the safety and efficiency of the system [9]. The DTS200

system is a nonlinear multi-variable system, which requires linearization around an operating point before applying control. In this study, we aim to apply state feedback control using the linear quadratic regulator (LQR) to the DTS<<200>> system to improve its performance. We also present a state observer and study its role in the system, estimate the vectors of states and disturbances, and evaluate the system's outputs and disturbances after applying the control on a non-linear DTS<<200>> real system.

B. Marhematical Model

The mathematical model of the three-tank hydraulic system is based on the mass balance equation of each reservoir. The mass balance equation for each tank takes into account the change in the liquid level over time due to the inflow and outflow rates [6]. The equation for tank 1, for example, can be expressed as the difference between the inflow and outflow rates equal to the change in the liquid level over time [10]. Similarly, the equations for tanks 2 and 3 can be written in a similar manner. These equations can be further simplified using Laplace transforms, which result in a set of first-order linear differential equations. By combining these equations and taking into account the hydraulic parameters of the system, a complete mathematical model of the three-tank hydraulic system can be developed.

$$\frac{dm}{dt} = A_n.\rho_n.\frac{dh_i}{dt} = \sum Q_{in} - \sum Q_{out} \tag{1}$$

Wich give
$$\begin{cases} A\frac{dh_1}{dt} = Q_1 \ _- Q_{13} \\ A\frac{dh_2}{dt} = Q_2 + Q_{32} - Q_{20} \\ A\frac{dh_3}{dt} = Q_{13} - Q_{32} \end{cases} \tag{2}$$

The symbols in equation (1) and (2) are detailed in TABLE I .

TABELE I Symbols of the studied system

Symbol	Description
A_n	The tank section
Q_1	Flow rate of pump P1.
Q_2	Flow rate of pump P2.
Q_{20}	Flow rate of tank T2
Q_{13}	Flow rate from tank T1 to tank T3
Q_{32}	Flow rate from tank T3 to tank T2
m	The mass of liquid
ρ_n	Fluid density
h_i	The level in tank i

The flow rate between a tank i and tank j is expressed as a function of heights h1, h2 and h3 by Bernoulli's equation as follows (3):

$$Qij = Sn.az, ij . sign (hi - hj) \sqrt{(2.g.|h_i - h_j|} \tag{3}$$

az,ij is the flow coefficient of the section connecting the element i to the element j via the V_{ij} valve [11]. The

discharge or disturbance rate for a tank is given by the following expression:

$$Qout = Sn, i \ (\ az, ij\sqrt{(2. g. h_i)}\ ) \qquad (4)$$

$$Qp, i = \ Sp, i \ . \ (\ az, ij\sqrt{(2. g. h_i)}) \qquad (5)$$

The system is nonlinear it nesseccery so to determinate a point around it one makes a linearization

C. Linearization of the system

In practice, a stationary linear system is generally considered to be easier to control, which often involves linearizing a nonlinear system about an operating point [12]. In the present case, the nonlinear model 2 can be assumed to have been solved for a nominal initial state $\tilde{X}$, a nominal input function $\tilde{U}$, and a nominal disturbance function $\check{V}$

$$\begin{cases} X = \tilde{X}(t) + \Delta X(t) \\ U = \tilde{U}(t) + \Delta U(t) \\ V = \tilde{V}(t) + \Delta V(t) \end{cases} \qquad (6)$$

The developed Taylor series of the variables in equation (6) are given below

$$X = \dot{\tilde{X}}(t) + \Delta \dot{X} = \ f\left(\tilde{X}(t) + \Delta X(t), \tilde{U}(t) + \Delta U(t), \tilde{V}(t) + \Delta V(t), t\right) \qquad (7)$$

$$\tilde{X}(t) + \Delta \dot{X} \triangleq f\left(\tilde{X}(t), \tilde{U}(t), \tilde{V}(t), t\right)$$
$$+ \frac{\partial f\left(\tilde{X}(t), \tilde{U}(t), \tilde{V}(t)\right)}{\partial U} . \Delta U(t)$$
$$+ \frac{\partial f\left(\tilde{X}(t), \tilde{U}(t), \tilde{V}(t)\right)}{\partial X} . \Delta X(t)$$
$$+ \frac{\partial f(\tilde{X}(t), \tilde{U}(t), \tilde{V}(t))}{\partial V} . \Delta V(t)$$
$$\qquad (8)$$

By removing higher order terms, we obtain
$$\dot{X} = A(t). x(t) + B(t). u(t) + E(t). v(t) \qquad (9)$$

After using JACCOBIAN matrix, we obtained:

$$\begin{cases} A(t) = \frac{\partial f(\tilde{x}, \tilde{u}, \tilde{v})}{\partial x} \\ B(t) = \frac{\partial f(\tilde{x}, \tilde{u}, \tilde{v})}{\partial u} \\ E(t) = \frac{\partial f(\tilde{x}, \tilde{u}, \tilde{v})}{\partial v} \end{cases} \quad \begin{cases} 0 = f(X_0, U_0, V_0) \\ X(t) = X_0 + \Delta X(t) \\ U(t) = U_0 + \Delta X(t) \\ V(t) = V_0 + \Delta V(t) \end{cases} \qquad (10)$$

$$\begin{cases} 0 = f(X_0, U_0, V_0) \\ X(t) = X_0 + \Delta X(t) \\ U(t) = U_0 + \Delta X(t) \\ V(t) = V_0 + \Delta V(t) \end{cases} \qquad (11)$$

$$\dot{X}(t) = \dot{X}_0 + \Delta \dot{X} \cong \ f(X_0, U_0, V_0) + \frac{\partial f(X_0, U_0, V_0)}{\partial X}. \Delta X(t) + \frac{\partial f(X_0, U_0, V_0)}{\partial U} \Delta U(t) + \frac{\partial f(X_0, U_0, V_0)}{\partial V}. \Delta V(t) \qquad (12)$$

$$A = \frac{\partial f(X_0, U_0, V_0)}{\partial x} = \begin{bmatrix} \frac{\partial f1}{\partial x1} & \cdots & \frac{\partial f1}{\partial xn} \\ \vdots & \ddots & \vdots \\ \frac{\partial fn}{\partial x1} & \cdots & \frac{\partial fn}{\partial xn} \end{bmatrix} \qquad (13)$$

$$B = \frac{\partial f((X_0, U_0, V_0))}{\partial u} = \begin{bmatrix} \frac{\partial f1}{\partial u_1} & \cdots & \frac{\partial f1}{\partial u_m} \\ \vdots & \ddots & \vdots \\ \frac{\partial fn}{\partial u_1} & \cdots & \frac{\partial fn}{\partial u_m} \end{bmatrix} \qquad (14)$$

$$E = \frac{\partial f((X_0, U_0, V_0))}{\partial v} = \begin{bmatrix} \frac{\partial f1}{\partial v_1} & \cdots & \frac{\partial f1}{\partial v_p} \\ \vdots & \ddots & \vdots \\ \frac{\partial fn}{\partial v_1} & \cdots & \frac{\partial fn}{\partial v_p} \end{bmatrix} \qquad (15)$$

n: the output number m: the number of entries. p: the number of disturbances[8]. In our system, we have: n=3, m=2 and p=3. According to these equations, our system gives the following results:

$$\begin{cases} A = \begin{bmatrix} -0.0105 & 0 & 0.0105 \\ 0 & -0.0201 & 0.0105 \\ 0.0105 & 0.0105 & 0.0209 \end{bmatrix} \\ B = \begin{bmatrix} 64.9351 & 0 \\ 0 & 64.9351 \\ 0 & 0 \end{bmatrix} \\ E = \begin{bmatrix} -0.0084 & 0 & 0 \\ 0 & -0.0059 & 0 \\ 0 & 0 & -0.0072 \end{bmatrix} \end{cases}$$

D. Simulation under Matlab

✓ Validation Linear model and operating point of the DTS<<200>> system :

We generated two blocks diagram within Simulink, operating under Matlab, to represent linear and nonlinear models of DTS<<200>>

Both the linear and nonlinear models were subjected to identical input signals.

The selection of our desired operating point was the result of numerous iterations, leading us to the following outcomes.

The selecting operating point

$$Xc1 \begin{bmatrix} 40 \\ 20 \\ 30 \end{bmatrix} \ \text{To} \ X_c \begin{bmatrix} 44 \\ 22 \\ 33 \end{bmatrix}$$
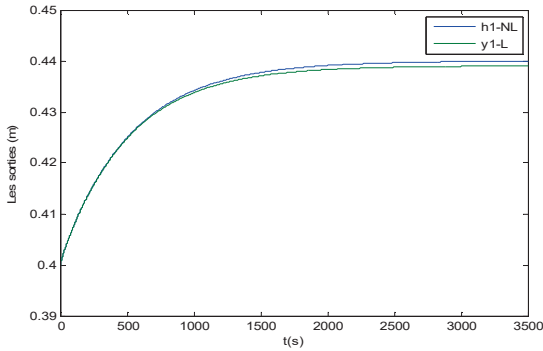
The outputs of L and NL models

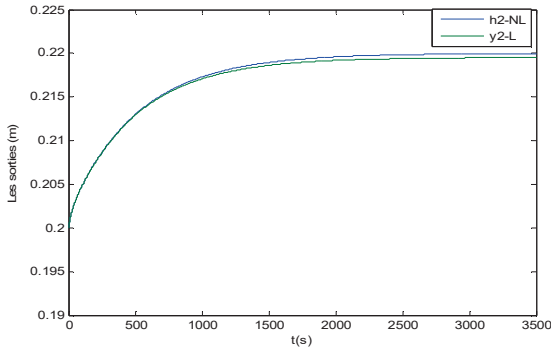Fig 2 The first outputs of Linear and Nonlinear DTS<<200>> models (m)

Fig 3 the seconds outputs of Linear and Nonlinear DTS<<200>> models (m)

Errors of modeling:

$$e1 = \frac{E*100\%}{0.04} = \frac{0.00103*100\%}{0.04} = 2.5\% \text{ (Error on first output } y_1)$$

$$e2 = \frac{E*100\%}{0.04} = \frac{0.000278*100\%}{0.04} = 2.25\% \text{ (Error on second output } y_2)$$

- Note that the variations on y1 and y2 are both small; we use this linear model in the rest of this work.

III. APPLYING QUADRATICAL LINEAR REGULATOR LQR ON DTS<<200>>
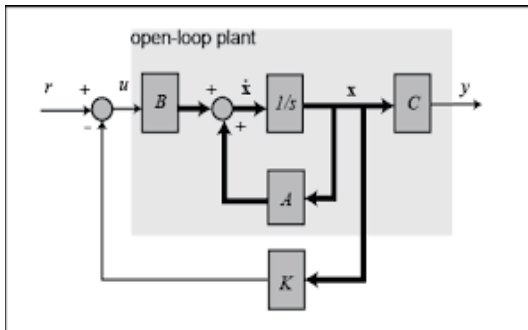
Fig 4 State feedback system

The LQR approach is about finding optimal control for systems by minimizing a cost function that combines state and input variables. It uses a gain matrix obtained from solving the Riccati equation to achieve this goal. LQR is commonly applied to linear systems and can also be adapted for nonlinear systems using different methods[3].

A. Consept of LQR

We have the system below:

$$\begin{cases} \dot{x}(t) = A.x(t) + B.u(t) \\ y(t) = C.x(t) \end{cases} \quad (16)$$

The classical LQR based optimal state-feedback controllers minimizes the quadratic cost function (17) with {x u,} being the state variables and control actions respectively[13].

$$J = \int_0^{+\infty}(x(t)^T.Q.x(t) + u(t)^T.R.u(t))dt \quad (17)$$

(Q, R are symmetric positives matrix)[14].

Minimization of the integral performance index (17) leads to the solution of continuous time Riccati equation given by (18) to find out the state-feedback control law (19)

$$P.A + A^T.P - P.B.R^{-1}.B^T.P + Q = 0 \quad (18)$$
$$u(t) = -k.x(t) \quad (19)$$

The gain matrix is given by

$$k = R^{-1}.B^T.P \quad (20)$$

Note: A condition to apply LQR on that system it must be controllable and observable system[15].

B. Application on DTS<<200>> system

Using Matlab, we verified the controllability and observabillity of our system DTS<<200>>[12].

C. Choosing of Q and R Matrix

Our choice is basing on maximum outputs and maximum controls[13]:

$$h_{1max} = 0.6 \quad h_{2max} = 0.4 \quad h_{3max} = 0.5$$

$$u_{1max} = 10^{-4} \quad u_{2max} = 10^{-4}$$

$$Q = \begin{pmatrix} 3.34 & 0 & 0 \\ 0 & 0 & 0 \\ 0 & 0 & 0.24 \end{pmatrix} \quad R = \begin{pmatrix} 5.74 & 0 \\ 0 & 0.7719 \end{pmatrix}$$

D. Calculating P matrix and the eigenvalues of vector e, and the gain matrix K:

We us the next formula on Matlab:

[K, P, e]= lqr (A, B, Q, R] we obtained the following results

$$P = 10^5 \begin{pmatrix} 0.6562 & 0.1626 & 0.9461 \\ 0.1626 & 0.17 & 0.24 \\ 0.9461 & 0.2465 & 0.939 \end{pmatrix}$$

$$e = \begin{pmatrix} -0.0536 \\ -0.0226 + 0.0005i \\ -0.0266 - 0.0005i \end{pmatrix}$$

$$K = 10^{-3} \begin{bmatrix} 0.6392 & 0.0178 & 0.1058 \\ 0.107 & 0.0900 & 0.2026 \end{bmatrix}$$

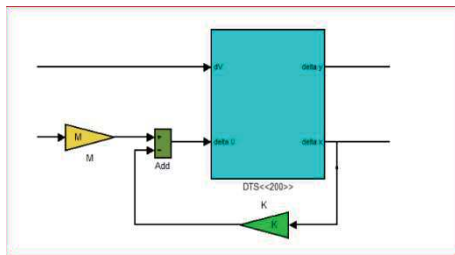## E. *Display output on Matlab Simulink space*

Fig 5 Block diagram of simulation of the application of the control by state feedback

Under Similink space under Matlab we created the block diagram in Fig 5, we obtained the following figures
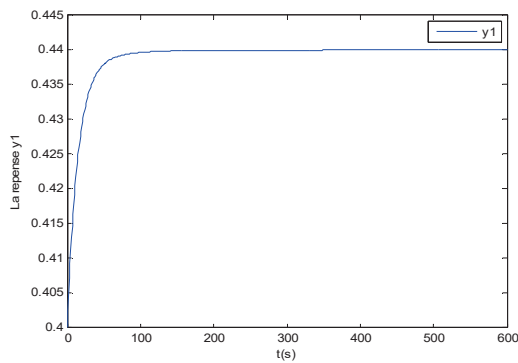

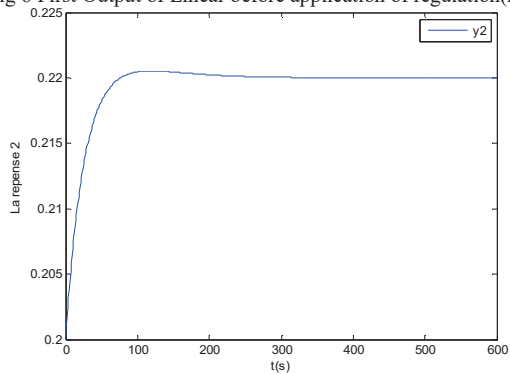Fig 6 First Output of Linear before application of regulation(m)

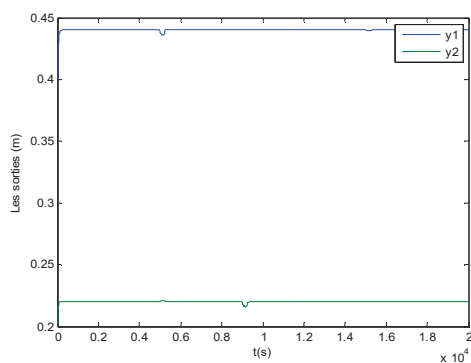Fig 7 Second Output of Linear before application of regulation (m)

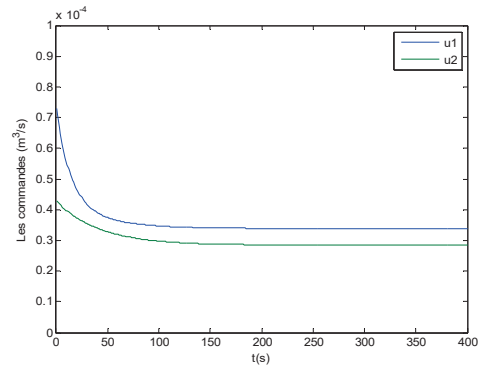Fig 8 Outputs of system after regulation under disturbances affect (m)

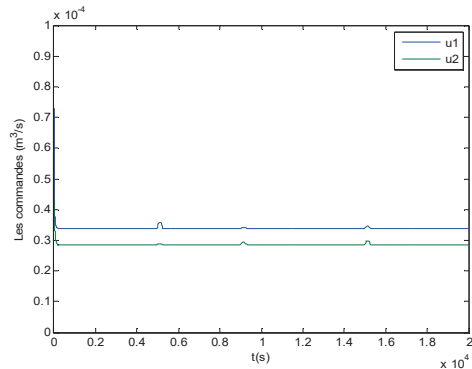Fig 9 System controls before regulation (m³/s)

Fig 10 System controls after regulation (m³/s) under disturbances

Note : y 1 and y2 are the outputs of the Linear DTS<<200>> model, u1 and u2 are the system controls

*Resuslts: The following table summarizes the results obtained after applying LQR on the DTS<<200>> system:

TABLE II summary table of the results of the LQR application on the DTS<<200>>

On output	y_{1L}	y_{2L}
A disturbance on y1 (5000s<t<5200)	A variation of 7%	A variation of 4%
A disturbance on y2 (9000<t<9200)	A Variation 0.5%	A Variation 17.5%

The LQR approach is employed to enhance the correction of the DTS <<200>> system by achieving quicker responses and reducing control efforts.

When applied to the nonlinear three-tank system (a real-world application), it demands a deep understanding of the system's state and precise determination of the disturbance vector. This necessitates the use of a state observer to estimate both the state and disturbance vectors, enabling control that is more effective. The next phase involves designing an accurate observer for estimating these vectors in the three-tank system.

IV. OBSERVER SYNTHESIS AND OBSERVATION OF DTS<<200>> LINEAR SYSTEM STATES

To deal with the problem of estimating the state of linear deterministic systems LUENBERGER has proposed an optimal solution.[5] For system in (12) we used the linear observer below

$$\begin{cases} \dot{\hat{x}} = A\hat{x}(t) + Bu(t) + L(y(t) - \hat{y}) \\ \hat{y} = C\hat{x}(t) \end{cases} \Longrightarrow$$

$$\begin{cases} \dot{\hat{x}} = A\hat{x}(t) + Bu(t) + L(y(t) - \hat{y}) \\ \hat{y} = C\hat{x}(t) \end{cases} \qquad (21)$$

$$e(t) = x(t) - \hat{x}(t) \qquad (22)$$

$$\text{Or } \dot{e} = (A - LC)e(t) \qquad (23)$$

A. *Estimate DTS<<200>> linear states and errors*

The eigenvalues of $A - LC$ are fixed arbitrarily if the system (16) is observable.

We use Matlab function *plac* to calcule L matrix: $L^T = place(A^T, C^T, P)$ / $P = 2 * P_{BF}$
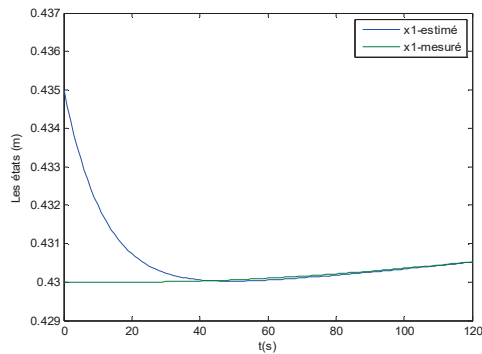

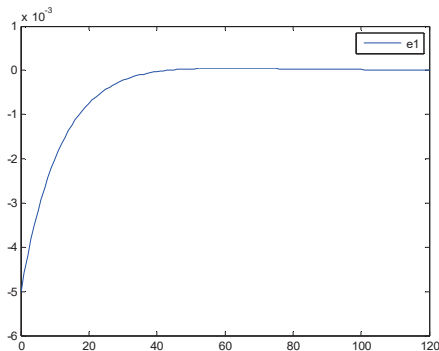Fig 11 The first measured and observed states

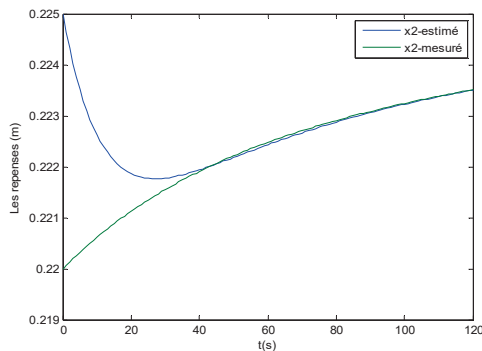Fig 12 Estimation error on the first state

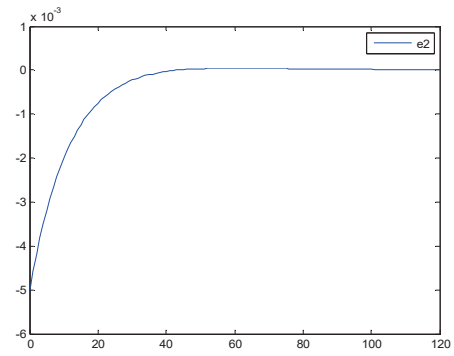Fig 13 The second measured and observed states

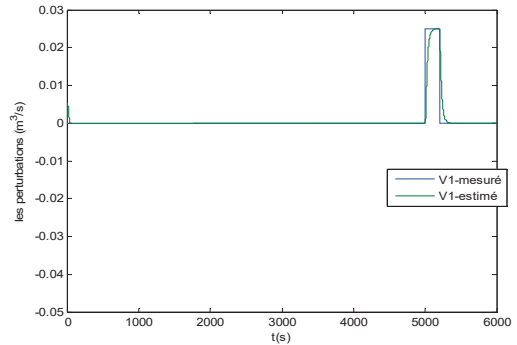Fig 14 Estimation error on the second state

Fig 15 the estimated perturbation vector

We observed that the estimation errors tend to converge to zero, indicating that the estimated states closely follow the true system states. Similarly, the estimated disturbance vector follows the system disturbance vector, even in the presence of additional disturbances. This highlights the effectiveness of the state observer in accurately estimating the system states and disturbances

B. *Association of stats feedback control and observation on the DTS <<200>> system*

The obtained control law given by equation (24*)*.

$$\hat{u} = -k\hat{x} + My_c \qquad (24)$$

(M is pre-compensation matrix)

Application on the DTS <<200>> linear model

In this part we created, a block diagram combined the state feedback control and the linear observer (Fig 15)
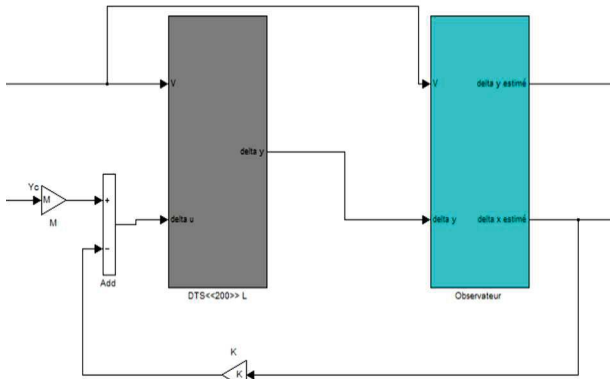
Fig 16 Block Diagram of DTS <<200>> Linear System Association of state feedback and observation

After simulation, we obtained the simulating responses below.
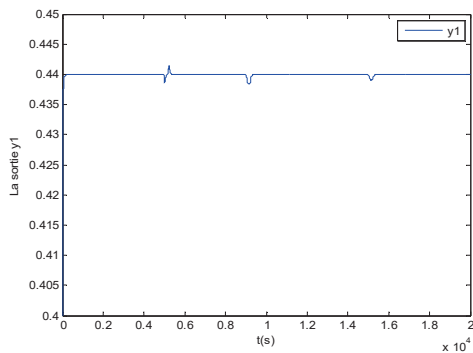

Fig 17 First output of DTS<<200>> Linear system outputs under disturbances effect (m)
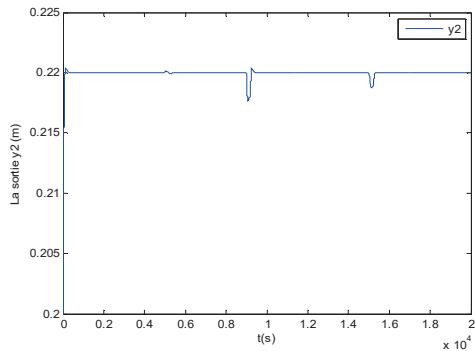
Fig 18 Second output of DTS<<200>> Linear system outputs under disturbances effect (m)
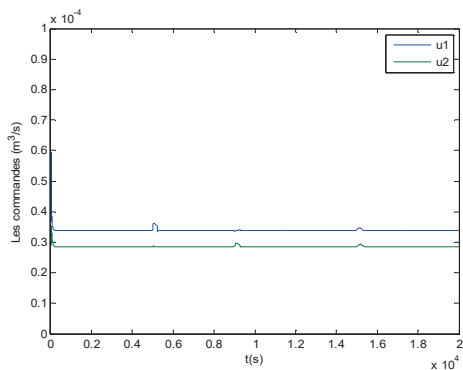
Fig 19 DTS<<200>> Linear system controls under disturbances effect (m^3/s)

On the DTS <<200>> nonlinear model:
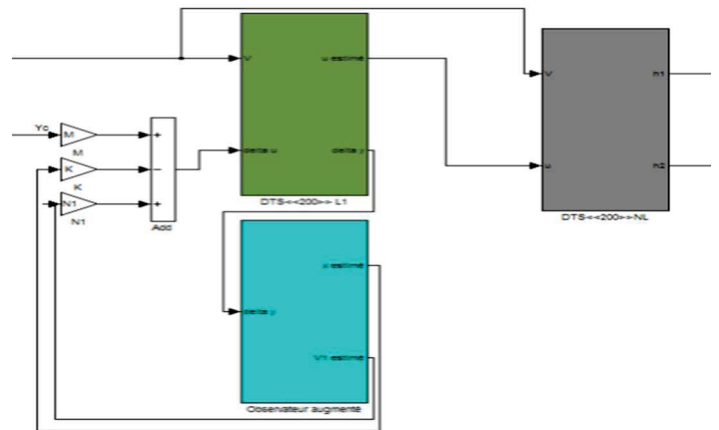
Fig 20 Block Diagram of DTS <<200>> nonlinear System Association of state feedback and observation
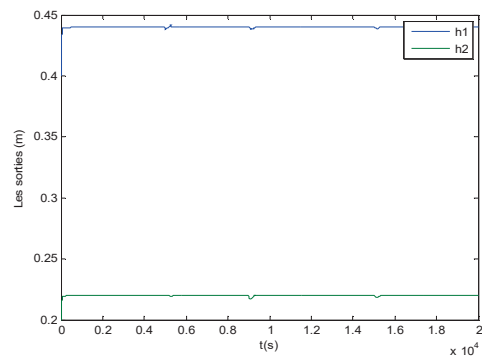
Fig 21 Outputs of Nonlinear DTS<<200>> system under disturbances effects (m)
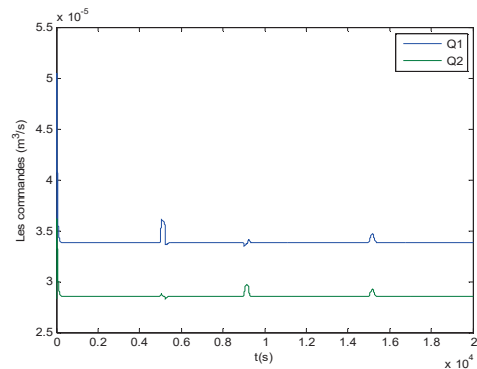
Fig 22 Controls of Nonlinear DTS<<200>> system under disturbances (m^3/s)

Note : h1 and h2 are the output of nonlinear DTS<<200>> system (Tank1 and Tank 2 levels), Q1 and Q2 are the control of the nonlinear system (Flow rates of pumps 1 and 2).

- *Comparative Study*

The following tables summery the results of simulation after application of LQR regulation on Linear and Nonlinear DTS<<200>> models.

TABLE III Effect of disturbances in BO and BF without and with compensation

	The variations due to the effect of disturbances without correction on		Variations due to the effect of disturbances with correction and without compensation on		Variations due to the effect of disturbances with correction and with compensation on	
	Y1	Y2	Y1	Y2	Y1	Y2
Disturbance 2.5% on Y1 (5000s<t<5200)	40%	21%	7.3%	4%	3.5%	0.5%
Disturbance 2.5% on Y2 (9000s<t<9200)	7%	33%	0.25%	17.5%	4%	11.5%

TABLE IV Comparison of L and NL system outputs

Linear DTS <<200>> System outputs (m)		Non Linear DTS <<200>> System outputs (m)		The modeling error	
y1	y2	h1	h2	on y1	on y2
0.4392	0.2196	0.44	0.4392	0.2%	0.2%

Using state feedback control on the nonlinear DTS<<200>> system allows for prediction of system outputs.

However, modeling errors can affect both linear and nonlinear systems. To address this, estimated outputs based on available measurements are used to control the real system, but the quality of the estimate is crucial, as it affects the difference between the linear system outputs and the estimated ones, as well as the disturbance vector. Ultimately, the goal of controlling the real DTS 200 system using state feedback has been successfully achieved.

V. CONCULUSION

The primary aim of this research is to investigate the control of a hydraulic system, namely the DTS<<200>> with three tanks, using the control by state feedback through the calculation of the gain matrix using the linear quadratic regulator (LQR) approach. The DTS<<200>> is a multivariable input feedback control system based on the linear quadratic LQR control, which computes the gain matrix and three outputs, of which two are controllable. In this study, we selected a mathematical model for the system based on a state representation, which was validated through simulation, and used thereafter. The main objective of the research is to control the h1 and h2 levels of the DTS<<200>> system by state feedback to reach a specific set point. We chose this command approach because it does not require precise parameterization and modeling accuracy. Moreover, the use of the LQR approach to calculate the gain matrix improves system performance, resulting in faster responses and weaker commands, which minimizes time and energy. Due to the unavailability of real measurements, a linear observer was proposed to estimate the state vector and disturbances. Finally, based on the simulation results, we concluded that the control by state feedback using the LQR approach to calculate the gain matrix leads to an enhanced system performance and enables the achievement of the objective of controlling the tank level while minimizing costs and energy.

References

[1] C. A. Neto and M. Embiruçu, "Tuning of PID Controllers: An Optimization-Based Method," *IFAC Proc. Vol.*, vol. 33, no. 4, pp. 367–372, Apr. 2000, doi: 10.1016/S1474-6670(17)38271-X.

[2] "[PDF] Comprehensive Model of DTS 200 Three Tank System in Simulink | Semantic Scholar." Accessed: Oct. 11, 2023. [Online]. Available: https://www.semanticscholar.org/paper/Comprehensive-Model-of-DTS-200-Three-Tank-System-in-Chalupa-Nov%C3%A1k/ccaf595f2b7f3971a0ecbb82bb77878f1e194954

[3] L. Kovács, "Classical and Modern Multivariable Control Designing Methods of the Three Tank System," vol. 48, pp. 1224–600, Jan. 2003.

[4] P. Chalupa, J. Novák, and V. Bobál, "Detailed Simulink Model of Real Time Three Tank System".

[5] J. Kortela, "Model-Predictive Control for the Three-Tank System Utilizing an Industrial Automation System," *ACS Omega*, vol. 7, no. 22, pp. 18605–18611, Jun. 2022, doi: 10.1021/acsomega.2c01275.

[6] É. C. de Lille, "Analyse et régulation des processus industriels," *Pierre Borne Geneviève Duphin-Tanguy Jean-Pierre Richard Frédéric Rotella Irène Zambettakis Paris Éditions Tech.*, vol. 2, 1993.

[7] P. Chalupa and J. Novák, "Modeling and model predictive control of a nonlinear hydraulic system," *Comput. Math. Appl.*, vol. 66, no. 2, pp. 155–164, 2013.

[8] H. Wang, H. Dong, L. He, Y. Shi, and Y. Zhang, "Design and Simulation of LQR Controller with the Linear Inverted Pendulum," in *2010 International Conference on Electrical and Control Engineering*, Jun. 2010, pp. 699–702. doi: 10.1109/iCECE.2010.178.

[9] J. L. Mata-Machuca, R. Martínez-Guerra, and D. Hernández-Sánchez, "Fault diagnosis for a class of nonlinear systems by means of a polynomial observer," in *2010 7th International Conference on Electrical Engineering Computing Science and Automatic Control*, Sep. 2010, pp. 158–163. doi: 10.1109/ICEEE.2010.5608644.

[10] "Detailed Simulink model of real time three tank system | Proceedings of the 2nd international conference on Circuits, Systems, Communications & Computers." Accessed: Oct. 11, 2023. [Online]. Available: https://dl.acm.org/doi/abs/10.5555/2209450.2209477

[11] "Linear Systems Control: Deterministic and Stochastic Methods | SpringerLink." Accessed: Oct. 11, 2023. [Online]. Available: https://link.springer.com/book/10.1007/978-3-540-78486-9

[12] "Fault diagnosis for a class of nonlinear systems by means of a polynomial observer | IEEE Conference Publication | IEEE Xplore." Accessed: Oct. 11, 2023. [Online]. Available: https://ieeexplore.ieee.org/abstract/document/5608644

[13] S. Das, I. Pan, K. Halder, S. Das, and A. Gupta, "Optimum weight selection based LQR formulation for the design of fractional order PID controllers to handle a class of fractional order systems," in *2013 International Conference on Computer Communication and Informatics*, Coimbatore, Tamil Nadu, India: IEEE, Jan. 2013, pp. 1–6. doi: 10.1109/ICCCI.2013.6466137.

[14] "Data-based Analysis and Control for Nonlinear Dynamical Systems - ProQuest." Accessed: Oct. 11, 2023. [Online]. Available: https://www.proquest.com/openview/6c5059802d10b6fb92f4446aa0506f94/1?pq-origsite=gscholar&cbl=18750

[15] "Controllability and Observability | SpringerLink." Accessed: Oct. 23, 2023. [Online]. Available: https://link.springer.com/chapter/10.1007/978-94-011-5654-7_9

Enhancing Environmental Sustainability and Operational Efficiency in Cement Manufacturing through Advanced PLC-Based Technology: A Case Study from Meftah Cement Plant

Samira Hadibi
Laboratory of Applied Automation
Department of Automation
Faculty of Hydrocarbons and
Chemistry, University M'hamed
Bougara
Boumerdes, Algeria
s.hadibi@univ-boumerdes.dz

Prof. Majid Kidouche
Laboratory of Applied Automation
Department of Automation
Faculty of Hydrocarbons and
Chemistry, University M'hamed
Bougara
Boumerdes, Algeria
kidouche_m@hotmail.com

Dr. Mohamed Zinelabidine Doghmane
Laboratory of Applied Automation
Department of Automation
Faculty of Hydrocarbons and
Chemistry, University M'hamed
Bougara
Boumerdes, Algeria
doghmane_m@yahoo.com

Abstract—The Meftah cement plant's commitment to environmental sustainability has led to the implementation of a comprehensive industrial pollution control program, primarily utilizing bag filters to mitigate the impact of dust emissions from cement manufacturing processes. This initiative aligns with stringent environmental standards set forth in performance contracts. To address operational challenges, particularly related to cleaning processes, servicing, and maintenance, the Meftah cement plant (S.C.M.I) has embarked on an upgrade of the filtration workshop. This upgrade seeks to optimize the overall operation and sequencing of the pollution control system. This study focuses on overcoming operational challenges and improving system efficiency by addressing the sequencing problem. To achieve this, we propose the replacement of the existing SEFRAM SFX+ sequencer-based control system with advanced SIMATIC S7300 SIEMENS PLC-based technology. The SIEMENS PLC technology offers adaptability to dynamic environments and is widely acknowledged in modern industries. The study begins by outlining the filtration process, followed by a detailed account of the migration strategy and the comprehensive system supervision approach undertaken. This project exemplifies the latest trends and innovations in engineering, procurement, and construction (EPC) within the cement manufacturing sector, contributing to the ongoing pursuit of sustainable and optimal maintenance management.

Keywords—component, Cement manufacturing, Environmental sustainability, Pollution control, PLC-based technology, digital sequencer, S7-300.

I. Introduction

Cement is the basic product resulting from the combination of the following raw materials: Limestone, clay, sand and iron ore. These materials are extracted from the rock surfaces of a quarry, then they are crushed into smaller size pieces by the crusher at the Quarry. After a proper proportioning, the raw materials are, then, blended and further ground into smaller pieces, called raw meal, in the cement plant. After final grinding, comes the calcination phase which is the core phase of the cement making process and takes place at a rotary furnace called kiln. Before entering the kiln, the raw meal passes through the pre-heating chamber which consists of series of vertical cyclone,

then, it is heated to a sintering temperature as high as 1450 °C in the rotary kiln. This high temperature initiates a series of chemical reactions between the materials compounds, which eventually turn the raw meal into cement clinker. The hot clinker discharged from the rotary kiln is cooled by mean of forced air which is extracted from the outer atmosphere by grate cooling fans. The excess air is drawn off at the cooler outlet by two draught fans through a bag filter to depollute the released gas from any clinker residual. The filtered gases are expelled into the atmosphere and the recovered clinker is reused by recirculating it back to the kiln. Afterwards, the clinker is grinded and is mixed with gypsum and tuff at different dosages to obtain the cement. The finished product is, then, shipped in bags or in bulk [1].

The Meftah cement plant has opted to upgrade the filtration system responsible for environmental protection during the calcination phase, which has a number of drawbacks, including the need to control and supervise cleaning processes, and the difficulties encountered in servicing and maintaining the equipment. To overcome the current operating issues, we propose to replace the existing SEFRAM SFX+ sequencer-based control system with a SIMATIC S7300 SIEMENS PLC-based technology, which provides a high degree of adaptability to changing environments and is widely used in modern industry.

II. The Bag Filter Operational Description

A. Bag Filter

The Bag Filter separates dust from the exhaust gas by collecting them with the filter media. The dust is accumulated on the surface of filter media. And the filter media is cleaned by reverse airflow called backwashing (pulse-jet), "Fig .1".

Our project is based on an industrial-scale bag filter located downstream of a rotary cement kiln. It is divided into two compartments (filtration chamber), north and south. Each has up to 1,000 filter bags. A bag filter can be divided into the followed components [2]:

1) The Inlet: The filter is connected to a supply of dusty air stream, this supply must ensure a good distribution of air over the entire filtering surface.

2) Filteration chamber: Dust collector body in which vertical filter bags are suspended.

3) Bag Filters: A filter bag consists of a metal frame on which a filter medium is placed. It ensure dust retention; which is in industrial terms 'the cake', and filtration.

4) The filtered air compartment: all the filter bags has an open to this compartment, hence, the filtred air is collected. It contains compressed air tanks in the form of horizontal cylinders.

In our filter, there are 40 cylinders of compressed air. Each one is connected to an isolation valve. From each cylinder, five (05) compressed air supply manifolds circulate above the filter bags, and they are connected to 05 unclogging solenoid valves. These compartments represent the unclogging air injection systems.

5) The hopper: This assembly must ensure the continuous evacuation of the dust stopped by the filter. The hopper is equipped with a vent to ensure that this evacuation must take place without any air inlet or outlet which may cause a vacuum in the filter.
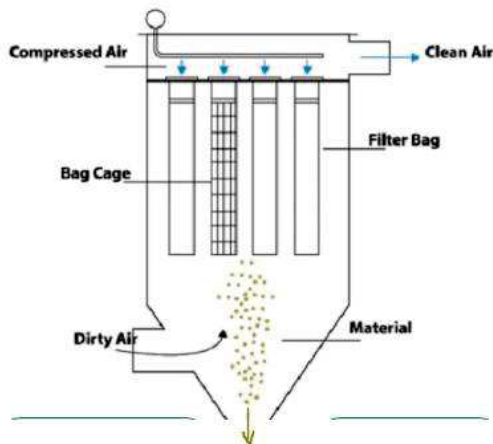

Fig. 1. Bag Filter dust collector

B. Bag Filter Operating Principle

1) Clogging: The dust-laden air which is aspirated into the filtration chamber by two draining ventilators. The large dust particles encounter a deflector and fall directly into the drum, while the rest is carried up by the airflow and attache itself to the filter elements. The latter is made up of several filter cells. The gases pass through the filter cells, from the outside inwards, and the dust accumulates on the filter medium called the dust cake[3].

2) Unclogging: As a result of cake formation, an increase in pressure drop is measured, which is defined as the static pressure difference between upstream and downstream of the filter medium. Therefore, filter elements must be periodically cleaned by reverse airflow. Cleaning is done by activating solenoid valves, one by one, that injects, in counter-current, a compressed air through the filter elements, which enables the dust cake to detach from the filter medium and rinses the filter bags.

The injection of the compressed air is managed by an SFX+ sequencer, which switches on and off the solenoid valves by analyzing the pressure drop measured by a differential pressure switch. If the pressure difference exceeds a predefined value, unclogging is triggered *[3]*.

3) Recovery phase: The dust is collected in one or more hoppers at the bottom of the filtration chamber, which are then evacuated by a rotary airlock. The filtered air is, then, exhausted via the chimney to the atmosphere [3].

III. BAG FILTER INSTRUMENTATION

A. Pressure switch

A pressure switch is a form of switch that operates an electrical contact when a certain set fluid pressure has been reached on its input. Many pressure switch offer an additional analog signal proportional to the pressure. As a result, not only is it identified whether the defined switching point is reached, but the measured real pressure is transmitted [4].

B. Differential pressure switches

The Differential pressure switches have been developed to activate an electrical contact when the difference between 2 pressure values of a process is greater than the defined limits. This pressure difference may be too high or too low [4].

C. Pt100

It is a type of resistance temperature sensor designed for temperature measurement in liquids and gases [4].

D. Rotary Airlock Valve

The Rotary Airlock Valve : the metal blades of a rotary airlock valve turn during operation. As they do, pockets form between them. The material being handled enters the pockets through the inlet port before rotating around inside the valve and then exiting through the outlet port [4].

IV. THE ACTUAL CONTROL SYSTEM

A. SFX+ Digital Sequencery

The SFX+ is a modular sequencer with differential or relative pressure measurement. It is used to control and monitor compressed air injection dust removal equipment. Its program is not accessible. Only the cleaning parameters are accessible and adjustable by the user [5].

B. SFX+ Operating mode

The SFX+ controls the filtration process, with six (06) sequencers installed within the filter. These sequencers are dedicated to controlling the bag filter unclogging unit. This unit is composed of 40 compressed air tanks (20 tanks for the north filter and 20 tanks for the south filter) and each of these tanks carries 05 solenoid valves (40 x 05 = 200 EV).

Each 02 solenoid valves are wired to the same output, so 100 outputs are used for the solenoid valves.

If the pressure drop exceeds a predefined value, $\Delta P > 110$ (mmH2O), the cleaning cycle in normal mode, OM1, starts by activating the solenoid valves cyclically, one after the other, each for a set time T1, from 1(s) to 255 (s). The rest

time between each two solenoid valves is defined as T2. The cleaning cycle is resumed after a rest time T3, adjustable from 0(s) to 255 (s) [5].

The accelerated cleaning cycle, OM2, starts if ΔP exceeds 160 (mmH2O), with a shortened T2 time.

A T4 time can be set in hours, to start an unclogging cycle if the sequencer has not operated for that time.

The compressed air spray sequence is set identically for both north and south filters, and is performed on the EVs of the first 10 tanks, as the cleaning sequence for the EVs of the remaining 10 cells is identical, since they are wired to the same outputs.

The control of each EV, associated with any non-isolated tank, is carried out with pressure control by a pressure switch. Sequencer outputs are indicated by LEDs.

C. The Sequencer inconvenient

- Centralized system
- No history to analyze operation
- Program not accessible
- High cost of cabinets

V. PROGRAMMABME LOGIC CONTROLLER PLC

A programmable logic controller, or PLC, is a programmable electronic device designed to control industrial processes using sequential processing. It adapts to the industrial environment, and performs automation functions to control pre-actuators and actuators using logic, analog or digital information.

The main strength of a PLC lies in its ability to communicate with the industrial environment via multipoint interfaces (MPI) and PROFIBUS-DP. In addition to its central processing unit with a wide range of CPUs. It is essentially made up of input/output modules, which can be extended up to 32 modules, serving as a communication interface with the industrial control process[6].

Its main advantages over the sequencer are :

- Ensures acquisition of sensor data, with access to the database
- Facilitates process maintenance
- Guided program manipulation
- Possibility of remote control (HMI interface)

In order to overcome the problems observed in the existing system, and with the aim of facilitating operations for the company's employees, SCMI's maintenance department proposed replacing the control system in use (SFX+ sequencer) with a SIMATIC S7-300 SIEMENS PLC.

VI. SIMATIC S7-300 PLC CONSTITUTION [7]

A. Power Supply module (PS)

In our project, we chose a "PS 307 10 A1" power supply module.

B. Central Processing Unit module

The 315C-2DP CPU was chosen for its extensive programming memory capacity, as well as its master/slave interface.

C. Input/Output module

The According to the system's I/O identification, there are:

1) Digital input/output modules: The TOR inputs counted for our project represent 4 inputs plus a safety margin of 10%, so we have 5 TOR inputs. Therefore, we selected: a module with 8 digital inputs / DI 8*24 VDC.
The number of digital outputs evaluated for our project represents 292 outputs plus a safety margin of 10%, so we have 322 digital outputs.
We have reduced the number of digital outputs by activating 2 solenoid valves at the same time (from 2 different cylinders to avoid jamming), given : Limited number of timers (256), large number of I/O modules required and wiring.
Hence the digital output count becomes 192 outputs plus a 10% safety margin, giving 212 digital outputs.
So we chose: 07 Module with 32 outputs / DO 23*24 VDC

2) Analog I/O modules: To change The set of analog inputs/outputs chosen for our project represents43 inputs plus a margin of 10%, so we have 48 inputs.
Thus we have used a module with 8 inputs: 06 Module Analog inputs / AI 8*16BIT

D. Coupler (IM)

Not used in our project.

E. Extention Chassis (UR) module

Not used in our project.

F. CP modules (Communication Port)

Not used in our project.

VII. SIMATIC S7-300 PROGRAMING

A programmable To control our bag filter, we'll create a program and implement it in the S7-300 PLC using SIEMENS' TIA PORTAL program design software for automation systems, including SIMATIC STEP 7 and SIMATIC Wincc, and PLCSIM program simulation.

TIA PORTAL software enables programming of the S7-300 PLC in [8] :

- GRAFCET (SFC)
- Block diagram (FBD)
- Relay Diagram (LD)
- Structured text (ST)
- Instruction list (IL)
- Contact diagram (CONT): This is the chosen programming language for our project

VIII. BLOC ORGANIZATION AND PROGRAMING

Programming in TIA PORTAL takes place in different blocks. There are the code blocks (OB, FB, SFB, FC, SFC), which contain the programs, and also the instance DB and global DB data blocks, which contain the program parameters.

Our project contains 01 OB1 organization block, 09 function blocks (FC1...FC9) and 02 DB data blocks[9].

A. Bloc OB1

This block is generated automatically when a project is created, and is the cyclic program called by the operating system. In this block we write our main system program and call the functions and data blocks we've programme, "Fig .2"
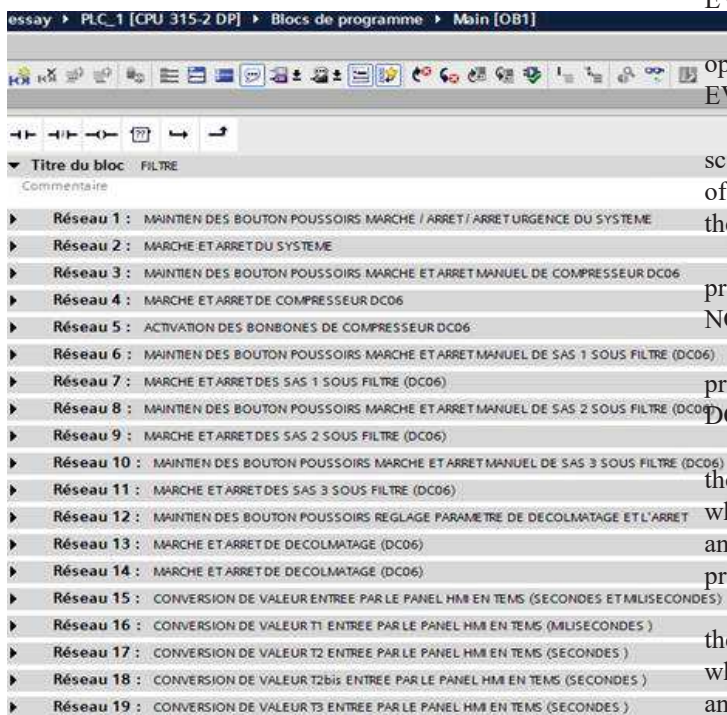

Fig .2. OB1 view

B. Data Bloc DB1

This This These data blocks are used purely to store information and data.

In our program, we used block DB10, which contains the following memory addresses: declogging times (T1, T2, T2bis and T3), as well as the number of solenoid valves to be forced, the number of cylinders to be deactivated and the maximum filter threshold ΔP. These values are specified via the HMI interface.

The DB20 block contains the temporary reservation variables used to convert the time values entered by the HMI into usable values for the program.

C. Function Bloc FC, SFC

The FC block is used for frequently used functions. It has no memory and saves its temporary variables in the local data stack and refers to the global data blocks to save its data.

In our project, we used 09 function blocks (FC1...FC9) as follows:

1) *FC1 Bloc:* We created this block to program the opening/closing cycle of the solenoid valves (from EV1 to EV25 of the DC06 north filter) with a compressed air injection time (solenoid valve activation) of a few milliseconds (T1) and a rest time between 2 compressed air injections of a few seconds (T2 / T2bis).authors.

2) *FC2 Bloc:* To This block is used to program the opening/closing cycle of solenoid valves (from EV 26 to EV50 of the DC06 north filter).
We've also added an additional network in the same block to program the T3 time, which represents the rest time between two cycles.

3) *FC3 Bloc:* We've created this block to program the opening/closing cycle of the solenoid valves (from EV51 to EV75 of the DC07 southern filter).

4) *FC4 Bloc:* The FC4 block is used to program the opening and closing of solenoid valves (from EV76 to EV100 of the DC07 southern filter).

5) *FC5 Bloc: T*he FC5 block contains the program for scaling the differential pressure measurement ΔP (mmH2O) of the north and south filter, and the temperature T (°C) at the filter inlet.

6) *FC6 Bloc:* This block contains the pressure scaling program (bar) for the 20 compressed air cylinders of the NORD DC06 filter.

7) *FC7 Bloc:* This block contains the pressure scaling program (Bar) for the compressed air cylinders of the SUD DC07 filter.

8) *FC8 Bloc:* This block has been created to program the turn-on of the 20 cylinders of the NORD DC06 filter when the compressed air pressure in the cylinder is 5 bar; and the refilling of the cylinders when the compressed air pressure falls below 03 bar.

9) *FC9 Bloc:* This This block is also used to program the functioning of the 20 cylinders of the SUD DC07 filter when the compressed air pressure in the cylinder is 5 bar; and the filling of the cylinders when the compressed air pressure falls below 03 bar.

10) *SFC blocks:* These blocs are used for special functions integrated into the S7 CPU. Not used in our project.

D. Function Bloc FB, SFB

The FB is a sub-program written by the user and executed by code blocks. It is associated with an instance data block relative to its memory and containing its parameters. SFBs are used for special functions integrated into the CPU. Not used in our project.

E. Variable Table

In the TIA portal environment, it is necessary to define the list of variables that will be used during programming. When you define a PLC variable, you need to associate it with: a name, the data type and the absolute address. In our program, we have used binary (Bool, Word,…), numerical (Int, Real,...) and temporal (Time,...) data types [9].

F. Improvements adopted in the program

- The pressure drop threshold to activate accelerated mode may be modified

- Possibility of triggering an EV to detect a malfunctioning EV

- Air tanks are refilled just when their pressure drops below 03 bar.

- Possibility of isolating a cylinder for maintenance purposes

- Manual start and stop

- Alarm triggering

IX. PROGRAM SIMULATION

The RUNTIME and the S7-PLCSIM PLC simulation software application are used to create a direct link between TIA portal and the S7-300, allowing us to run and test our program virtually, and remedy any errors, without having access to the target hardware.

To run the simulation, we need to load the program already written into the S7-300 PLC's CPU, then compile it to make it executable by the CPU, "Fig .3".
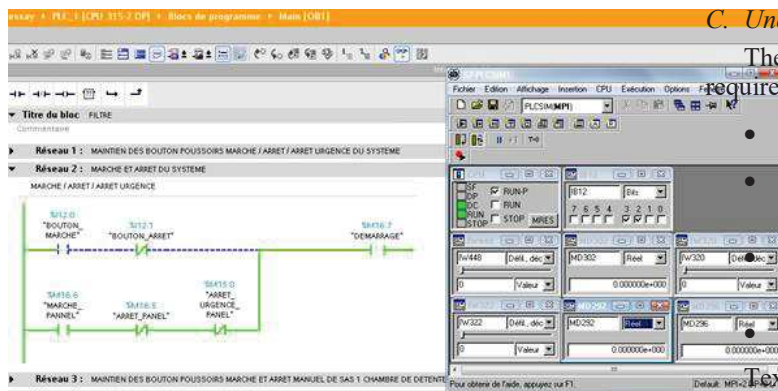

Fig .3. S7-PLCSIM Simulation

X. WINCC IN TIA PORTAL

WinCC in TIA Portal allows you to create views for monitoring, controlling and visualizing the system. For creating views, predefined objects are provided that can be used to display procedures and define process values.

To control and command the process, we've configured 07 views that enable us to consult and command the process value.

A. Main View

It is the process view, and includes all sub-processes which are represented in separate views. They can be accessed by pressing the desired button, "Fig .4".
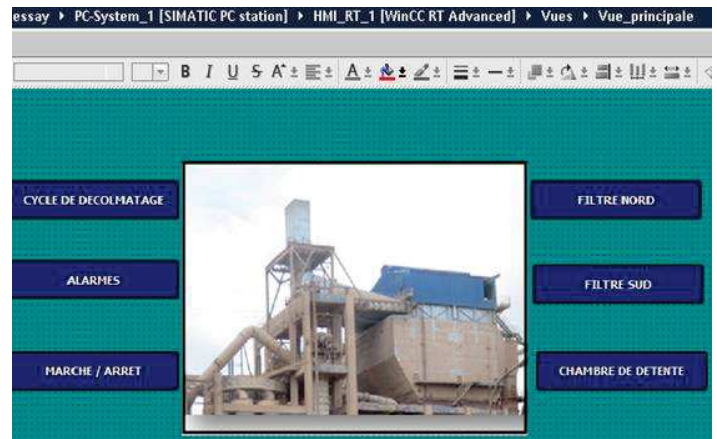

Fig .4. Main View

B. Start/Stop View

It is the This view is used to start, stop and the emergency stop of the process, as well as selecting the automatic or manual operating mode of each device.

Button configuration: each button is animated by a color: green (start), RED (stop), YELLOW (emergency stop) and BLUE (automatic mode).

C. Unclogging Cycle View

The unclogging view allows us to insert the time values required for unclogging:

- T1: EV activation time.

- T2: rest time between two compressed air shots (normal cycle).

T2bit: rest time between two compressed air shots (accelerated cycle).

- T3: rest time between two cycles.

Text On the other hand, it allows us to set the maximum threshold value of the differential pressure in the filter.

Each button is animated by a color: RED (Stop unclogging), GREEN (Parameter setting).

D. North DC 06 filter View

It is a detailed view, showing the north filter and all the cylinders, solenoid valves, rotary SAS, compressor, conveyor belt and piping. It also shows the buttons and ΔP pressure indicator in the filter, "Fig. 5".
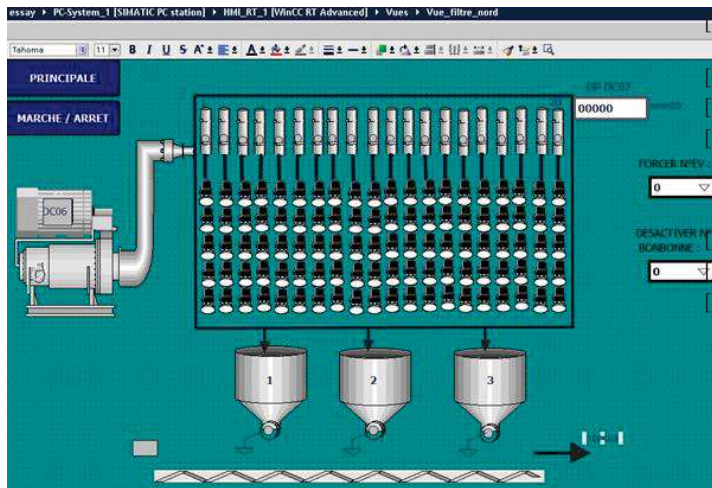
Fig. 5. North DC06 Filter view

E. South DC 07 filter View

It is the same view as the NORTH DC06 filter.

F. Alarm View

The operator panel triggers an alarm when a certain analog value (pressure or temperature measurement) exceeds the programmed maximum threshold.

When the alarm condition is true, a warning triangle appears in the main view and the alarm table is displayed. Once the alarm has disappeared, the triangle disappears.

In addition, we've added warning lights to this view to indicate when the north and south filters have been shut down if two of the three airlocks have been shut down. Yellow (on) red (off), , "Fig .6".

Fig .6. Alarm trigering

XI. CONCLUSION

Our graduation project consisted in replacing the control device used to control the bag filter with a PLC-based S7300 controller. To do this, we assimilated the process operating

principle, the control parameters and the improvements to be made. Then we used TIA PORTAL V13 to configure and program the SIMTIC S7-300 PLC, and PLCSIM to simulate the program. To finish, we designed an HMI to supervise our system using WINCC.

REFERENCES

[1] "Cement manufacturing process," Meftah cement plant Documentation.

[2] https://fr.wikipedia.org/wiki/Filtre_%C3%A0_manches.

[3] MEF-300-L02. DEPOUSSIERAGE CLINKER - Operator Manual (SCMI).

[4] SEFARM ELECTRONIC, Technical Notice N° FI72.029.1016.

[5] SEFARM ELECTRONIC, technical manual N° FI72.0350.0215.

[6] JAI ANDALOUSSI Zakariae, MOUHSSINE Sara, ZEKRI Ikram, "Industrial Programmable Logic Controller SIEMENS," Master Thesis, University Hassan II Mohammedia-Casablanca School of Technical Education Mohammedia, 2011/2012.

[7] Siemens Programmable Logic Controller - Siemens software.

[8] SIEMENS. http://www.siemens.com

[9] J.-P. Thomesse, " Engineering of man-machine systems, " Engineering Techniques, 2004

Using a fractional PID controller to control a gas turbine

Bengana Chahrazad
Department of Automation and Process Electrification
Laboratory of Applied Automation (LAA)
Faculty of Hydrocarbons and Chemistry
Universityof M'hamed Bougara
Boumerdès, 35000, Algeria
c.bengana@univ-boumerdes.dz

Aibeche Abderezzak
Department of Automation and Process Electrification
Laboratory of Applied Automation (LAA)
Faculty of Hydrocarbons and Chemistry
Universityof M'hamed Bougara
Boumerdès, 35000, Algeria
aibeche_umbb@univ-boumerdes.dz

Mohamed Zinelabidine Doghmane
Departmentof Tank Assessment
Direction of Operations Exploration
Division of Exploration Sonatrach
Hassi Messaoud 30500, Ouergla, Algeria
doghmane_m@yahoo.com

Madjid Kidouche
Department of Automation and Process Electrification
Laboratory of Applied Automation (LAA)
Faculty of Hydrocarbons and Chemistry
Universityof M'hamed Bougara
Boumerdès, 35000, Algeria
m.kidouche@univ-boumerdes.dz

Abstract—**The gas turbine typically consists of a compressor, a combustion chamber and a turbine that will be developed. The mathematical model of the dynamical system is represented by a set of equations that describe the system's dynamic behavior with the desired performance. The turbine model used here will actually be an algebraic function rather than a "Differential model" state space. The high power, smooth operation and high performance of gas turbines make it one of the most requested means for driving mechanical loads. For this reason we must always look for the best means and solutions to maintain and enjoy the performance that it is able to provide. That's why we carried out this comparative study between the two types of classic PID (Derivative Integral Proportional) regulators and fractional PID to choose the most robust.**

Keywords—Gas turbine, Compressor, Combustion room, Classic PID regulator, Fractional PID regulator.

I. INTRODUCTION

Although the development of the gas turbine has long slowed down due to the competition of the steam turbine, the first traces of this invention can be found in 1731 in the work of the English man John Barber, who was the first to file a patent on this concept. The gas turbine is an internal combustion engine. By sucking and compressing the atmospheric air in the axial compressor, the energy power of the compressed air increases in its combustion room, using the heat released by combustion, and it converts this thermal power into useful mechanical energy during the relaxation process that takes place in the turbine section. The resulting mechanical energy is transmitted through a coupling to a receiving machine that may be a compressor, alternator, [1]. The thermodynamic cycle of the gas turbine f is based on the Joule cycle, which consists of four operating stages: adiabatic compression, isobar heating, adiabatic relaxation, and isobar cooling [2].

II. TYPES OF GAS TURBINE AND ITS USE

There are two types of gas turbine [3]:
- Single-shaft gas turbine
- Twin-shaft gas turbine

Industrial gas turbines are generally used for:
- Production of electricity
- the combined heat-force production
- Pumping and compression[2].

III. COMPONENTS AND OPERATING MODE OF THE GAS TURBINE

A. Operating Mode

The HP (high pressure) turbine rotor reaches 20% of its nominal speed thanks to a launch device. The air is sucked and compressed in the axial compressor up to 6 bars. The lighting is made using two lighting candles placed inside combustion chambers 1 and 12.
The compressor speed continues to increase to its nominal value using the IGV (gear driven valve). The gases coming out of the wheel (HP) pass through the diaphragm to be guided by the variable swing steering line and turn the wheel (BP) (low pressure) at an appropriate speed [4].

B. Main Components Of The Turbine

The main components of a gas turbine are:
- The auxiliary part
- Aspiration part
- The compression section
- The combustion system
- The turbine section(HP and BP)
- Section of exhaust[4], [5]

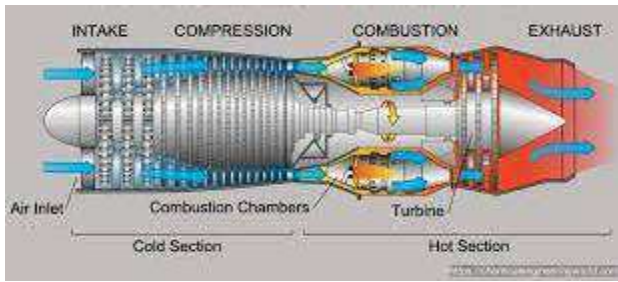Fig. 1 represents the main components of the gas turbine

Fig .1. Main components of the gas turbine

IV. CLASSIFICATION OF GAS TURBINE

There are three modes of classification of gas turbines that are presented below.

1. The construction method;
2. The operating mode;
3. Thermodynamic mode of operation

There are two thermodynamic cycles:

A. Open- Cycle Gas Turbine

The aspiration and exhaust in this turbine is carried out directly into the atmosphere.
This type of turbine is the most common and is divided into two classes:

- Single-cycle turbine:

A single fluid for the generation of mechanical energy is used in this type of turbine, after the release the gases still possessing an energy potential are lost into the atmosphere through the exhaust.

- Regenerated Cycle Turbine:

In this type of turbine, the thermodynamic cycle involves several motor fluids in order to increase equipment efficiency.

Currently, a wide use of gas turbine is in different fields and especially in the field of hydrocarbons due to their wide range of power and their own advantages.

To increase the efficiency of such equipment, a first solution is to recover as heat part of the remaining energy in the turbine exhaust gases before they are discharged into the atmosphere. For this purpose, an exchanger is used and the recovered heat is used to heat the air out of the compressor before it enters the combustion chamber. With such equipment, an efficiency of 23 to 25 percent can be achieved. This efficiency is much higher than the efficiency of a single tree line turbine without an exchanger [6].

V. CLASSSIC AND FRACTIONAL PID CONTROLLER

A. Classic PID Controller

PID control is a method of regulation often used for enslavement. It is a system capable of achieving and maintaining a record through the measures it carries out. PID is the most widely used technique for controlling industrial processes. The main reasons for its wide acceptance in the industry are due to its ability to control the majority of processes, its actions that are well understood, and its relatively simple implementation **[7]**.

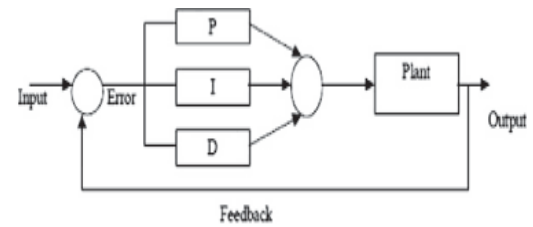Fig. 2 represents the control with a PID regulator diagram

Fig .2. Control with a PID regulator diagram

The PID control, also called a "corrector, regulator, or controller, consists of three terms: P, I, and D; hence, "P" stands for the proportional term, "I" for the integral term, and "D" for the command derivative term. PID regulators are widely used in industrial control because they make it possible to adjust, using their three parameters, the performance (damping and response time) of a regulation of a process modeled by a second order [7].

B. Regulation

Regulation is the action of automatically adjusting a quantity so that it constantly keeps its value or remains close to the desired value, regardless of the disturbances that may occur. Regulation consists of bringing a physical quantity X (pressure, speed, flow rate, level, temperature, etc.) to a fixed value, called "cosign W." A regulator is used for this, consisting of a comparator and a corrector. The comparator deduces the difference e between the set point W and the measurement X. The corrector generates a regulating variable Y, whose purpose will be to cancel the difference. It is this regulating variable Y (expressed in %) that controls the energy modulation device (static relay, valve). The regulator inserted in a control chain imposes an operating constraint on the energy modulation subsystem by regulating a variable according to a control law commonly called an algorithm.

There are four basic algorithms, which are:

• A.O.N (All Or Nothing).
• P proportional.
• I Integral.
• D Derivative. [8]

C. Functional aspects of the PID regulator

Proportional action (P) [7]:

$$C(p) = Kp * \varepsilon (p) \tag{1}$$

Integral Proportional Action (PI) :

$$C(p) = Kp * \varepsilon(p) + K * \varepsilon (p)/p \tag{2}$$

Derivative proportional action (PD)[9] :

$$C(p) = Kp (1 + T_D . p) \tag{3}$$

Derivative Integral Proportional Action (PID)[10]

$$C(p) = \varepsilon(p) * [Kp + K_I * 1/p + K_D * p] \tag{4}$$

D. The Fractional Order Regulator $PI^\alpha D^\mu$

The fractional PID is proposed to improve the performance of linear served systems, it is a generalization of the classic PID corrector, it has the form $PI^\alpha D^\mu$ called where μ and α are positive real such as: $0 < \alpha < 1$, $0 \mu < 1$. The output equation of the fractional order corrector in the time domain is given in the form: [11].

$$\mu(t) = Kp * (e(t) + (1/T_I) * D^\alpha * (e(t)) + T_D * D^\mu * e(t)) \qquad (5)$$

The analytical expression of the fractional PID is given by the following equation:

$$C(p) = K_P + (K_I/p^\alpha) + K_D * p^\mu \qquad (6)$$

With :

- K_p: It is a proportional action.
- T_I: The constant integration
- T_D: The constant of derivation
- $K_D * p^\alpha$: The derivative of fractional order
- K_I: The integral action
- K_D: The derivative action
- α: The Approximation Order
- μ: Gamma Derivative Order

And $K_I = K_P * T_I$, $K_D = T_D * K_P$

Fractional-order systems are dynamic systems written by differential equations of fractional order. The purpose of fractional calculation is to generalize traditional derivatives to non-entry orders[11].

Fig. 3 represents the internal parallel structure of the fractional $PI^\alpha D^\mu$, defined by parallel connections between the proportional parts, fractional order integral and fractional order derivative

Compared to conventional correctors, fractional-order correctors have two additional parameters noted γ and μ, which have the order of integration and 10 derivations, respectively. According to the variation of these two parameters, different possibilities of fractional order correctors can be distinguished[12].
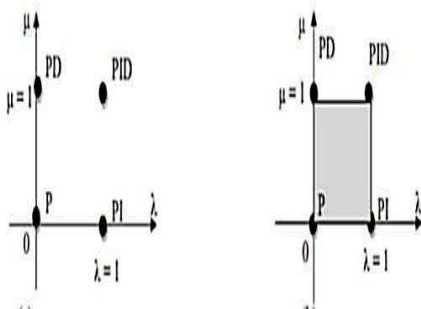

Fig .3. Fractional $PI^\alpha D^\mu$:(a) whole order,   (b) fractional order

E. Comparison Of PI And PID Correctors

The classic PI and classic PID fractionalization is obtained by changing the integrator term in the transfer functions of the previous correctors. The integrator 1/s is fractionalized as follows [13], [14].

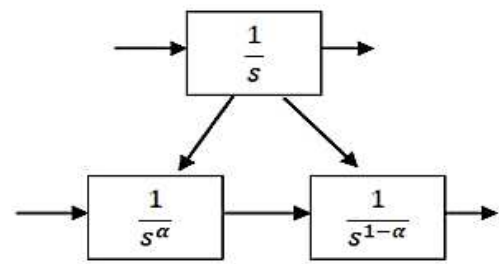Fig. 4 represents fractionalization diagram of an integrator

Fig .4. Fractionalization of an Integrator

VI. The System And Its Mathematical Model

This example models a gas turbine auxiliary power unit (APU) based on the Brayton Cycle. The Compressor and Turbine blocks are custom components based on the Simscape™ Foundation Gas Library. The power input to the system is represented by heat injection into the combustor; actual combustion chemistry is not modeled. A single shaft connects the compressor and the turbine so that the power from the turbine drives the compressor. The APU is a free turbine that further expands the exhaust stream to produce output power.

Three PID controllers regulate the shaft speed, the turbine inlet temperature, and the compressor surge margin. System inputs are defined for three scenarios: varying shaft speed, varying surge margin, and varying APU vane opening. Running the first scenario produces the typical operating line on the compressor map. Running the second and third scenarios show where the maximum power output maximum global efficiency occurs.

A. Power Cycles And Thermodynamic Cycle Of Gas Turbine

Gas turbine plants can work with a Brayton cycle. The Brayton cycle is a thermodynamic gas heat-carrying cycle. It is also known as the Joule cycle. For the purposes of cycle analysis, it is assumed that a gas turbine plant operates with a recovery circuit, although in practice the Joule cycle is also used in an open circuit station, as shown in the following figure , Fig. 5 that represents open cycle gas turbine [14].
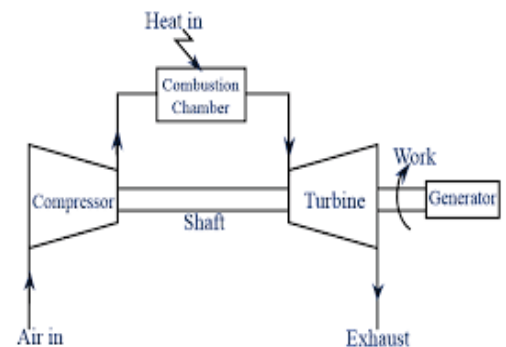

Fig .5. Open cycle gas turbine

B.   Brayton Ideal Cycle

The ideal working cycle of a gas turbine is the Brayton cycle; it consists of two reversible adiabats (isentropic) and two constant pressure processes. The gas is compressed isentropically from point 1 to 2, heating at constant pressure from 2 to 3, and then an isentropic release in the turbine from

point 3 to 4. Cooling occurs from point 4 to point 1, in a heat exchanger (closed cycle) or in the atmosphere (open cycle) [15]. Fig. 6 represents P-V and T-s diagrams for an ideal Brayton cycle.
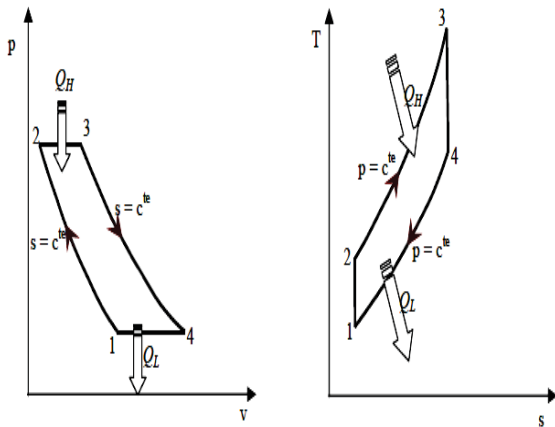

Fig .6. P-V and T-s diagrams for an ideal Brayton cycle.

The power developed in the turbine, with a relatively negligible variation in the kinetic energy of the gas, P_T is equal to the drop of enthalpy is expressed by:

$$|P_T|=H_3-H_4=m*(h_3-h_4) \tag{7}$$

P_T: Kinetic Energy

H: Specific Enthalpy

h:Standard specific enthalpy.

m: Mass flow

In the case where the specific heat is dependent on the temperature, this equation can be rewritten in the form:

$$|P_T|=m*\int^{T3,T4} C_p(T)\, dT \tag{8}$$

C_p: Specific heater at constant pressure.

T: time.

And the rate of detent through the turbine is given by:

$$\sigma_T= P_3/P_4 \tag{9}$$

σ_T: rate of detent.

P: pressure.

Which is linked to the absolute temperature ratio through the turbine by:

$$T_3/T_4=\sigma_T^{(K-1)/K} \tag{10}$$

T : absolute temperature.

Where K is the ratio of specific heat at constant pressure to constant volume.

$$K=C_p/C_v \tag{11}$$

$$C_p-C_v=R_{pv} \tag{12}$$

K: the ratio of specific heat

C_v: specific heater at constant volume.

R_{pv}: Gas specific-constant.

The combination of equations 9 and 10 and replacing in 7:

$$|P_T|=m*C_p*(1-(1/\sigma_T^{(K-1)/K})) \tag{13}$$

The compression rate through the compressor is also given by:

$$\sigma_c= P_2/P_1 \tag{14}$$

σ_c: the compression rate

And :

$$T_2/T_1=\sigma_c^{(K-1)/K} \tag{15}$$

The power of the compressor would also be indicated by:

$$P_c=m_a*(h_1-h_2)=m_a*C_p*T_2*(1-(1/\sigma_T^{(K-1)/K})) \tag{16}$$

P_c=power of the compressor

Suppose that $\sigma_c= \sigma_T= \sigma$,i.e no pressure loss in the cycle, a common condition in the ideal case, the net work of the cycle is given by:

$$P_{Ut}=|P_T|- P_c=m*Cp*(T3-T2) *(1-(1/\sigma^{(K-1)/K})) \tag{17}$$

P_{Ut}: network of the cycle.

The first expression between brackets on the right side of the equation (17) is obviously the heat brought by combustion:

$$Q = m*C_p (T_3-T_2) \tag{18}$$

Q: Heat Flow

The second expression must then be the thermal efficiency of the cycle which is a function of σ and of K:

$$\eta_{th}=1-(1/\sigma^{(K-1)/K}) \tag{19}$$

η_{th}= the thermal efficiency.

Although the above equations apply to gases whose specific heat is constant, the trends they predict apply to all gases. The thermal efficiency of the cycle is a function of σ, and K is propotionel to σ and independent of temperatures T_1 and T_3 of cycle. The specific work can be determined by rewriting the equation (17) in terms of T1 and T3 sing the equation (10):

$$W_{Ut}=C_p*[T_1*(1- \sigma^{(K-1)/K}) +T_3*(1-(1/\sigma^{(K-1)/K}))] \tag{20}$$

W_{Ut}: The specific work.

For any gas, an increase of σ of its lower value of 1.0 (where the work is zero) decreases one term of the equation (20) and increases the other. The net work thus passes through a maximum for an optimal value of σ. The optimum compression rate can be evaluated for the ideal cycle by differentiating the useful work of the equation (14) from τ and equating the derivative to zero. This gives a value of T_2 expressed by :

$$T_2=\surd (T_1*T_3) \tag{21}$$

And for the same rate of compression and detent, we will then have:

$$(T_2=T_4)_{id}= \surd (T_1*T_3) \tag{22}$$

And :

$$\sigma_{id}= (T_2/T_1)^{(K/K-1)}= (T_3/T_1)^{K/(2(K-1))} \tag{23}$$

C. The Pumping Phenomenon.

Pumping is a monodimensional axial instability that affects the decompression system globally. If the flow rate decreases, the losses tend to increase in the compressor. When the operating point crosses the pumping line, the machine is more likely to provide enough energy to counter pressure gradients adversaries and the flow is affected by a low frequency pressure wave that moves from the bottom up. When the machine operates in such a regime, strong fluctuations in the average flow rate can be observed, which can even go up to a total reversal of the direction of the flow.

The extreme fatigue supported by blades makes it very dangerous for the compressor. This instability also has a strong hysteresis. Often, to get out of a pumping regime, the only solution is to greatly increase the flow in the machine (or restart it when possible). In the literature, three types of pumping are observed, in functions characteristic of the compression system [16]:

- Classic pumping
- Deep pumping
- Changed pumping

Fig. 7 represents pumping damage to a blade.

Fig .7. Pumping Damage to a blade .

When the phenomenon is well established, the flow in the compressor is therefore subject to periodic axial (pumping) and circumferentiel (tuning) disturbances.

We have seen the mathematical modeling of a gas turbine system composed of a compressor, a combustion chamber and a turbine. The useful operating range in an axial compressor that is part of the gas turbine is limited by the aerodynamic instabilities that are pumping and rotating detachment. Several mathematical models have been developed to explain the operation of the gas turbine. These models provide a good understanding of the system, thus providing an effective way to develop control strategies to increase the scope of operation and improve the performance of the gas turbine.

Fig. 8 represents the brayton cycle of gas turbine with custom components (Matlab/Simulink model)
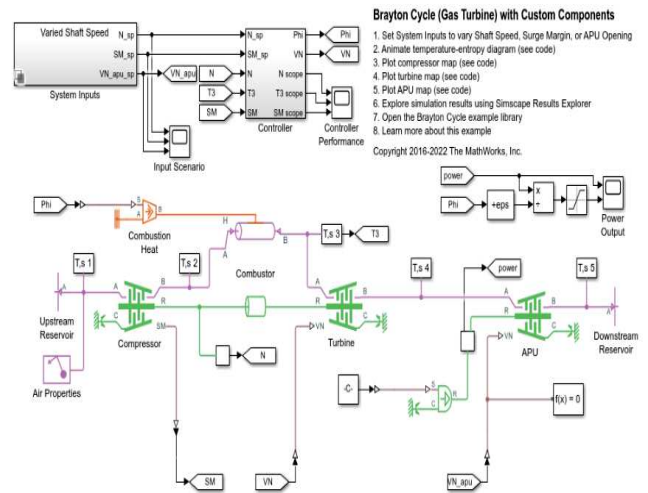

Fig .8. Brayton cycle of gas turbine with custom components (Matlab/Simulink model)

VII. Simulation And Results Of Controlling A Gas Turbine With A Fractional PID Controler And A Classic PID

To control a system, and make sure it behaves in the desired way. This requires continuous monitoring of a set of variables taking into account their mutual ineractions. The purpose of this part is to make a cascade regulation of two parameters speed and temperature and a separate regulation pumping with two types of traditional PID regulator and fractional PID and to do a comparative study between the latter to maintain the stability the speed and of the system and one chooses the most performing.

A. Simulate The Dynamic Behavior Of The System.

The simulation software is used to simulate the dynamic behavior of a system that is represented by a mathematical model. At each stage of the model simulation, the state of each part of the system is calculated using time-based or event-based solvers. Simulation software also incorporates visualization tools, such as data display systems, to monitor the simulation during its execution.

B. Simulation And Analysis Results.

In our simulation we used two methods. Simulation by SimScape software and simulation by Simulink software. In both methods we can further simulate our system as it is in reality. Since the results of the simulation by both methods are virtually identical. In the following paragraphs, we only give the results obtained with SimScape and these several tests by observing the behavior with the Classic PI regulator and fractional PI before and after injecting the disturbance and white noise to study the robustness of both regulators.

We will do a simulation with a cascade regulation of two types of regulators a classic PI regulator and fractional PI.

C. Simulation With Classic PI Regulator.

The values of parameters K_P and K_I for classic PI regulator are:

For the temperature regulator:

$$K_P = 1, K_I = 1$$

For the speed regulator:

$$K_P= 0.5, K_I=1$$

For the pumping regulator:

$$K_P=1, K_I=1$$

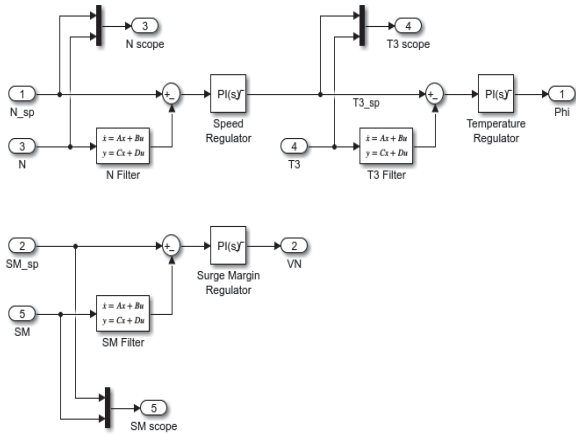Fig. 9 represents functional system block diagram with classic PID

Fig .9.   Functional system block diagram with classic PID

D. Simulation With Fractional PI.

- Fractional operator 1:

Gamma Derivative Order =-0.9
Frequency range = [wb,wh] =[1e-3,1e-3]
Approximation order =7

- Fractional operator 2:

Gamma Derivative Order =-0.9
Frequency range = [wb,wh] =[1e-3,1e-3]
Approximation order =7

- Fractional operator 3:

Gamma Derivative Order =-0.992
Frequency range = [wb,wh] =[1e-3,1e-3]
Approximation order =7

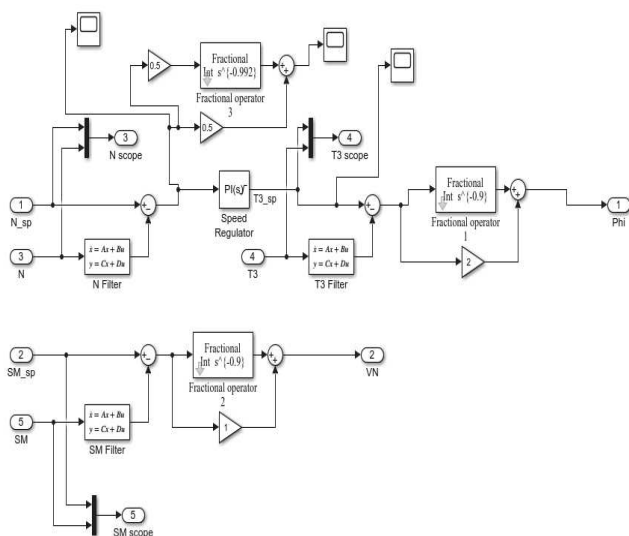Fig. 10 represents Functional system block diagram with fractional PI.

Fig .10.   Functional system block diagram with fractional PI.

E. Simulation Without Disturbance.

Fig. 11 represents the classic PI command signal.
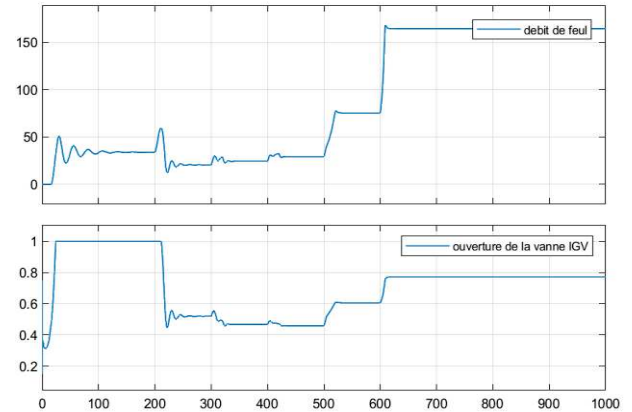

Fig .11.   Classic PI command signal.

Fig. 12 represents the fractional PI command signal.
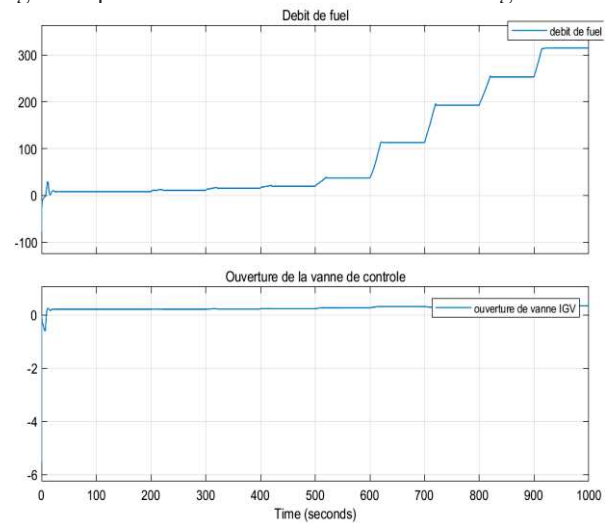

Fig .12.   Fractional PI command signal.

Fig. 13 represents curves that represent the behavior of the system with a classic PI regulator without disturbance.

Fig .13.   Curves that represent the behavior of the system with a classic PI regulator

Fig. 14 represents curves that represent the behavior of the system with a fractional PI regulator without disturbance.

Fig .14. Curves that represent the behavior of the system with a fractional PI regulator

F. Simulation With Disturbance.

- Input data after disturbance
  Disturbance=283K   at t=700s

Fig. 15 represents classic PI control signal with disturbance.

Fig .15. Classic PI control signal with disturbance =283k at the moment =700s

Fig. 16 represents curves that represent the behavior of the system with a classic PI regulator with disturbance.

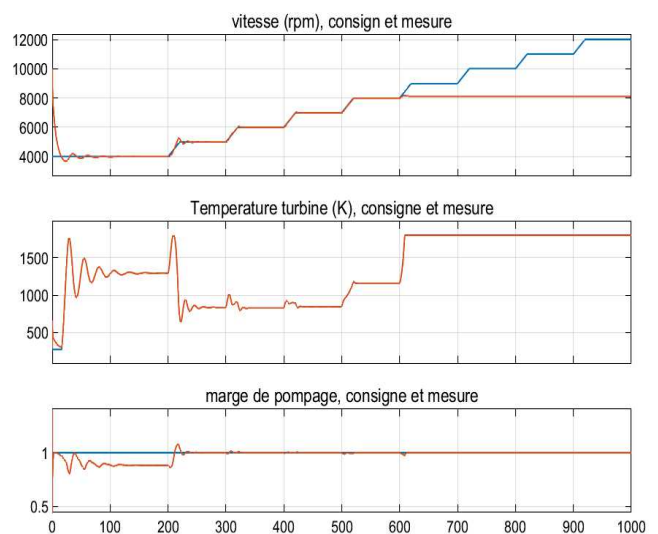Fig .16. System behavior with a classic PI regulator and with disturbance=283 k injected at the moment t=700s

Fig. 17 represents fractional PI control signal with disturbance.

Fig .17. Fractional PI control signal with disturbance =283k at the moment =700s

Fig. 18 and Fig. 19 represent curves that represent the behavior of the system with a fractional PI regulator with disturbance.

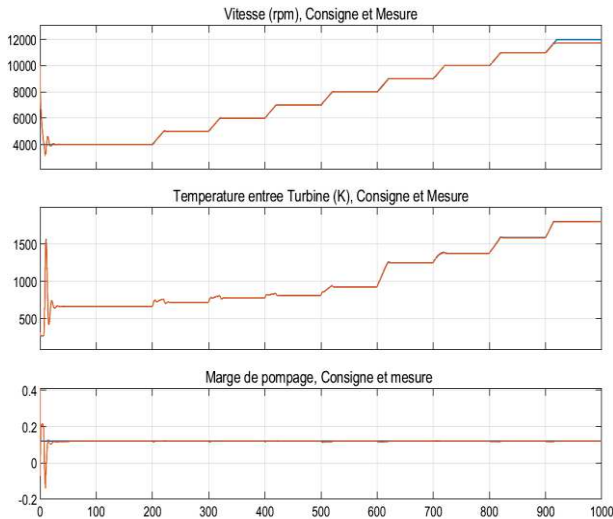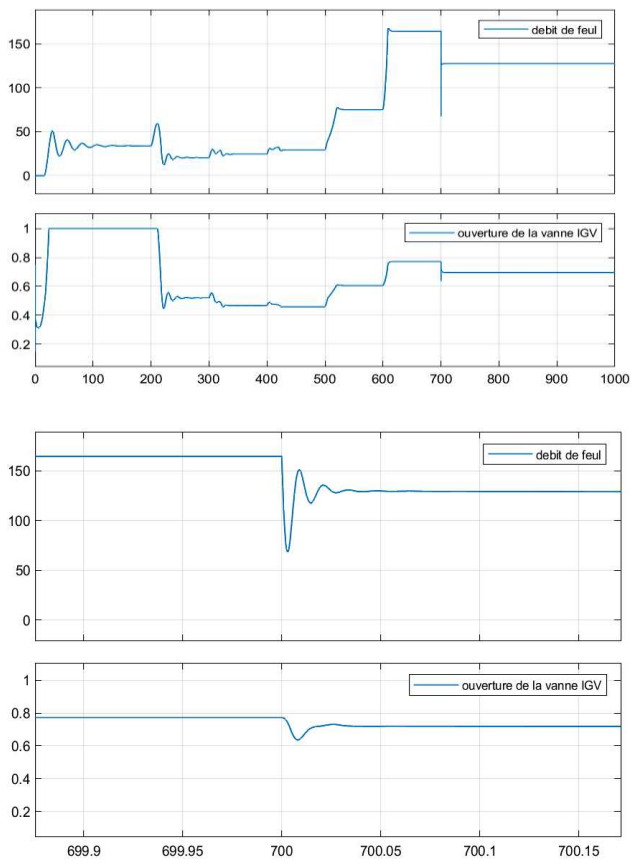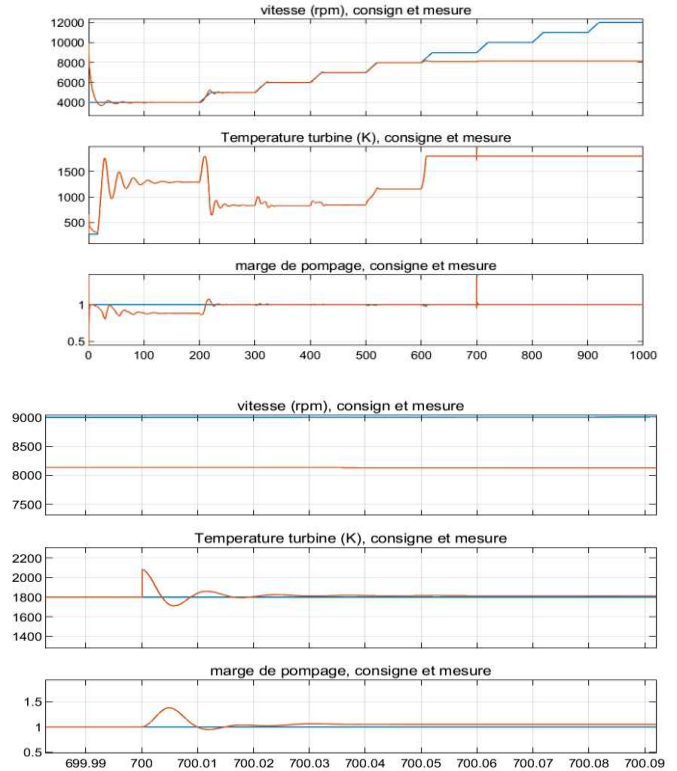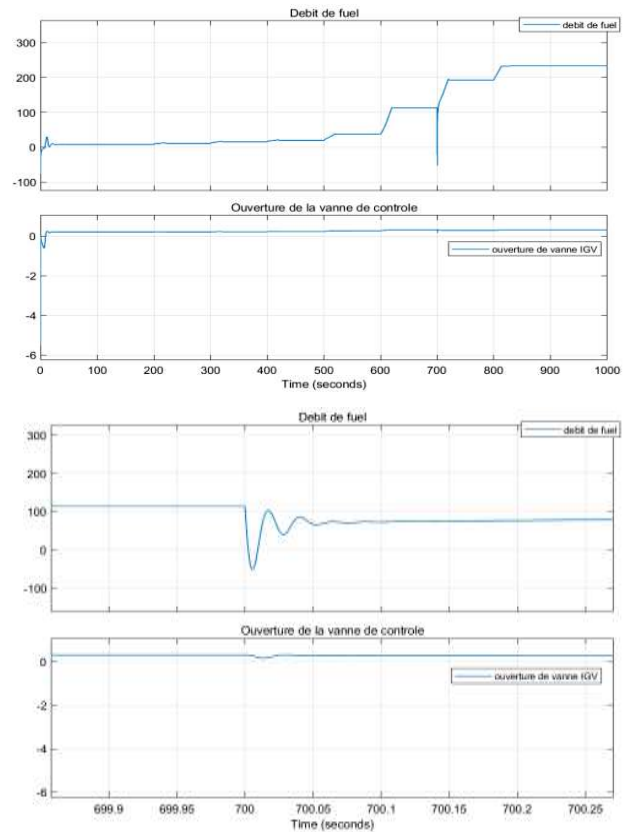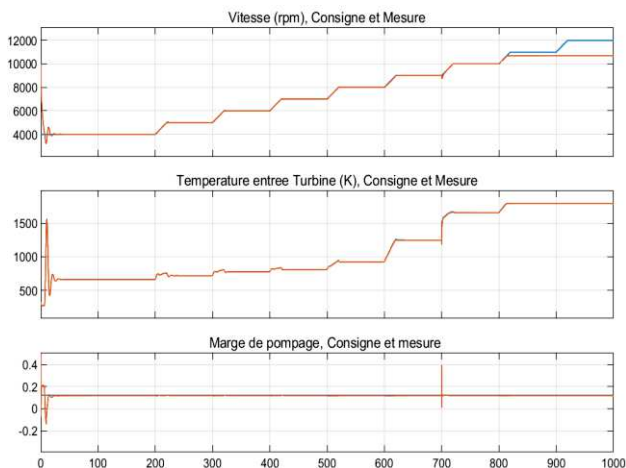Fig .18. System behavior with a fractional PI regulator and with disturbance=283 k injected at the moment t=700s
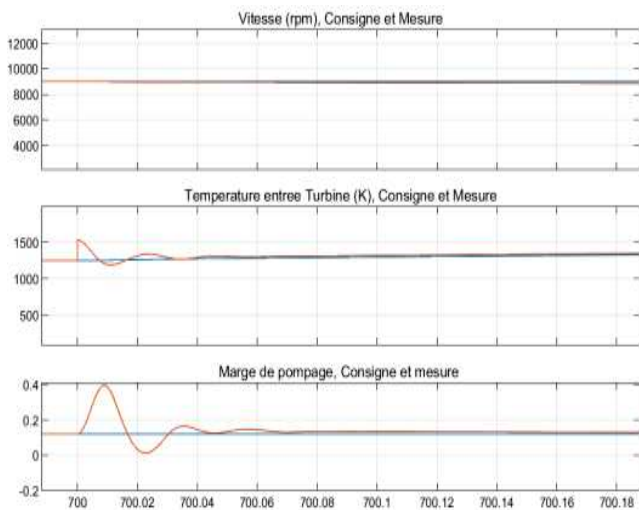

Fig .19. System behavior with a fractional PI regulator and with disturbance=283 k injected at the moment t=700s

By applying the same disturbance simultaneously to both classic PID and fractional PID systems, we observed that:

1. No disturbance affects the speed which guards the same behavior during its absence.

2. At the moment of the injection of the disturbance, a peak of temperature and pumping occurs when:

➢ The system with classic PID receives a pumping influence of almost 1.5 times greater than the fractional PID alone of 0.5.

➢ On the other hand, the temperature reaches the same peak amplitude and restores in the same way when it returns to its previous behavior. The fast alignment of the temperature and pumping values means that the regulators are robust to disturbances and that it ensures system performance.

3. Whatever the disturbance; the regulators are robust; they reject disturbances and regain performance.

G. Results Of The Simulation.

➢ The fractional PID regulator is more efficient, it always tries to reach the instructions and keep the system performance, although the classic PID is not bad also it has a degree of robustness.

➢ With the optimization of fractional PID parameters and orders, better behavior can be achieved

➢ Both fractional PID and classic PID controllers are robust; they ensure system performance and reject disturbances and noise regardless of its values.

➢ The compressor keeps its behavior and line of operation every time.

VIII. CONCLUSION

We make a cascade regulation of two parameters speed and temperature and a separate pumping regulation with two types of classic and fractional PID regulators and make a comparative study between the two to keep the performance of the system and choose the most performing one.

We have noticed that the fractional PID is the most robust and most performing regulator.

REFERENCES.

[1] GE Power Generation GE Gas turbine design philosophy

[2] FUTURA MAISON futura.science.com

[3] H. Cohen, G. Rogers, and H. saravana mutto, "Gas turbine theory", Essex, Longman Limited, 2002

[4] L. ELKALI, "Study and modeling of a turbo-alternator", University of Msila 2013/2014.

[5] "modelling and blurred control of the speed and temperature cycle of a gas turbine type MS5002C",university 20 August 1955 Skikda 2015/2016

[6] A. Herzallah, "thermodynamic study, maintenance and reliability of a gas turbine MS 5002", University of Boumerdes, 2007

[7] http://projet.eu.org/pedago/sin/term/6asservissement_ PID

[8] K. Ahmed, "Study & Simulation of the adjusted drive of the PGT-25 gas turbine,The Natural Gas Compression Station W.EL BAYED," Industrial Maintenance University Abu BakarBoulkaid 2015.

[9] A. Mezache,S. Barkati, "Modelling and Control of DC and AC Electrical Machinery", Industrial Control Option students, University of M'sila, 2010/2011.

[10] M . Idhir, F. Rehrah, "Comparative study of PID regulators and Flou Application to a DC Engine (MCC)", Industrial Automatismes, Abderrahmane Mira University , Bejaïa, 2011/2012.

[11] P. Ivo Fractional-order nonlinear systems:modeling, analysis and simulation, Springer Science and Business Media, 2011.

[12] Y. Bensafia, S. Ladaci, K. Khettab, « Performance Analysis of Fractionalized Order PID Controller with the Conventional PID Controller," CEIT. Sousse, Tunisia, 14, pp. 22-25, march 2014 [International Conference on Control, Engineering & Information Technology]

[13] S. Ladaci, Y. Bensafia, « Fractionalization: A new tool for robust adaptive control of noisy plants », Grenoble, France, pp. 379-384, February 4-6, 2013[6th IFAC Workshop on Fractional Differentiation and Its Applications, FDA"13]

[14] I. PETRAS, S. GREGA, « Digital Fractional Order Controllers Realized by PIC Microprocessor: Experimental Results, Proceedings of the ICCC2003 », High Tatras, Slovak Republic, pp. 873–876,May 26-29

[15] Bouam, "Improving the performance of gas turbines used in the hydrocarbon industry by injecting water steam at the top of the combustion chamber", PhD thesis, M'hamed Bougara-Boumerdes University, Algeria, 2009.

[16] J.T. Gravdahl, O. Egeland, "Compressor surge and rotating stall modelling and control", Advances in Industrial Control. Springer Verlag London Limited, 1999.

Stick-slip vibration Suppression in Drill-String Based on PSO-PID Controller

TELLAA Mawloud
Department of Automation and Electrification of Process
Applied Automation
Laboratory,Faculty of Hydrocarbons and Chemistry
University M'Hamed Bougara-Boumerdes,
Boumerdes 35000, Algeria
m.tellaa@univ-boumerdes.dz

AIBECHE Abderrezak
Department of Automation and Electrification of Process
Applied Automation
Laboratory,Faculty of Hydrocarbons and Chemistry
University M'Hamed Bougara-Boumerdes,
Boumerdes 35000, Algeria
aibeche_umbb@univ-boumerdes.dz

DOGHMANE Mohamed Zinelabidine
Department of Automation and Electrification of Process
Applied Automation
Laboratory,Faculty of Hydrocarbons and Chemistry
University M'Hamed Bougara-Boumerdes,
Boumerdes 35000, Algeria
Reservoirs Evaluation Department, DOE, Exploration Division, SONATRACH
Hassi Messaoud 30500, Algeria
MohamedZinelabidine.Doghmane@Sonatrach.dz

KIDOUCHE Madjid
Department of Automation and Electrification of Process
Applied Automation
Laboratory,Faculty of Hydrocarbons and Chemistry
University M'Hamed Bougara-Boumerdes,
Boumerdes 35000, Algeria
mkidouche@univ-boumerdes.dz

Abstract—**Vibrations in rotary drilling systems can harm equipment, borehole quality, and drilling efficiency, while also increasing non-productive time. Current mitigation relies on manual parameter adjustments, an unreliable method. Researchers are developing automatic strategies, with recent success using a particle swarm optimization (PSO)-based Proportional-Integral-Derivative (PID) controller. However, its effectiveness in mitigating stick-slip vibrations remains untested. This paper investigates the use of a PID controller fine-tuned by the particle swarm optimization algorithm using integral squared error ISE fitness function to enhance vibration control in rotary drilling systems, with a focus on stick-slip vibrations.**

Keywords—Particle Swarm Optimization, PID, Rotary drilling systems, Stick-slip, Vibration mitigation.

I. INTRODUCTION

The rotary drilling system in the petroleum industry extracts oil and gas from underground wells using two key components: surface equipment (hoisting system, rotary table, and drilling fluid system) and a subsurface drillstring (comprising thick-walled drill collars and specialized instruments). Drill collars are secured by stabilizers, and the force applied to the bit is known as Weight on Bit (WOB). The torque from the rotary table to the drillstring is Torque on Bit (TOB), while drilling fluid serves lubrication and pressure compensation purposes. The drilling process can cause axial, lateral, and torsional vibrations. Axial vibrations result from bit contact, lateral from pipe eccentricity, and torsional from non-linear contact with the borehole wall, leading to Stick-Slip vibrations. [1]

Stick-slip is detrimental, as it causes destructive vibrations in drilling systems. It results from alternating sticking and sliding of surfaces with varying friction torques. Even slight changes in drive speed can trigger it. Reducing Stick-Slip and torsional vibrations is a significant focus of research. Various methods have been explored, such as altering WOB and increasing rotary table speed. Sliding mode control and back-stepping control have been applied to mitigate these vibrations, along with hybrid controllers. However, enhancing controller performance remains a challenge [2 ,3].

In recent years, research efforts have focused on mitigating torsional vibrations. Tang et al.'s study [3] demonstrated that reducing the weight on the bit (WOB) eliminates stick-slip, albeit with a slight implementation delay. Another study by Tang et al. [4] explored increasing rotary table speed but didn't consider drill string stiffness. Various control methods, including sliding mode and hybrid controllers, have been applied to address torsional vibrations and prevent bit sticking. Liu [7] conducted experimental comparisons of rotational velocities with predefined values set by drillers. Abdulgalil and Siguerdidjane [8] employed back-stepping control successfully to eliminate stick-slip vibrations. Hybrid controllers, as discussed by Mendil et al. [10, 11], combined different techniques to minimize torsional vibrations [12]. These approaches aim to enhance drilling performance while reducing vibrations.

This paper introduces a novel approach using a PID controller combined with Particle Swarm Optimization (PSO) to improve vibration suppression. The study aims to

demonstrate the importance of optimizing PID controller parameters for enhanced performance in suppressing stick-slip vibrations. The manuscript provides a detailed description of the proposed method and a comparative analysis with conventional PID control.

In Section 2, the drilling system and vibrations are briefly explained. Section 3 introduces the mathematical model of vibrations, the PID controller, and its importance. Section 4 outlines the PSO algorithm and its application to the drilling system. Section 5 discusses open and closed-loop results and compares them with traditional PID control.

II.   DRILLING SYSTEM

The power system, hoisting system, circulating system, rotating system, well control system, and monitoring system are the six fundamental systems that make up the drilling rig [13, 14]. The hoisting system includes elements including draw-works, an auxiliary brake, a traveling system, a hook, and a derrick and supports drilling and completing operations. The drilling strings inside the wellbore are spun by the rotary system to push the bit to fracture rock [15]. The circulating system's functions include moving cuttings from the bottom of the hole to the surface, preventing debris from settling, regulating the temperature of the drill bit, and preserving the structural integrity of the wellbore walls. The well control system is used to shut down and/or control the well in an emergency to restore pressure balance. The monitoring and control system ensures the effective operation of all rig components to satisfy the needs of the drilling process, while the power and transmission system supplies energy to the entire system., Fig. 1. offers a visual representation of the rotary drilling system.
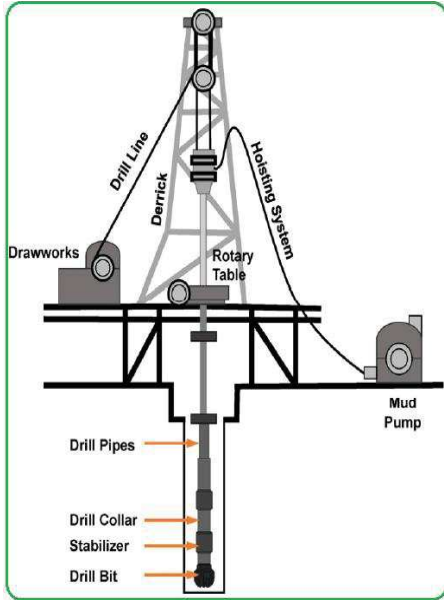

Fig. 1.   Schematic of oil well drill string system [9]

III.   MATHIMATICAL MODEL

In this study, we adopt a three-element model based on the mass-spring-damper framework.

A. Drilling string model

In this research, a mass-spring-damper model is applied to replicate the behavior of a rotary drilling system [3]. This model encompasses three degrees of freedom, with the upper disc symbolizing the rotary table, the middle disc signifying the tool string, and the lower disc representing the drill bit. You can find a concise summary of the model's parameters in Table 1. Additionally Fig. 2 portrays the three degrees of freedom model.
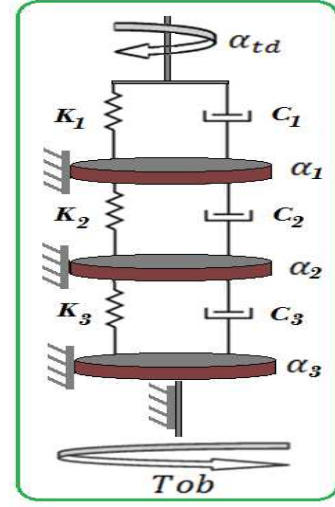
Fig. 2.   Equivalent mass-spring-damper three-element model [3, 14].

The mathematical representation of the latter is articulated through equation (1) [14]:

$$
\begin{cases}
\ddot{\alpha}_1 = \dfrac{1}{J_1}\left(\cdots - \mu\dot{\alpha}_1 \right) \\
\ddot{\alpha}_2 = \dfrac{1}{J_2}\left(\cdots - \mu\dot{\alpha}_2 \right) \\
\ddot{\alpha}_3 = \dfrac{1}{J_3}\left(\cdots - Tob \right)
\end{cases}
\tag{1}
$$

we define $u = \dot{\alpha}_{td}$, and the states variables as :

$x_1 = \dot{\alpha}_1$ $x_2 = \dot{\alpha}_2$, $x_3 = \dot{\alpha}_3$, $x_4 = \alpha_{td} - \alpha_1$,
$x_5 = \alpha_1 - \alpha_2$ and $x_6 = \alpha_2 - \alpha_3$,

the Equation (1) is written then as:

$$
\begin{cases}
\dot{x}_1 = -\dfrac{c_2 + c_1 + \mu}{J_1}x_1 + \dfrac{c_2}{J_1}x_2 + \dfrac{k_1}{J_1}x_4 - \dfrac{k_2}{J_1}x_5 + \dfrac{c_1}{J_1}u \\
\dot{x}_2 = \dfrac{c_2}{J_2}x_1 - \dfrac{c_2 + c_3 + \mu}{J_2}x_2 + \dfrac{c_3}{J_2}x_3 + \dfrac{k_2}{J_2}x_5 - \dfrac{k_3}{J_2}x_6 \\
\dot{x}_3 = \dfrac{c_2}{J_3}x_2 - \dfrac{c_2 + \mu}{J_3}x_3 + \dfrac{k_3}{J_3}x_6 - \dfrac{1}{J_3}Tob \\
\dot{x}_4 = \dot{\alpha}_{td} - x_1 \\
\dot{x}_5 = x_1 - x_2 \\
\dot{x}_6 = x_2 - x_3
\end{cases}
\tag{2}
$$

TABLE I.   PARAMETERS DESCRIPTION FOR THE DESIGNED ROTARY DRILLING MODEL [13, 19].

Parameter	Description	Unit
α_{td}	The top drive angular displacement	[rad]
$\alpha_{i=1,2,3}$	The angular displacements	[rad]
$k_{i=1,2,3}$	Torsional stiffness coefficient	[N.m/rad]
$c_{i=1,2,3}$	Internal damping coefficient	[N.m.s/rad]
μ	Wall friction coefficient	[N.m]
$J_{i=1,2,3}$	The inertia	[kg.m2]
Tob	The torque on bit	[N.m]

B. Generalized model of Rock-bit interaction :

Within the literature, various functions have been employed to characterize the interaction between the drill bit and the rock. However, in the context of our specific investigation, we will utilize the generalized model as outlined by the expression[14]:

$$Tob = \mu_n Nr \left(\frac{x_3}{\sqrt{x_3^2 + \Omega_0^2}} + \frac{p\Omega_0 x_3}{x_3^2 + \Omega_0^2} \right) + Dx_3 \left(\frac{x_3}{\Omega_1} - 1 \right) \quad (3)$$

Where the model coefficients are given in the following table [14]:

TABLE II.   PARAMETERS USED IN ROCK-BIT GENERAL MODEL

parameter	description	value
μ_n	friction coefficient	28 nm
n	the force vector	9.81 * wob
r	the contact radius vector	0.1 m
Ω_0	chain transition speed	1
Ω_1	transition speed for the well	31.4159
p	the initial friction parameter	1.5
d	the linear damping vector	0.28

C. PID controller

The Proportional Integral Derivative (PID) control stands as the most commonly employed control strategy for regulation. Its widespread adoption across industries can be attributed to its simplicity in tuning and its reliable operation. The general expression for the PID control equation is as follows [10]:

$$C(t) = K_p e(t) + K_i \int_0^t e(\tau)d\tau + K_d \frac{de(t)}{dt} \quad (4)$$

Where, K_P, K_i , K_d represent the parameters of the PID controller denote respectively : the proportional coefficient, the integral time constant and the differential coefficient.
To ensure stability, the derivative component is filtered to prevent singularities. Equation (4) represents the standard PID configuration, which is employed prior to applying the PSO algorithm for parameter optimization.

IV.   PROPOSED OPTIMISATION METHOD

A. Standard PSO algortitm

The PSO algorithm is a global, stochastic optimization method originating from swarm intelligence, drawing inspiration from the coordinated movements of flocks of birds and schools of fish. It operates on the principle of information exchange within a population of particles. The algorithm's initialization involves providing random solutions, with each particle steering its course towards two primary targets: its personal best result (pBest) and the best [15], position achieved by its neighboring particles (gBest). The evaluation of particle performance is determined by a fitness function, which assesses whether the optimal solution has been attained. During each iteration, all solutions undergo updates based on the fitness function, following a set of recursive equations[17],:

$$x_i(t+1) = x_i(t) + v_i(t) \quad (5)$$

$$v_i(t+1) = w \times v_i(t) + A_1 \times rand \times (p_{best}(t) - x_i(t)) \\ + A_2 \times rand \times (G_{best}(t) - x_i(t)) \quad (6)$$

where w is the inertia weight factor, v_i (t) is the velocity of particle i at iteration t, x_i (t) is the particle position at iteration t, A_1 and A_2 are two positive constant parameters called acceleration coefficients, $rand$ is the random function in the range [0, 1], $Pbest(t)$ is the best position of the ith particle and $Gbest(t)$ is the best position among all particles in the swarm up to iteration t.

B. ISE (integral square of error)performance criteria:

The Integral of the Square Error (ISE) is a widely used performance criterion in control theory and engineering. It measures the cumulative square of the error between the desired system response and the actual system response over a specific time interval. In other words, it quantifies how far the system's behavior deviates from the desired behavior over time.

Mathematically, ISE is calculated by integrating the square of the error function with respect to time. This integral provides a way to assess the overall system performance, taking into account both the magnitude and duration of errors. A lower ISE value indicates a better system response and a higher level of accuracy

$$e(t) = y_{ref}(t) - y_{sys}(t) \quad (7)$$

The ISE performance criterion allows this. Such a criterion is defined by the flowing equation [15]:

$$J_{ISE} = \int (e(t))^2 dt \quad (8)$$

V. SIMULATION RESULTS AND DISCUSSION
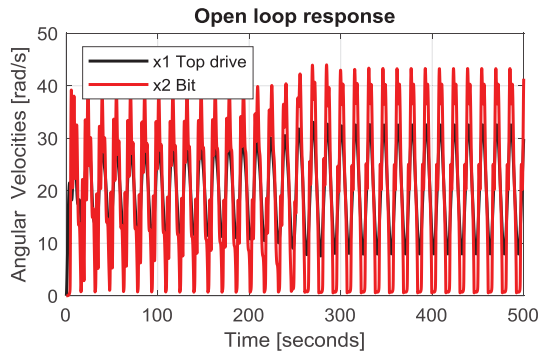
A. Open loop response

Fig. 3.   The open-loop responses of rotary drilling systems without control

The Fig.3 illustrates the step response of a drilling rotary system without controller. We can see the bit velocity has big vibration, the regulation time is very long, the dynamic and static character of the system is not good, and the ability of tracking rotary table speed is bad.

B. Closed loop using PID Controller without optimisation

Below are the appropriately selected PID controller parameter values:

K_p=0.009 ;
K_i=0.0023 ;
K_d=0.011;

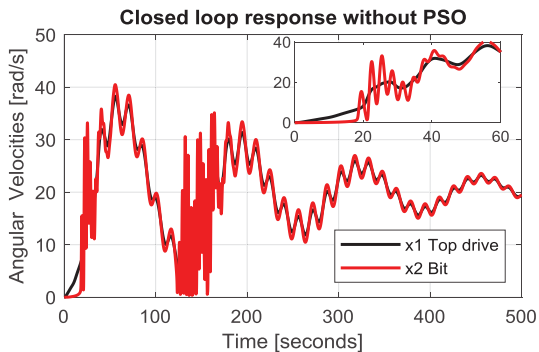The simulation yields the following results

Fig. 4.   The closed-loop responses of rotary drilling systems with PID controller without PSO

In Fig. 4, the step response of a drilling rotary system is shown, featuring a PID controller without any tuning. Notably, the figure reveals that the bit velocity exhibits minor oscillations, but the time response is considerably protracted. The system shows a delayed ability to track the rotary table speed, characterized by substantial oscillations and eventual stabilization after an extended period

C. Closed loop using PID Controller with PSO

The PSO algorithm was initialized with the subsequent parameter settings :

TABLE III.   PARTICLE SWARM OPTIMIZATION ALGORITHM PARAMETERS

Parameter	value
Size of the swarm " no of birds "	n = 50;
Maximum number of "birds steps"	bird_setp =50
Dimension of the problem	dim = 3
Upper limits of (Kp,Ki,Kd)	Bmax=[10 10 10]
Lower limits of (Kp,Ki,Kd)	Bmin=[0 0 0]
PSO parameter C1	c2 =1.2
PSO parameter C2	c1 = 0.12
PSO momentum or inertia	w =0.9

After the optimization process by PSO algorithm was finished we get these parameters below

Kp = 1.1699;

Ki = 0.3249;

Kd = 8.9144;

The simulation results of the drilling string model controlled with PID tuned by PSO is given below

Reference of Angular velocity = 20 rad/s for 0<t< 100 s
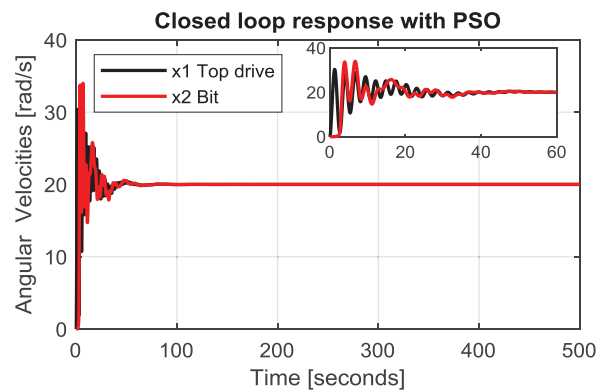
Fig. 5.   The closed-loop responses of rotary drilling systems with PID controller optimized by PSO

In Fig. 5, the step response of a drilling rotary system is depicted, featuring a PID controller fine-tuned using the PSO algorithm. Notably, the figure showcases the rapid elimination of stick-slip vibrations, achieving a considerably shorter time response compared to the original system. Furthermore, there is no overshooting observed beyond the 30-second mark

D. Comparative Study

The simulation results visualized in Fig. 3, revealing pronounced stick-slip vibrations within the drill string system. Various components of the system exhibit periodic vibrations, with the drill bit being the most severely affected, indicated by both viscous and sliding states. These outcomes validate the model's effectiveness in safeguarding drilling tools from damage.

Our study delves into the PID controller's ability to mitigate stick-slip vibrations. As demonstrated in Fig. 4 and Fig. 5,

the controller successfully reduces stick-slip vibrations, but it's the PID controller with PSO optimization that completely eliminates the phenomenon in a short time, ensuring a stable drilling process. These findings underscore the practical applicability of our proposed control methods within the drilling industry

VI. CONCLUSION

In this study, our primary goal was to optimize the mitigation of stick-slip vibrations in rotary drilling systems. We achieved this by employing a PID controller fine-tuned using the PSO algorithm with ISE as the fitness function. The results were highly encouraging, as the PSO algorithm effectively and rapidly suppressed stick-slip vibrations. However, it's important to note that further improvements in PSO's performance could be achieved by increasing the population size, albeit at the expense of longer parameter optimization.

For future research, we recommend exploring the extension of integer order PID controllers to non-integer order PID controllers for enhanced vibration control in drillstring systems. Additionally, we suggest investigating alternative tuning methods to compare their effectiveness with the presented approach. Future investigations may also encompass the consideration of various coupled vibrations, including axial, torsional, and lateral vibrations, during controller development. Ultimately, the next steps involve integrating the developed controller into a prototype rotary drilling system and deploying it in a real-world context within an Algerian drilling field

REFERENCES

[1] R. I. Leine , D. H. van Campen , W. J. G. Keultjes, (2002) ,Stick-slip Whirl Interaction in Drillstring Dynamics.

[2] M .Kidouche, M.Z .Doghmane, A. Ahriche, (2021). Decentralized Overlapping Control Design with Application to Rotary Drilling System, IETE Journal of Research, DOI: 10.1080/03772063.2021.1886602

[3] L.Tang, X. Zhu, C. Shi, J. Tang, and D.Xu, (2015). Study of the influences of rotary table speed on stick-slip vibration of the drilling system, Petroleum, Vol. 1 No. 4, pp. 382-387.

[4] L.Tang, X. Zhu, X.Qian, and C.Shi, (2017), Effects of weight on bit on torsional stick-slip vibration of oilwell drill string, Journal of Mechanical Science and Technology, Vol. 31 No. 10,pp. 4589-4597.

[5] E. Navarro-López, E. Licéaga Castro, (2009). Non-desired transitions and sliding-mode control of a multi-DOF mechanical system with stick-slip oscillations, Chaos Solitons Fract, Vol. 41, no. 4, pp. 1561–2200.

[6] V. Vaziri, M. Kapitaniak, M. Wiercigroch, (2018) .Suppression of drill-string stick–slip vibration by sliding mode control: numerical and experimental studies," Eur. J. App. Math, Vol. 29, no. 5, pp. 805–25, Oct. 2018.

[7] Y.Liu, (2015). Suppressing stick-slip oscillations in underactuated multibody drill-strings with parametric uncertainties using sliding-mode control," IET Control Theory, Vol. 9,no. 1, pp. 91–102, Jan. 2015.

[8] F. Abdulgalil, and H. Siguerdidjane, (2005).Backstepping design for controlling rotary drilling system," in Proceedings of 2005 IEEE Conference on Control Applications,. CCA 2005, Toronto, Ont., Canada, Aug. 28–31, 2005, pp. 120–4.

[9] A. Krama, M. Gharib, S. Refaat, S.,Sassi, S. (2022). Hybrid fuzzy sliding mode for stick-slip suppression in drillstring systems. Journal of Mechanical Science and Technology 36 (3) (2022) 1089~1102.http://doi.org/10.1007/s12206-022-0202-y

[10] C.Mendil, M.Kidouche, M Z.Doghmane,(2021). Hybrid sliding PID controller for torsional vibrations mitigation in rotary drilling systems, Indonesian Journal of Electrical Engineering and Computer Science, Vol. 22, No. 1, April 2021, pp. 146~158, ISSN: 2502-4752, DOI: 10.11591/ijeecs.v22.i1.pp146-158

[11] C. Mendil, M .Kidouche, M.Z .Doghmane, (2022). Sliding Mode Controller Design for Torsional Vibrations Minimization Under Rock-Bit Interaction Effects. In: Hatti, M. (eds) Artificial Intelligence and Heuristics for Smart Energy Efficiency in Smart Cities. IC-AIRES 2021. Lecture Notes in Networks and Systems, vol 361. Springer, Cham. https://doi.org/10.1007/978-3-030-92038-8_61

[12] Z. Guan et al., (2021).Theory and Technology of Drilling Engineering , China University of Petroleum Press and Springer Nature Singapore Pte Ltd., https://doi.org/10.1007/978-981-15-9327-7_2

[13] TG. Ritto , M.Ghandchi-Tehrani, (2019). Active control of stick-slip torsional vibrations in drill-strings Journal of Vibration and Control, Vol. 25(1) 194–202 ,DOI: 10.1177/1077546318774240.

[14] C. Mendil, M .Kidouche, M.Z .Doghmane, S. Benammar, K.F .Tee, (2021) , Rock–bit interaction effects on high-frequency stick-slip vibration severity in rotary drilling systems, Multidiscipline Modeling in Materials and Structures, Vol. 17 No. 5, pp. 1007-1023. https://doi.org/10.1108/MMMS-10-2020-0256

[15] J. -y. Cao, B. -g. Cao, (2006), Design of Fractional Order Controllers Based on Particle Swarm Optimization, 1ST IEEE Conference on Industrial Electronics and Applications, pp. 1-6, doi: 10.1109/ICIEA.2006.257091

[16] H. Ramezanian, S . Balochian, A. Zare, (2013). Design of Optimal Fractional-Order PID Controllers Using Particle Swarm Optimization Algorithm for Automatic Voltage Regulator (AVR) System. J Control Autom Electr Syst 24, 601–611 https://doi.org/10.1007/s40313-013-0057-7

[17] K. Oprzędkiewicz, K. Dziedzic, (2017). A Tuning of a Fractional Order PID Controller with the Use of Particle Swarm Optimization Method. In: Rutkowski, L., Korytkowski, M., Scherer, R., Tadeusiewicz, R., Zadeh, L., Zurada, J. (eds) Artificial Intelligence and Soft Computing. ICAISC 2017. Lecture Notes in Computer Science(), vol 10245. Springer, Cham. https://doi.org/10.1007/978-3-319-59063-9_35

[18] Problems and Solutions Drilling Engineering Problems and Solutions A Field Guide for Engineers and Students M. E. Hossain and M. R. Islam

[19] https://www.pason.com/stories/technology/stick-slip-a-costly-torsional-vibration

Kalman filter-Based PID Controller Design for Stick-Slip Mitigation in Rotary Drilling Systems

1st Zebboudj Ahmed Hichem
Laboratory of Applied Automation (LAA), Department of Automation and Electrification of Processes
Faculty of Hydrocarbons and Chemistry (FHC), Institute of Electrical & Electronic Engineering, University M'hamed Bougara
Boumerdes, Algeria
a.zebboudj@univ-boumerdes.dz

2nd Akroum Hamza
Laboratory of Applied Automation (LAA), Department of Automation and Electrification of Processes
Faculty of Hydrocarbons and Chemistry (FHC, University M'hamed Bougara
Boumerdes, Algeria
akroum@univ-boumerdes.dz

3rd Doghmane Mohamed Zinelabidine
OPE, Exploration Division SONATRACH
Hassi Messaoud 30500, Algeria
MohamedZinelabidine.Doghmane@Sonatrach.dz

4th Kidouche Madjid
Laboratory of Applied Automation (LAA), Department of Automation and Electrification of Processes
Faculty of Hydrocarbons and Chemistry (FHC), University M'hamed Bougara
Boumerdes, Algeria
mkidouche@univ-boumerdes.dz

Abstract—**Stick-slip vibrations in rotary drilling systems significantly impact drilling efficiency, causing severe wear and tear on equipment and affecting hole quality. This study focuses on utilizing the Kalman filter to estimate the velocity of the drilling tool. By continuously monitoring the system state through sensor data, the Kalman filter provides precise velocity estimates. These velocity estimates are then integrated into a Proportional-Integral-Derivative (PID) control strategy. The PID controller uses the state estimates to modulate drilling parameters such as torque, effectively mitigating stick-slip vibrations. Simulations validate the proposed approach, showing a reduction in stick-slip vibrations. This results in improved drilling efficiency, reduced equipment wear, and enhanced hole quality. The adaptability of the controller to changing drilling conditions makes it a solution for various drilling scenarios.**

Keywords—Kalman filter, PID controller, Velocity, Stick-Slip Vibration

I. INTRODUCTION

The oil industry relies heavily on rotary drilling systems to extract hydrocarbons from vast underground reservoirs [1]. These systems typically consist of a drill bit that rotates as it penetrates the Earth's surface and a drill string that holds it while transmitting drilling forces [2]. Rotary drilling systems are a pillar of the oil industry, enabling the exploration and production of these priceless natural resources by providing access to underground oil and gas reserves [3]. They are crucial tools for oil and gas extraction because of their effectiveness, depth capabilities, and ability to adapt to different geological conditions. This guarantees a steady supply of energy around the world [4].

Torsion vibrations and the stick-slip phenomena are closely related difficulties in rotary drilling equipment [5]. Torsional vibrations are the oscillatory motion of the drill string caused by torque transmission from the drill bit to the surface [3]. These vibrations can cause stress and wear on drilling components, potentially resulting in equipment breakdowns and decreased drilling efficiency [6]. The stick-slip phenomenon is a direct result of these torsional vibrations. It appears as unpredictable, violent movement of the drill bit during rotation, which can result in substantial damage such as high tool wear, decreased drilling speed, and compromised borehole quality [7]. Stick-slip worsens the problems caused by torsional vibrations, resulting in operational inefficiencies and increased drilling costs.

Modeling the nonlinear dynamics of a drill string under torsional vibration is an important aspect of addressing the challenges it poses in rotary drilling systems [8]. By understanding the complex behavior of the drill string, it becomes possible to develop effective control strategies [9]. In this study, a strategy based on the Kalman Filter coupled with a PID controller is proposed because it is a good combination in this context [10], [5]. The Kalman Filter provides accurate real-time estimates of the drill string's state, including its velocity and position, enabling precise monitoring of torsional vibrations. These estimates are then integrated into the PID controller, which actively adjusts drilling parameters to mitigate vibrations and maintain stable drilling operations [11]. This integrated approach not only enhances drilling efficiency but also extends equipment life, reduces maintenance costs, and ultimately contributes to more successful and cost-effective drilling outcomes.

II. GENERALITY ABOUT THE DRILLING SYSTEMS

Drilling systems are complex and vital equipment used in various industries, most notably in the exploration and extraction of natural resources like oil, gas, and minerals. These systems consist of several key components, including the drill bit, which is the cutting tool that bores into the ground, and the drill string, a connected series of pipes and components that transmits drilling forces and rotates the drill bit. The drill string is typically powered by a rotary table or top drive, and a drilling mud circulation system circulates drilling fluid to cool the bit, remove cuttings, and maintain well pressure [12].

Additional surface components (Fig.1) include the draw works, which manage the hoisting of the drill string in and out of the well, and the derrick or mast, which provides structural support for these operations. Moreover, there is a crown block and traveling block arrangement that assists in lifting and lowering the drill string. Blowout preventers and casing are used to ensure safety and well integrity, particularly during drilling and well completion activities. Drilling systems vary in size and complexity depending on the specific application, and their components must work in tandem to efficiently and safely drill boreholes in various geological formations [2].
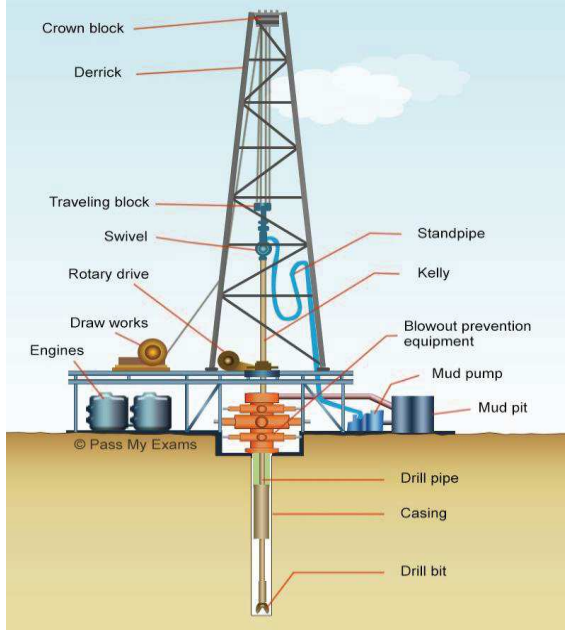

Fig. 1 Rotary drilling system descriptive schema.

III. MODELIZATION OF THE DRILLING SYSTEM

The drilling system's mathematical model is developed by picturing it as a system in which the pipes function as torsional springs and the collars are rigid bodies. We assume a constant rotating speed for the top drive to simplify the study. To simplify the analysis, we state that the dominant interaction between the drill string and the geological formation occurs at the drill bit, with lateral and axial vibrations considered negligible. Furthermore, the model employs a dry frictional description, which considers bit-formation interaction as a mix of cutting operations and frictional forces [13].

A. Drill-String Model

The drill-string model created in this work as shown in fig.2 is based on separating the drill-string into three pieces that are connected in series, with each portion represented by a torsion pendulum with viscous and dry frictions at its ends. The upper portion is connected to the top drive, while the bottom portion is connected to the borehole assembly (BHA), which is subject to viscous friction and bit torque. The mathematical model of the drill string is given in eq(1):
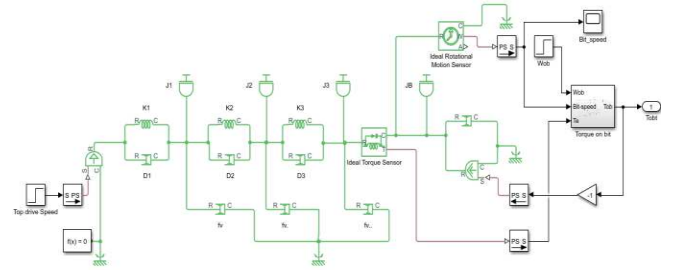

Fig. 2 Simscape model of the drill string

$$\begin{cases} \ddot{\Phi}_1 = \frac{K_1}{J_1}(\dot{\Phi}_{td} - \Phi_1) + \frac{D_1}{J_1}(\dot{\Phi}_{td} - \dot{\Phi}_1) - \frac{K_2}{J_1}(\Phi_1 - \Phi_2) - \frac{D_2}{J_1}(\dot{\Phi}_1 - \dot{\Phi}_2) - \frac{f_v}{J_1}\dot{\Phi}_1 \\ \ddot{\Phi}_2 = \frac{K_2}{J_2}(\Phi_1 - \Phi_2) + \frac{D_2}{J_2}(\dot{\Phi}_1 - \dot{\Phi}_2) - \frac{K_3}{J_2}(\Phi_2 - \Phi_3) - \frac{D_3}{J_2}(\dot{\Phi}_2 - \dot{\Phi}_3) - \frac{f_v}{J_2}\dot{\Phi}_2 \\ \ddot{\Phi}_3 = \frac{K_3}{J_3}(\Phi_2 - \Phi_3) + \frac{D_3}{J_3}(\dot{\Phi}_2 - \dot{\Phi}_3) - \frac{f_v}{J_3}\dot{\Phi}_2 - \frac{1}{J_3}T_{ob} \end{cases}$$

$$(1)$$

Where $\dot{\Phi}_{td}$ is the top drive angular velocity, $\Phi_1; \Phi_2; \Phi_3$ are respectively the angular displacement of the top drive, the drill pipes, and the BHA. Tob is the torque on the bit, given in (2), and it represents the nonlinearity of the system, constituting the main dynamic of the rock-bit interaction behavior, Table 1 presents a detailed description of the parameters used in the model

Table 1. Description of symbols used in the system model

Parameters	Description	Unit
$J_{i=1,2,3}$	The equivalent moment of inertia of the rope section i	$[Kg.m^2]$
$K_{i=1,2,3}$	The stiffness coefficient of the rope section i	$[N.m/rad]$
$D_{i=1,2,3}$	The internal damping coefficient of the top drive, drill pipes and BHA respectively	$[N.m.S/rad]$
f_v	The viscous damping coefficient of the BHA	$[N]$
Tob	The nonlinear estimated value of the torque on bit	$[N.m]$

B. Rock-bit Interaction

The contact between the drill bit and the rock formation during drilling operations is a complicated phenomenon impacted by a variety of elements [14]. These considerations include the rock formation's type and geological features, the design of the drill bit, and drilling parameters such as rotating speed and weight. This interaction is often described as a nonlinear frictional force caused by the stick-slip phenomenon, which occurs when the drill bit's rotational velocity varies fast. This interaction can be represented by different model such as the Karnop model given by eq (2):

$$Tob = Tc + Tf$$

$$Tc = \frac{1}{2} R^2_{bit} \varepsilon d \qquad (2)$$

$$Tf = \begin{cases} Te & if \; |\Phi_3| < D_v \;\; and \; |Te| < Ts \\ T_s sign(Te) & if \; |\Phi_3| < D_v \;\; and \; |Te| > Ts \\ T_d sign(\Phi_3) & if \; |\Phi_3| \geq D_v \end{cases}$$

$$T_{s/d} = \frac{1}{2} g W_{ob} \mu_{s/d}$$

Where T_e is the applied external torque, and ε is the intrinsic specific energy (that is bigger when the formation is harder), d is the depth of cut and R_{bit} is the bit radius (if the bit has a larger radius this leads to bigger torque on bit), $\mu_{s/d}$ is the static/dynamic frictional coefficient, g is the gravity, and W_{ob} is the weight on bit.
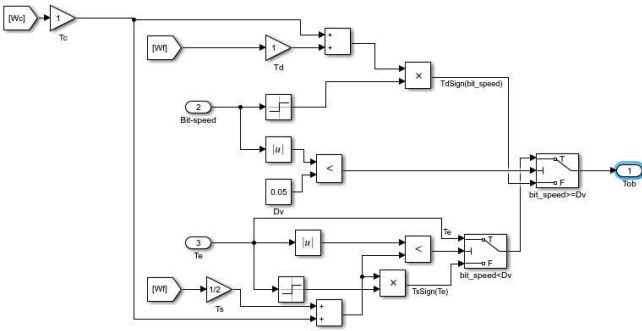Fig.3 shows the Simulink model of Karnop friction

Fig . 3 Simulink model of Karnop friction

C. Kalman Filter

The Kalman filter is a mathematical algorithm used for estimation, prediction, and filtering in various fields [15], particularly in control systems, robotics, and signal processing. It is particularly useful in situations where you have a system with noisy measurements and you want to estimate the true state of the system. The standard form of a discrete-time linear Kalman filter can be described by two main equations:

- State Prediction Equation (Time Update):

This equation is used to predict the current state of a system at a future time step based on the previous state and a control input (if applicable). It is often called the "Time Update" equation (3).

$$\hat{x}(k) = A * \hat{x}(k-1) + B * u(k) + \Gamma * T_{ob}(k) \qquad (3)$$

Predict the covariance matrix for the predicted state:

$$P(k) = A * P(k-1) * A^T + Q \qquad (4)$$

Where $\hat{x}(k)$: The estimated state vector at time k, and A is the state transition matrix, which describes how the system evolves over time, and B is the control-input matrix (if there is a control input u(k)), u(k) is the control input at time k (if applicable), and Tob(k): The process noise, representing random disturbances in the system, P(k) is the error

covariance of the state estimate at time k, and Q is the process noise covariance.

- Measurement Update Equation (Measurement Update):

This equation is used to update the state estimate with new measurements, taking into account the measurement noise and the difference between the predicted state and the actual measurement. Calculate the Kalman gain K(k):

$$K(k) = \frac{P^-(k) * C^T}{\left(C * P^-(k) * C^T + R\right)} \qquad (5)$$

Update the state estimate:

$$\hat{x}(k) = \hat{x}^-(k) + K(k) * \left[y(k) - C * \hat{x}^-(k)\right] \qquad (6)$$

Update the error covariance matrix:

$$P(k) = \left(I - K(k) * C\right) * P^-(k) \qquad (7)$$

Where $\hat{x}^-(k)$ is the updated state estimate at time k, $P^-(k)$ is he updated the error covariance, and K(k) is The Kalman gain at time k, which determines the weight given to the measurement update, and y(k) is the actual measurement at time k, C is the measurement matrix, which relates the state to the measurements. It defines how the measurements are related to the state variables, R is the measurement noise covariance.

The Kalman filter is an adaptive algorithm that updates the Kalman gain and state estimation in response to the system's changing dynamics and uncertainty. Setting K(k) to a constant value (such as K(k) = p) is not a recommended method since it does not account for changes in the system or measurement noise. Instead, at each time step, the Kalman gain is computed dynamically based on the changing state estimation and measurement noise characteristics, figure 4 shows the implementation of Kalman filter in the system.
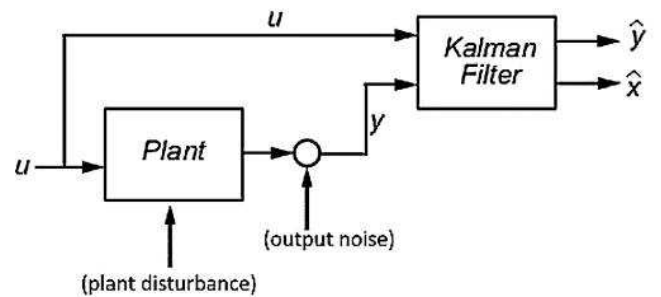
Fig. 4 Kalman estimator sheam

D. PID Controller

A PID controller is a type of feedback control system that is frequently used to help regulate and stabilize diverse operations. It combines three control actions in order to keep a desired setpoint by minimizing the difference between the setpoint and the actual process variable. The output of the controller is defined by three components: the proportional term (P), which scales the error; the integral term (I), which accounts for accumulated previous errors over time; and the derivative term (D), which predicts and compensates for quick changes in the error [11]. A PID controller is

mathematically described by the equation (8), the parameters of the PID can easily be determined using tune function in MATLAB Simulink.

$$u(t) = K_p * e(t) + K_i * \int_0^t e(\tau)d\tau + K_d * \frac{de(t)}{dt} \qquad (8)$$

And $e(t) = Q_{ref} - \hat{\Phi}_3 \qquad (9)$

Here, u(t) is the control output, e(t) is the error (difference between setpoint and process variable), $\hat{\Phi}_3$ is the estimated velocity of the BHA and Kp, Ki, and Kd are the proportional, integral, and derivative gains, respectively. The PID controller can be fine-tuned by adjusting these gains to optimize system performance and achieve desired control outcomes, the gain optimization can take some time.

IV. RESULTS AND DISCUSION

To investigate the open-loop model and demonstrate the presence of significant torsional vibrations in the high-frequency stick-slip mode within the system, as well as to assess the effectiveness of the closed-loop model employing a Kalman filter-based PID controller, we employed the MATLAB R2018a Simscape/Simulink environment. This platform facilitated the realization of the model described in equation (1).

A. Open Loop Responses

Figure 5(a) depicts the initial strong torsional vibrations at a WOB of 150N, which progressively settle over time due to the low WOB value. Figure 5(b), on the other hand, shows the enhanced WOB of 4005N creating high-frequency oscillations of the drill bit, resulting in periodic full pauses followed by sliding phases. This phenomenon reduces the rate of penetration while increasing torque needs.
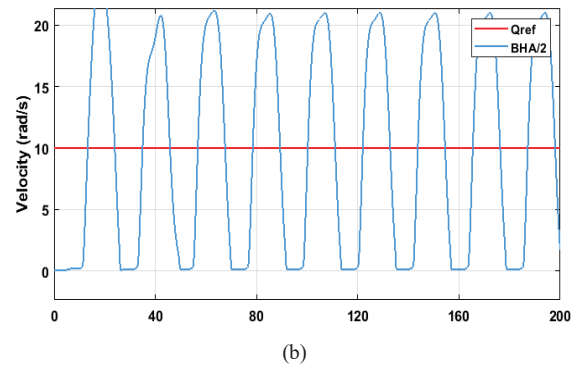

(a)

(b)
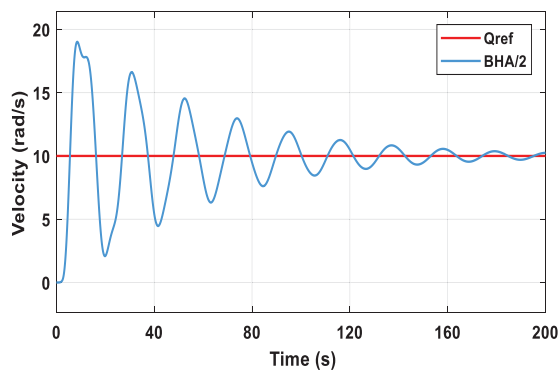
Fig . 5 Stick-Slip severity for Qref=10rpm and with: (a) Wob=150N, (b) Wob = 4005N

B. Kalman Filter Results

In Figure 6, we illustrate the Kalman state estimation in a dynamic scenario with a constant Wob (Weight on Bit) of 150N. Notably, the estimation of the bit velocity demonstrates a remarkable ability to closely follow its specified reference trajectory. However, it is essential to acknowledge that a slight static error is present in the estimation, indicating the need for fine-tuning or further optimization to achieve perfect alignment with the reference value.
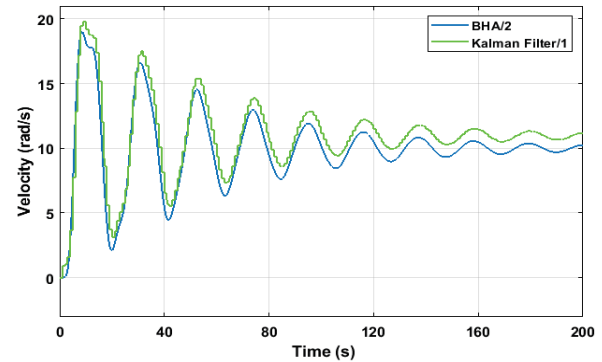
Fig . 6 KF response with Wob=150N of the bit velocity

C. Kalman Filter-Based PID controller Results

Figure 7 shows bit velocity in a dynamic system in an understandable manner. This system includes a PID controller and makes use of the Kalman filter's estimated state information. The results show a decrease in torsional vibration. It is crucial to note, however, that certain oscillations continue to exist inside the system, although at a lower intensity. Surprisingly, when the observation goes beyond the first 100-second interval, a further modification in system behavior is seen, emphasizing the necessity for a full investigation of long-term performance.

Fig . 7 KF-based PID response with Wob=150N of the bit velocity

CONCLUSION

In this research, we focused on addressing the stick-slip phenomenon within rotary drilling systems by designing a Kalman filter-based PID controller. The primary objective was to estimate the bit velocity accurately and effectively mitigate the stick-slip issue. The Kalman filter demonstrated its proficiency in providing reliable bit velocity estimates, wh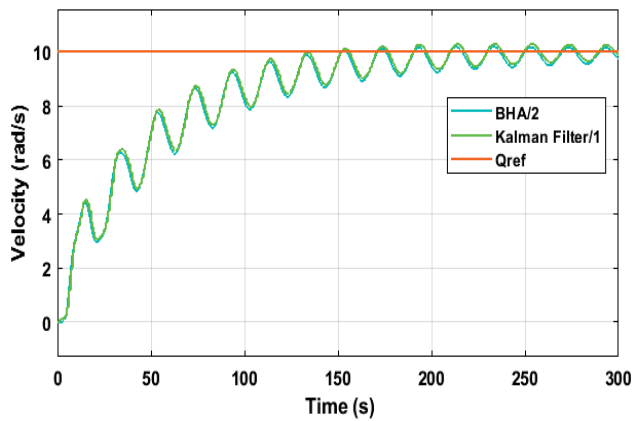ile the PID controller played a crucial role in enhancing the system's performance in the presence of torsional vibrations. However, an important observation surfaced during the experimentation phase: the stabilization time, although effective in reducing vibrations, was unacceptably long. Prolonged stabilization times could potentially lead to material damage and are impractical for real-time drilling operations, therefore in this case the PID controller is not robust due to the high nonlinearity of the system. To overcome this limitation and ensure optimal drilling performance, we propose to linearize the system or to apply a hybrid control approach. This approach combines the PID controller with a nonlinear controller, such as a sliding mode controller, and use Extended Kalman filter to improve the estimation. By doing so, we aim to significantly enhance system performance, reduce the stabilization time to a minimum, and ultimately ensure efficient and safe drilling operations. This integrated approach represents a promising solution to overcome the limitations of the conventional PID controller in stick-slip mitigation, offering a more viable and practical alternative for real-world drilling systems.

REFERENCES

[1] "C. Mendil, M. Kidouche & M. Z. Doghmane (2021): Hybrid Backstepping Sliding Mode Controller for Stick–slip Vibrations Mitigation in Rotary Drilling Systems, IETE Journal of Research, DOI: 10.1080/03772063.2021.1919217."

[2] "Besselink et al. (2016) Analysis and Control of Stick-Slip Oscillations in Drilling Systems. IEEE TRANSACTIONS ON CONTROL SYSTEMS TEHNOLOGY, DOI: 10.1109/TCST.2015.2502898 "

[3] "Mendil et al. (2022) Sliding Mode Controller Design for Torsional Vibrations Minimization Under Rock-Bit Interaction Effects. In book: Artificial Intelligence and Heuristics for Smart Energy Efficiency in Smart Cities DOI: 10.1007/978-3-030-92038-8_61"

[4] "Georgiou et al.(2020) Tracking Control for Directional Drilling Systems Using Robust Feedback Model Prediction Control. ELSEVIER IFAC 53-2(2020)11974-11981."

[5] "Riane, Rami & Doghmane, mohamed zinelabidine & Kidouche, Madjid & Djezzar, Sofiane. (2022). Observer-Based H ∞ Controller Design for High Frequency Stick-Slip Vibrations Mitigation in Drill-String of Rotary Drilling Systems. Vibration. 5. 264-289. 10.3390/vibration5020016.."

[6] "Kessai, Idir & Benammar, Samir & Doghmane, mohamed zinelabidine. (2022). Dynamic Failure Analysis and Lifetime Estimation of Tool-string in Rotary Drilling System under Torsional-Axial Coupled Vibrations. Engineering Failure Analysis. 134. 106037. 10.1016/j.engfailanal.2022.106037.."

[7] "Kessai, Idir & Benammar, Samir & Doghmane, mohamed zinelabidine & Tee, Kong Fah. (2020). Drill Bit Deformations in Rotary Drilling Systems under Large-Amplitude Stick-Slip Vibrations. Applied Sciences."

[8] "Mendil, Chafiaa & Kidouche, Madjid & Doghmane, mohamed zinelabidine & Benammar, Samir & Tee, Kong Fah. (2021). Rock–bit interaction effects on high-frequency stick-slip vibration severity in rotary drilling systems. Multidiscipline Modeling in Materials and Structures. ahead-of-print. 10.1108/MMMS-10-2020-0256.."

[9] "Abdelhamid et al. (2012) ADAPTIVE BACKSTEPPING CONTROLLER DESIGN USING TUNING FUNCTIONS APPROACH: APPLICATION TO ELECTRO-HYDRAULIC SERVO SYSTEM Magister in University of Boumerdes."

[10] "Hong, L. & Girsang, Irving & Dhupia, Jaspreet. (2016). Identification and control of stick-slip vibrations using Kalman estimator in oil-well drill strings. Journal of Petroleum Science and Engineering. 140. 10.1016/j.petrol.2016.01.017.."

[11] "C. Mendil, M. Kidouche, and M. Z. Doghmane, 'Hybrid sliding PID controller for torsional vibrations mitigation in rotary drilling systems'.IJEC 2021, doi: 10.11591/ijeecs.v22.i1.pp146-158."

[12] K. O. Afebu, Y. Liu, and E. Papatheou, "Machine learning-based rock characterisation models for rotary-percussive drilling," *Nonlinear Dyn*, vol. 109, no. 4, pp. 2525–2545, Sep. 2022, doi: 10.1007/s11071-022-07565-6.

[13] Z. Cai, X. Lai, M. Wu, C. Lu, and L. Chen, "Equivalent-input-disturbance-based robust control of drilling trajectory with weight-on-bit uncertainty in directional drilling," *ISA Transactions*, vol. 127, pp. 370–382, Aug. 2022, doi: 10.1016/j.isatra.2021.08.032.

[14] "Doghmane, mohamed zinelabidine & Kidouche, M. & Ahriche, A.. (2021). Decentralized Overlapping Control Design with Application to Rotary Drilling System. IETE Journal of Research. 69. 1-10. 10.1080/03772063.2021.1886602.."

[15] "Riane, R. & Kidouche, M. & Illoul, R. & Doghmane, mohamed zinelabidine. (2020). Unknown Resistive Torque Estimation of a Rotary Drilling System Based on Kalman Filter. IETE Journal of Research. 68. 1-12. 10.1080/03772063.2020.1724834.."

Finite Element Modeling, Interraction Analysis and Control of Coupled Axial-Torsional Vibrations in Rotary Drilling Systems

Sabrina MEDDAH
Laboratory of Applied Automation
Department of Automation, FHC,
Univesity M'hamed Bougara
Boumerdes, Algeria
s.meddah@univ-boumerdes.dz

Madjid KIDOUCHE
Laboratory of Applied Automation
Department of Automation, FHC,
Univesity M'hamed Bougara
Boumerdes, Algeria
mkidouche@univ-boumerdes.dz

Sid Ahmed TADJER
Laboratory for the electrification of
industrial enterprises
Department of Automation, FHC,
Univesity M'hamed Bougara
Boumerdes, Algeria
s.tadjer@univ-boumerdes.dz

Mohamed Zinelabidine DOGHMANE
Laboratory of Applied Automation
Reservoirs Evaluation Department, OPE,
Exploration Division, SONATRACH,
Boumerdes, Hassi Messaoud, Algeria
m.doghmene@univ-boumerdes.dz;

Abdelhakim IDIR
Laboratory of Applied Automation
Electrical Engineering Department,
University Mohamed Boudiaf
Msila, Algeria
a.idir@univ-msila.dz

Abstract— **Rotary drilling systems experience strong coupling between axial and torsional vibrations, which has a complex impact on drilling performance. Many researchers have studied each type of vibration separately, but the robustness of the developed controllers depends on the coupling effects of the other ignored vibrations. To ensure the robustness of such controllers, it is necessary to analyze the interaction effect of the control systems, especially the axial-torsional effects. PID controllers have been successfully used to solve many engineering problems with high coupling interactions. This paper investigates the interaction between axial and torsional vibrations based on finite element model and proposes a PID controller for the coupled system based on the interaction analysis results. The main contribution of this study is to improve the controller robustness in mitigating the coupled vibrations and the use of finite element model to analyze the coupling interactions. The results demonstrate the improvement provided by this research work.**

Keywords—Axial-torsional coupled vibrations, Interaction analysis, Finite element model, PID controller

I. INTRODUCTION

In today's world, the predominant sources of energy are oil and gas, both of which are typically extracted from subsurface reservoirs through drilling [1]. This essential process relies heavily on rotary drilling systems, comprising a rotational component driven by a Top drive, which is linked to the bottom hole drill bit via a drill string. Broadly, the rotary drilling system consists of two primary sections: the surface-based drilling rig, featuring a tower (derrick or mast) housing lifting and floor equipment for rod handling, screwing, unscrewing, and drill bit replacement [2, 3]. The subsurface equipment, on the other hand, constitutes the drill string assembly, comprising two main segments—the upper one composed of drill pipes and the lower one made up of thicker pipes referred to as the Bottom Hole Assembly (BHA).

Numerous researchers have dedicated their efforts to investigating the various types of vibrations encountered during petroleum well drilling [4-6]. For instance, axial vibration, initially observed as it travels along the same axis as drilling penetration, holds substantial influence over the Rate of Penetration (ROP). In severe cases, it leads to discontinuous contact between the drill bit and geological rock, known as bit-bounce. Furthermore, lateral vibrations, typically occurring at the BHA level without axial propagation to the surface, can be severe and contribute to the whirling phenomenon, potentially acting as exciters of axial vibrations [7]. Torsional vibrations, triggered by the elasticity of the drill string and the highly nonlinear torque-bit interaction, can, in extreme cases, result in the stick-slip phenomenon. Stick-slip vibrations can lead to various failures in both surface and subsurface equipment of the rotary drilling system, in addition to reducing ROP and increasing drilling costs [8-10]. While previous research has extensively examined and analyzed the impact of vibrations on rotary drilling systems and proposed controllers for real-time mitigation, they often overlook the effects of axial vibration on stick-slip severity [11]. Furthermore, few researchers have investigated the strong coupling effect of axial-torsional vibration on the robustness of controllers designed to mitigate such vibrations [12, 13].

The aim of this article is to explore the interaction between axial and torsional vibrations, and based on this analysis, propose a f PID controller to mitigate these coupled vibrations [14]. The remainder of this manuscript is structured as follows: the second section provides an in-depth overview of rotary drilling systems, focusing on various coupled vibration types. This section concludes with the development of a finite element mathematical model for rotary drilling systems subject to coupled axial-torsional vibrations. In the third section, we introduce the theory of interaction analysis and apply it to the axial-torsional vibration model. Building on the results from the third section, the fourth section delves into the theory and design of the PID controller for the system under consideration, with the primary objective of optimal mitigation of both torsional and axial vibrations. Section five presents the results obtained with the PID controller across different drilling scenarios to test and showcase the performance of the proposed approach. Additionally, we provide a statistical comparative study between the proposed approach and conventional PID controllers to demonstrate the real-time robustness of our controller. Based on the results obtained, we conclude the manuscript with final remarks and recommendations for future research endeavors.

II. ROTARY DRILLING SYSTEMS

A. System Description

One of the prominent systems within the petroleum industry is the rotary drilling system, primarily designed for the excavation of boreholes from the surface to targeted subsurface reservoirs. This system achieves its function by inducing rotational motion to the drilling tool, a process meticulously governed by the top drive mechanism [15]. The linkage between the Top drive and the drill bit is facilitated through a composite assembly of drill pipes commonly referred to as the drill string. The successful operation of this equipment hinges on three fundamental functions [16].

The rotary drilling system can be dissected into two integral components: the drilling rig, situated prominently on the terrestrial surface, and the drill string, which operates beneath the earth's surface [17]. The drilling rig encompasses a towering structure known as a derrick or mast, housing essential lifting and floor equipment, essential for the manipulation, fastening, and unfastening of rods, as well as the substitution of drilling tools. In contrast, the drill string encompasses the subterranean segment of the drilling apparatus. It comprises the upper component, constituted by a series of rods, and the lower portion identified as the Bottom Hole Assembly (BHA). The BHA encompasses crucial elements such as the drilling tool, the drill collar, and stabilizers [18-20]. During drilling operations, three distinct types of vibrations may manifest either concurrently or individually, each capable of causing significant damage and failures within the system's equipment. These vibrations can be categorized based on their propagation directions into three primary types: axial vibrations, lateral vibrations, and torsional vibrations [19]. It is worth noting that multiple types of vibrations can coexist, resulting in coupled modes, such as axial-torsional, torsional-lateral, or lateral-axial-torsional. This study places particular emphasis on the coupled axial-torsional vibration mode, primarily due to its prevalence and its potential deleterious effects on rotary drilling systems [21].

B. Coupled Vibrations' Modes

- Torsional-Lateral Vibrations

In specific drilling scenarios, the response of the drill string to torsional vibrations may be influenced by the lateral coupling effect, leading to the emergence of critical angular velocities not apparent in the response of uncoupled torsional vibrations. Therefore, a comprehensive consideration of both coupling effects on the angular velocity of the drill string and the interaction between the drill bit and the geological formation becomes imperative in such instances [17]. Although such coupling occurrences are relatively infrequent, their investigation remains significant [22]. Regrettably, the current research study under scrutiny has not specifically addressed this particular type of coupling. However, other types of coupled vibrations have been discussed in the next subsections.

- Lateral-Axial Vibrations

Within the domain of rotary drilling systems, lateral vibrations can instigate the whirling phenomenon, which constitutes a critical state capable of inflicting damage upon the drill string and associated equipment [23]. Recent scientific inquiries have elucidated that random whirling, in particular, exerts a more pronounced influence on axial vibrations compared to forward and backward whirling. Specifically, the occurrence of random whirling induces alterations in the drill string's curvature, consequently engendering axial vibration waves. It is worth highlighting that the emergence of whirling and bit-bounce typically transpires simultaneously, often following prior torsional vibrations. In light of the salience of torsional vibrations and their intricate coupling with other vibration modes, the present study will center its focus on coupled vibrations encompassing torsional vibrations [19]. It is essential to emphasize that the coupling effects observed in drilling systems are intricate and contingent upon multiple factors, including drilling conditions, formation properties, and drill string configuration. Consequently, this present study primarily concentrates on coupled axial-torsional vibrations, which represent one of the most prevalent forms of coupled vibrations encountered in drilling operations. The primary objective herein entails the proposition of a PID controller capable of effectively mitigating the detrimental impacts of coupled axial-torsional vibrations on the drilling system. Through the enhancement of controller robustness, the proposed approach seeks to improve system performances.

- Axial-Torsional Vibrations

The coupling phenomenon between axial and torsional vibrations, closely linked to the transformation of WOB transmitted to the drill bit through the drill-string, represents a prevalent occurrence during drilling operations. This coupling mode may engender the stick-slip phenomenon, eventually leading to whirling, wherein axial vibration waves are generated and propagate towards the surface [20]. Moreover, the arrival of a reflected axial vibration wave from the surface or a contact point within the drill string can trigger the release of the drill bit from the stick phase, precipitating the slip phase and culminating in a repetitive cycle. Given the insightful analysis of these interactions, the present study dedicates its focus to the mode of coupled axial-torsional vibrations, owing to its frequent manifestation and pronounced impact on the rate of penetration (ROP) and equipment integrity. This endeavor aims to undertake a comprehensive investigation of the coupled phenomena involving the bit-bounce and the stick-slip [21].

III. FEM OF SYSTEM UNDER AXIAL-TORSIONAL VIBRATIONS

The method of finite element modelling has been used to construct the mathematical model of rotary drilling system under coupled vibrations, in which the drill string is presented as an acorn-shaped tree [24]. Using the Lagrange method, we were able to express it dynamic as a base element rotating with axial and angular displacement at the level of two extrema: $u = N_u q$, $\theta_u = N_\theta q$, with N_u, N_θ are the matrix, Q stands for the coordinate vectors of two nodes, as given by equation (1).

$$q = \begin{Bmatrix} u_1 \\ \theta_{u_1} \\ u_2 \\ \theta_{u_2} \end{Bmatrix} \qquad (1)$$

u_i: represents the translation in the axial direction, θ_i the rotation around x axes, and :

$$\xi = x / l_e \tag{2}$$

With l_e is the length of the element. The form matrices as function of ξ are given by equations (3-6).

$$N_1 = 1 - \xi \tag{3}$$

$$N_2 = \xi \tag{4}$$

$$N_u = \{N_1, 0, N_2, 0\} \tag{5}$$

$$N_\theta = \{0, N_1, 0, N_2\} \tag{6}$$

The local displacement angle is highly interconnected to the torsional vibrations; when the latter occurs at a given position in the drill string, the other location of the drill string stay rotating with the similar rotational velocities for a short period, which create a torsion at the drill pipes. Therefore, the elementary mass distribution along the drill string (with the same direction of rotation) is given by the matrix described by equation (7).

$$M_e = \int_0^1 \left[\rho A l_e N_u^T N_u + \rho J l_e N_\theta^T N_\theta \right] d\xi \tag{7}$$

Where ρ is the density, A is the shaft section, and J: is the moment of inertia [25]. Moreover, the matrix of mass distribution for a single element is obtained by integration of the Me given by equation (8).

$$M_e = \begin{bmatrix} \dfrac{\rho A l_e}{3} & 0 & \dfrac{\rho A l_e}{6} & 0 \\ 0 & \dfrac{\rho J l_e}{3} & 0 & \dfrac{\rho J l_e}{6} \\ \dfrac{\rho A l_e}{6} & 0 & \dfrac{\rho A l_e}{3} & 0 \\ 0 & \dfrac{\rho J l_e}{6} & 0 & \dfrac{\rho J l_e}{3} \end{bmatrix} \tag{8}$$

The stiffness matrix is calculated by:

$$K_e = \int_0^1 \left[\frac{EA}{l_e} N_u'^T N_u' + \frac{GJ}{l_e} N_\theta'^T N_\theta' \right] d\xi \tag{9}$$

By integrating K_e in equation (9), the rigidity matrix for a particular element is obtained as (10). It has been supposed that the damping at the element of drill string is of Rayleigh type, and it is represented by equation (11).

$$K_e = \begin{bmatrix} \dfrac{EA}{l_e} & 0 & -\dfrac{EA}{l_e} & 0 \\ 0 & \dfrac{GJ}{l_e} & 0 & -\dfrac{GJ}{l_e} \\ -\dfrac{EA}{l_e} & 0 & \dfrac{EA}{l_e} & 0 \\ 0 & -\dfrac{GJ}{l_e} & 0 & \dfrac{GJ}{l_e} \end{bmatrix} \tag{10}$$

$$C = \alpha M + \beta K \tag{11}$$

M and K are the total matrices of mass and rigidity of the system composed of n elements. $\alpha = \beta = 0.01$. These coefficients define damping Rayleigh-type. The values of α

and β have been calculated by using the formula in equation (12).

$$\xi_i = \frac{1}{2} \left(\frac{\alpha}{\omega} + \beta \omega_i \right) \tag{12}$$

ξ: is the damping ratio, which is usually 5%, and ω is the natural frequency of the system. The equation of motion of the system is then written as:

$$M\ddot{q}(t) + C\dot{q}(t) + Kq(t) = F(t) \tag{13}$$

In this paper, the torque on bit (TOB) mathematical model has been inspired from *Yigit and Christoforou*, Year [ref], as given by equation (14).

$$TOB = WOB.r_b . \left(\mu \left(\rule{3cm}{0.5cm} \right) \right) \tag{14}$$

Where $\xi 0$ is the coefficient of the model, δc is thedepth by each cycle, and

$$\delta_c = 2\pi ROP / w \tag{15}$$

$$ROP = C_1 F_0 \sqrt{w} + C_2 \tag{16}$$

F0 is the variation in weight between the hook weight and the total weight, w is the average speed of rotation, C_1 and C_2 are constant, and $\mu(\theta)$ is a function that characterizes the friction process, it is given by equation (17).

$$\mu(\dot{\theta}) = \mu_0 \left(\frac{\rule{2.5cm}{0.4cm}}{1 + \alpha_2 \rule{0.4cm}{0.3cm}} \right) \tag{17}$$

$\alpha 1$ is the first friction coefficient of the model, while $\alpha 2$ is the second friction coefficient of the model, ν is the Poisson coefficient, and $\dot{\theta}$ is rotational velocity of the drill bit [26]. The matrices M, C, and K are automatically generated when running the script in Matlab environment. The system's external force vector is denoted by *F(t)*. It depends on the input torque (*U₀*), hook weight (*F₀*), weight of each element, weight on bit (WOB), torque on bit (TOB), and weight on bit (U0) (Fig.1). The Wob formula used in this study is given by equation (19).

$$WOB = \begin{cases} k_c (x - s) & x > s \\ 0 & x < s \end{cases} \tag{18}$$

x is the axial displacement, s: is the elevation of the training surface, and kc is the stiffness of contact with the formation and s is given by equation (20).
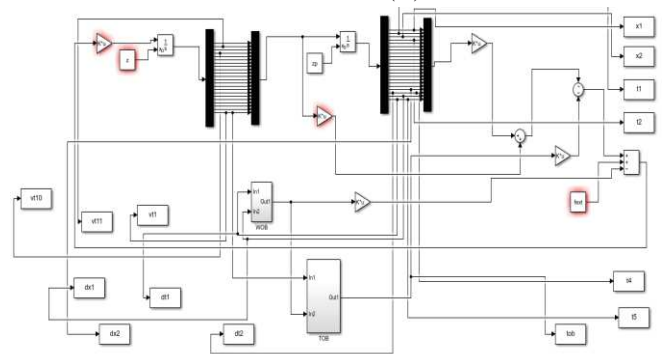
$$S = s_0 \sin(\theta) \tag{19}$$

Fig. 1. Inputs and outputs of rotary drilling system as a TITO (Two-input Two-output) system

IV. INTERACTION ANALYSIS

A. RGA

The closed-loop interaction in a MIMO system is the influence of transmitances so that a signal or perturbation affects several sorties ($y_i(s), i \neq j$), or alternatively, that a single output $y_i(s)$ is affected by several signals ($c_j(s), i \neq j$) or multiple perturbations [13]. In order to ensure a low level of engagement, Bristol proposed the method of relative gains (RGA) in 1966. This method is based on the open-loop system's statistical gains matrix calculation. Each RGA component is determined by:

$$\lambda_{i,j} = \frac{\left(\frac{\partial y_i}{\partial u_j}\right)_{u_k=0, k \neq j}}{\left(\frac{\partial y_i}{\partial u_j}\right)_{y_k=0, k \neq i}} \tag{20}$$

The numerator is the statistical gain in an open boucle between u_j and y_i, while the denominator is the statistical gain between u_j and y_i when all other outputs are perfectly controlled [15]. The gain relatif λ_{ij} indicates whether the gain of an open cylinder [u_j– y_i] changes while all other cylinders are closed.

$$RGA = k_s .* \left[k_s^{-1}\right]^T \tag{21}$$

$$k_{sij} = \lim_{s \to 0} G_{ij}(s), i,j = 1, \ldots, m \tag{22}$$

.∗: element by element multiplication. Ks : is the statistical gains matrix. Ks_{ij}:. the statistical gain between u_j and y_i. The algebraic sum of the elements of the RGA along a row i or a column j is equal to 1. For a zero Ks_{ij} element, the corresponding relative gain λ_{ij} is zero. The level of interaction in the system is very low if the RGA's diagonal ($\lambda_{ij} : i = j$) elements are close to 1, but it is strong if the opposite is true (i.e., if the elements are below or above 1).

- if $\lambda_{ij} = 0$, There is no connection between input j and output i.
- if $0 < \lambda_{ij} < 1$, There is interaction between the regulatory spheres. This would be a better choice because it would minimize interactions.
- if $\lambda_{ij} = 0.5$, There is a level of interaction, and the effects of the other regulatory spheres are similar. Input point on output point i.
- if $\lambda_{ij} = 1$, There is no interaction between the couple entry-level regulation block [u_j–y_i] and the other regulation blocks.
- If $\lambda_{ij} = 0.5$, There is a level of interaction, and the effects of the other regulatory spheres are similar. Entry point j on exit point i.
- if $\lambda_{ij} > 1$, The interaction is strong, thus one must establish it. It would be the preferred option in the command configuration, though.

- if $\lambda_{ij} < 0$, If the other loop are closed, there are strong interactions, and the response of the corresponding boucle may alter in sense of variation (inverse response system) [9]. In addition, if the considered boucle ever opens, the boucle itself may become unstable or the system as a whole may become unstable, so the appropriate pair need not be selected in the command configuration.

B. Axial-Torsional vibration interaction analysis

The selection of the control setup pertains to pairs with a relative gain (λ_{ij}) that is in proximity to 1.from the results of RGA obtained we have :

$\lambda_{12}, \lambda_{21}, \lambda_{32}, \lambda_{41}, \lambda_{54}, \lambda_{63}, \lambda_{74}, \lambda_{83}$:Strong interactions between the couples [y_1-u_2] , [y_2-u_1] , [y_3-u_2] , [y_4-u_1] and [y_5-u_4] , [y_6-u_3] , [y_7-u_4] , [y_8-u_3] need not be selected in the command configuration. $\lambda_{11}, \lambda_{22}, \lambda_{31}, \lambda_{42}, \lambda_{54}, \lambda_{64}, \lambda_{73}, \lambda_{84}$:Strong interactions make the following option the preferred one in the command setup for couples :[y_1-u_1] , [y_2-u_2] , [y_3-u_1] , [y_4-u_2] and [y_5-u_3] , [y_6-u_4] , [y_7-u_3] , [y_8-u_4].

V. SIMULATION RESULTS

A. FEM Model Open loop responses

The discernible variation in friction torque magnitudes engenders a consequential impact on the oscillatory behavior of the angular velocity of the drill bit, thereby giving rise to the manifestation of pronounced amplitude stick-slip oscillations. Figures (2) and (3) portray the dynamic behavior of the drill bit in the context of stick-slip vibrations using FEM model compared to lamped model. Notably, the angular velocity of the drill bit surges to a magnitude that is twice that of the top drive's angular velocity. This discernible dissimilarity can be ascribed to the conversion of potential energy, which accumulates within the drillstring during the stick phase, into kinetic energy. This resultant kinetic energy increment augments the driving torque applied to the bit, thus compelling the drill bit to attain a heightened rotational velocity. Comparatively, the model characterized by FEM demonstrates a heightened sensitivity to the stick-slip phenomenon when contrasted with the lamped. This distinction is evident in the greater count of stick-slip cycles exhibited within the former model.
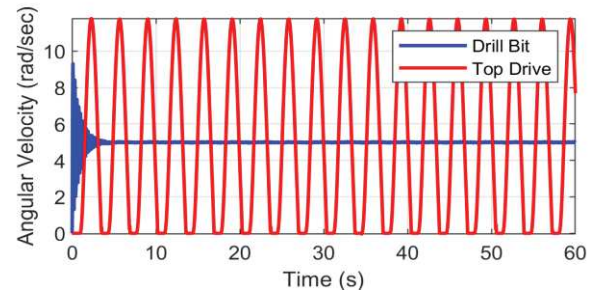

Fig. 2. Angular velocities of top drive and drill bit using lampled model
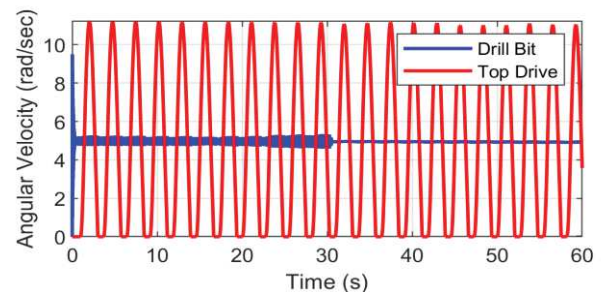

Fig. 3. Angular velocities of top drive and drill bit in 200-DoF Model with rough drilling

Figures 4 and 5 show the results of the system in open loop form for axial and torsional vibrations respectively. It is clear that the severity of these vibrations is very

considerable. The designed PID is implemented and tested, figure 6 and 7 show the obtained results, it is clear that the controller has arrived to minimize the stick-slip vibrations in 20 s and reduced the effect of bit bounce of the axial vibrations.
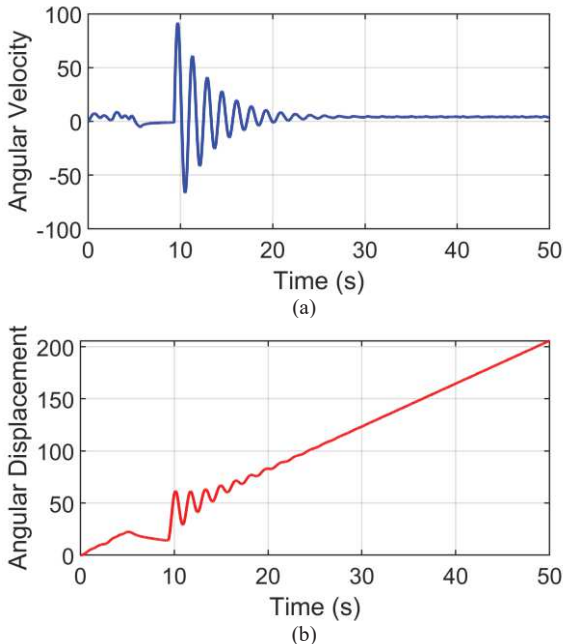

(a)

(b)

Fig. 4. Angular responses: (a) Angular velocityt, (b) Angular Displacement
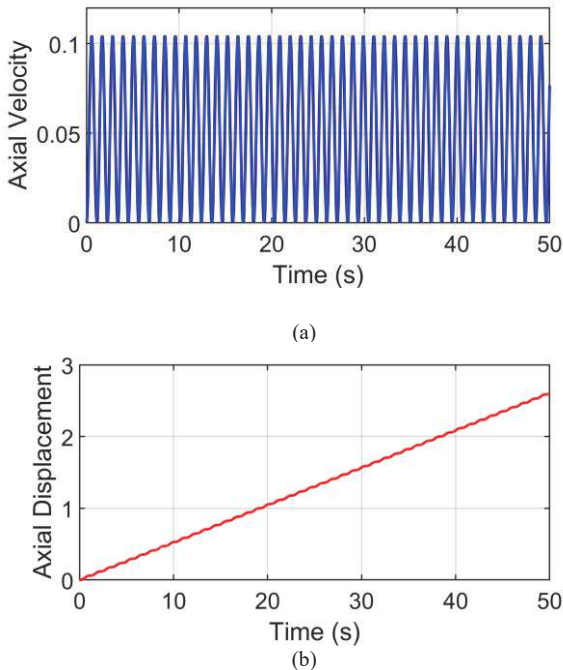

(a)

(b)

Fig. 5. Axial responses: (a) Axial velocity, (b) Axial displacement.

VI. CONCLUSIONS

Following a thorough examination of the system FEM model and an in-depth investigation into the behavior of axial and torsional vibrations at the drill bit level under open-loop conditions, it becomes evident that the system is
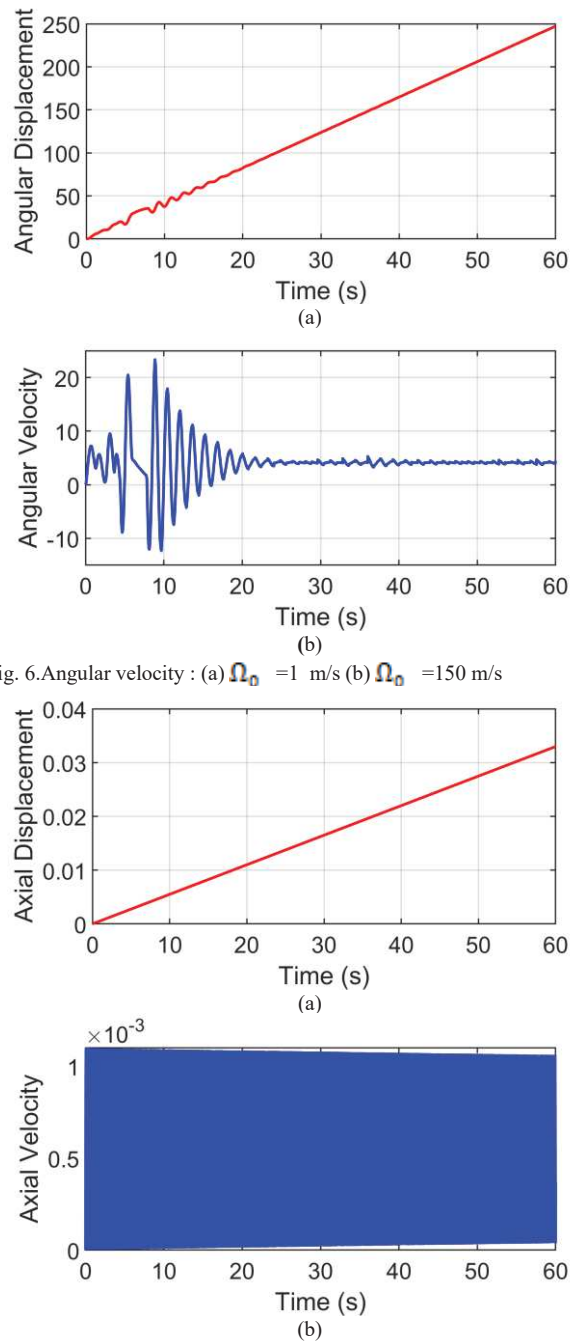

(a)

(b)

Fig. 6. Angular velocity : (a) Ω_0 =1 m/s (b) Ω_0 =150 m/s

(a)

(b)

Fig. 7. Axial velocity : (a) Ω_0 =1 m/s (b) Ω_0 =150 m/s

These vibrational anomalies hold the potential to inflict significant harm upon the rotary drilling system, ultimately resulting in diminished Rates of Penetration (ROP) and escalated drilling expenditures. Consequently, the imperative lies in the development of a resilient controller capable of mitigating these co-occurring vibrations, thereby enhancing drilling efficiency.

susceptible to exhibiting stick-slip and bit-bounce phenomena arising from these vibrations. Moreover, the interaction analysis, as predicated on Relative Gain Array (RGA), affirms the presence of a robust coupling effect between axial and torsional vibrations, indicating the potential utility of these control pairs to bolster the controller's efficacy in suppressing the coupled vibrations. The proposed controller must exhibit adeptness in attenuating the stick-slip and bit-bounce phenomena with

notable effectiveness, thereby fostering smoother drilling operations and amplifying overall drilling efficiency.

In forthcoming research endeavors, a comprehensive exploration will be undertaken to formulate and implement the proposed controller, subjecting it to rigorous evaluation across diverse operational scenarios, thereby shedding light on its performance characteristics in a practical context.

REFERENCES

[1] S.A. Sina, H. Haddadpour, Axial–torsional vibrations of rotating pretwisted thin walled composite beams, International Journal of Mechanical Sciences, Volume 80, 2014, Pages 93-101, ISSN 0020-7403, https://doi.org/10.1016/j.ijmecsci.2013.12.018

[2] Shor, Roman J., Dykstra, Mark W., Hoffmann, Olivier J., and Matthew Coming. "For Better or Worse: Applications of the Transfer Matrix Approach for Analyzing Axial and Torsional Vibration." Paper presented at the SPE/IADC Drilling Conference and Exhibition, London, England, UK, March 2015. doi: https://doi.org/10.2118/173121-MS

[3] KeivanKiani, Longitudinal, transverse, and torsional vibrations and stabilities of axially moving single-walled carbon nanotubes, Current Applied Physics, Volume 13, Issue 8, 2013, Pages 1651-1660, ISSN 1567-1739, https://doi.org/10.1016/j.cap.2013.05.008

[4] TY - JOUR, Mucchi, Emiliano, Ren, Fushen, Wang, Baojin, Chen, Suli, Yao, Zhigang, Bai, Baojun, 2016, Nonlinear Model and Qualitative Analysis for Coupled Axial/Torsional Vibrations of Drill String, 1646814, 2016, 1070-9622, https://doi.org/10.1155/2016/1646814, DO - 10.1155/2016/1646814, JF - Shock and Vibration, PB - Hindawi Publishing Corporation

[5] Farid Rajabali, HamedMoradi, GholamrezaVossoughi, Coupling analysis and control of axial and torsional vibrations in a horizontal drill string, Journal of Petroleum Science and Engineering, Volume 195, 2020, 107534, ISSN 0920-4105, https://doi.org/10.1016/j.petrol.2020.107534

[6] Hosseinzadeh, A., and Bakhtiari-Nejad, F. (August 17, 2017). "A New Dynamic Model of Coupled Axial–Torsional Vibration of a Drill String for Investigation on the Length Increment Effect on Stick–Slip Instability." ASME. J. Vib. Acoust. December 2017; 139(6): 061016. https://doi.org/10.1115/1.4037299

[7] Vadim S. Tikhonov, Fedor D. Baldenko, Olga S. Bukashkina, Valery Yu. Liapidevskii, Effect of hydrodynamics on axial and torsional oscillations of a drillstring with using a positive displacement motor,Journal of Petroleum Science and Engineering, Volume 183, 2019, 106423, ISSN 0920-4105, https://doi.org/10.1016/j.petrol.2019.106423

[8] Sunit K. Gupta, Pankaj Wahi, Global axial–torsional dynamics during rotary drilling, Journal of Sound and Vibration, Volume 375, 2016, Pages 332-352, ISSN 0022-460X, https://doi.org/10.1016/j.jsv.2016.04.021

[9] Kamel, Jasem M., and Ahmet Yigit. "Modeling and Analysis of Axial and Torsional Vibrations of Drillstrings with Drag Bits." Paper presented at the International Petroleum Technology Conference, Doha, Qatar, January 2014. doi: https://doi.org/10.2523/IPTC-17258-MS

[10] S. Tashakori, G. Vossoughi, H. Zohoor and N. van de Wouw, "Prediction-Based Control for Mitigation of Axial–Torsional Vibrations in a Distributed Drill-String System," in IEEE Transactions on Control Systems Technology, vol. 30, no. 1, pp. 277-293, Jan. 2022, doi: 10.1109/TCST.2021.3065669

[11] Liu, X., Vlajic, N., Long, X. et al. Coupled axial-torsional dynamics in rotary drilling with state-dependent delay: stability and control. Nonlinear Dyn 78, 1891–1906 (2014). https://doi.org/10.1007/s11071-014-1567-y

[12] Chafiaa Mendil1 , Madjid Kidouche2 , Mohamed Zinelabidine Doghmane, Hybrid sliding PID controller for torsional vibrations mitigation in rotary drilling systems, Indonesian Journal of Electrical Engineering and Computer Science, Vol. 22, No. 1, April 2021, pp. 146~158, ISSN: 2502-4752, DOI: 10.11591/ijeecs.v22.i1.pp146-158

[13] Q. Zhang and S. Xv, "Stick-Slip Vibration Suppression of Drill String Based on Fractional Order PID," 2019 International Conference on

Computer Network, Electronic and Automation (ICCNEA), 2019, pp. 468-473, doi: 10.1109/ICCNEA.2019.00092

[14] C. Mendil, M. Kidouche& M. Z. Doghmane (2021) Hybrid Backstepping Sliding Mode Controller for Stick–slip Vibrations Mitigation in Rotary Drilling Systems, IETE Journal of Research, DOI: 10.1080/03772063.2021.1919217

[15] Pritesh Shah, SudhirAgashe, Review of fractional PID controller, Mechatronics, Volume 38, 2016, Pages 29-41, ISSN 0957-4158, https://doi.org/10.1016/j.mechatronics.2016.06.005

[16] Riane, R.; Doghmane, M.Z.; Kidouche, M.; Djezzar, S. Observer-Based H∞ Controller Design for High Frequency Stick-Slip Vibrations Mitigation in Drill-String of Rotary Drilling Systems. Vibration 2022, 5, 264-289. https://doi.org/10.3390/vibration5020016

[17] Idir Kessai, Samir Benammar, M.Z. Doghmane, Dynamic failure analysis and lifetime estimation of Tool-string in rotary drilling system under Torsional-Axial coupled vibrations, Engineering Failure Analysis, Volume 134, 2022, 106037, ISSN 1350-6307, https://doi.org/10.1016/j.engfailanal.2022.106037

[18] Mendil, C., Kidouche, M., Doghmane, M.Z. (2022). Sliding Mode Controller Design for Torsional Vibrations Minimization Under Rock-Bit Interaction Effects. In: Hatti, M. (eds) Artificial Intelligence and Heuristics for Smart Energy Efficiency in Smart Cities. IC-AIRES 2021. Lecture Notes in Networks and Systems, vol 361. Springer, Cham. https://doi.org/10.1007/978-3-030-92038-8_61

[19] Kessai, I., Doghmane, M.Z., Benammar, S. (2022). Weight-On-Bit Variations Analyses in the Drillstring of Rotary Drilling Systems Under Stick-Slip Vibrations. In: Hatti, M. (eds) Artificial Intelligence and Heuristics for Smart Energy Efficiency in Smart Cities. IC-AIRES 2021. Lecture Notes in Networks and Systems, vol 361. Springer, Cham. https://doi.org/10.1007/978-3-030-92038-8_72

[20] Mendil, C., Kidouche, M., Doghmane, M.Z., Benammar, S. and Tee, K.F. (2021), "Rock–bit interaction effects on high-frequency stick-slip vibration severity in rotary drilling systems", Multidiscipline Modeling in Materials and Structures, Vol. 17 No. 5, pp. 1007-1023. https://doi.org/10.1108/MMMS-10-2020-0256

[21] M. Z. Doghmane, M. Kidouche& A. Ahriche (2021) Decentralized Overlapping Control Design with Application to Rotary Drilling System, IETE Journal of Research, DOI: 10.1080/03772063.2021.1886602

[22] Doghmane, M.Z., Bacetti, A., Kidouche, M. (2021). Stick-Slip Vibrations Control Strategy Design for Smart Rotary Drilling Systems. In: Hatti, M. (eds) Artificial Intelligence and Renewables Towards an Energy Transition. ICAIRES 2020. Lecture Notes in Networks and Systems, vol 174. Springer, Cham. https://doi.org/10.1007/978-3-030-63846-7_20

[23] Mendil, C., Kidouche, M., Doghmane, M.Z. (2021). A Study of the Parametric Variations Influences on Stick-Slip Vibrations in Smart Rotary Drilling Systems. In: Hatti, M. (eds) Artificial Intelligence and Renewables Towards an Energy Transition. ICAIRES 2020. Lecture Notes in Networks and Systems, vol 174. Springer, Cham. https://doi.org/10.1007/978-3-030-63846-7_67

[24] Mendil, C., Kidouche, M., Doghmane, M.Z. (2021). Modeling of Hydrocarbons Rotary Drilling Systems Under Torsional Vibrations: A Survey. In: Hatti, M. (eds) Artificial Intelligence and Renewables Towards an Energy Transition. ICAIRES 2020. Lecture Notes in Networks and Systems, vol 174. Springer, Cham. https://doi.org/10.1007/978-3-030-63846-7_24

[25] Mendil, C., Kidouche, M., Doghmane, M.Z. (2021). Modeling of Hydrocarbons Rotary Drilling Systems Under Torsional Vibrations: A Survey. In: Hatti, M. (eds) Artificial Intelligence and Renewables Towards an Energy Transition. ICAIRES 2020. Lecture Notes in Networks and Systems, vol 174. Springer, Cham. https://doi.org/10.1007/978-3-030-63846-7_24

[26] Bensafia, Y., Khettab, K. and Idir, A. 2022. A Novel Fractionalized PID controller Using The Sub-optimal Approximation of FOTF. Algerian Journal of Signals and Systems . 7, 1 (Mar. 2022), 21-26. DOI: https://doi.org/10.51485/ajss.v7i1.149

[27] Abdelhakim Idir, KhatirKhettab, YassineBensafia, Design of an Optimally Tuned Fractionalized PID Controller for DC Motor Speed Control Via a Henry Gas Solubility Optimization Algorithm, International Journal of Intelligent Engineering and Systems 2022, Volume 15, Numéro 3, Pages 59-70, http://dspace.univ-msila.dz:8080//xmlui/handle/123456789/4458

Enhancing Voltage Stability and Reducing Active Power Loss by the Integration of STATCOM and TCSC in the IEEE 9-Bus System

Mohamed Amir Labed
department of electrical engineering.
Brothres Mentouri Constantine 1 University
Constantine, Algeria
mohamedamir.labed@student.umc.edu.dz

Mohamed Benidir
department of transport engineering.
Brothres Mentouri Constantine 1 University
Constantine, Algeria
mcbenidir@yahoo.fr

Hocine Sekhane
department of electrical engineering.
20 August 1955 Skikda University
Skikda, Algeria
docsekhoc@gmail.com

Abstract—**This conference paper delves into the integration of two prominent Flexible AC Transmission System (FACTS) devices, namely Static Synchronous Compensator (STATCOM) and Thyristor-Controlled Series Compensator (TCSC), to ameliorate power flow in a default state. The study investigates the impact of strategically implementing these FACTS devices at different locations within the standard IEEE 9-bus system. Using the Power System Analysis Toolbox (PSAT) in MATLAB, a comprehensive analysis was conducted, comparing the outcomes in terms of voltage stability and reductions in active and reactive power losses. The findings of this research illuminate the nuanced interplay between STATCOM and TCSC devices, providing valuable insights into their effectiveness in enhancing power system stability. By systematically evaluating voltage profiles and minimizing active and reactive power losses, this study contributes significant knowledge to the field of power systems engineering.**

Keywords—STATCOM, TCSC, Power Flow Optimization, Voltage Stability, FACTS Devices, IEEE 9-Bus System, PSAT MATLAB, Comparative Analysis.

I. INTRODUCTION

Today's power grid is dealing with new challenges like increased demand, integration of renewable energy sources, and the need for enhanced stability and efficiency. In power systems, factors like continual load growth, outage of components and deregulation policies may lead to issues such as power congestion, static and dynamic instabilities [1,4]. For treating such consequences, using flexible AC transmission system (FACTS) devices is the most commonplace strategy [5]. Flexible AC Transmission Systems (FACTS) technology was originally developed for transmission systems, however, nowadays its application in RDS has been growing rapidly [6]. Utilization of smart grid systems is a huge advantage to mankind, in particular to those involved in electric power industries and utilities [7].

This conference paper is focused on energy systems engineering, specifically focusing on the strategic integration of two distinguished FACTS devices: the Static Synchronous Compensator (STATCOM) and the Thyristor-Controlled Series Compensator (TCSC).
The integration of these devices has shown remarkable potential in reducing voltage fluctuations and minimizing active and reactive power losses, thus augmenting the overall grid performance. The IEEE 9-bus system, a standard benchmark in power system analysis, serves as the testing system for our comprehensive study. By deploying these FACTS devices at various strategic points within this system, in our study's insights stem from practical considerations. By placing the devices near the faulted buses. By understanding the specific bus locations where these devices prove most effective, real-world power systems can make informed decisions.

The motivation behind this research stems from the critical need to enhance grid reliability, especially when dealing with changing renewable energy sources. Understanding the optimal placement and functioning of FACTS devices is pivotal in ensuring a robust electricity network capable of fluently adapting to dynamic demands. Through meticulous analysis and comparative evaluations, this study aims to provide valuable insights into the real-world applications of STATCOM and TCSC devices.

While we didn't employ complex algorithms, the simplicity of our approach enhances its adaptability. Placing FACTS devices near faulted buses allows for seamless integration into various grid scenarios. The devices strategic positioning ensures adaptability to dynamic conditions, accommodating renewable energy fluctuations and demand variations.

In this paper, we thoroughly analyze how STATCOM and TCSC impact voltage stability and power losses. Our findings not only add to academic knowledge but also provide practical insights for engineers and policymakers in the power sector. By understanding these device interactions, we enable informed decisions in implementing advanced FACTS technologies. This knowledge contributes to building a stronger, more efficient, and sustainable electricity grid for the future.

II. PROBLEM FORMULATION

A. Load flow analysis

Power flow analysis is applied for planning, operation, economic scheduling and exchange of power between utilities [8, 9].

The Gauss-Seidel method, one of the earliest computational techniques used for power flow solutions, marked a significant step in power systems analysis. However, its drawback is its slow convergence, often requiring numerous iterations to find a solution. To overcome this, the Newton-Raphson (NR) method was introduced. Unlike Gauss-Seidel, NR quickly resolves convergence issues, especially in common network setups, making it highly efficient. This efficiency led to its widespread adoption in the industry. NR was pivotal in overcoming early computer memory limitations, showcasing its adaptability and importance in power systems analysis. The apparent complex power injected into the bus n is given by the following relationship:

$$S_i^* = V_i^* \sum_{k=1}^{n}(Y_{ik}V_k) \qquad (1)$$

Where V_i and V_k are the voltage in bus i and k, Y_{ik} line admittance.

Equation (1) can be resolved into real and imaginary parts as follows:

$$P_i = \sum_{\substack{i=1 \\ k=1}}^{n}|V_i V_k|(G_{ik} \cos \delta_{ik} + B_{ik} \sin \delta_{ik})$$
$$Q_i = \sum_{\substack{i=1 \\ k=1}}^{n}|V_i V_k|(G_{ik} \sin \delta_{ik} - B_{ik} \cos \delta_{ik}) \qquad (2)$$

P_i, Q_i active and reactive power on bus number i, δ_{ik} is the phase angle difference between the voltage at bus i and k, G_{ik} and B_{ik} represent transfer conductance and transfer susceptance respectively between bus i and bus k.

The following equation represents the branch power loss (P_{loss}) is:

$$P_{loss\,i,j} = \left(\frac{P_{i,j}^2 + Q_{i,j}^2}{V_i^2}\right) R_{ij} \qquad (3)$$

$R_{i,j}$, $P_{i,j}$, $Q_{i,j}$ are resistance, active and reactive powers respectively from bus i to bus j, V_i is voltage in the bus i [10].

B. STATic synchronous COMpensator (STATCOM)

It is a reactive power compensation device connected in shunt to transmission and distribution systems, capable of generating and/or absorbing reactive power.
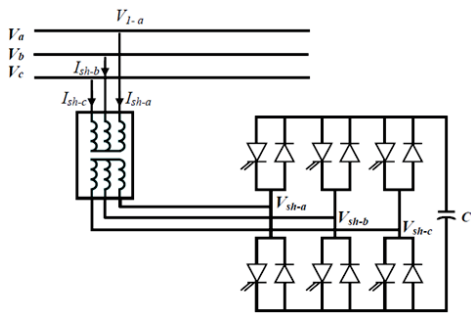

Fig. 1. Basic structure of STATCOM.

C. Thyristor Controlled Series Capacitor (TCSC)

A TCSC is composed of a capacitor bank in parallel with an inductor controlled by thyristors. The total impedance seen by the line is a parallel combination of capacitance and the equivalent inductance which varies according to the firing angle of the thyristors. Several control modules can be aligned in series in the line to be compensated [11, 12].
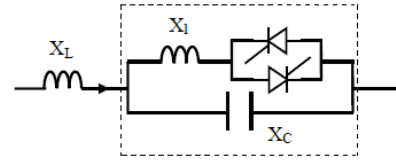

Fig. 2. Basic structure of TCSC.

III. RESULTS AND DISCUSSION

In our study, we carefully examined the IEEE 9-bus system to understand how it behaves in different situations. This system includes 9 buses, 6 lines, 3 transformers, 3 generators, and 3 loads, making it a standard power grid setup, the figure 3 present the used system. First, we studied the network when everything was working normally, acting as our base scenario. Then, we created a challenge by simulating a fault at bus number 7. To overcome this challenge, we strategically placed two different Flexible AC Transmission System (FACTS) devices near bus 7.

The primary focus of this analysis was to evaluate the impact of these interventions on the network's performance metrics. Particularly, the study concentrated on comparing the voltage stability enhancements achieved by the STATCOM and TCSC devices. Additionally, the investigation delved into the reduction of both active and reactive power losses, pivotal factors for ensuring efficient power transmission.

We mention that in our study's insights stem from practical considerations. By placing the devices near the faulted buses. By understanding the specific bus locations where these devices prove most effective, real-world power systems can make informed decisions.
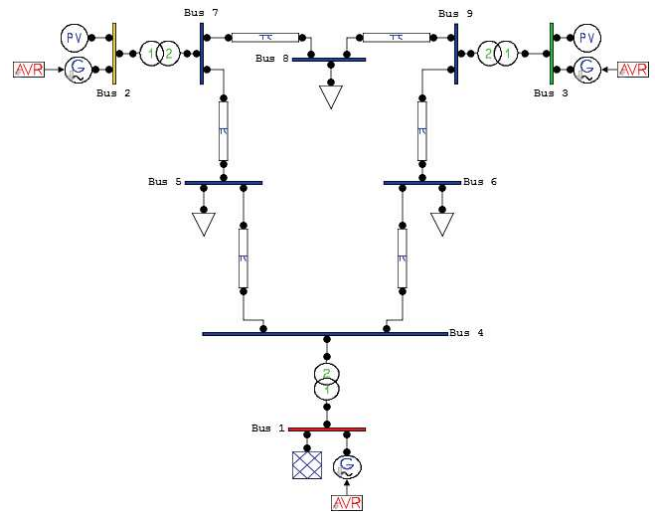

Fig. 3. IEEE 9-bus system.

A. With STATCOM

We are going to place the STATCOM at the same bus as the default or at the nearby buses so we have :

Case 1 : STATCOM At bus 7
Case 2 : STATCOM at bus 5
Case 3 : STATCOM at bus 8

Figure 4 illustrates the voltage improvement resulting from the implementation of the STATCOM at different locations.

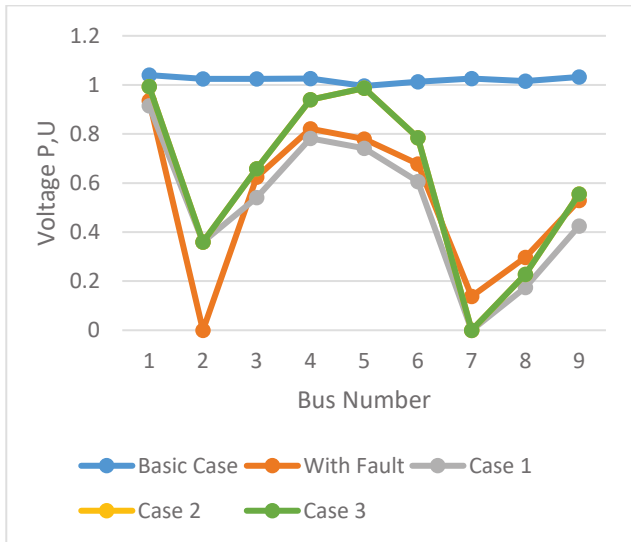It is evident that Case 3 presents the most significant voltage enhancement.

Fig. 4. Voltage improvement with STATCOM.

B. With TCSC

As a series device, the TCSC is now located between the nearby buses of the default where:

Case 1 : TCSC between bus 5 and 7
Case 2 : TCSC between bus 7 and 8
Case 3 : TCSC between bus 2 and 7

In Figure 5, the impact of implementing TCSC at various locations on voltage enhancement is illustrated.

Notably, Case 2 clearly shows the most significant improvement in voltage stability among the different situations.
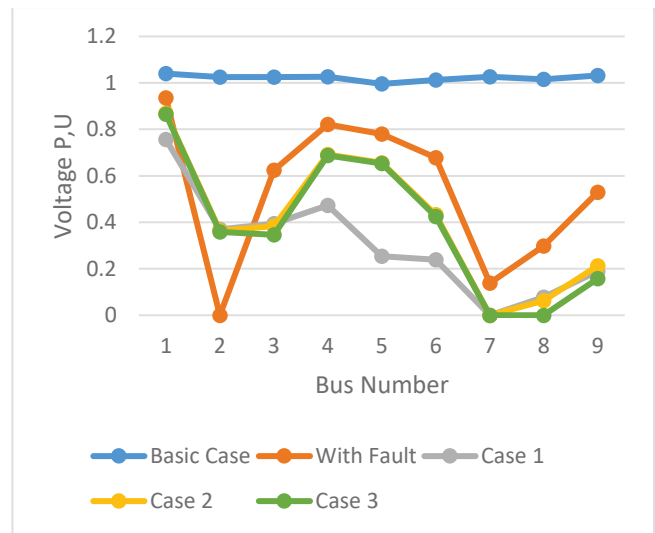

Fig. 5. Voltage improvement with TCSC.

Figure 6 illustrates a comparison between the optimal locations for both devices.

It is evident that the STATCOM significantly improves the voltage profile correction at the default location, outperforming TCSC.

Figure 7 presents the percentage reduction in active power losses achieved by both devices.

As previously mentioned, the STATCOM demonstrated superior voltage improvement as well as the most effective minimization of power losses.

In Table 1, the total active and reactive power achieved by each case is provided. It is worth noting that the best results for both STATCOM and TCSC devices are presented in this table.

It is evident that STATCOM outperforms TCSC, delivering superior results in both active and reactive power, as clearly indicated.
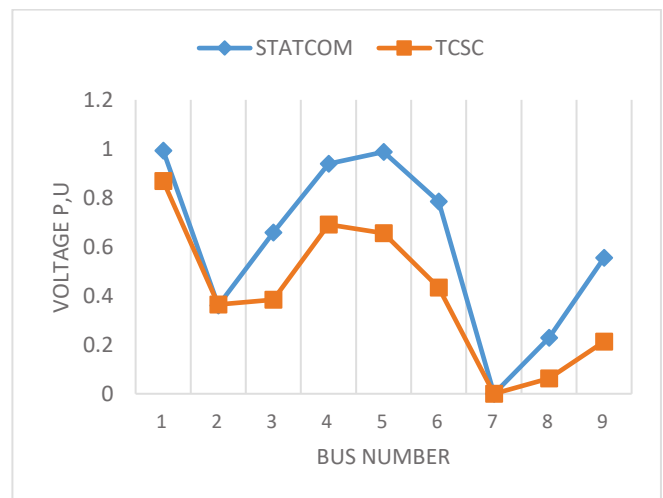

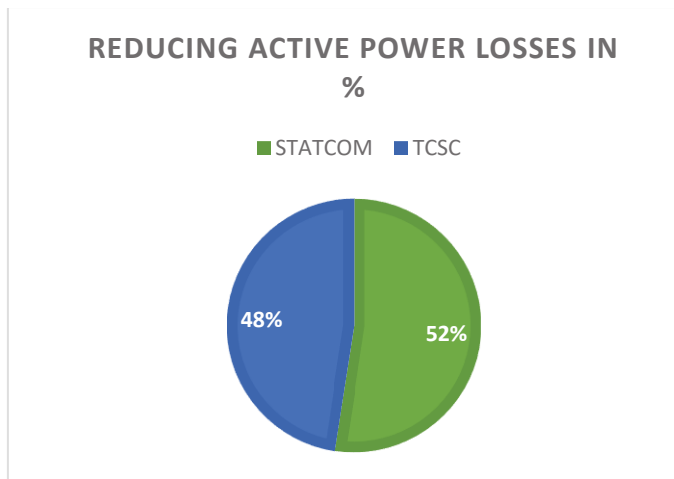Fig. 6. Comparison between STATCOM and TCSC.

Fig. 7. Minimization rate of the active power losses for each device.

TABLE I. TOTAL ACTIVE AND REACTIVE POWER LOSSES WITH DIFFRENTE CASES.

Cases	Total Active Power Losses Mw	Total Reactive Power Losses Mvar
Without fault	4,64	92,16
With fault	4,64	92,16
With TCSC	4,64	92,16
With STATCOM	4,22	75,66

IV. CONCLUSION

In conclusion, this study rigorously investigated the integration of Flexible AC Transmission System (FACTS) devices, specifically Static Synchronous Compensator (STATCOM) and Thyristor-Controlled Series Compensator (TCSC), within the IEEE 9-bus system. Through meticulous analysis and comparison, it became evident that STATCOM significantly outperformed TCSC in terms of voltage stability improvement and active power loss minimization.

Our performance metrics align seamlessly with the broader goals of enhancing energy efficiency and reducing carbon footprints. By optimizing power flow and stability, our integration approach supports the transition to sustainable energy solutions. It aids in minimizing energy wastage, making significant strides toward sustainability targets.

The integrating STATCOM and TCSC devices could face challenges in scenarios of rapid load fluctuations. The devices might need careful calibration to handle sudden changes, ensuring grid stability and voltage regulation. Additionally, situations with high renewable energy inputs might require strategic placement to maintain stability.

The integration of advanced FACTS technologies, as highlighted in our study, significantly enhances grid reliability and resilience. In the face of extreme weather events or other disruptive factors, these technologies provide rapid response capabilities. They stabilize the grid swiftly, mitigating risks and ensuring uninterrupted power supply to consumers.

REFERENCES

[1] Mistry KD, Roy R. "Enhancement of loading capacity of distribution system through distributed generator placement considering techno-economic benefits with load growth", Int J Electr Power Energy Syst vol 54, 2014, pp. 505–15,

[2] Verma K, Niazi K. "A coherency based generator rescheduling for preventive control of transient stability in power systems", Int J Electr Power Energy Syst, vol 45, 2013, pp.8-10.

[3] Sajjadi SM, Haghifam M-R, Salehi J. "Simultaneous placement of distributed generation and capacitors in distribution networks considering voltage stability index", Int J Electr Power Energy Syst ,vol 46, 2013, pp.366–75.

[4] Li G, Yue H, Zhou M, Wei J. "Probabilistic assessment of oscillatory stability margin of power systems incorporating wind farms", Int J Electr Power Energy Syst 2014, 58, pp.47–56.

[5] Nguimfack-Ndongmo JdD, Kenné G, Kuate-Fochie R, Cheukem A, Fotsin HB, Lamnabhi-Lagarrigue F. "A simplified nonlinear controller for transient stability enhancement of multimachine power systems using SSSC device". Int J Electr Power Energy Syst 2014,vol 54, pp. 650–7.

[6] R. Sirjani, and A. R. Jordehi, "Optimal placement and sizing of distribution static compensator (D-STATCOM) in electric distribution networks: A review," Renewable and Sustainable Energy Reviews, vol.77, pp. 688–694, 2017.

[7] M. E. El-Hawary, "The smart grid-state-of-the-art and future trends," Electric Power Components and Systems, vol. 42, no. 3-4, pp. 239–250, 2014.

[8] B. Stott, "Review of load-flow calculation methods," Proceedings of the IEEE, vol. 62, pp. 916-929,1974

[9] J. Arrillaga and C. Arnold, "Computer analysis of power systems" Wiley Online Library, 1990.

[10] Labed M.A., Zellagui M., Benidir M., Sekhane H., Tebbakh N. "Optimal hybrid photovoltaic distributed generation and distribution static synchronous compensators planning to minimize active power losses using adaptive acceleration coefficients particle swarm optimization algorithms", Electrical Engineering & Electromechanics, 2023, no. 6, pp. 84-90.

[11] LU Wei, " Optimal load shedding for the prevention of major power outages" Doctor from the Polytechnic Institute of Grenoble on July 6, 2009.

[12] Passelergue J.C., " Interactions of FACTS devices in large electrical networks" Doctoral thesis, Institut Nationale Polytechnique de Grenoble, 1998.